UNIVERSITÉ DE SHERBROOKE
Faculté de génie
Département de génie mécanique

Modélisation numérique des écoulements convectifs de nanofluides en régimes laminaire et turbulent

Numerical modeling of convective nanofluid flows in the laminar and turbulent regimes

Thèse de doctorat
Specialité: génie mécanique

Ghofrane Sekrani

Sherbrooke (Québec) Canada

October 2018

JURY MEMBERS

Prof. Sébastien Poncet (UdeS)
Supervisor

Prof. Pierre Proulx (UdeS)
Co-supervisor

Prof. Martin Désilets (UdeS)
Examiner

Prof. Alina Adriana Minea
(Gheorghe Asachi Tech. Univ. Iasi)
Examiner

Prof. Hachimi Fellouah (UdeS)
Examiner

RÉSUMÉ

Les transferts de chaleur par convection jouent un rôle important dans divers secteurs industriels tels que la climatisation, le transport, la production chimique, la microélectronique et la production d'électricité. Les fluides caloporteurs conventionnels tels que l'eau, l'éthylène glycol et l'huile sont caractérisés par des propriétés thermiques relativement limitées, ce qui réduit l'efficacité des systémes thermiques mis en jeu. L'avancée récente dans le domaine des nanotechnologies a donné naissance à un nouveau type de particules métalliques, et non métalliques, de tailles nanométriques, caractérisées par une conductivité thermique trés élevée. Ces particules, appelées nanoparticules, sont généralement dispersées dans un fluide de base et le mélange résultant constitue une nouvelle classe de fluides caloporteurs nommés nanofluides.

Le domaine des nanofluides est un champ de recherche très vivant et leur application dans les processus industriels devient de plus en plus répandue pour leurs remarquables propriétés optiques, magnétiques, diélectriques ou électromagnétiques. Dans le présent projet, seules les performances thermiques des nanofluides seront abordées.

Les nanofluides ont montré leur capacité à modifier les propriétés de transport et de transfert de chaleur du fluide de base, ce qui constitue un grand potentiel d'amélioration pour les processus de transfert de chaleur. Cependant, bien que l'ajout de nanoparticules solides aux fluides de base augmente leur conductivité thermique, cela s'accompagne d'une diminution de leur capacité calorifique et d'une augmentation de leur viscosité. Ceci entraine une augmentation de la puissance de pompage requise. Les coûts de production des nanoparticules et la difficulté à préparer des nanofluides stables dans le temps rendent, pour l'instant, l'application des nanofluides dans l'industrie encore limitée.

Dans ce contexte, l'objectif principal de ce projet de recherche est d'évaluer en détail les caractéristiques d'écoulements de nanofluides et les paramètres clés affectant leur performance dans le processus de transfert de chaleur. Pour ce faire, des modèles numériques ont été développés puis validés soigneusement avec des données issues de la littérature pour des écoulements convectifs en régimes laminaire et turbulent. Bien que les configurations choisies soient relativement canoniques, elles permettent d'évaluer les possibles avantages des nanofluides dans des systèmes thermiques industriels et d'étudier l'influence des principaux paramètres de contrôle, comme le débit d'entrée et la fraction en nanoparticules entre autres.

Mots-clés : Nanofluides, Écoulements en conduite et canal, CFD, Transfert Thermique, Turbulence, Indices de performance.

ABSTRACT

Convective heat transfer plays an important role in various industrial sectors such as air-conditioning, transportation, chemical production, microelectronics or power generation. Conventional heat transfer fluids such as water, ethylene glycol or oil exhibit relatively limited heat transfer properties, which hinders the efficiency of thermal systems. The recent advances in the field of nanotechnology gave rise to a new class of nanometeric metallic and non-metallic particles characterized by their substantially higher thermal conductivities. These particles, referred as nanoparticles, are dispersed into a conventional fluid, creating a new class of heat transfer fluids named nanofluids.

The study of nanofluids is a viable research field and their application in various industrial processes becomes more widespread due to their thermal, optical, magnetic, and electromagnetic properties. In the present study, only the thermal efficiency of nanofluids will be investigated.

Nanofluids have shown their ability to enhance the heat transfer performances of the host fluid, which constitutes a great potential to increase the energetic efficiency of thermal systems. However, adding solid nanoparticles to a base fluid would not only increase its thermal conductivity but, it is also accompanied with a decrease of its heat capacity and an increase of its dynamic viscosity, which may lead to an increased required pumping power. The two main drawbacks of nanofluids, which limit their use in industrial systems remain the prohibitive cost to produce nanoparticles and the difficulty to prepare and stabilize nanofluids over a wide life cycle.

In this context the main objective of this research project is to study in detail the nanofluid flow characteristics and the key parameters affecting their performance in heat transfer process. To this end, Computational Fluid Dynamics techniques are used to propose a numerical model able to simulate nanofluid flows taking into account several phenomena due to the presence of the nanoparticles into a base fluid and then evaluate the benefits from their using in industrial applications.

Keywords: Nanofluids, Pipe and channel flows, CFD, Heat Transfer, Turbulence, Performance criteria.

"Loving others is how we access true reality and affect every atom of the Universe. That is nanotechnology. This is the blueprint to immortality. And its time is now"
-Rav Berg

ACKNOWLEDGEMENTS

I would like to sincerely thank my supervisor, Prof. Sébastien Poncet, for the patient guidance, encouragement and advice he has provided me throughout my time as his student. I have been extremely lucky to have a supervisor who cared so much about my work, and who responded to my questions and queries so promptly. You have set an example of excellence as a researcher, mentor, instructor, and role model. I am very grateful for the opportunity to be a member of your research group.

I am also indebted to my co-supervisor, Prof. Pierre Proulx, for all of his guidance over the course of this PhD work. Your enthusiasm, inspiring ideas, and insightful feedback have been absolutely invaluable.

To the examiners: Prof. Adriana Minea, Prof. Hachimi Fellouah and Prof. Martin Désilets, thank you for accepting to be members of my PhD thesis committee. It is a honour to submit my work to the views of academics whom I consider references in their fields.

I would like to extend my heartfelt gratitude to my family for their continuous love, support and encouragement over the years, no matter the path I chose to take. In particular, I would like to thank my two lovely sisters, Sabrine and Nada, and my kindest aunt, Rym. You are the salt of the Earth and the light of the world.

I must also express my gratitude to my dearest parents, Houcine and Amal, from whom I learned patience, ambition, perseverance and perfection. Without your support, I would have never had the courage to overcome the adversities and hardships of life. Despite the thousands miles between us, I still take your lessons with me, every day. I look forward to seeing you soon! Love you always.

I would like to show my appreciation to all of my friends and colleagues with whom I have shared great memories during my time at Sherbrooke. Special thanks to Marouen and Sergio for their valuable assistance whenever I needed them.

Last but not least, I would like to thank and dedicate this thesis to my unique brother, Yassine, who is the number one reason I was able to achieve my dream to be a Doctor of mechanical engineering. I truly appreciate everything that you have done to provide me with a pleasant and comfortable environment so I can focus on achieving my dreams. I undoubtedly could not have done this without your help and support. You are and you will always be my source of inspiration.

TABLE OF CONTENTS

LIST OF FIGURES

LIST OF TABLES

GLOSSARY

Terme technique	**Définition**
C_p	heat capacity, $J.kg^{-1}.K^{-1}$
C_k, C_μ	constants, $-$
f	friction coefficient, $-$
h	heat transfer coefficient, $W.m^{-2}.K^{-1}$
k	thermal conductivity, $W.m^{-1}.K^{-1}$
L	pipe length, m
Mo	Mouromtseff number, $-$
Nu	Nusselt number, $-$
p	pressure, Pa
Pr	Prandtl number, $-$
Q	heat flux, W
Re	Reynolds number, $-$
T	temperature, K
U, V, W	components of the mean velocity vector, $m.s^{-1}$

LIST OF SYMBOLS

Symbole	**Définition**
α	particle Biot number, $-$
Δ	difference
η	overall energetic efficiency, $-$
φ	particle volume fraction, $m^{-3}.m^{-3}$
μ	dynamic viscosity, $Pa.s$
μ_T	turbulent dynamic viscosity, $Pa.s$
ν	kinematic viscosity, $m^2.s^{-1}$
ν_T	turbulent kinematic viscosity, $m^2.s^{-1}$
ρ	density, $kg.m^{-3}$
τ	shear stress, Pa

LIST OF ACRONYMS

Acronyme	**Définition**
bf	refers to base fluid
m	mean quantity
av	average
nf	refers to nanofluid
np	refers to nanoparticle
DNS	Direct Numerical Simulation
LES	Large Eddy Simulation
PEC	Performance Evaluation Criterion
RANS	Reynolds-Averaged Navier-Stokes
RNG	ReNormalization Group
RSM	Reynolds Stress Model
SST	Shear Stress Transport
VOF	Volume Of Fluid

CHAPTER 1

INTRODUCTION

1.1 Background and motivation

Heat transfer is one of the most important processes in many industrial applications, such as microelectronics, transportation, manufacturing, metrology, defense, and energy supply industries due to the increase in energy demand and prices. However, the inherent low thermal conductivity of conventional fluids, such as water, oils, and ethylene glycol, is a primary limitation for the development of efficient and compact engineering equipment and especially heat transfer systems [96].

The Maxwell's theory [148] showed that an enhancement of the thermal conductivity may be achieved by dispersing millimeter or micrometer-sized solid particles into a base fluid. However one major drawback associated with the use of such large size particles is their rapid settling, which may result into a complete separation of the two phases along with the clogging of heat exchangers due to the sedimentation of the solid aggregates formed by the large size particles. This type of solid-fluid suspensions requires also the addition of a large number of particles resulting in significantly greater pressure drop, hence increased pumping power, corrosion of the walls and a noticeable increase in the wall shear stress.

Recent advances in nanotechnology have led to the manufacturing of nanometer-sized particles referred to as nanoparticles. The latter has an equivalent diameter lower than 100 nm. In 1995, a new class of heat transfer fluids named nanofluids has been then suggested by dispersing nanoparticles in traditional host fluids [47]. As opposed to milli- or micro-sized suspensions, more stable suspensions may be achieved by introducing nanoparticles. Moreover, the former benefit from over hundred times larger surface/volume ratio than that of microparticles and exhibit much higher thermal conductivity than that of base fluids [102].

Nanofluids have attracted the attention of many researchers as well as engineers all over the word because of their capability to improve the thermal conductivity of the working fluids which can lead to a higher energy efficiency and a better performance of the system. Therefore, several experimental and numerical studies have been conducted to explore the mechanisms involved in the convective heat transfer processes of nanofluids.

The first step in this direction is to better understand the mixture flow characteristics and the forces acting between solid and liquid phases. To this purpose, Computational

Fluid Dynamics (CFD) techniques have proven to be an excellent tool, providing much more details than what can be attained by experimental methods, even if their reliability is dependant on the quality of the assumptions required to achieve a computationally feasible model. This is particularly true for heat transfer with nanofluid where the internal flow complexity has prevented a definite consensus on a reliable benchmarked numerical approach for their study owing to different reasons. Firstly, the determination of appropriate correlations for the nanofluid thermophysical properties becomes a major issue for the simulation process because of their diversity in the literature. Moreover, there is still not a clear consensus on the appropriate numerical approach (single versus two-phase model, choice of the turbulence closure ...) to model nanofluids. To date, most models account for the main nanoparticle properties such as their shape, size, material and volume concentration but it is important to take into account also other phenomena such as the Brownian motion, the thermophoresis, the stability of the solution, the viscous drag force and friction, among other parameters.
Therefore, the present thesis is an attempt to overcome some of these issues: firstly select the suitable numerical approach to model nanofluid flows, secondly use the appropriate nanofluid thermophysical properties, and then, investigate the effect of different parameters on the hydrodynamic and thermal fields, namely the nanoparticle type and size and the Reynolds number. To this end, two different canonical configurations for which reliable experimental or analytical results are available in the literature are considered: an uniformly heated cylindrical pipe (purely forced convection) and a heated wall-mounted obstacle in a rectangular channel (conjugated conduction/convection).

1.2 Objectives and originality

The utmost purpose of this project is first to develop an efficient numerical model dedicated to convective nanofluid flows then to evaluate in detail the main nanofluid flow characteristics and their effect on the heat transfer performance. To this end, the following points are introduced and discussed:

- Carry out laminar forced convection computations of nanofluid flows using direct numerical simulation and quantify the influence of the nanoparticles diameter and type on the hydrodynamic and thermal fields with an emphasis on the sedimentation process.
- Develop useful empirical correlations for the friction coefficient and the average Nusselt number and extend them to a wide range of Reynolds numbers and volume fractions of nanoparticles.

- Perform a numerical benchmark combining different choices of multiphase and turbulence models for the modelling of convective heat transfer and nanofluid flows, determining the best compromise between accuracy and computational costs.
- Investigate the heat transfer performance and the entropy generation of nanofluids flowing within a 2D channel with a heated wall mounted obstacle (conjugated heat transfer).
- Discuss the benefit of using nanofluid for heat transfer enhancement regarding different merit criteria.

1.3 Thesis Outline

The thesis is organized in six chapters, as will be outlined further. Chapter 2 contains a review of the most relevant studies on the nanofluid properties, performance mechanisms and numerical approaches. Afterwards, the results on laminar forced convection of nanofluid flows in a uniformly heated pipe using direct numerical simulations will be discussed in Chapter 3, followed by the study on convective turbulent heat transfer of water-based Al_2O_3 nanofluids in an uniformly heated pipe in Chapter 4. The governing equations of different turbulence models, RANS, used in the previous chapter will be developed in Appendix A. In Chapter 5, a study of conjugated heat transfer and entropy generation of Al_2O_3–water nanofluid flows over a heated wall-mounted obstacle will be carried out. Finally, some concluding remarks and future perspectives will be presented in Chapter 6.

CHAPTER 2

State of the Art

In the recent years, nanofluids have attracted the attention of researchers and engineers due to their interesting thermophysical properties which make them an excellent candidate that can replace the classical thermal fluids such as water, oil and ethylene glycol. Despite their numerous advantages, the effectiveness of nanofluids at the industrial scale is still a subject of debate as inherent phenomena associated with nanofluid flows are yet to be investigated. Thereupon, this chapter will comprehensively review and critically discuss the most relevant studies existing in the literature on the nanofluid properties, as well as their applications, thermal performances and numerical modellings.

2.1 Nanofluid properties

Well dispersed nanoparticles even at low-volume fractions in a host fluid may enhance the mixture thermal conductivity, k_{nf}, over the base fluid values. For examples, Xian et al. [222] reported an enhancement up to 13% and 15 % of water thermal conductivity when adding 0.4% volume fraction of Al_2O_3 and Cu, respectively. An enhancement of about 34% of thermal conductivity was found by Liu et al. [135] by adding 3% volume fraction of alumina nanoparticles into water with mean diameter equal to 33 nm. Biercuk et al. [30] observed a 125% increase in thermal conductivity at 1% nanotube loading at room temperature. Though leading to a significant increase in thermal conductivity, adding nanoparticles to a base fluid can also lead to a decrease in the heat capacity [115, 185] and an increase in the dynamic viscosity of the mixture [115]. A compromise must then be found between the increase in thermal conductivity and the loss of heat storage capacity without consuming excessive pumping power.

The suspension of ultrafine particles into a base fluid can strongly alter the transport properties and the heat transfer performance of a given nanofluid. However, traditional models failed to provide satisfactory insights on the thermal properties of nanofluids, in particular the thermal conductivity and the dynamic viscosity. Recently, a large number of theoretical, experimental and numerical investigations have been undertaken to determine the appropriate correlations that can better describe the thermophysical properties of nanofluids.

2.1.1 Density

The enhancement in the nanofluid density can be represented by the mixture rule, firstly suggested for microscopic dispersions. The experimental results showed that the mixture rule can also be used for the mixtures containing nanosized particles. The nanofluid density can be expressed as:

$$\rho_{nf} = \rho_{np}\varphi + (1 - \varphi)\rho_{bf} \tag{2.1}$$

Pak and Cho [172] and Ho et al. [94] examined the validity of equation (2.1). They experimentally evaluated the density of Al_2O_3-water nanofluid at room temperature. They found an excellent agreement between the experimental data and the predicted values from Eq.(2.1) as illustrated in Figure 2.1.

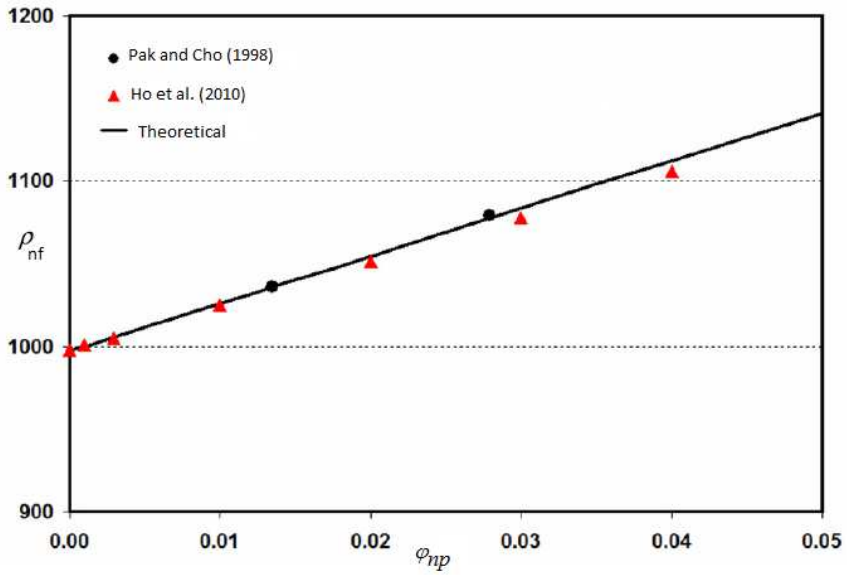

Figure 2.1 Effect of the volume fraction on the density of Al_2O_3-water nanofluid [115].

Khanafer and Vafai [115] developed a new correlation for the nanofluid density which was a function of the temperature and the nanoparticle volume fraction based on the experimental data of Ho et al. [94]. Their correlation can be expressed as:

$$\rho_{nf} = 1001.064 + 2738.6191\varphi - 0.2095T \tag{2.2}$$

where $0 \leq \varphi \leq 0.04$ and $5 \leq T^{\circ}(C) \leq 40$.
The maximum relative error was around 0.22%, and they found that the decreasing rate of the density of Al_2O_3-water nanofluid with increased temperature was insignificant.

2.1.2 Specific heat

To determine the nanofluid specific heat, there are two major correlations suggested by Pak and Cho (Eq.2.3) [172] and Xuan and Roetzel (Eq.2.4) [234]:

$$Cp_{nf} = Cp_{np}\varphi + (1-\varphi)Cp_{bf} \tag{2.3}$$

$$Cp_{nf} = \frac{\varphi(\rho Cp)_{np} + (1-\varphi)(\rho Cp)_{bf}}{\rho_{nf}} \tag{2.4}$$

The first correlation (Eq.2.3) is based on the mixture rule, which assumes that the equivalent specific heat is obtained by a simple volumetric combination of the specific heat of the components. Only few researchers have opted for this correlation in their studies [129, 160, 172]. The second correlation (Eq.2.4) is based on the assumption that there is a thermal equilibrium that exists between the nanoparticles and the base fluid. Thus, the nanofluid's specific heat can be defined from a thermal balance including the mixture rule. This equation has been widely used by [21], [4] or [192] among other references. Mansour et al. [146] evaluated the behavior of the two above-mentioned correlations to describe the specific heat of nanofluids. They found that both correlations provided significantly different results. However, they affirmed that the two expressions can be considered equivalent in the calculation of the nanofluid specific heat. On the other hand, O'Hanley et al. [168] and Khanafer and Vafai [115] claimed that the Xuan and Roetzel's correlation [234] can provide a better estimate of the nanofluid specific heat, as opposed to the Pak and Cho's correlation [172], which was found to overestimate the values of this property.

As opposed to the density and the specific heat, there are far more theoretical, experimental and numerical models existing in the literature for the evaluation of the dynamic viscosity and thermal conductivity of nanofluids as defined in the following sections.

2.1.3 Thermal conductivity

Thermal conductivity is an important parameter for the enhancement of the heat transfer performance of nanofluids. A wide range of experimental and theoretical studies were conducted in the literature to model the thermal conductivity of nanofluids. The classical models, originated from continuum formulation which typically involves the particle

size/shape and volume fraction and assumes diffusive heat transfer in both fluid and solid phases, have been used to predict the thermal conductivity of nanofluids. Since the model reported by Maxwell [148], other classical models have been suggested by Bruggeman [39], Hamilton and Crosser [86], Jeffery [103], Wasp [226], Davis [56], and Lu and Lin [138].
The Maxwell model was developed to determine the effective thermal conductivity of liquid-solid suspensions for low volumetric concentrations of spherical particles. This model is applicable to statistically homogeneous low volume fraction liquid-solid suspensions with randomly dispersed and uniform spherical particles in size and expressed as:

$$\frac{k_{nf}}{k_{bf}} = \frac{k_{np} + 2k_{bf} + 2\varphi(k_{np} - k_{bf})}{k_{np} + 2k_{bf} - \varphi(k_{np} - k_{bf})} \tag{2.5}$$

Bruggeman [39] suggested a model to study the interactions between random distributions of spherical particles and can be applicable for large volume fractions. The Bruggeman model can be written as follows:

$$\frac{k_{nf}}{k_{bf}} = \frac{(3\varphi - 1)\frac{k_{np}}{k_{bf}} + [3(1-\varphi) - 1] + \sqrt{\Delta}}{4} \tag{2.6}$$

where $\Delta = \left[(3\varphi - 1)\frac{k_{np}}{k_{bf}} + 3(1-\varphi) - 1\right]^2 + 8\frac{k_{np}}{k_{bf}}$.
For low particle volume fraction, the model of Bruggeman results in approximately the same results as of the Maxwell's model [148].
For non-spherical particles, Hamilton and Crosser [86] developed a model for the effective thermal conductivity of two-component mixtures. Their model was a function of the thermal conductivities of both base fluid and particle, particle volume fraction, particle type and particle shape. They considered also the nanoparticle aggregation. The Hamilton and Crosser model [86] can be expressed as follows:

$$\frac{k_{nf}}{k_{bf}} = \frac{k_{np} + (n-1)k_{bf} + (n-1)\varphi(k_{np} - k_{bf})}{k_{np} + (n-1)k_{bf} - \varphi(k_{np} - k_{bf})} \tag{2.7}$$

where n is an empirical shape factor given by $n = 3/\psi$, and ψ is the particle sphericity, defined by the ratio of the surface area of a sphere with volume equal to that of the particle, to the surface area of the particle. It is noteworthy that, when the particle sphericity is equal to unity (n=3), the Hamilton and Crosser's equation reduces to the Maxwell's model [148].
The Maxwell equation and derivatives have been used quite extensively, especially for early attempts on nanofluid flows. However, the most hindering drawbacks of these models are

their inability to take into account the important physical parameters such as temperature, particle size and Brownian motion. For instance, Dian [63] experimentally evaluated the ability of the classical models to predict the thermal conductivity of Al_2O_3- water nanofluid measured in a temperature range between 15 and 55°. They found a close agreement between the measured thermal conductivity and the Hamilton and Crosser [86] and the Bruggeman [39] models only at the low temperature (15°). However, the values predicted by the experiment departed from models with increased temperature, as illustrated in Figure 2.2. They concluded that the classical models cannot predict the observed enhanced thermal conductivity of nanofluids.

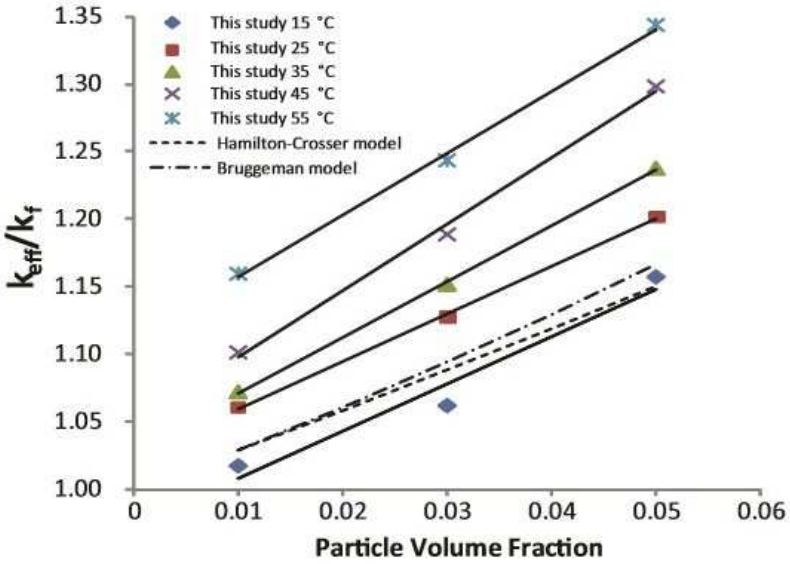

Figure 2.2 Thermal condutivity vs volume fraction of Al_2O_3 nanoparticles dispersed in water for different temperatures. [63].

The thermal conductivity of nanofluids is dependent on parameters associated with the characteristics of the base fluid and the nanoparticles (such as geometry, dimensions, and physical properties) and to the existing interactions between the nanoparticles and the base fluid (interfacial effects). The adequate description of these parameters allows the adequate characterization of the nanofluid. Therefore, a number of mechanisms have been studied to interpret the enhancement of the thermal conductivity including the volume fraction of nanoparticles, size, shape, Brownian motion, and liquid molecular layering. Despite of the numerous pertinent theoretical and empirical models for nanofluid thermal conductivity, the models are still limited to specific cases as shown in Table 2.1. Many researchers assessed the uncertainties in estimations of the nanofluid thermal conductivity and they noticed that the results depend on the used correlation. They also mentioned the

existence of a lot of uncertainties in determining thermal conductivity [155, 158]. For the same nanofluid type, Al_2O_3-water, they referred this discrepancy to the different initial condition and nanoparticles fabrication method .

Until today, there are no universal theoretical or empirical model available in the literature for predicting the nanofluid thermal conductivity. Therefore, there is a debate in the scientific community on the mechanisms involved in the heat transfer enhancement of nanofluids, which will be discussed in detail in the next section2.2.

Table 2.1 Summary of existing models for the thermal conductivity of nanofluids.

Model	Correlation	Relevant information
Lu and Lin [138]	$\frac{k_{nf}}{k_{bf}} = 1 + (k_{np}/k_{bf})\varphi + 2.27\varphi^2$	-Spherical and non-spherical particles
Jeffery [103]	$\frac{k_{nf}}{k_{bf}} = 1 + 3\eta\varphi + \varphi^2(3\eta^2 + \frac{3\eta^2}{4} + \frac{9\eta^3}{16}\frac{k+2}{2k+3} + ...)$	-High-order terms represent pair interactions of randomly dispersed spherical particles
Jang and Choi [101]	k_{nf}=$k_{bf}(1-\varphi)$ +$k_{np}\varphi$ +3C$\frac{d_{bf}}{d_{np}}$ $k_{bf}Re_d^2$ Pr φ	-Based on kinetics, Kapitza resistance and convection -Takes into account: the Brownian motion, temperature variation, nanoparticle size and volume fraction.
Chon et al. [48]	$\frac{k_{nf}}{k_{bf}} = 1 + 64.7\varphi^{0.74}\frac{d_{bf}}{d_{np}}^{0.369}\frac{k_{np}}{k_{bf}}^{0.747} \times Pr^{0.9955}Re^{1.2321}$ Re= $\frac{\rho_{bf}k_BT}{3\pi\mu_{bf}^2 l_{bf}}$	-Based on the Brownian motion
Bhattacharya et al. [24]	$\frac{k_{nf}}{k_{bf}} = \frac{K_{np}}{k_{bf}}\varphi + (1-\varphi)$	-Based on the Brownian motion
Koo and Kleinstreuer [120, 121]	$k_{nf} = k_{static} + k_{Brownian}$ $= \frac{k_{np}+2k_{bf}+2\varphi(k_{np}-k_{bf})}{k_{np}+2k_{bf}-\varphi(k_{np}-k_{bf})}k_{bf}$ $+5\times10^4\beta\varphi\rho_{np}c_p\sqrt{\frac{K_bT}{\rho_{np}D}}f(T,\varphi)$	-CuO/ethylene-glycol, CuO/water -Considers surrounding liquid travelling with randomly moving nanoparticles -Based on Brownian motion
Xue [235]	$\frac{k_{nf}}{k_{bf}} = \frac{1-\varphi+2\varphi\frac{k_{np}}{k_{np}-k_{bf}}ln\frac{k_{np}+k_{bf}}{2k_{bf}}}{1-\varphi+2\varphi\frac{k_{bf}}{k_{np}-k_{bf}}ln\frac{k_{np}+k_{bf}}{2k_{bf}}}$	-Nanospheres with interfacial shell
Prasher [178]	$\frac{k_{nf}}{k_{bf}} = (1+\mathrm{A}Re^mPr^{0.333}\varphi)\frac{k_{np}+2k_{bf}+2\varphi(k_{np}-k_{bf})}{k_{np}+2k_{bf}-\varphi(k_{np}-k_{bf})}$ A=40000 and m=2.5	-Accounts for convection caused by Brownian motion from particles
Murshed et al. [161]	$k_{nf} = \frac{(k_{np}-k_{lr})\varphi k_{lr}[\gamma_1^2-\gamma^2+1]+(k_{np}+k_{lr})\gamma_1^2[\varphi\gamma^2(k_{lr}-k_{bf})+k_{bf}]}{\gamma_1^2(k_{np}-k_{lr})-(k_{np}+k_{lr})\varphi[\gamma_1^2+\gamma^2-1]}$ $\gamma = 1 + \frac{t}{r_{np}}$ $\gamma_1 = 1 + \frac{t}{d_{np}}$	-Considers the effect of particle size, concentration and interfacial layer
Xuan et al. [233]	$\frac{k_{nf}}{k_{bf}} = \frac{k_{np}+2k_{bf}+2\varphi(k_{np}-k_{bf})}{k_{np}+2k_{bf}-\varphi(k_{np}-k_{bf})} + \frac{\rho_{np}\varphi C_p}{2k_{bf}}\sqrt{\frac{k_BT}{3\pi r_c\eta}}$	-Includes the effects of random motion, particle size, concentration and temperature
Li and Peterson [131]	$\frac{k_{nf}-k_{bf}}{k_{bf}} = 0.764\varphi + 0.0187(T-273.15) - 0.462$ $\frac{k_{nf}-k_{bf}}{k_{bf}} = 3.761\varphi + 0.0179(T-273.15) - 0.307$	-Al_2O_3/water nanofluid -CuO/water nanofluid
Buongiorno [41]	$\frac{k_{nf}}{k_{bf}} = 1 + 2.92\varphi - 11.99\varphi$	-TiO_2/water nanofluid
Maiga et al. [143]	$\frac{k_{nf}}{k_{bf}} = 1 + 2.72\ \varphi + 4.97\ \varphi^2$ $\frac{K_{nf}}{k_{bf}} = 1 + 2.8273\ \varphi + 28.905\ \varphi^2$	-Al_2O_3/water nanofluid -Al_2O_3/ethylene-glycol
Patel et al. [175]	$\frac{K_{nf}}{k_{bf}} = 1 + 0.135(\frac{k_{np}}{k_{fb}})^{0.273}\varphi^{0.467}(\frac{T}{20})^{0.547}(\frac{100}{d_{np}})^{0.234}$	-Oxide and metallic nanofluids
Timofeeva et al. [214]	$k_{nf} = (1+3\varphi)k_{bf}$	-Al_2O_3/water nanofluid
Duangthongsuk and Wongwises [64]	$\frac{k_{nf}}{k_{bf}} = \mathrm{a} + \mathrm{b}\varphi$ a=1.0225, b=0.0272 for T=15°C a=1.0204, b=0.0249 for T=25°C a=1.0139, b=0.0250 for T=35°C	-TiO_2/water nanofluid
Corcione [52]	$\frac{k_{nf}}{k_{bf}} = 1 + 4.4Re^{0.4}Pr^{0.66}(\frac{T}{T_{fr}})^{10}(\frac{k_{np}}{k_{bf}})^{0.234}\varphi^{0.66}$ T_{fr} is the freezing point of the base liquid	-Al_2O_3/water nanofluid
Godson et al. [82]	$\frac{k_{nf}}{k_{bf}} = 0.9508 + 0.9692\varphi$	-Ag/water nanofluid

2.1.4 Dynamic viscosity

The dynamic viscosity is one of the key properties of nanofluids. It is believed that the viscosity is as critical as the thermal conductivity in engineering system because it is expected that nanofluids increase the thermal conductivity of base fluids without increasing the pressure drop that may affect the process of the convective heat transfer. The prediction of the nanofluid viscosity has always been a challenging task that needed a special attention from researchers. There are several theoretical and empirical models to predict nanofluid viscosity that have been suggested in the literature.

Over the last few decades, only few theoretical models have been elaborated for the estimate of the particle suspension viscosities. It is very interesting to mention that almost all of the existing formulas were derived from Einstein's pioneering work [67] which was mainly based on the the assumption of a linear viscous behaviour of the fluid containing the dilute and suspended spherical particles. Einstein [67] calculated the energy dissipated by the fluid flow around a single particle, and associated with the work required to move this particle relatively to the surrounding fluid. His work led to the following formula:

$$\mu_{nf} = (1 + 2.5\varphi)\mu_{bf} \tag{2.8}$$

Einstein's correlation was found to be valid for relatively low particle volume fraction (less than 2%), however at higher concentrations, it underestimates the effective viscosity of the mixture.

Later, a substantial effort has been devoted to the "correction" of the Einstein's model. Brinkman [37] modified Einstein's formula to the following so that it can be used for moderate particle concentrations (up to 4 %):

$$\mu_{nf} = \frac{1}{(1-\varphi)^{2.5}}\mu_{bf} \tag{2.9}$$

Lundgren [139] proposed an equation under the form of a Taylor series of particle concentration:

$$\mu_{nf} = (1 + 2.5\varphi + 6.25\varphi^2 + O(\varphi^3))\mu_{bf} \tag{2.10}$$

If the terms $O(\varphi^2)$ and higher are to be neglected, the above correlation reduces to that of Einstein.

Batchelor [17] considered the effect of the Brownian motion of particles on the bulk stress of an approximately isotropic suspension of rigid and spherical particles. His work yielded

to the following expression:

$$\mu_{nf} = (1 + 2.5\varphi + 6.5\varphi^2)\mu_{bf} \tag{2.11}$$

Alternatively, Frankel and Acrivos [76] suggested the following expression:

$$\mu_{nf} = \frac{9}{8}\left[\frac{(\varphi/\varphi_m)^{1/3}}{1-(\varphi/\varphi_m)^{1/3}}\right]\mu_{bf} \tag{2.12}$$

where φ_m is the maximum particle volume fraction that guarantees the good dispersion of particles into the base fluids and it can be determined experimentally. Graham [83] generalized the work of Frankel and Acrivos [76] for low particle concentrations:

$$\mu_{nf} = (1 + 2.5\varphi)\mu_{bf} + \left[\frac{4.5}{(\frac{h}{r_{np}}).(2+\frac{h}{r_{np}}).(1+\frac{h}{r_{np}})^2}\right]\mu_{bf} \tag{2.13}$$

where r_{np} and h are the particle radius and the inter-particle spacing, respectively.
According to these correlations, the viscosity of nanofluid solely depends on the viscosity of the base fluid and the concentration of the particles, whereas experimental studies showed that many factors can affect the dynamic viscosity of nanofluids including the temperature, the particle size and shape, the shear rate, etc.
In general, all the previous analytical models can be used for the determination of the viscosity of the nanoparticle suspension. However, their validity for some applications remains highly questionable. In fact, Nguyen et al. [164] reported that Einstein, Brinkman, Lundgren and Batchelor models have all underestimated the nanofluid's viscosity even for a relatively low particle concentration. Compared to the experimental studies on the thermal conductivity of nanofluids, there are limited rheological investigations reported in the literature [5, 143, 157, 159, 225]. Among the few studies on the dynamic viscosity behavior, the issued addressed by researchers were mainly related to the factors influencing the nanofluid viscosity such as the bulk temperature, the Brownian motion, the size and shape of nanoparticles, etc. It is noteworthy that most of the experimental studies revealed an increase in the viscosity of mixtures with the addition of nanoparticles and this increase was found to be proportional to the particle volume fraction and inversely proportional to the bulk temperature [1, 5, 164, 173].
The formulation of unified theory that can reasonably predict the nanofluid viscosity behavior remains interesting challenge for researchers and the existing models of nanofluid's viscosity based on the experimental results are still limited to certain nanofluids under

specific conditions. A summary of the experimental models used for the estimate of the dynamic viscosity of nanofluids are listed in Table 2.2.

A good understanding of the rheological properties of nanofluids and their effect on the heat transfer processes is crucial for the design of more efficient and highly reliable heat exchangers.

Table 2.2 Summary of the experimental models for the determination of the dynamic viscosity of nanofluids.

Model	Correlation	Relevant information
Khanafer and Vafai [115]	μ_{nf} = -0.4491+$\frac{28.837}{T}$+0.574φ_{np} -0.1634φ_{np}^2+23.053$\frac{\varphi_{np}^2}{T^2}$ + 0.0132 φ_{np}^3-2354.735$\frac{\varphi_{np}}{T^3}$+23.498$\frac{\varphi_{np}^2}{d_{np}^2}-3.0185\frac{\varphi_{np}^3}{d_{np}^2}$	-Al_2O_3-water $1\% \leq \varphi \leq 9\%$ $20 \leq T^{\circ} \leq 70$, 13nm$\leq d_{np} \leq$131nm
	$\mu_{nf} = (1 + 3.544\varphi + 169.46\varphi^2)\ \mu_{bf}$	-TiO_2-water, d_{np} = 27nm, $0 \leq \varphi \leq 0.1$
Nguyen et al. [164]	$\mu_{nf} = 0.904\ e^{0.483\varphi}\ \mu_{bf}$	-Al_2O_3-water, $d_{np} = 47nm$
	$\mu_{nf} = (1 + 0.025\varphi + 0.015\varphi^2)\ \mu_{bf}$	-Al_2O_3-water, $d_{np} = 36nm$
	$\mu_{nf} = (1.475 - 0.319\varphi + 0.051\varphi^2 + 0.009\varphi^3)\ \mu_{bf}$	-CuO-water, $d_{np} = 29nm$
Buongiorno. [41]	$\mu_{nf} = (1 + 39\varphi + 533.9\varphi^2)\ \mu_{bf}$	-Al_2O_3-water, d_{np} = 13nm
	$\mu_{nf} = (1 + 5.45\varphi + 108.2\varphi^2)\ \mu_{bf}$	-TiO_2-water, d_{np} = 27nm
Maiga et al. [143]	$\mu_{nf} = (1 + 7.3\varphi + 123\varphi^2)\ \mu_{bf}$	-Al_2O_3-water, d_{np} = 28nm
	$\mu_{nf} = (1 - 0.19\varphi + 306\varphi^2)\ \mu_{bf}$	-Al_2O_3-Ethylene-glycol, d_{np} = 28nm
Moldoveanu et al. [157]	$\mu_{nf} = (4135\varphi^2 - 91.72\varphi + 2.06)\ \mu_{bf}$	-Al_2O_3-water
	$\mu_{nf} = (-769\varphi^2 + 42\varphi + 1.1)\ \mu_{bf}$	-SiO_2-water
	$\mu_{nf} = (5 \times 10^{-}6T^2 - 3 \times 10^{-3}T + 0.5)\ \mu_{bf}$	- 0.5% Al_2O_3 + 0.5% SiO_2-water
Palm et al. [173]	μ_{nf} = 0.034 - 2×10^{-}4T + 2.9×10^{-}7T^2	-Al_2O_3-water, φ = 1%
	μ_{nf} = 0.039 - 2.3×10^{-}4T + 3.4×10^{-}7T^2	-Al_2O_3-water, φ = 4%
Nguyen et al. [165]	μ_{nf} = (1.125 -0.0007×T)μ_{bf}	-φ = 1% for Al_2O_3, TiO_2 and CuO-water
	μ_{nf} = (2.1275 -0.0215×T + 0.0002 ×T^2)μ_{bf}	-φ = 4% for Al_2O_3, TiO_2 and CuO-water
Wang et al. [225]	$\mu_{nf} = (1 + 7.3\varphi + 123\varphi^2)\ \mu_{bf}$	-Al_2O_3-water and Al_2O_3-EG
Tseng and Lin [217]	μ_{nf} = 13.47exp(35.98φ)μ_{bf}	-TiO_2-water, $0.05 \leq \varphi \leq 0.12$
Drew and Passman [62]	$\mu_{nf} = (1 + 2.5\varphi)\mu_{bf}$	-$\varphi \leq 5\%$, Cu/water, Au, CNT, graphene
Song et al. [204]	$\mu_{nf} = (1 + 56.5\varphi)\mu_{bf}$	-SiO_2-water
Chen et al. [44]	$\mu_{nf} = (1 + 10.6\varphi + \varphi^2)\mu_{bf}$	-TiO_2-ethylene-glycol
Abu-Nada et al. [1]	μ_{nf} = -0.155 - $\frac{19.582}{T} + 0.794\varphi + \frac{2094.47}{T^2} - 0.192\varphi^2$ $-8.11\frac{\varphi}{T} - \frac{27463.863}{T^3} + 0.127\varphi^3 + 1.6044\frac{\varphi^2}{T} + 2.1754\frac{\varphi}{T^2}$	-Al_2O_3-water
Circione [52]	$\mu_{nf} = \frac{1}{1-34.84(d_p/d_f)^{-0.3}\varphi^{-1.03}}\ \mu_{bf}$	-SiO_2-ethanol

2.2 Parameters influencing the heat transfer enhancement

In nanoparticle-fluid mixtures, several mechanisms/parameters can strongly affect the heat transfer process such as the microscopic motion of the particles (Brownian motion), the particle structure and their surface properties.

2.2.1 Brownian motion

The random motion of nanoparticles within the base fluid is also called Brownian motion, and it results from continuous collisions between the nanoparticles and the molecules of the base fluid [68] as illustrated in Figure 2.3.

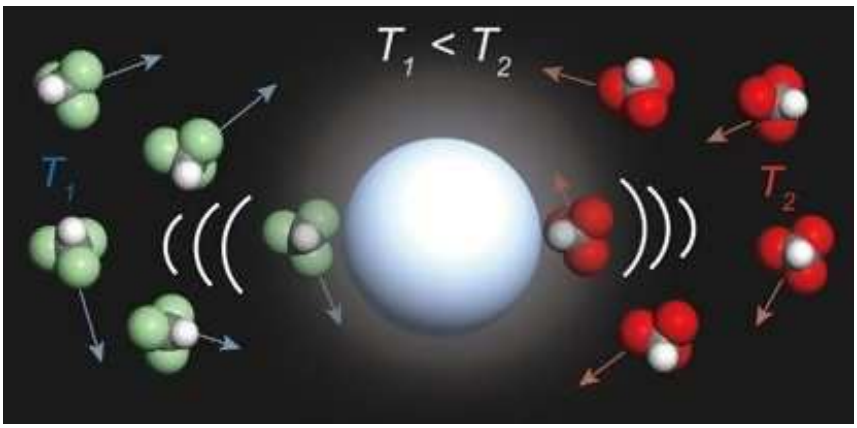

Figure 2.3 Brownian motion in non-equilibrium system [38].

The concept of Brownian motion suggests that the molecular collisions between particles are random and take place at the molecular time-scale, τ_M. During time periods of the order of the momentum timescale of the particle, the effects of the Brownian motion may be expressed as the action of a random force, $\vec{F}_{Br}$, which acts on the particle continuously. This force is opposed to the fluid drag. The equation of motion for the particle is defined as follows:

$$m_s \frac{d\vec{v}}{dt} = 6\pi\alpha\mu f_{K_n}(\vec{u} - \vec{v}) + \vec{F}_{Br}. \tag{2.14}$$

where f_{K_n} is the drag force which is a function of the Knudsen number of the particles, $K_n = \frac{K_B T}{\sqrt{2}\pi d^2 p L}$, m_s is the mass of particles and α is the radius of the particle.
When the fluid velocity does not change with time (steady motion), equation (2.14) becomes:

$$\frac{d}{dt}(\frac{d\vec{x}}{dt}) = -\frac{9\mu f_{K_n}}{2\alpha^2\rho_s}\frac{d\vec{x}}{dt} + \frac{3}{4\alpha^3\rho_s}\vec{F}_{Br}. \tag{2.15}$$

where ρ_s is the density of the particles.
In order to quantify the effects of the Brownian motion, one must quantify the random force, $\vec{F}_{Br}$, on the velocity and position of the nanoparticles. The motion of the particles in the fluid does not have a preferred direction and the ensemble-average displacement of the particles is:

$$\frac{d}{dt}\langle\vec{x}.\frac{d\vec{x}}{dt}\rangle = \frac{9k_BT}{8\alpha^3\rho_s} - \frac{9\mu f_{K_n}}{2\alpha^2\rho_s}\langle\vec{x}.\frac{d\vec{x}}{dt}\rangle \tag{2.16}$$

where K_B is the Boltzmann constant.
The initial conditions of equation (2.16) are that the particle position and velocity are equal to zero. Therefore, the last expression may be integrated twice to yield the following expression for the ensemble-averaged dispersion of the particle:

$$\langle\vec{x}.\vec{x}\rangle = \frac{2k_BT}{6\pi\alpha\mu f_{K_n}} \tag{2.17}$$

It is noteworthy that the particle dispersion, due to the Brownian motion, is independent of the density and the other characteristics of the particle and only depends on the size of the particle and the form of the hydrodynamic drag. The dispersion coefficient, D_0, is defined as half the derivative of the Brownian dispersion. The dispersion of an isolated spherical particle can be written as follows:

$$D_0 = \frac{d}{2dt}\langle\vec{x}.\vec{x}\rangle = \frac{k_BT}{6\pi\alpha\mu f_{K_n}} \tag{2.18}$$

Therefore, in order to simulate appropriately the Brownian motion, a User Defined Function (UDF) should be added into the specific simulation code and it is desirable to perform a Lagrangian simulation for the motion of an ensemble of particles. A computational time interval Δt is chosen a priori for the numerical integration of the particle motion. Δt is typically much higher than the characteristic time of molecular collisions. To incorporate simply and practically the effects of the Brownian motion on the Lagrangian trajectories of the particles, the time-averaged dispersion of the particles should be equal to the value predicted by equation (2.18). Consequently, the random force is equal to:

$$\vec{F}_{Br} = \frac{4}{3}\alpha^3\rho_s\vec{R}\sqrt{\frac{2k_BT}{6\pi\alpha\mu f_{K_n}}} \tag{2.19}$$

where $\vec{R}$ is a random vector, whose components are Gaussian random numbers with zero mean and unit variance.

Jang et al. [101] were the first to describe the Brownian motion of nanoparticles as a key mechanism governing the thermal behavior of nanofluids. Buongiorno [41] developed an alternative model to explain the abnormal convective heat transfer enhancement in nanofluids, while considered seven slip mechanisms: the inertia, Brownian diffusion, thermophoresis, diffusiophoresis, Magnus effect, fluid drainage, and gravity. He also claimed that, over these seven mechanisms, only the Brownian diffusion and thermophoresis are the important slip mechanisms in nanofluids [41]. In order to evaluate the Brownian motion effect on the heat transfer performance, Tarybakhsh et al. [210] investigated numerically the laminar forced convective flow of Al_2O_3-water nanofluid in a tube under constant wall temperature condition. The results showed that the Brownian motion of nanoparticles significantly affected the macroconvection heat transfer capability of the nanofluid by inducing microconvection/mixing and by varying the viscosity of nanofluids. They found that the hydrodynamic interaction between the nanoparticles strongly enhanced the thermal transport capability and assumed that the Brownian motion is one of the key factors responsible for the high effective thermal convection of nanofluids. Haris et al. [90] evaluated a laminar fully developed convective heat transfer of Al_2O_3-water nanofluid inside a circular tube. They claimed that the random motion of nanoparticles can alter the structure of the flow field and led to heat transfer enhancement.
The Brownian motion was found to be the key factor in the heat transfer performance by several research groups. However, other investigators claimed that the random motion has little effects on the heat transfer performance. In this context, Keblinski et al. [112] evaluated four possible explanations for the anomalous increase in heat transfer which were: Brownian motion of the particles, molecular-level layering of liquid/particle interface, the nature of heat transport in the nanoparticles, and the effects of nanoparticle clustering. They affirmed that Brownian motion is not a significant mechanism in the enhancement of heat conduction. Wang and Xu [225] assessed experimentally different possible microscopic energy transport mechanisms in nanofluids and concluded that the Brownian motion does not contribute to the energy transport in nanoparticle-fluid mixtures as they found that at 10 % alumina volume fraction, the thermal conductivity increased by roughly 0.5 % when taking into account Brownian motion.

2.2.2 Thermophoretic force

The thermophoretic force on nanoparticles arises from the presence of a temperature gradient in the fluid causing the concentration of nanoparticles to change around the heating and cooling sides relative to the mean value as shown in Figure 2.4.

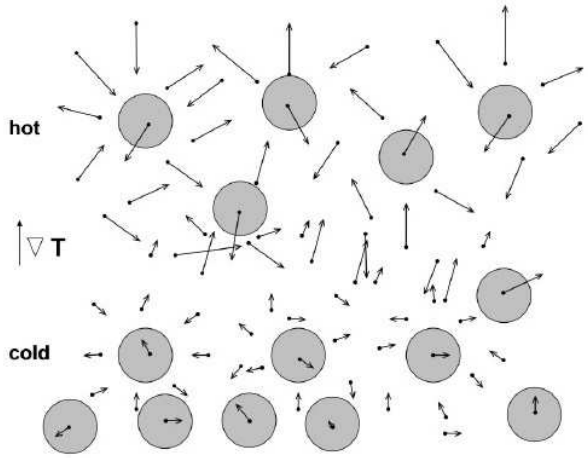

Figure 2.4 Thermophoretic motion of small spherical particles [153].

Figure 2.4 illustrates that when there is a temperature gradient in the particulate system, small particles tend to disperse faster in hotter region and slower in colder region, which causes an accumulation of particles in the colder region.
The effect of thermophoresis on small particles is often expressed in terms of a thermophoretic velocity, υ_{tp}, or of a thermophoretic force, F_{tp} [153]. The two act in the direction opposite to the temperature gradient and are defined as follows:

$$\upsilon_{tp} = -k_{tp}\frac{\mu f_{kn}}{\rho_f}\frac{\nabla T}{T_\infty} \tag{2.20}$$

and

$$F_{tp} = -6\pi\mu^2 f_{tp}\alpha K_{tp}\frac{\nabla T}{\rho_f T_\infty} \tag{2.21}$$

The function K_{tp} depends on the Knudsen number, K_n, and the properties of the fluid and of the solid particles. In nanofluid flow, both base fluid and particles can be treated as a continuum where the motion of the particles affects the fluid velocity field. According to this model, the discontinuities (slip) in both velocity and temperature fields are likely to manifest in the interface region between particles and fluid. In this region, the type of particle motion as well as the discontinuity can greatly affect the function K_{tp}. The latter can be expressed in terms of the Knudsen number, K_n, as well as both velocity and temperature slips as follows:

$$K_{tp} = \frac{2C_s(k_f + 2k_s K_n)}{(1 + 6C_m K_n)(2k_f + k_s + 4k_s C_t K_n)} \tag{2.22}$$

The parameters C_n, C_m and C_t are determined empirically from the flow field around the particles and the discontinuities on the fluid-particle interface. When $K_n \leq 0.1$, $C_n = 1.17$,

$C_m = 1.14$ and $C_t = 2.18$ [153]. A group of researchers paid attention to the effect of this force on the heat transfer enhancement of nanofluid, since the nanoparticles redistribution can affect the heat transfer coefficient [228]. Aminfar and Motallebzadeh [9] numerically investigated the influence of Brownian motion, gravity and thermophoretic forces on the Al_2O_3 nanoparticle concentration distribution and velocity field. They noted that the distribution of the nanoparticle concentration was inhomogenous throughout the pipe. They affirmed that the factors leading to the non homogeneity of the concentration were the Brownian motion and, to a lesser degree, the thermophoretic force. It has been found that the thermophoretic force affected the nanoparticle velocity close to the wall region more than in the centerline region and this is due to the difference in the temperature gradient between the upper and the lower sides of the tube. The effect of the nanoparticle diffusion in a fully developed laminar forced convection of alumina-water nanofluid in a microchannel has been studied theoretically by Hedayati et al. [88]. They found that the Brownian and the thermophoretic forces possess important and opposite role. In that, whenever the nanoparticle concentration gradient is developed by the thermophoretic force, the Brownian motion tends to counter balance the former effect which helps maintaining the dispersion of the nanoparticles into the base fluid over a longer time period. Koo and Kleinstreuer [121] investigated the effects of the Brownian and the thermophoretic forces on the effective thermal conductivity. They noted that the effect of the Brownian force was significantly more important than that of the thermophoretic one.
A large number of studies found that the thermophoretic force has a little effect on the thermal transport behavior compared to the Brownian motion, but it is still important enough to be taken into account so that its effect on the heat transfer mechanisms will be closely evaluated.

2.2.3 Nanoparticle aggregation

The different forces acting on the nanofluids may cause an agglomeration phenomenon and may produce clusters of different sizes which affect the heat transfer in different ways. In fact, nanofluids contain at least four scales [221]: the molecular, the micro, the meso, and the macroscale. It was shown that the spatial distribution of particles and the formation of aggregates can strongly affect the thermal transport properties of nanofluids [77, 153, 178, 214, 232]. Figure 2.5 clearly illustrates the aggregation of suspensions in the form of chains which create several highly conducting paths (or bridges) that can conduct heat more effectively [153].

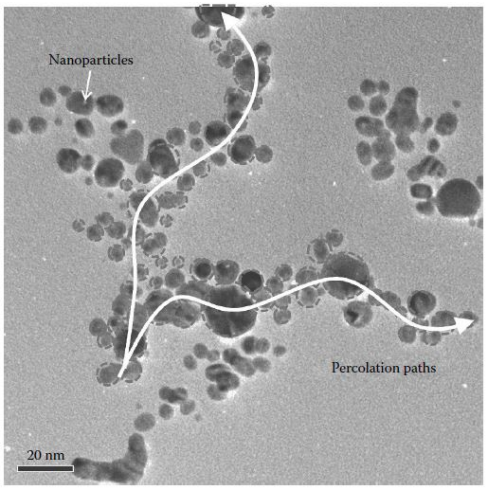

Figure 2.5 Schematic of aggregation model and thermal percolation paths [130].

The aggregation is a complex process and the size distribution of the aggregates play a significant role in the transport of energy within nanofluids. In order to model the aggregation process one may combine the forces acting on pairs of particles in a single potential energy function, Φ, which represents the net potential resulting from all the attractive and repulsive forces [153] as illustrated in Figure 2.6. This figure plots the potential function in dimensionless form versus the interparticle distance, δ, and it is illustrated that the potential function exhibits a high-energy minimum followed by a lower-energy local maximum and a low-energy secondary minimum.

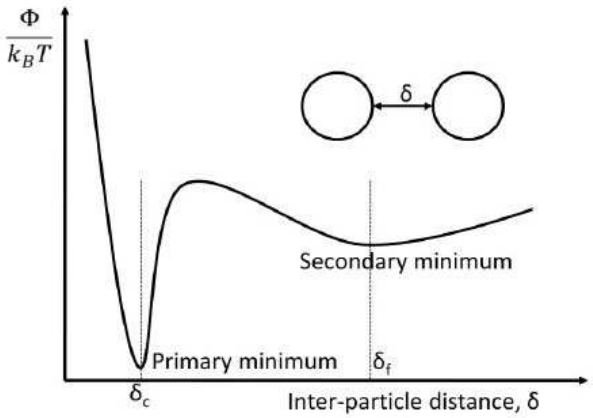

Figure 2.6 Inter-particle potential for the particle-particle interactions [153].

The inter-particle distances corresponding to the two minima, δ_c and δ_f, define two stable configurations of the aggregate system of particles [153]. Simple energetic considerations prove that when the inter-particle distance corresponds to the primary minimum, δ_c, the

bonds formed between the particles are very strong. This binding process is called coagulation, and the bonds of the coagulants that are formed are very strong. The bonds corresponding to the secondary minimum, δ_f, are weaker bonds, the aggregation process at this point is known as flocculation and the clusters formed as flocs. The binding forces of flocs are weak.

Therefore, clustering in nanofluids is unavoidable and must be considered since the formation of aggregates of particles influences significantly the internal structure of the suspension and this has an effect on the transport properties of nanofluids. He et al. [87] evaluated the effect of the nanoparticle aggregation. They found that the aggregation of small nanoparticles tends to greatly increase the heat transfer rate, particularly at lower Reynolds numbers. Liu et al. [135] assessed different mechanisms that can affect the nanofluid thermal conductivity. They found that the aggregate nanoparticle size has a positive effect on the enhancement of the thermal conductivity and then in the heat transfer performance. They attributed this behavior to the fact that the increase in aggregate size can offer a fast heat transfer path for adjacent particles. Philip et al. [177] suggested that nanofluids containing well dispersed nanoparticles, without aggregates, did not exhibit a significant enhancement of the heat transfer rate, while the maximum enhancement was observed when chain-like aggregates were uniformly dispersed without clumping.

On other hand, some researchers disagreed with the positive effect of nanoparticle aggregation. For example, Xuan et al. [233] showed that the nanoparticle aggregation and the formation of aggregates reduced the efficiency of the energy transport enhancement of the suspended nanoparticles. Karthikeyan et al. [110] experimentally evaluated the formation of clusters. They dispersed 5% volume fraction of CuO with a mean diameter of 36 nm, and they observed just after few minutes that the nanoparticles were agglomerated and formed clusters as large as few micrometers. They reported that the increase of the cluster size was accompanied by an increase in the sedimentation rate, and consequently the heat transfer rate was reduced. The effect of the nanoparticle aggregation on the enhancement of the heat transfer with nanofluids is still under debate and is not conclusive.

2.2.4 Type of nanofluid

The type of nanoparticles can strongly affect the nanofluid properties such as viscosity, thermal conductivity and heat capacity, which can greatly influence the heat transfer performance. Heris et al. [91] numerically investigated the convective heat transfer of three water-based nanofluids flowing through a square duct in the laminar regime with constant boundary conditions. They noted that the type of the nanoparticles substantially affected the thermal transport rate of nanofluids. Their results showed that the Nusselt number

increased by up to 77%, 68% and 59% for Cu, CuO and Al_2O_3 nanofluids, respectively, compared to pure water. The turbulent convection heat transfer of three different nanofluids namely CuO, Al_2O_3 and SiO_2, dispersed in ethylene-glycol/water mixture and flowing through a uniformly heated circular tube, have been investigated by Namburu et al. [162]. They claimed that the heat transfer enhancement strongly depends on the nature of the nanofluids. At a fixed volume fraction of 6%, they found that the heat transfer coefficient was higher for the CuO nanofluid, and lower for the SiO_2 nanofluids. They attributed their findings to the higher Prandtl number and the thermal conductivity of CuO-water nanofluid compared to the remaining ones. Hussein et al. [98] measured the heat transfer enhancement of a forced convection of TiO_2 and SiO_2 nanofluids suspended in water inside a flat copper tube. They found a significant heat transfer enhancement. At 4% nanoparticle concentration, the Nusselt number increased by 11% and 22.5% for TiO_2 and SiO_2, respectively, compared to pure water. The reader can refer to the monograph of Bianco et al. [29] for a detailed review.

2.2.5 Nanoparticle size

It is worthy to note that nanoparticles are often characterized with large distributions. Overall, the enhancement is mainly related to the standard deviation of the particles size distribution. Therefore, the role of the nanoparticle size on the thermal transport behavior of nanofluids can not be overlooked as discussed in [8] or in [101]. These authors found that the size of the particles may affect the mechanisms involved in the heat transfer such as the Brownian and the thermophoresis forces. Jang and Choi [102] showed that the nanofluid thermal conductivity depends on the nanoparticle size and directly affects the Brownian motion of nanoparticles. They affirmed that as the size of nanoparticles decreased, the Brownian motion of nanoparticles becomes greater, which enhances the heat transfer rate since from equation (2.18) it is clear that the Brownian diffusion coefficient is inversely proportional to the nanoparticle diameter. This implies that the reduction of particle size can increase the probability of collisions between molecules of host fluid and nanoparticles and creates a quasi-convection state at certain small zone between molecules of base fluid and nanoparticles and thus leads to better heat transfer rate [211]. Heris et al. [91] also investigated the effect of Al_2O_3 diameter on the heat transfer process. They observed that the Nusselt number decreased from 6.35 to 5.6 when the alumina's diameter increased from 10 to 50 nm at a volume fraction of 0.5%. In their experimental study Putra et al. [180] reported that the thermal conductivity was enhanced by decreasing the particle diameter. Their results indicated that the increase in the thermal conductivity of nanofluids is related

to the size, the shape of nanoparticles, surface area and the thermal conductivity of the base fluid.

2.3 Numerical Simulations

The enhanced heat transfer potential of base fluids can offer the possibility to develop highly compact and effective heat transfer equipment for many industrial applications including electronics, transportation and biomedicine. In that, several experimental studies have been conducted to explore the mechanisms involved in the convective heat transfer processes of nanofluids. Despite its promising results, experimental work remains a challenging and costly process, which require complex arrangements and specific instrumentations. In essence, Computational Fluid Dynamics (CFD) has been proven to be an important numerical tool to study fluid flow characteristics especially in nanofluid fields. The numerical models may be divided into two categories: the single-phase (SP) and the two-phase models.

2.3.1 Single-phase model

The single-phase model treats the nanofluid as a homogenous fluid, since the nanoparticles suspended in the base fluid are very small ($10 \leq d_{np} \leq 100\ nm$) and largely affected by the Brownian motion [90, 210]. For this reason, the nanoparticles can be easily fluidized and it is assumed that the base fluid and the solid nanoparticles are in thermal equilibrium and the relative velocity between the phases is zero. The conservation equations of this model are similar to the homogenous fluid with effective thermophysical properties which are predicted by using theoretical models and/or empirical correlations assuming Newtonian fluids, incompressible. The governing equations are as below:

* Conservation of mass

$$\nabla \cdot (\rho_{eff} \vec{V}) = 0 \tag{2.23}$$

* Conservation of momentum

$$\rho_{eff} \vec{V} \cdot \nabla \vec{V} = -\nabla P + \nabla \cdot (\mu_{eff} \nabla \vec{V}) + \rho_{eff} \nabla g \tag{2.24}$$

* Conservation of energy

$$\rho_{eff} \nabla \cdot (\vec{V} H) = -\nabla \cdot q - \tau : \nabla \vec{V} \tag{2.25}$$

where eff referred to effective.

The single-phase model showed its ability to predict the experimental data as found by [4],

[14] and [26]. This approach has been attracted the attention of many researchers due to its simplicity and also it requires less time of calculation than other approaches. The main challenge in the single-phase model is the calculation of the nanofluid properties, since in the literature there are many theoretical, experimental and numerical models available. In fact, some numerical studies showed that different properties models provide different results [4, 26, 125, 162]. In addition, the single-phase model has also some limitation, such as the assumption that the nanoparticles are easily fluidized and that the different forces acting on nanofluids such as the friction between the fluid and the solid particles, sedimentation, thermophoresis, etc, are neglected. For these reasons, many researchers have used two-phase approach to achieve a better prediction of nanofluid flows and to better understand the heat transfer mechanisms in nanofluids.
A review on the researches (numerical studies) performed using single-phase model is detailed in Chapters 3 and 4.

2.3.2 Two-phase models

In order to gain a better understanding of the heat transfer processes in nanofluids, a large number of researchers used two phase models where the slip velocity between the particles and the base fluid may not be zero as a result of the Brownian forces, the Brownian diffusion, the sedimentation and the dispersion of nanoparticles.
The two-phase model can be described by two approaches, namely; the Eulerian-Eulerian and the Eulerian-Lagrangian.

A) **Eulerian-Eulerian method.**

In CFD, there are there different Eulerian-Eulerian methods including volume of fluid (VOF), Eulerian and mixture.

- **VOF:**

The VOF model solves a single set of momentum equations for all phases and tracks their volume fraction throughout the domain of study by solving the continuity equation for the secondary phases. The total summation of the volume fractions for all the phases is equal to unity. Therefore, the magnitude of the primary phase volume fraction can be easily evaluated. Using this method, all the thermophysical properties are calculated by taking a weighted average of the different phases based on their volume fraction within each control volume. The single set of momentum equations is solved to evaluate the velocity components which are common for all the phases. In the same manner, a common temperature is calculated from a single energy equation [4].
The conservation of mass can be expressed as follows:

$$\nabla.(\varphi_q \rho_q V_q) = 0 \tag{2.26}$$

where $\sum_{q=1}^{n} \varphi_q = 1$ and all properties are calculated like N = $\sum_{q=1}^{n} \varphi_q N_q$.
The momentum and energy equations are identical to equations (2.24) and (2.25).
A very limited number of researches applied the VOF method for nanofluid flows. Morajevi and Ardehali [160] performed a three-dimensional numerical simulation of a laminar forced convection of Al_2O_3-water nanofluid inside a mini-channel heat sink. Their findings showed that the VOF model was in a better agreement with the experimntal results than the single-phase model. Akbari et al. [3] studied a laminar flow of Al_2O_3-water nanofluid under a constant wall heat flux boundary condition. They conducted a comparative study between the single and the two-phase approaches using VOF, mixture and Eulerian models. They found that the two-phase models provided closer prediction of the convective heat transfer coefficients to the experimental data than the single-phase model. The results showed that the two-phase approaches were all essentially the same, however, the authors recommended the VOF model since it was the less computationally expensive model. Davarnejad and Jamshidzadeh [55] numerically investigated a turbulent convective heat transfer flow of a MgO-water nanofluid comparing the predictions of three CFD models including SP, VOF and mixture approaches. Their results showed that the two phase models provided more accurate results than the SP approach, particularly at higher nanoparticle volume fractions, where the average deviation from the experimental data was about 2% and 11%, respectively. Further studies are still needed in order to determine the capability of the VOF model in predicting nanofluid flows.

– **Mixture model:**

The mixture model is assuming that the coupling between phases is strong, and particles follow the flow. The two phases are considered to be interpenetrating, meaning that each phase has its own velocity, vector field, and within any control volume. There is a volume fraction of primary phase and also a volume fraction of the secondary phase wherein the sum of volume fractions of different phases is equal to one. In the mixture model, the primary phase influences the secondary phase via drag and turbulence, while the secondary phase in turn influences the primary phase via reduction in mean momentum and turbulence. The mixture model considers that only one setoff velocity component is solved from the differential equations for mixture momentum conservation and the velocities of dispersed phases are inferred from the algebraic balance equations.
The mixture model is based on the following assumptions [160]:

∗ A single pressure is shared by all phases.

* The secondary dispersed phases are assumed to consist in spherical particles of uniform particle size being specified during calculations.
* The interactions between different dispersed phases are neglected.
* The concentrations of the secondary dispersed phases are solved from scalar equations taking into account the correction due to phase slip.

The governing equations describing the mixture approach and a detailed review on the use of this model are presented in Chapters 3 and 4.

– **Eulerian method:**

In the Eulerian model there are different kinds of coupling between phases. The pressure is shared by all the phases, while separate continuity, momentum, and energy equations are employed for different phases including primary and secondary phases. The volume of each phase is calculated by integrating its volume fraction throughout the domain, while the summation of all the volume fractions is equal to unity [4]. The relevant equations are:

* Conservation of mass

$$\nabla \cdot (\varphi_q \rho_q \vec{V_q}) = 0 \tag{2.27}$$

where $\vec{V_q}$=$\int_a \varphi_q$ dV, and $\sum_{q=1}^{n} \varphi_q$=1

* Conservation of momentum (q^{th} phase)

$$\nabla \cdot (\varphi_q \rho_q \vec{V} \vec{V}) = \varphi_q \nabla P + \varphi_q \nabla \cdot (\mu_q \nabla \vec{V}) + \varphi_q \rho_q \vec{g} + \sum_{p=1}^{n} \vec{R_{pq}} + \vec{F_{lift,q}} \tag{2.28}$$

where, $\sum_{p=1}^{n} \vec{R_{pq}} = \sum_{p=1}^{n} S_{pq}(\vec{V_p} - \vec{V_q})$ represent the interaction forces between the phases, S_{pq}=$(\varphi_q \varphi_p \rho_q f)/\tau_p$ where $\tau_p = (\rho_p d_p^2)/(18\ \mu_q)$ and f denotes the drag friction. f is calculated according to Shiller and Naumann [190] as:

$$f = \frac{C_p Re}{24} \tag{2.29}$$

where

$$C_D = \begin{cases} \frac{24(1+0.16Re^{0.687})}{Re} & Re_p \leq 1000 \\ 0.44 & Re_p > 1000 \end{cases} \tag{2.30}$$

and

$$Re = \frac{\rho_q \mid \vec{V_p} - \vec{V_q} \mid d_p}{\mu_q} \tag{2.31}$$

The lift force can be calculated from the Drew and Lahey equation [61]:

$$\vec{F_{lift,q}} = -0.5\rho_p\varphi_q(\vec{V_p} - \vec{V_q}) \times (\nabla\vec{V_q}) \tag{2.32}$$

∗ Conservation of energy

$$\nabla \cdot (\varphi_q\rho_q\vec{V_q}H_q) = -\nabla \cdot (K_q\nabla \cdot T_q) - \tau_q : \nabla\vec{V_q} + \sum_{p=1}^{n}\vec{Q_{pq}} \tag{2.33}$$

where $\vec{Q_{pq}}$= h ($\vec{V_p}$ - $\vec{V_q}$) and the heat exchange coefficient is h = $(6K_q\varphi_q\varphi_pNu_p)/d_p^2$. Nu_p is determined from the Ranz and Marshal [181] model:

$$Nu_p = 2 + 0.6Re^0.5Pr_q^{0.333} \tag{2.34}$$

where Pr_q=$(Cp_q\mu_q)/k_q$.

In the literature, there are few numerical studies based on the Eulerian method. Lotfi et al [137] were the first who implemented the two phase Eulerian approach to study nanofluid flows. They investigated the turbulent forced convection of Al_2O_3-water nanofluid in a horizontal tube by using single-phase, mixture and Eulerian approaches. The results showed that the mixture model predicted more accurately the experimental data more than the two others models, and that the single-phase and the Eulerian models underestimated the Nusselt number. The Eulerian two-phase model has been considered to simulate a laminar forced convection of copper-water nanofluid inside a microchannel by Kalteh et al [109]. They observed that the relative velocity and temperature difference between phases were negligible and the nanoparticle volume concentration distribution was uniform. They claimed that the Eulerian model gave higher heat transfer enhancement in comparison to the single-phase approach. They noted that the most important advantage of the Eulerian two-phase model in comparison to homogenous model is that it does not need to select appropriate nanofluid thermophysical property correlations. In their other study of laminar convection of alumina-water nanofluid flow inside a heat skin, Kalteh et al. [108], found the same behavior of the Eulerian model which was in better agreement with experimental results than the single-phase model, the maximum deviation from experimental values were 12.61% and 7.42% for homogenous and two-phase methods, respectively. They concluded that the Eulerian model is more appropriate than the homogenous model to simulate nanofluids.

B) **Eulerian-Lagrangian method.**

In the Eulerian-Lagrangian approach, the fluid is considered as a continuous phase with disperse particles inside it, where the particles are tracked in a Lagrangian frame, while the fluid is evaluated in the Eulerian frame. To ensure that the fluid phase can be considered as continuous, a Knudsen number should be calculated as follow: $K_n = \lambda/d_p$, where λ indicates molecular mean free path. The interaction between the fluid and the particles is introduced as source term in momentum and energy equations. The governing equations are:

* Conservation of mass

$$\nabla \cdot (\rho_q V_f) = 0 \tag{2.35}$$

* Conservation of momentum

$$\nabla \cdot (\rho_f V_f V_f) = -\nabla P + \nabla \cdot (\mu_f \nabla V_f) + S_{p,m} \tag{2.36}$$

* Conservation of energy

$$\nabla \cdot (\rho_f C p_f V_f T) = \nabla \cdot (k_f \nabla T_f) + S_{p,e} \tag{2.37}$$

where $S_{(p,m)}$ is the source term which represents the momentum transfer between the fluid and the particles and can be evaluated by calculating momentum variation of particles as they move through the fluid phase. $S_{(p,e)}$ is the source term which represents the energy transfer between the fluid and the particles and can calculated from the energy variation of particles as they move through the fluid phase. $S_{(p,m)}$ and $S_{(p,e)}$ are defined as below [108]:

$$S_{p,m} = \sum n_p \frac{m_p}{\delta V} F \tag{2.38}$$

$$S_{p,e} = \sum n_p \frac{m_p}{\delta V} C_p \frac{dT_p}{dt} \tag{2.39}$$

where F and m_p are the total force per unit mass of the particle acting on it and the mass of the particle, respectively, and n_p is the number of solid particles within a cell volume. F is the total forces which can affect the flow such as gravity, drag force, magnetic force, Brownian force, thermophoretic force, Saffman's lift force and virtual mass force.
The energy equation for the particles is defined as follows:

$$m_p C_{p,p} \frac{dT_p}{dt} = Nu_p \pi d_p k_f (T_f - T_p) \tag{2.40}$$

where Nu_p can be evaluated using the equation (2.34) proposed by Ranz and Marshall [181].

The Eulerian-Lagrangian approach (called Euler-Discrete Phase Model (DPM)) has been used by few researchers in the nanofluid fields. A comparison between Eulerian-Lagrangian and single-phase approaches was carried out by He et al. [87] to investigate the effects of Reynolds number, nanoparticle concentration and various nanoparticle aggregate sizes on laminar flow of TiO_2-water nanofluid inside a tube. The heat transfer coefficient calculated by Euler-Discrete Phase Model (DPM) was higher than that calculated with the single-phase approach. They referred this difference to the consideration of nanoparticle movement and their interaction with the base fluid using the Euler-DPM approach. In order to compare the predictions between single-phase and Eulerian-Lagrangian models, Bianco et al. [27] noted that the results obtained by the Eulerian-Lagrangian approach were slightly more accurate than those gave by the single-phase approach with a maximum difference in the average heat transfer coefficient between the two approaches was about 11%. Mahdavi et al. [140] studied numerically the heat transfer of three types of nanofluids consisting of Alumina, Zirconia and Silica nanoparticles dispersed in water flowing in a vertical tube. Both the mixture model and the discrete phase model were used to estimate the thermal and hydrodynamic behaviors of nanofluids. They highly recommended the DPM to simulate heat transfer in a vertical tube with laminar nanofluid flows. They compared the predictions of mixture and DPM models and they cited many benefit as following:

* Mixture model results highly depend on transport properties coming from experimentation however, there is no need to employ the mixture properties for DPM and it only needs appropriate interaction or diffusion forces, empirical or analytical.
* Mixture considers nanofluid as two phases, but DPM considers the nanofluid as fluid and solid, as it is in the reality.
* Effects of slip mechanism like Thermophoresis and Brownian forces can be seen as diffusion terms in mixture equations and need to be implemented in program. On the other hand, in DPM, the velocity is calculated for fluid and solid separately and eventually the relative velocity between them has the key role.

Nevertheless, even if DPM models correctly the nanofluid flow, it is still weak to simulate higher nanoparticles loading due to inclusion of other phenomena such as aggregation and clustering.
An excellent review on different numerical approaches for nanofluid simulation can be found in references [15] and [107].

CHAPTER 3

Further Investigation on Laminar Forced Convection of Nanofluid Flows in a Uniformly Heated Pipe using Direct Numerical Simulations

3.1 Avant-propos

Auteurs et affiliations:

1. Ghofrane Sekrani: étudiante au doctorat*
2. Sébastien Poncet: Professeur agrégé*

*Université de Sherbrooke, Faculté de génie, Département de génie mécanique.

Date d'acceptation: 26 octobre 2016.

État de l'acceptation: version finale publiée le 2 novembre 2016.

Revue: Applied Sciences.

Titre en français:

Simulations numériques directes de la convection forcée pour des écoulements de nanofluides en régime laminaire dans un tube uniformément chauffé.

Contribution au document: Cet article contribue à la thèse en mettant en évidence l'effet du choix des modèles numériques (monophasique ou diphasique) sur la prédiction des transferts de chaleur dans un tube uniformément chauffé pour des écoulements de nanofluides en régime laminaire. Les résultats permettent en outre de quantifier l'influence du diamètre et du type de nanoparticules sur les champs hydrodynamiques et thermiques, en mettant l'accent sur le phénomène de sédimentation.

Résumé en français: Dans le présent article, les écoulements laminaires de nanofluides ont été étudiés dans un tube horizontal uniformément chauffé en régime de convection forcée par simulations numériques directes. Deux modèles, monophasique et diphasique, avec des propriétés thermophysiques constantes ou dépendantes de la température ont été utilisés. Dans tous les cas étudiés, des comparaisons avec les données expérimentales ont montré que le modèle de mélange fonctionne mieux que le modèle monophasique. Les propriétés du fluide dépendantes de la température ont également montré une meilleure prédiction du champ thermique. Une attention particulière a été accordée à l'indépendance du maillage. Par la suite, le modèle diphasique a été utilisé pour étudier l'influence de la taille des nanoparticules sur le flux de chaleur et l'écoulement du fluide, en mettant l'accent sur le processus de sédimentation. Quatre diamètres de nanoparticules ont été considérés: 10, 42, 100 et 200 nm pour des nanofluides cuivre-eau et alumine-eau. Pour le plus grand diamètre $d_{np} = 200$ nm, les nanoparticules de Cu étaient plus sédimentées d'environ 80%, tandis que les nanoparticules d'Al_2O_3 ne sédimentaient que de 2.5%. En outre, il a été constaté que l'augmentation du nombre de Reynolds améliore le taux de transfert thermique, tandis qu'il diminue le coefficient de frottement permettant aux nanoparticules de rester plus dispersées dans le fluide de base. L'effet du type de nanoparticules sur le coefficient de transfert thermique a également été étudié pour six différents nanofluides à base d'eau. Les résultats ont montré que le nanofluide Cu-eau possède le coefficient de transfert thermique le plus élevé, suivi par C, Al_2O_3, CuO, TiO_2 et SiO_2, respectivement. Tous les résultats ont été présentés et discutés pour quatre valeurs différentes de la concentration en nanoparticules, $\varphi = 0$, 0.6%, 1% et 1.6%. Des corrélations empiriques pour le coefficient de frottement et le nombre de Nusselt moyen ont également été fournies et synthétisent tous les résultats présentés.

Mots clés: Nanofluide, simulation numérique, transfert de chaleur, sédimentation.

Abstract:

In the present paper, laminar forced convection nanofluid flows in a uniformly heated horizontal tube were revisited by direct numerical simulations. Single and two-phase models were employed with constant and temperature-dependent properties. Comparisons with experimental data showed that the mixture model performs better than the single-phase model in the all cases studied. Temperature-dependent fluid properties also resulted in a better prediction of the thermal field. A particular attention was paid to the grid arrangement. The two-phase model was used then confidently to investigate the influence of the nanoparticle size on the heat and fluid flow with a particular emphasis on the sedimentation process. Four nanoparticle diameters were considered: 10, 42, 100 and 200 nm for both copper-water and alumina/water nanofluids. For the largest diameter $d_{np} = 200\ nm$, the Cu nanoparticles were more sedimented by around 80 %, while the Al_2O_3 nanoparticles sedimented only by 2.5 %. Besides, it was found that increasing the Reynolds number improved the heat transfer rate, while it decreased the friction factor allowing the nanoparticles to stay more dispersed in the base fluid. The effect of nanoparticle type on the heat transfer coefficient was also investigated for six different water-based nanofluids. Results showed that the Cu-water nanofluid achieved the highest heat transfer coefficient, followed by C, Al_2O_3, CuO, TiO_2, and SiO_2, respectively. All results were presented and discussed for four different values of the concentration in nanoparticles, namely $\varphi = 0$, 0.6, 1 and 1.6%. Empirical correlations for the friction coefficient and the average Nusselt number were also provided summarizing all the presented results.

Keywords: Nanofluid, numerical simulation, heat transfer, sedimentation.

3.2 Introduction

Heat transfer is one of the most important processes in many industrial and heating-cooling applications, such as microelectronics, transportation, manufacturing, metrology, defense, and energy supply industries [96, 231]. However, the inherent low thermal conductivity of conventional fluids, such as water, oils, and ethylene glycol, is a primary limitation in developing efficient heat transfer systems. The Maxwell's theory [148] showed that an enhancement of the thermal conductivity may be achieved by dispersing millimeter or micrometer-sized solid particles into a base fluid. However one major drawback associated with the use of such large size particles is their rapid settling, which may result into a complete separation of the two phases along with the clogging of heat exchangers due to the sedimentation of the solid aggregates formed by the large size particles. This type of solid-fluid suspensions requires also the addition of a large number of particles resulting in significantly greater pressure drop, hence increased pumping power, corrosion of the walls and a noticeable increase in the wall shear stress. Thus, Choi and Eastman [47] suggested a novel approach to enhance heat transfer processes in industrial applications by exploiting the properties of nanoparticles and their dispersion in a host fluid. These metallic or non-metallic nanoparticles have an equivalent diameter d_{np} lower than 100 nm. As opposed to milli- or microsized suspensions, very stable suspensions may be achieved by introducing nanoparticles. Moreover, nanoparticles benefit from a 10^3 times larger surface/volume ratio than that of microparticles and exhibit much higher thermal conductivity than that of base fluids. For examples, the thermal conductivities of copper or alumina at room temperature are about 670 and 70 times greater than that of water, respectively [102]. On the contrary, it leads most of the time to a decrease in the heat capacity [115, 185] and an increase in the dynamic viscosity of the mixture [115]. A compromise must be then found between the increase in thermal conductivity without loosing too much heat storage capacity and consuming too much power for pumping. If well stabilized, nanofluids represent nowadays a major technological and economical challenge and should offer very interesting perspectives for any heat transfer process.

The exponential increase in the number of publications about nanofluids [29] prevents from making an exhaustive state-of-the-art review on the topic. Many authors concentrated on measuring the thermophysical properties of various nanofluids showing that their properties depend on a large number of parameters such as the type of nanoparticle, their size, their mass or volume fraction, the type and the concentration of the surfactant, the pH of the mixture, the Brownian motion and the thickness of the interfacial nanolayer among other parameters (see in [29, 54, 107, 115, 185]). Others developed experimental set-ups

to measure the convective heat transfer and temperature profiles in pipes [93, 227], coaxial [85] or plate [147] heat exchangers among other geometries. Most authors focused on measuring global thermal quantities due to the difficulty to measure velocity and temperature profiles in such insulated systems. It has relatively slowed down the development of accurate models dedicated to nanofluid flows, especially regarding the agglomeration and sedimentation processes.

Only few in-house solvers have been developed to investigate convective nanofluid flows. Most of them assume the flow as being a single-phase flow with constant or variable nanofluid properties in canonical configurations. For example, Mehrez et *al*. [150] numerically investigated the entropy generation and the mixed convection heat transfer of copper/water-based nanofluids in an inclined open cavity with uniform heat flux at the wall. During the last decade, many other authors compared the performance of the different single and two-phase models with constant or temperature-dependent properties in the context of nanofluid flows [3, 14, 20, 26, 125, 137]. A detailed state-of-the-art review has been besides recently proposed by Kakaç and Pramuanjaroenkij [107]. Bianco *et al*. [26] compared the predictions of single and two-phase models (discrete phase model) with constant or temperature-dependent properties for a laminar forced convection flow of Al_2O_3/water-based nanofluids. They concluded that models with temperature-dependent properties lead to higher values of the heat transfer coefficient and Nusselt number, while decreasing the wall shear stress. With variable properties and for a volume fraction of Al_2O_3 nanoparticles equal to 4%, similar results have been found using single- and two-phase models with a maximum difference of 11%. On the contrary, Lotfi *et al*. [137] showed that the mixture model performs better than the single-phase model and the Eulerian one. Akbari *et al*. [3] compared three different two-phase models and a single-phase model to the experiments of Wen and Ding [227] for Al_2O_3/water-based nanofluids. The mixture, Volume of Fluid (VOF) and Eulerian models provided very similar results for the thermal field, while the single-phase model strongly underestimated the heat transfer coefficient. No clear consensus arises then from these former studies on the choice of the appropriate single- or two-phase flow models. Some attempts have also been achieved to investigate the influence of constant or variable thermophysical properties on the performances of single-phase flow models. In that, Labonté *et al*. [125] showed that the model with constant properties tends to underestimate the wall shear stress and overestimate the heat transfer coefficient. Azari *et al*. [14] found that the single-phase model with constant physical properties provides an acceptable agreement with the experimental data and the temperature-dependent model improves the predictions of the discrete two-phase flow model for low volume fractions in nanoparticles, typically $\varphi = 0.03\%$. On the contrary,

at higher particle concentrations $\varphi = 3.5\%$, the two-phase flow performs best. Numerical modeling of laminar convective nanofluid flows even in relatively simple geometries remains very challenging, since the choice of the single- or two-phase flow models appears to be very case dependent.

Analytical models have also been developed to investigate the entropy generation in similar configurations. For example, one could cite the recent work of Bianco et *al*. [28], who investigated the entropy generation of Al_2O_3-water nanofluid turbulent forced convection in a pipe with constant wall temperature by means of a second law analysis. They showed in particular that the type of inlet conditions greatly influences the mechanisms responsible for entropy generation. Such analysis could be then very helpful to optimize nanofluid flows from an exergetic point of view.

The present paper focuses on the convective heat transfer in a cylindrical pipe for laminar flows of Al_2O_3/water-based nanofluids. This choice is justified by the large number of former works using this nanofluid in a similar flow configuration (laminar or developing flows in a pipe with constant heat flux) [11, 99]. Moreover, such nanofluid is of a particular interest due to its non-corrosive properties and its good thermal conductivity enhancement using very low volume fractions in nanoparticles. For examples, Wang and Li [222] obtained an enhancement of 13% using only a volume fraction equal to 0.4% and Liu *et al*. [135] measured an increase of 34% for a nanoparticle diameter equal to 33 nm and a volume fraction of 3%. The reader can refer to the reviews by Kakaç and Pramuanjaroenkij [106, 107] for more details about the thermal enhancement using nanofluids.

The objective of the present paper is four-fold: (1) to properly revisit the laminar forced convection flows of Al_2O_3/water-based nanofluids using direct numerical simulations; (2) to extend the results to a wider range of Reynolds numbers as proposed by [3]; (3) to quantify the influence of the nanoparticle diameter and the type of nanoparticle on the hydrodynamic and thermal fields with an emphasis on the sedimentation process; (4) to provide useful empirical correlations for the friction coefficient and average Nusselt number. The experimental set-up developed by Wen and Ding [227] and the former numerical simulations of Akbari *et al*. [3] using the same model have been chosen for comparisons in the case of Al_2O_3/water-based nanofluids with the present simulations. The paper is then organized as follows: the numerical modeling and its validation are presented in Sections 3.3 and 3.4 respectively. The influence of the Reynolds number, the concentration in nanoparticles, their diameter and the type of nanoparticles on the heat transfer process and the hydrodynamic field are then discussed in details in Section 3.5, before some concluding remarks in Section 5.5.

3.3 Numerical approach

Three-dimensional calculations are carried out in the case of forced convection nanofluid flows in a heated pipe. Single- and two-phase flow models are both considered with constant or temperature-dependent properties using a finite-volume solver.

3.3.1 Geometrical modeling

The problem under consideration involves nanoparticles of diameter d_{np} perfectly monodispersed in pure liquid water. The geometry corresponds to the experimental set-up developed by Wen and Ding [227]. It consists of a horizontal cylindrical pipe of a length $L = 0.97$ m and a diameter $D = 2R = 0.0045$ m, heated with a uniform heat flux $q_w = 21898\ W.m^{-2}$ along the wall (Figure 3.1).

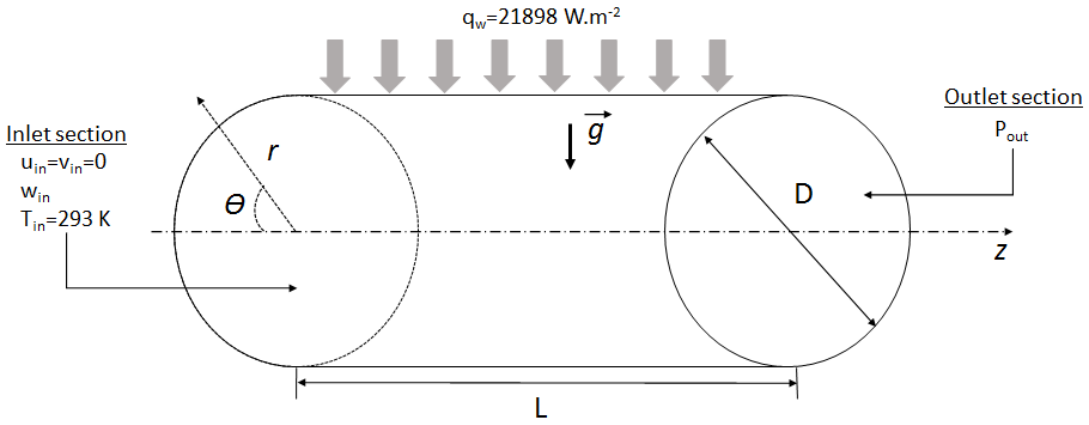

Figure 3.1 Schematic view of the computational domain with the boundary conditions.

3.3.2 Numerical method

The governing equations for the conservation of mass, momentum and energy are solved using a finite volume solver in a Cartesian frame. These equations are discretized in space by a second-order upwind scheme. The pressure-velocity coupling is achieved using the SIMPLEC algorithm. All calculations are performed in steady-state. It has been carefully checked that unsteady calculations led to similar results.

Fluid properties and two-phase modeling

Water properties

The physical properties of water are considered to be temperature-dependent while those of the solid nanoparticles are kept constant (see Table 3.1). The following equations are

used to evaluate the properties of pure liquid water (henceforth subscripted by bf for base fluid) as a function of temperature T:

– Density [220]:

$$\rho_{bf} = 2446 - 20.674T + 0.11576T^2 - 3.12895\times10^{-4}T^3 + 4.0505\times10^{-7}T^4 - 2.0546\times10^{-10}T^5 \tag{3.1}$$

– Viscosity [48]:

$$\mu_{bf} = A \times 10^{\left(\frac{B}{T-c}\right)} \tag{3.2}$$

where, $A = 2.414 \times 10^{-5}$, $B = 247.8$ and $C = 140$.

– Specific heat [21]:

$$Cp_{bf} = \exp\left(\frac{8.29041 - 0.012557T}{1 - 1.52373 \times 10^{-3}T}\right) \tag{3.3}$$

– Conductivity [57]:

$$k_{bf} = -0.76761 + 7.535211 \times 10^{-3}T - 0.98249 \times 10^{-5}T^2 \tag{3.4}$$

Note that the above equations are similar to those used in the former numerical simulations of Akbari et *al*. [3] to ensure direct comparisons.

Table 3.1 Thermophysical properties of different types of nanoparticles.

	ρ $(kg.m^{-3})$	C_p $(J.kg^{-1}.K^{-1})$	k $(W.m^{-2}.K^{-1})$
C	220	710	129
Cu	8933	385	401
CuO	6510	540	18
Al_2O_3	3880	729	42.3
TiO_2	4175	692	8.4
SiO_2	2220	745	1.4

Single-phase model

The single-phase model assumes that the phases are in thermal equilibrium and the relative velocity between the base fluid and the nanoparticles is null. It treats then the nanofluid as a homogeneous fluid with effective thermophysical properties evaluated by theoretical models or empirical correlations.

All the nanofluid properties are function of the base fluid (bf) and nanoparticles (np) properties as well as the volume fraction φ of the nanoparticles. It is recalled that all

properties of the base fluid are temperature-dependent and evaluated using Equations (3.1)-(3.4). Plenty of correlations are available in the literature [29, 107] and it appears crucial to use the most appropriate ones for the effective nanofluid properties to produce accurate results with the single-phase model. The present correlations are chosen to enable direct comparisons with Akbari et *al.* [3]. Two correlations for the thermal conductivity k_{nf} and for the dynamic viscosity μ_{nf} are considered here. The equations used to evaluate the nanofluid properties (density [227], heat capacity [116, 234], viscosity [142, 184]) are as follows:

$$\rho_{nf} = (1-\varphi)\rho_{bf} + \varphi\rho_{np} \tag{3.5}$$

$$Cp_{nf} = \frac{(1-\varphi)(\rho Cp)_{bf} + \varphi(\rho Cp)_{np}}{\rho_{nf}} \tag{3.6}$$

$$\mu_{nf} = (1 + 0.025\varphi + 0.015\varphi^2)\mu_{bf} \tag{3.7}$$

$$\mu_{nf} = (1 + 7.3\varphi + 123\varphi^2)\mu_{bf} \tag{3.8}$$

Note that the relations for the dynamic viscosity do not take into account the hysteresis cycle observed by Hachey et *al.* [84] for commercial and highly concentrated solutions of Al_2O_3/water-based nanofluids. The thermal conductivity k_{nf} is evaluated using two different correlations suggested by [163] and [102] respectively:

$$k_{nf} = \left[\frac{k_{np}(1+2\alpha) + 2k_{bf} - 2\varphi(k_{bf} - k_{np}(1-\alpha))}{k_{np}(1+2\alpha) + 2k_{bf} + \varphi(k_{bf} - k_{np}(1-\alpha))}\right] k_{bf} \tag{3.9}$$

$$k_{nf} = k_{bf}(1-\varphi) + \gamma k_{np}\varphi + C_d \frac{d_{bf}}{d_{np}} k_{bf} {Re_{np}}^2 Pr\varphi \tag{3.10}$$

where $\alpha = 2R_b k_{bf}/d_{np}$ is the particle Biot number, $R_b = 0.77 \times 10^{-8}\ K.m^2/W$ is the interfacial thermal resistance, $\gamma = 0.01$ is a constant taking into account the Kapitza resistance per unit area, $C_d = 18 \times 10^{-6}$ and Re_{np} the particle Reynolds number defined as:

$$Re_{np} = \left(\frac{\bar{C}_{RM} d_{np}}{\nu_{bf}}\right) \tag{3.11}$$

In the present case, the random motion velocity $\bar{C}_{RM}$ is fixed to 0.1 m/s as recommended by [102].

The general forms of the governing differential equations (conservation of mass, momentum and energy) for the single-phase model are:

$$\nabla \cdot (\rho \vec{V}) = 0 \tag{3.12}$$

$$\rho \vec{V} \cdot \nabla \vec{V} = -\nabla P + \nabla \cdot (\mu \nabla \vec{V}) + \rho \vec{g} \tag{3.13}$$

$$\rho \nabla \cdot (\vec{V} H) = -\nabla \cdot q - \tau : \nabla \vec{V} \tag{3.14}$$

Mixture model

Several approaches exist to model two-phase flows, such as the volume of fluid (VOF) method, the mixture model, the Eulerian model or the discrete phase model (DPM) among other models. Akbari et *al*. [3] already demonstrated the superiority of two-phase models over the single-phase one. The Eulerian, VOF and mixture models giving very similar results in their case, only the mixture model will be considered here due to its simplicity, stability and lowest computational costs required.
The mixture model treats the nanofluid as a single fluid consisting of two strongly coupled phases. It defines the concept of phase volume fractions, which are continuous functions and their sum equals one. Each phase has its own velocity. The governing equations of the two-phase model are:

– Conservation of mass:

$$\nabla \cdot (\rho_m \vec{V}_m) = 0 \tag{3.15}$$

– Conservation of momentum:

$$\rho_m \vec{V}_m \cdot \nabla \vec{V}_m = -\nabla P_m + \nabla \cdot (\mu_m \nabla \vec{V}_m) + \rho_m g + \nabla \cdot (\sum_{k=1}^{n} \varphi_k \rho_k \vec{V}_{dr,k} \vec{V}_{dr,k}) \tag{3.16}$$

where the mixture velocity, density and viscosity are respectively:

$$\vec{V}_m = \frac{\sum_{k=1}^{n} \varphi_k \rho_k \vec{V}_k}{\rho_m} \tag{3.17}$$

$$\rho_m = \sum_{k=1}^{n} \varphi_k \rho_k \tag{3.18}$$

$$\mu_m = \sum_{k=1}^{n} \varphi_k \mu_k \tag{3.19}$$

– The drift velocity of the k^{th} phase writes:

$$\vec{V}_{dr,k} = \vec{V}_k - \vec{V}_m \tag{3.20}$$

– Conservation of energy:

$$\nabla \cdot (\sum_{k=1}^{n} \varphi_k \rho_k \vec{V}_k H_k) = -\nabla \cdot q_m - \tau_m : \nabla \vec{V}_m \tag{3.21}$$

– Conservation of the volume fraction in nanoparticles:

$$\nabla \cdot (\varphi_{np} \rho_{np} \vec{V}_m) = -\nabla \cdot (\varphi_{np} \rho_{np} \vec{V}_{dr,np}) \tag{3.22}$$

– The slip velocity is defined as the velocity of a second phase (np: nanoparticles) relative to the primary phase (bf: base fluid):

$$\vec{V}_{pf} = \vec{V}_{np} - \vec{V}_{bf} \tag{3.23}$$

– The drift velocity is related to the relative velocity by:

$$\vec{V}_{dr,np} = \vec{V}_{pf} - \sum_{k=1}^{n} \frac{\varphi_k \rho_k}{\rho_{eff}} \vec{V}_{fk} \tag{3.24}$$

– The relative velocity is evaluated through the following equation proposed by Manninen *et al.* [145]:

$$\vec{V}_{pf} = \frac{\tau_{np}}{f_{drag}} \frac{(\rho_{np} - \rho_{eff})}{\rho_{np}} \vec{a} \tag{3.25}$$

where f_{drag} is the drag function calculated from Schiller and Naumann [190]:

$$f_{drag} = \begin{cases} 1 + 0.15 Re_{np}^{0.687} & Re_{np} \leq 1000 \\ 0.0183 Re_{np} & Re_{np} > 1000 \end{cases} \tag{3.26}$$

with $Re_{np} = (V_m d_{np}) / \nu_{eff}$ and $\vec{a} = \vec{g} - (\vec{v}_m \cdot \nabla)\vec{v}_m$.

Boundary conditions and grid resolution

The governing equations for the two models are solved with the following boundary conditions:

– At the inlet ($z = 0$):

$$w = w_{in}, u = v = 0, \quad T = T_{in} = 293K \tag{3.27}$$

– On the pipe wall ($r = R = D/2$):

$$u = v = w = 0, -k_{eff}\frac{\partial T}{\partial r}|_{r=R} = q_w \tag{3.28}$$

– At the pipe outlet, the gauge pressure is set equal to zero and all the normal diffusion fluxes and the mass balance correction are applied.

Several different grid distributions were tested to ensure the independence of the numerical results to the grid size. A structured mesh is used throughout the domain, with 140 nodes in the circumferential direction, 220 in the radial direction and 800 in the axial direction. A grid refinement close to the wall and in the pipe entrance is deemed necessary, where the highest velocity and temperature gradients occur (see Figure 3.2). This mesh grid provides grid-independent solutions for all cases studied.

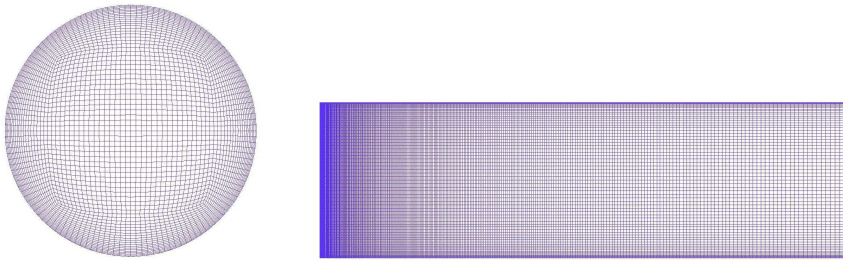

(a) (b)

Figure 3.2 Schematic view of the mesh grid: (a) in a given cross-section and (b) along the axial direction.

The calculations are performed in parallel using Mammouth Parallel 2 of the Calcul Québec cluster with 2 nodes having each 8 processors. The convergence is typically reached after 4000 iterations corresponding to a CPU time of about 6 hours.

3.4 Validation of the numerical model

In this section, the results are discussed in terms of the inlet Reynolds number $Re = w_{in}D/\nu_{nf}$. The maximum value of the Richardson number reached here is $Ri_{max} = Gr/Re^2 = 0.0115$, which ensures that a forced convection regime is achieved (Gr the Grashof number based on D, the nanofluid properties and the temperature difference $T_{r=R,max} - T_{in}$) for all the cases studied.

3.4.1 Performances of the mixture model

In order to first validate the selected numerical model, the local heat transfer coefficient $h(z)$ is evaluated along the pipe length. The mixture model is used together with temperature-dependent properties for water and Equations (3.7) and (3.10) for the nanoparticle properties. Due to the lack of precise information on the temperature measurement procedure in the experiments of Wen and Ding [227], four different averaging methods are used to evaluate the wall temperature of the simulated cases. Comparisons with the measurements of Wen and Ding [227] and the numerical simulations of Akbari *et al.* [3], for $Re = 1600$ and $\varphi = 0.6$ %, are performed using the mixture model. Figure 3.3a illustrates that using an average over an upper arc of $\pm$ 45° leads to closer results to the experiments with an average error between 0.37 and 13.84% along the pipe. The temperature was probably measured experimentally near the top of the tube where the fluid is warmer due to buoyancy forces. This averaging method will be used adopted for the remainder of the study.

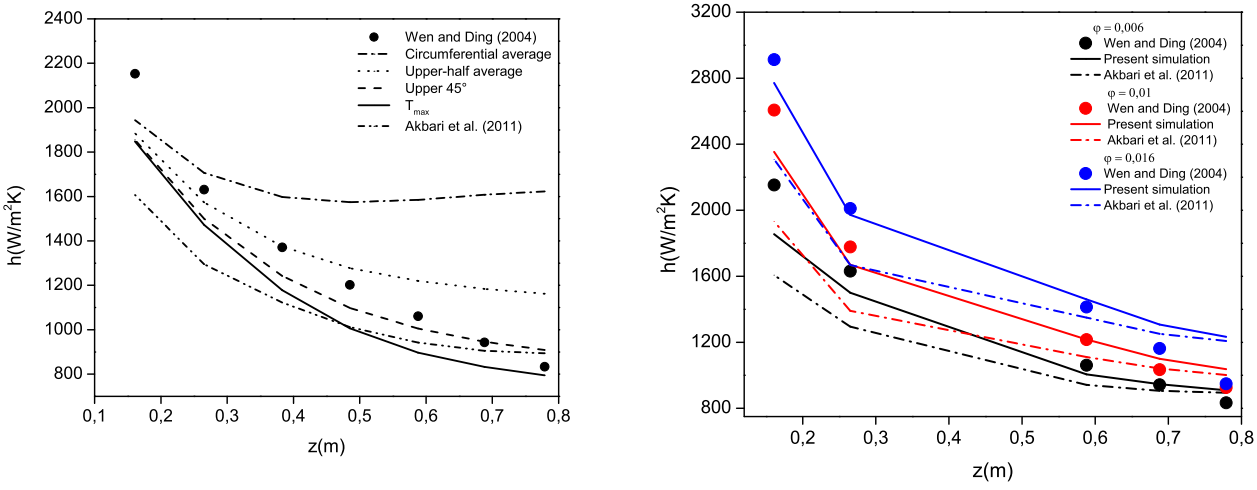

(a) (b)

Figure 3.3 Axial variations of the local heat transfer coefficient $h(z)$ predicted by the mixture model for Al_2O_3 water-based nanofluids: (a) different methods for the evaluation of the wall temperature T_w for $\varphi = 0.006$; (b) three nanoparticle concentrations ($\varphi = 0.006$, 0.01 and 0.016). Comparisons for $Re = 1600$ and $d_{np} = 42$ nm with the experimental data of Wen and Ding [227] and the numerical simulations of Akbari et *al.* [3].

Figure 3.3b compares the values of the convective heat transfer coefficient $h(z)$ of the present simulations with the numerical results of Akbari *etal.* [3] and the experimental data of Wen and Ding [227] for $Re = 1600$ and three volume fractions of Al_2O_3 nanoparticles

$\varphi = 0.6$, 1 and 1.6%, respectively. The present numerical results agree fairly well with the experiments [227] with an exponential decrease of the heat transfer coefficient along the tube as expected from energy balance equation. The main discrepancy is observed close to the inlet due to the choice of the boundary conditions in the present calculations. It is noteworthy that the present simulations improve the predictions of Akbari *et al.* [3] using exactly the same solver and methods. It points out in particular the necessity to use an appropriate mesh grid in the near-wall regions and globally a more dense grid. Compared to [3], the number of mesh points is multiplied by a factor 86. The mesh grid sensitivity studies are generally performed using small increments of values such that no noticeable effect is observed.

Figure 3.4 provides further comparisons in terms of the average heat transfer coefficient h_{av} for the same three cases. The present results obtained using the mixture model show an acceptable agreement with the experimental ones. The numerical data exhibit an average enhancement of about 36% with increasing φ from 0.6% to 1.6%, which is to be compared to the value 24.3% in the experiments. Once again, the present simulations improve the previous ones of Akbari *et al.* [3] pointing out the influence of the mesh grid. This improvement may be attributed to the increase of the thermal conductivity and some authors [90, 93, 227] proposed that it is also associated to the decrease of the thermal boundary layer thickness.

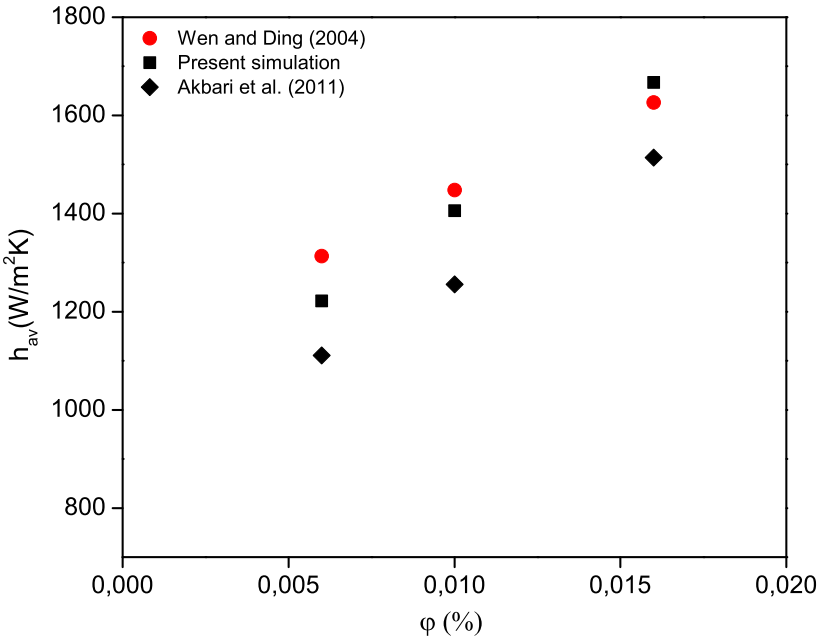

Figure 3.4 Influence of the concentration of Al_2O_3 nanoparticles φ on the average heat transfer coefficient for $Re = 1600$ and $d_{np} = 42\ nm$. Comparisons with the experimental data of Wen and Ding [227] and the numerical simulations of Akbari et *al.* [3].

3.4.2 Comparative analysis of single-phase and mixture models

Many authors [3, 21, 27, 137] have already shown that the mixture model performs better than single-phase or other two-phase models like the Eulerian or volume of fluid models. Nevertheless, it is crucial to use appropriate correlations for the effective nanofluid properties to obtain accurate results with single-phase models.

First, the single-phase (using Equations 3.7) and (3.10 for μ_{nf} and k_{nf} respectively) and the mixture models with temperature-dependent are compared in Figure 3.5 for $Re = 1600$ and four concentrations of nanoparticles. The single-phase model fails to predict the right axial distributions of the local heat transfer coefficient $h(z)$. An exponential decrease of $h(z)$ with the axial distance z is observed however with a noticeable underestimation for all cases with $\varphi \neq 0$. As expected, for $\varphi = 0$, both models predict the same profile. Though the nanofluid properties take into account the volume fraction of nanoparticles φ, the single-phase model appears insensitive to φ as the same heat transfer coefficient distribution is obtained whatever the value of $\varphi \leq 0.016$. This confirms the previous results of Akbari *et al.* [3] and Bianco *et al.* [26]. On the other hand, the heat transfer

coefficient predicted by the mixture model clearly increases with increased nanoparticle concentration in agreement with previous observations [3, 21, 27, 137].

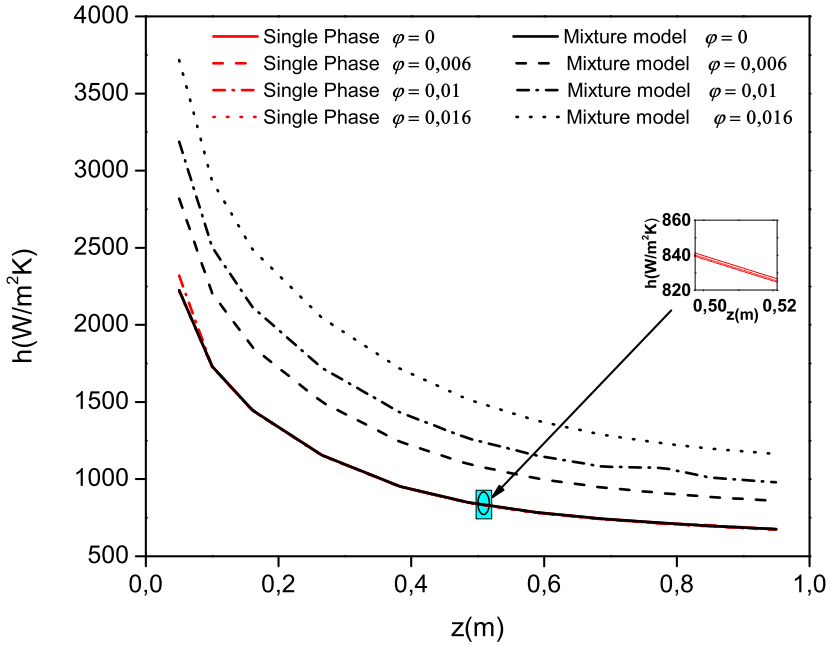

Figure 3.5 Local heat transfer coefficient obtained for $Re = 1600$, $d_{np} = 42$ nm and Al_2O_3-water based nanofluids: comparison between the single-phase and mixture models with temperature-dependent properties.

The superiority of the mixture model may be easily explained. In fact, the latter ensures a more accurate treatment of the two-phase mixture, compared to the single-phase model, which does not take into account neither the spatial variations of the distribution in nanoparticles in the base fluid, nor the relative velocity of each phase. The mixture model seems a better model to describe the nanofluid flow. In fact, the slip velocity between the fluid and the nanoparticles is not zero due to several factors such as the Brownian motion or gravity, which induces for example the sedimentation of the solid particles.

One could argue that the single-phase model does not perform well due to inappropriate correlations for the thermal conductivity and the dynamic viscosity of the nanofluid. Thus, several correlations have been tested and the results are summarized in Table 3.2 for $Re = 1600$, $d_{np} = 42$ nm and Al_2O_3-water based nanofluids. Two volume fractions $\varphi = 0.006$ and 0.016 have been considered. Simulation 1 combines Eqs (3.7) and (3.10), whereas simulation 2 uses Eqs (3.8) and (3.9). It is clear that the two sets of correla-

tions provide rather the same results in terms of the average value of the heat transfer coefficient with differences of about 17% and 33% for $\varphi = 0.006$ and 0.016, respectively, compared to the experiments. It shows in particular that for these sets of parameters, the correlations do not considerably influence the accuracy of the single-phase model. As shown previously, the results are not influenced by the particle volume fraction. Though the effect of Brownian motion is accounted for in Equation (3.10), it has no noticeable influence in laminar flows. This confirms the previous work of Keblinski *et al.* [112], who suggested that the motion of nanoparticles due to the Brownian motion is too slow to transport a significant amount of heat through a nanofluid. They ignored the effect of Brownian motion in the enhancement of thermal conductivity of nanofluids.

Table 3.2 Influence of the different correlations on the average heat transfer coefficient h_{av} $(W.m^{-2}.K^{-1})$ for $Re = 1600$, $d_{np} = 42\ nm$ and Al_2O_3-water based nanofluids. The relative error is given in brackets. Simulation 1 combines Eqs (3.7) and (3.10), whereas simulation 2 uses Eqs (3.8) and (3.9). Results obtained using the single-phase model.

φ	Experiments [227]	Simulation 1	Simulation 2
0.006	1313.54	1089.66	1086.37
		(17.04%)	(17.29%)
0.016	1626.12	1085.69	1075.72
		(33.23%)	(33.85%)

For the sake of simplicity when developing new numerical models, it may be interesting to consider the mixture model with constant properties if satisfactory results may be obtained. Figure 3.6 displays the axial distributions of the local heat transfer coefficient for $Re = 1600$, $d_{np} = 42\ nm$ and Al_2O_3-water based nanofluids with four concentrations of nanoparticles. The results are obtained using Eqs (3.7) and (3.10) either with constant (CP) or variable (VP) properties for the base fluid. In all cases, the local heat transfer coefficient h decreases exponentially with the axial distance z. Using temperature-dependent properties (VP) leads to very satisfactory results as already shown in Figure 3.3a. On the contrary, using constant properties (CP) leads to a strong overestimation of the heat transfer coefficient, with more pronounced differences towards the thermally fully developed flow region. In fact, the thermal conductivity of the nanofluid increases drastically with decreasing values of both temperature and density. Using VP, the circumferential wall temperature appears to be non-uniformly distributed in the tangential direction, whereas the CP model exhibits a more uniform and axisymmetric behavior. The VP model takes then into account buoyancy effects, which result in a noticeable increase of

the fluid temperature in the upper half of the pipe. This confirms previous results such as those suggested by [26] except from the previous work of Labonte *et al.* [125], who showed that CP lead to an underestimation of the heat transfer coefficient. This difference may be attributed to the different multiphase models used.

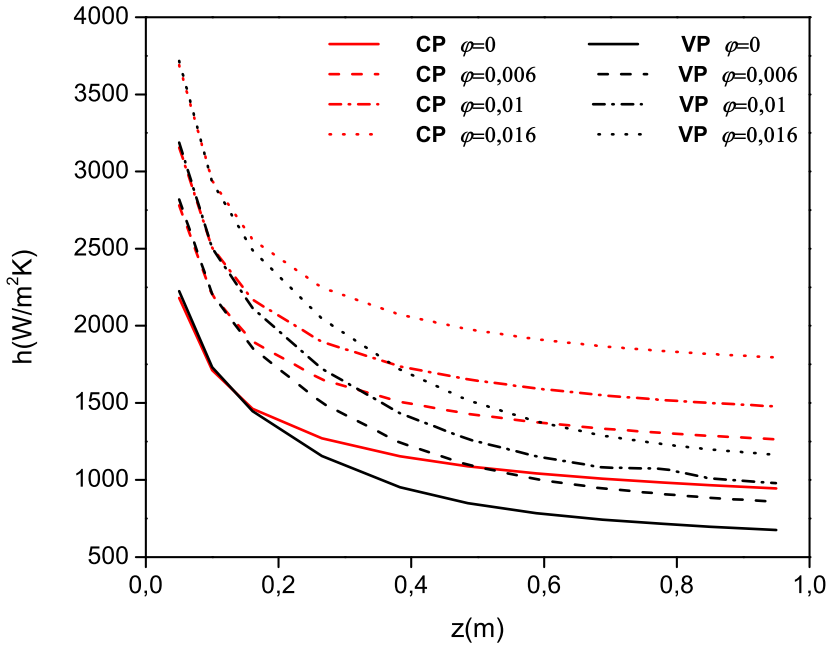

Figure 3.6 Local heat transfer coefficient obtained for $Re = 1600$, $d_{np} = 42\ nm$ and Al_2O_3-water based nanofluids: Influence of temperature-dependent properties on the performances of the mixture model.

It is important to note that taking into account temperature-dependent properties does not increase the computational cost. Using the same mesh grid, both calculations take about 4 hours using 8 processors on Mammouth Parallel 2. Calculations using VP lead to a rather faster convergence as compared to the CP case.

3.5 Results and Discussion

All the results presented in the following have been obtained using the mixture model with temperature-dependent properties and Eqs (3.7) and (3.10) to model the nanofluid properties. The influence of the Reynolds number Re, the volume fraction φ, the diameter d_{np} of the nanoparticles and the type of nanoparticles on the hydrodynamic and the thermal fields are successively discussed in details in the following sections.

3.5.1 Influence of the volume fraction of nanoparticles and Reynolds number for Al_2O_3/water-based nanofluids

The combined effects of the Reynolds number and the volume fraction of nanoparticles on the average heat transfer coefficient are plotted in Figure 3.7. It can be clearly observed that an average enhancement of the convective average heat transfer coefficient of about 40% is achieved when the Reynolds number increases from $Re = 600$ to 1600 for all nanoparticle concentrations φ. A linear dependency of h_{av} is obtained against to φ for the three Re numbers.

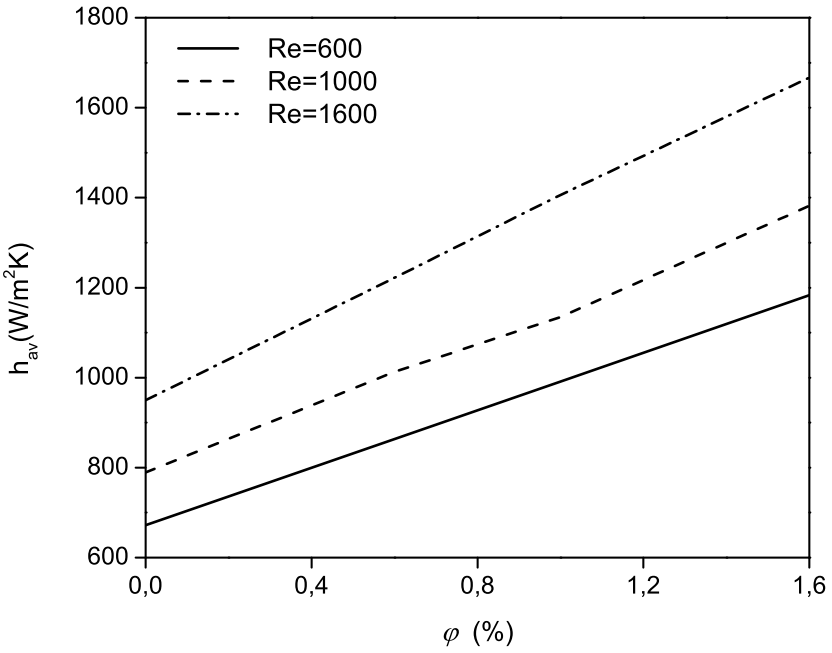

Figure 3.7 Effects of the Al_2O_3 nanoparticle concentration φ and Reynolds number Re on the average heat transfer coefficient h_{av} for $d_{np} = 42\ nm$.

Figure 3.8 shows the axial distribution of the heat transfer coefficient ratio h_{nf}/h_{bf} along the pipe for $d_{np} = 42\ nm$, $Re = 1600$ and three volume fractions of Al_2O_3 nanoparticles. It clearly indicates an average thermal enhancement of 28%, 48% and 75.6% for $\varphi = 0.006$, 0.01 and 0.016, respectively. This ratio h_{nf}/h_{bf} is rather constant in the axial direction z/D with a local maximum around $z/D \simeq 85$ whatever φ and a second local maximum at $z/D \simeq 175$ for $\varphi = 0.01$.

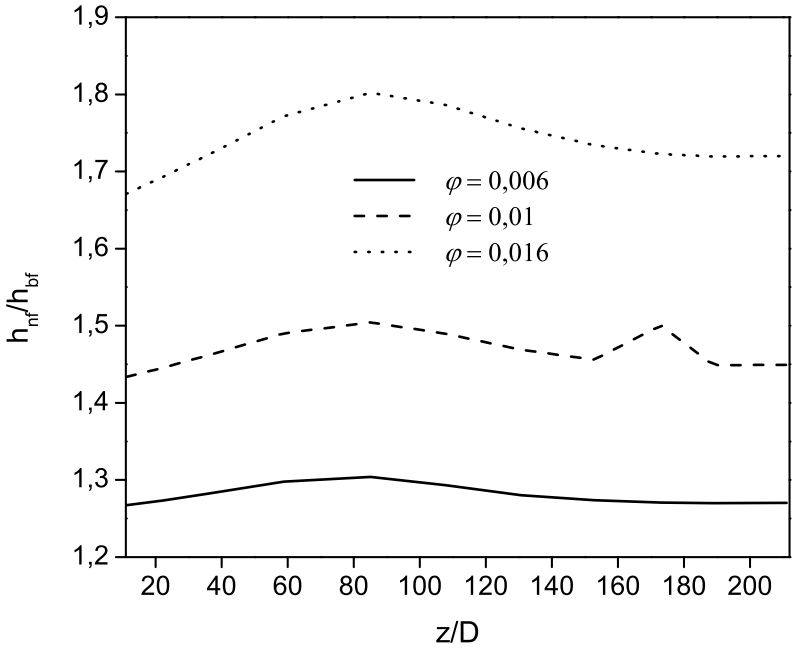

Figure 3.8 Axial variations of the heat transfer coefficient ratio h_{nf}/h_{bf} for $d_{np} = 42\ nm$, $Re = 1600$ and three volume fractions in Al_2O_3 nanoparticles: $\varphi = 0.006$, 0.01 and 0.016.

Figure 3.9 illustrates the temperature contours at four axial positions $z = 0.2$ m ($z/D = 44.4$), 0.4 m ($z/D = 88.9$), 0.6 m ($z/D = 133.3$) and 0.8 m ($z/D = 177.8$) for $d_{np} = 42$ nm, $Re = 1600$ and four concentrations φ. The temperature contours change from a circular form at $z = 0.2$ m, to an elliptical one at $z = 0.4$ m then to a kidney shape from $z = 0.6$ m to the tube outlet for all concentrations of nanoparticles. The circumferential wall temperature appears to be non-uniformly distributed in the tangential direction, especially at $z = 0.8$ m, with maximum values at the top of the tube. It can be simply explained by density variations, since the warm nanofluid has a lowest density and can rise due to the buoyancy force to the upper half of the tube inducing a stratification of the fluid temperature. This suggests the necessity to consider temperature-dependent properties for the nanofluid in order to predict this effect. The hot temperature region located at the top of tube for $\varphi = 0$ shown in Figure 3.9d progressively disappears when increasing the nanoparticle volume fraction. For example, the wall temperature T_w decreases noticeably when φ increases: at $z = 0.8$ m, the maximum wall temperature decreases from 332 K to 293 K for $\varphi = 0$ (Figure 3.9d) and $\varphi = 0.016$ (Figure 3.9p), respectively. The maximum temperature difference is inversely proportional to the nanoparticle volume

fraction. It is reduced almost by a factor 2 between $\varphi = 0.016$ and $\varphi = 0$. More generally, the introduction of even higher volume fractions (for this range of parameters) tends to homogeneize the temperature distribution at a given cross-section. It may be explained by considering nano-convection effect, which is linearly related to φ [101]. This effect is induced by the Brownian motion of the nanoparticles. Brownian motion caused by the thermal interaction between the nanoparticles and the base fluid is stronger within regions of higher fluid temperature that is why the upper half of the tube is more affected. The influence of Brownian force on the thermal conductivity enhancement is strongly debated in the scientific community, some authors assume that it plays a key role [101, 120], while others ignore its effect [112].

Note that the same phenomena are observed for the two other values of the Reynolds number.

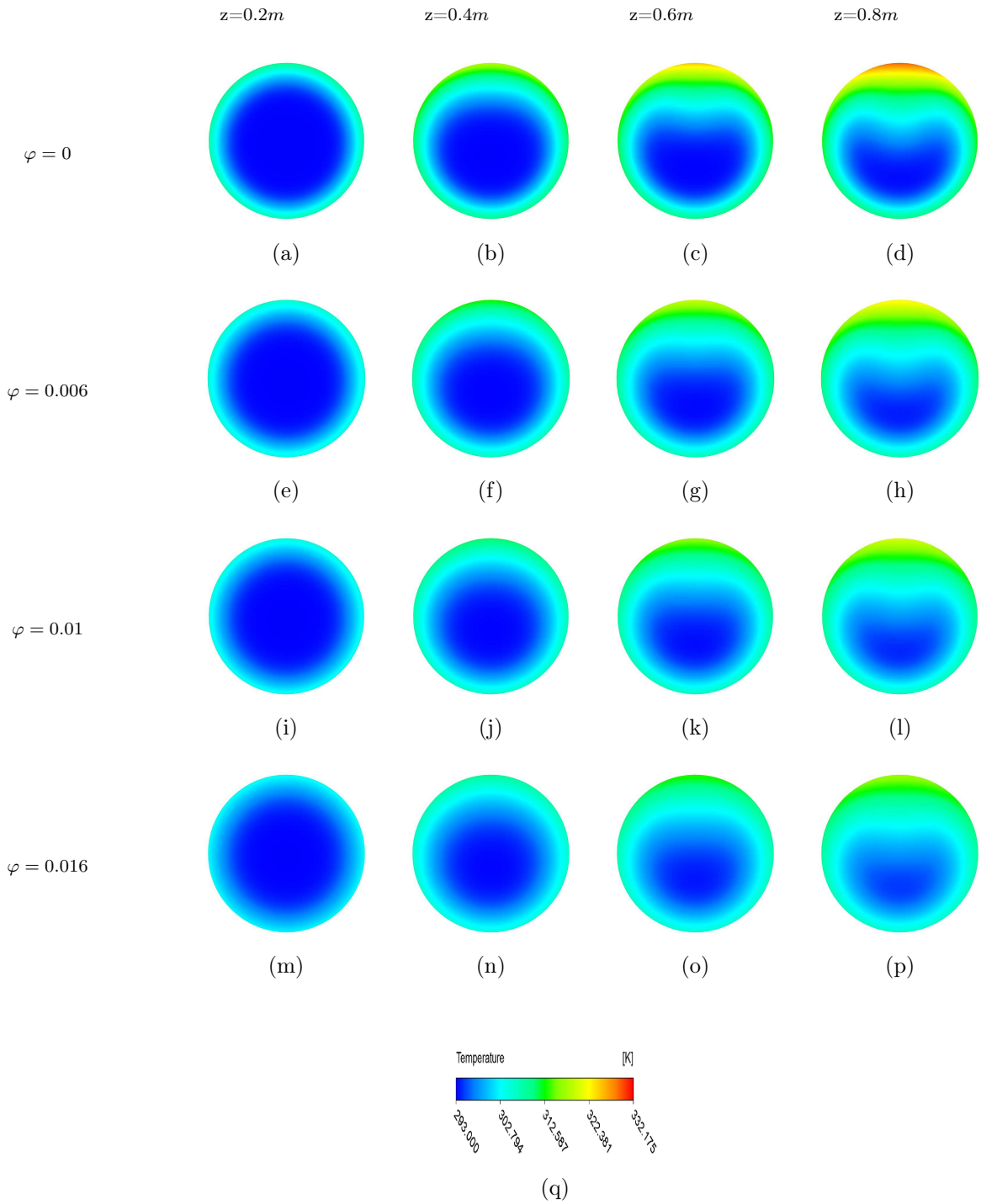

Figure 3.9 Maps of temperature T at four axial positions: $z = 0.2$ m (a,e,i,m), $z = 0.4$ m (b,f,j,n), $z = 0.6$ m (c,g,k,o) and $z = 0.8$ m (d,h,l,p). Results obtained for $d_{np} = 42\ nm$, $Re = 1600$ and four volume fractions of Al_2O_3 nanoparticles: $\varphi = 0\ (a-d)$, $0.006\ (e-h)$, $0.01\ (i-l)$ and $0.016\ (m-p)$.

Figure 3.10 displays the corresponding streamlines colored by the axial velocity component w at four cross-sections along the pipe. Due to the increased temperature at the wall, a secondary flow is observed. It consists of a pair of symmetrical counter-rotating vortices with respect to the tube axis. These vortices are induced by buoyancy forces: an upward flow restricted in a thin layer along the wall rises up a warm fluid and a downward flow along the tube axis drops a cool fluid [78, 169]. For pure water ($\varphi = 0$), Figure 3.10a shows clearly that the buoyancy force already appears at $z = 0.2$ m and induces the secondary flow. The contours of the axial velocity component are axisymmetric at this axial position for all nanoparticle concentrations and the recirculation cells are symmetric. This indicates that the velocity is not yet affected by the buoyancy force, which is due to the fact that, at this location, the circumferential temperature gradients are very small. When the fluid moves further downstream, the recirculations are slightly shifted and moves across the median plane, above the plane at $z = 0.4$ m and just below the plane at $z = 0.8$ m, for all values of φ. The maximum value of w is also slightly shifted downward below the horizontal tube axis when moving to the pipe outlet. This shift results from the important increase in the intensity of the secondary flow. This loss of axisymmetry is due to both the boundary layer development and the increasing influence of the buoyancy force, which becomes more pronounced along the tube, increasing then the strength of the secondary flow. At $z = 0.8$ m, the axial velocity contours exhibit an ellipsoid-shaped form for $\varphi = 0$. At the same time, the circular streamlines in the lower half of the tube indicate a weaker secondary flow, while the curved ones in the upper half indicate that a hot fluid is confined and accompanied by a more intense secondary flow. At $z = 0.8$ m, the form of the axial velocity contours change from an ellipsoid-shaped pattern for $\varphi = 0$ to a rather more circular form for $\varphi = 0.016$ as illustrated in Figures 3.10d and 3.10p, respectively. For $\varphi = 0.016$, the shape of the velocity contours remains practically unchanged indicating a fully developed region from z=0.4 m. This result agrees well with the previous observations confirming that the nanoparticles suppress the buoyancy force induced secondary flow, stabilizes the flow with a strong homogeneity of the fluid temperature within the tube.

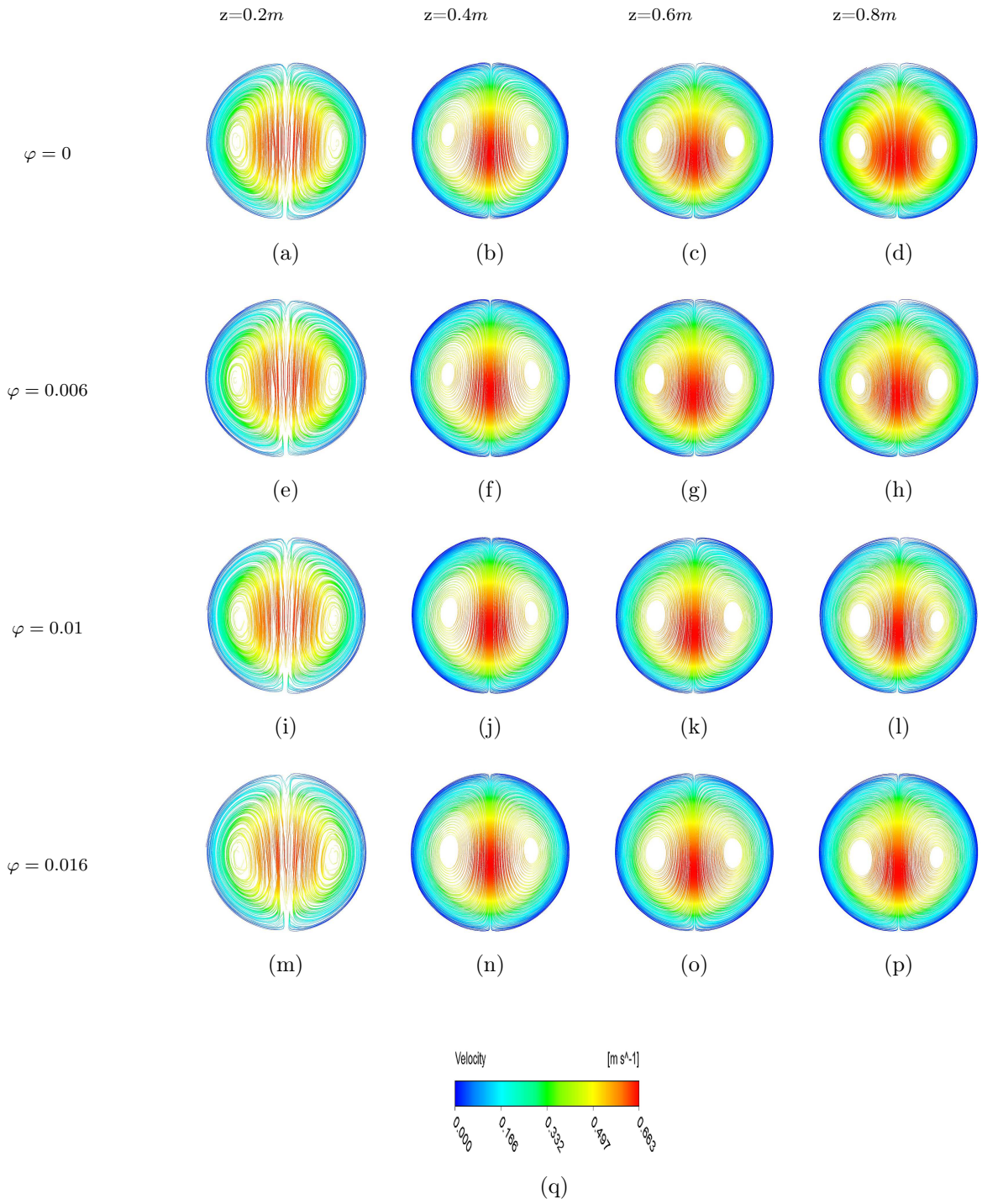

Figure 3.10 Streamline patterns colored by the axial velocity component w at four axial positions: $z = 0.2$ m (a,e,i,m), $z = 0.4$ m (b,f,j,n), $z = 0.6$ m (c,g,k,o) and $z = 0.8$ m (d,h,l,p). Results obtained for $d_{np} = 42\ nm$, $Re = 1600$ and four concentrations of Al_2O_3 nanoparticles: $\varphi = 0$ $(a - d)$, 0.006 $(e - h)$, 0.01 $(i - l)$ and 0.016 $(m - p)$.

The same behavior is observed for all volume fractions of nanoparticles indicating that the latter has no remarkable influence on the hydrodynamic field. Nevertheless, the intensity of the secondary flow decreases when increasing φ for all axial positions especially at $z = 0.8$ m as shown in Figure 3.11. This is consistent with previous observations [51, 65, 117]. The wall layer vorticity also decreases with increased values of φ. The weak influence of the nanoparticle concentration on the velocity and temperature fields results from the ability of nanoparticles to homogenize the fluid temperature and therefore impeding buoyancy forces. Only few studies considered the influence of the nanoparticles on the development of the secondary flow and the homogenization of the temperature field. When φ is increased, the molecular diffusion increases accompanied with an increase in the thermal conductivity and a reduction in the specific heat capacity, as proposed by [65]. Colla *et al.* [51] invoke the role of the Brownian diffusion.

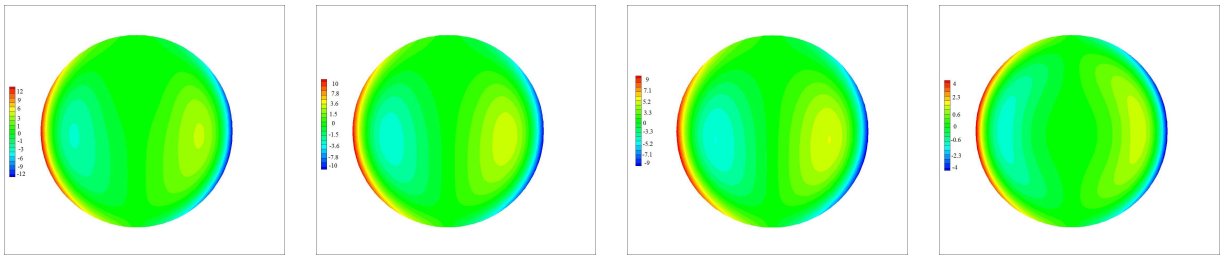

(a) (b) (c) (d)

Figure 3.11 Contours of the streamwise vorticity at $z = 0.8$ m: (a) $\varphi = 0$, (b) $\varphi = 0.006$, (c) $\varphi = 0.01$ and (d) $\varphi = 0.016$. Results obtained for $d_{np} = 42\ nm$, $Re = 1600$ and Al_2O_3 nanoparticles.

3.5.2 Influence of the nanoparticle diameter for Al_2O_3 and Cu/water-based nanofluids

In real thermal engineering applications, increasing the nanoparticle diameter leads to higher agglomeration effects resulting in the sedimentation of the agglomerates. Such particle-particle interactions are not taken into account in the present model. Only the Brownian motion and the ratio between gravity and buoyancy forces are modeled here. The nanoparticle diameter d_{np} has then no remarkable effect on the heat transfer coefficients as it will be shown in the following. More interestingly however, the influence of d_{np} on the axial distributions of the nanoparticle concentration φ is quite remarkable.
Figure 3.12 displays the axial profiles of φ at three radial locations $r/R = 0.98$ (top wall), $r/R = 0$ (axis) and $r/R = -0.98$ (bottom wall) for two types of nanofluid (copper and alumina water-based), three nanoparticle diameters $d_{np} = 42$, 100 and 200 nm and for

$Re = 1600$ and $\varphi = 1.6\%$. Firstly, the concentration is rather constant along the center line of the tube ($r/R = 0$) for the two nanofluids and all the nanoparticle diameters, remaining between 1.6% and 1.596%. For $d_{np} = 42$ nm, along the top wall of the tube, the nanoparticle concentration decreases by 1.5% and 3% for Al_2O_3 and Cu nanoparticles, respectively (Figure 3.12a). As the nanoparticle diameter grows, the concentration decreases along the top wall due to gravity effects. For example, φ is reduced by 22.5% and 43.75% for Al_2O_3 and Cu nanoparticles, respectively, for $d_{np} = 200$ nm. By conservation of the average value of φ at a given cross-section, the concentration of nanoparticles along the bottom wall increases. Because of their higher density, this effect is more noticeable for copper/water-based nanofluids as illustrated in Figures 3.12c, 3.12f and 3.12i. The latter shows that φ increases by 0.75%, 17.5% and 87.5% for $d_{np} = 42$, 100 and 200 nm, respectively. The concentration of Al_2O_3 appears quite constant, with an increase of only 2.5% for $d_{np} = 200$ nm. This behavior can be easily explained since the density of copper is twice the alumina one.

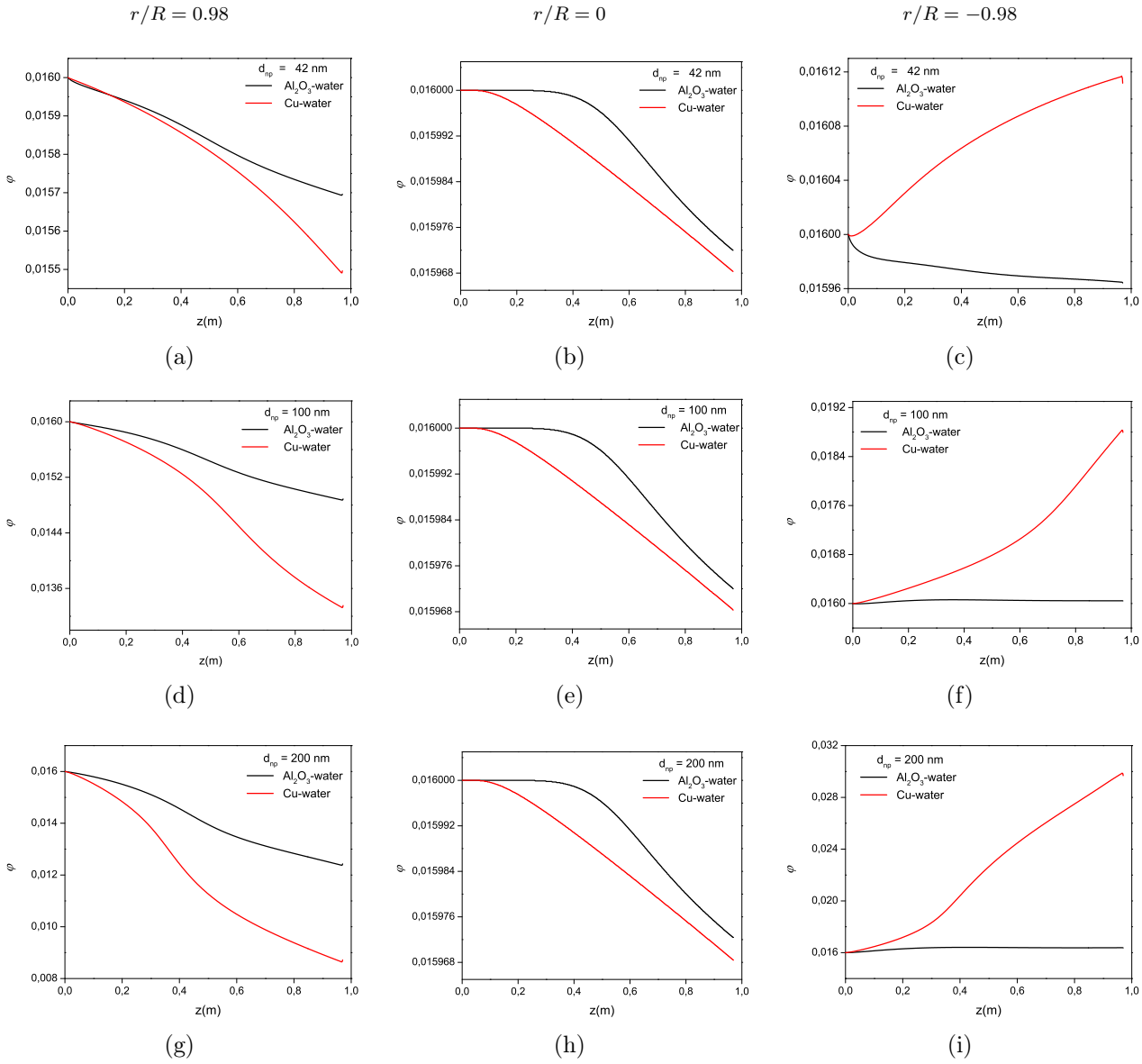

Figure 3.12 Axial variations of the volume fraction φ at three radial locations: $r/R = 0.98$ (a,d,g), $r/R = 0$ (b,e,h) and $r/R = -0.98$ (c,f,i). Results obtained for Cu and Al_2O_3 nanoparticles of three different diameters $d_{np} = 42\ nm$ (a,b,c), $100\ nm$ (d,e,f) and $200\ nm$ (g,h,i) with $\varphi = 0.016$ and $Re = 1600$.

The influence of the mean diameter of the Al_2O_3 nanoparticles on the heat transfer is not shown here, but it can be noticed that increasing d_{np} does not affect the average heat transfer coefficient. For $\varphi = 0.016$ and $Re = 1600$, $h_{av} = 1796.7\ W/m^2K$ and $1795.5\ W/m^2K$ for $d_{np} = 10$ and 200 nm, respectively. However, the average heat transfer coefficient may be strongly modified by the size of the nanoparticles for copper-water

nanofluids, which sediment more with only 12% of the particles still in suspension in the base fluid as shown previously for $d_{np} = 200$ nm (Figures 3.12g and 3.12i).

Figure 3.13 illustrates the effect of the global Reynolds number Re on the distributions of the concentration in copper nanoparticles along the tube for $d_{np} = 200$ nm, $\varphi = 0.016$ and two Reynolds numbers $Re = 600$ and 1600 at three radial locations $r/R = 0.98$ (near the top wall), $r/R = 0$ (pipe axis) and $r/R = -0.98$ (near the bottom wall). Even for this large nanoparticles, the concentration of nanoparticles along the tube axis remains almost constant. Throughout the pipe length, the variation of φ is 0.13% for $Re = 1600$ and 0.75% for $Re = 1600$. At $r/R = 0.98$, φ decreases by a factor 2 then 4 for $Re = 1600$ and $Re = 600$, respectively. It results in a huge increase in nanoparticle concentration at the bottom of the pipe (Figure 3.13c): φ increases by 87.5% and 137.5% for $Re = 1600$ and 600, respectively. Almost all the copper nanoparticles are sedimented and there are only few copper nanoparticles suspended in pure water at the top of the tube for $Re = 600$. The Reynolds number plays an important role to keep the nanoparticles well dispersed in the base fluid and reduce the sedimentation process, inducing a better stability of the nanofluid and higher resulting heat transfer.

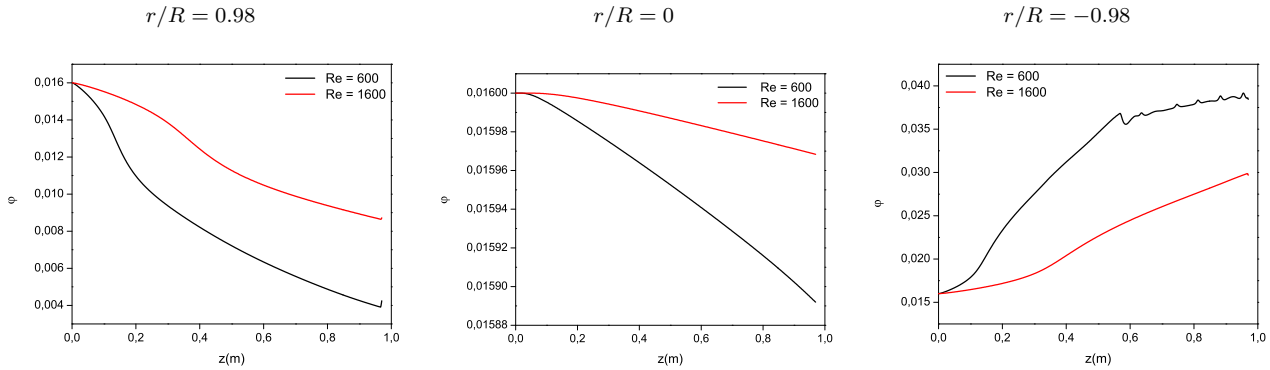

Figure 3.13 Axial variations of the volume fraction φ in Cu nanoparticles at three radial locations: (a) $r/R = 0.98$, (b) $r/R = 0$ and (c) $r/R = -0.98$. Results obtained for Cu nanoparticles of diameter $d_{np} = 200$ nm with $\varphi = 0.016$ and two Reynolds numbers $Re = 600$ and 1600.

3.5.3 Influence of the type of nanoparticles for water-based nanofluids

The axial variations of the heat transfer coefficient of six types of nanoparticles for $\varphi = 1.6\%$, $d_{np} = 42\ nm$ and $Re = 1600$ are shown in Figure 3.14. This later figure illustrates that the local heat transfer coefficients for all water-based nanofluids exhibit

the same behavior, with an exponential decrease with increased distance along the pipe. The nanofluid with copper nanoparticles achieves the highest heat transfer coefficient, followed by C, Al_2O_3, CuO, TiO_2, and SiO_2, respectively. This behavior was expected since the copper has the highest thermal conductivity amongst the other nanofluids as shown in Table 3.1.

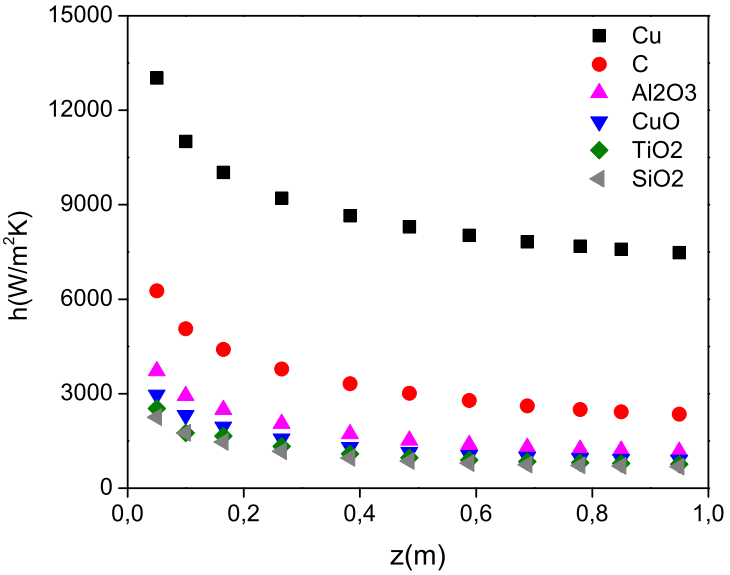

Figure 3.14 Axial variations of the local heat transfer coefficient h for six types of nanoparticles with $d_{np} = 42\ nm$, $\varphi = 0.016$ and $Re = 1600$.

In the other hand, a major hindrance associated with the use of copper nanoparticles is the sedimentation phenomenon, as illustrated earlier for $\varphi = 1.6\%$ and $d_{np} = 200\ nm$. They sediment 34 times higher than the Al_2O_3 nanoparticles under the same operating conditions. For this reason, the choice of the appropriate nanofluid does not depend only on its thermal conductivity, but should also take into account their stability and the suspension of the nanoparticles in the base fluid for a long term use.

3.5.4 Summary

For engineering applications, empirical correlations are of primary importance to predict the average heat transfer coefficient as a function of the flow and geometrical parameters for an effective design of thermal systems such as heat exchangers. This is particularly challenging for convective nanofluid flows as opposed to single-phase flows, because of the influence of various parameters due to the presence of the solid nanoparticles. An attempt has been done in the following. First, the well-known correlation proposed by Shah [197]

for laminar flows under a constant heat flux boundary condition and used by Wen And Ding [227] is considered:

$$Nu_{Shah} = 1.953 \left(RePr\frac{D}{x} \right)^{1/3} \qquad 33.3 \leq RePr\frac{D}{x} \tag{3.29}$$

A second correlation was proposed by [197] for $RePr\frac{D}{x} \leq 33.3$ but it was carefully checked here that it led to very similar results. For simplicity, only Equation (3.29) will be used in the following.

All the results obtained in this paper using direct numerical simulations may be expressed in terms of Nusselt number using the following correlation:

$$Nu_{DNS} = Nu_{Shah} \left(1 + 1.7 \left(\frac{Re}{Pr^4} \right)^{1/3} \varphi \right) \qquad 6.6 \leq RePr\frac{D}{x} \leq 46.5 \qquad Pr \geq 1 \tag{3.30}$$

It is noteworthy that the validity range of Equation (3.30) has been extended to $6.6 \leq RePr\frac{D}{x} \leq 46.5$ compared to Equation (3.29). The present correlation is valid for all values tested in the present work except for the simulations involving copper nanoparticles for which $Pr \leq 1$. Both geometrical (through x and D) and flow (Re and Pr) parameters are considered in Equation (3.30). The influence of the solid nanoparticles is taken into account through φ but also through their thermophysical properties used to define Re and Pr. Figure 3.15 confirms that Equation 3.30 fits particularly well with all simulations for $Pr \geq 1$.

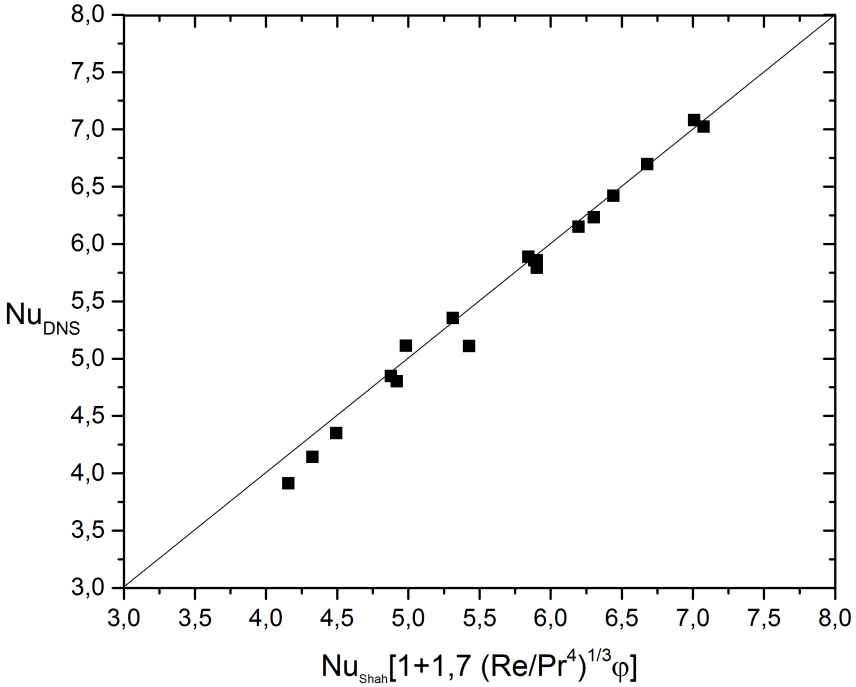

Figure 3.15 Verification of Equation (3.30).

The second term $1.7\,(Re/Pr^4)^{1/3}\,\varphi$ in Equation (3.30) is small compared to 1 in all cases. The results are then well fitted with Equation (3.29) and so with the correlation provided by Rea et *al*. [184] for Al_2O_3/water-based nanofluids, $431 \leq Re \leq 2000$ and $\varphi \leq 0.06$. It corresponds to Equation (3.29) with a prefactor equal to 2.0398 instead of 1.953.

The second interesting quantity for engineering applications is the variations of the average friction factor f_{av} as a function of the Reynolds number Re. The friction factor is calculated as proposed by Choi and Cho [46]:

$$f = \frac{8\tau_w}{\rho u_m^2} \tag{3.31}$$

where u_m is the mean fluid velocity and τ_w is the wall shear stress. It may be convenient to find correlations under the form: $f = ARe^{\alpha}$. Figure 3.16 summarizes the results obtained for Al_2O_3/water-based nanofluids with alumina nanoparticles of diameter $d_{np} = 42\ nm$ and for four volume fractions φ. As for pure water flows, the average friction factor f_{av} decreases for increased values of Re. Complementary calculations have been performed for turbulent flows up to $Re = 15000$. In the laminar regime, f_{av} varies according to the relation $f_{av} = 11.381Re^{-0.756}$, whereas, in the turbulent regime, f_{av} follows: $f_{av} = 1.05Re^{-0.358}$. A discontinuity is also observed in the transitional regime. The presence of

nanoparticles in the base fluid affects the variations of the average friction factor compared to pure water flows. However, the friction factor f_{av} appears to be insensitive to the nanoparticle concentration φ. The results are to be compared to the classical Darcy relations for single-phase flows in pipes, where: $A = 64$ and $\alpha = -1$ for laminar flows and $A = 0.3164$ and $\alpha = -0.25$ for turbulent flows in smooth pipes.

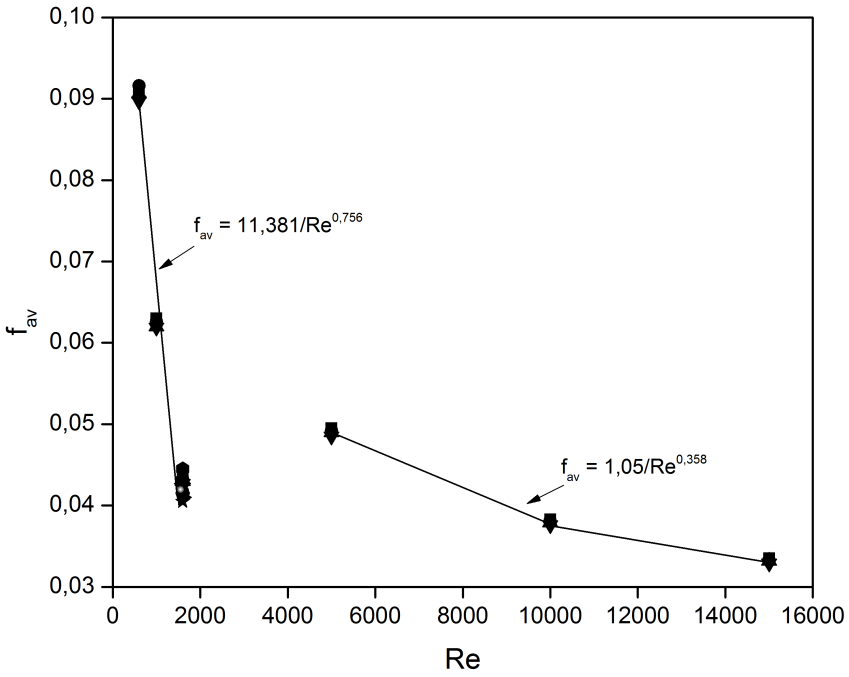

Figure 3.16 Influence of the Reynolds number Re on the average friction coefficient f_{av}. Results obtained for all values of φ, d_{np} and all types of nanofluids.

In the laminar regime, the results agree particularly well with the correlation of Suresh et *al.* [208] obtained for Al_2O_3-Cu/water-based nanofluid with $Re < 2300$ and $\varphi \leq 0.1\%$: $A = 26.4f(\varphi)$ and $\alpha = -0.8737$.

3.6 Conclusions

Laminar forced convection flows of water-based nanofluids through a uniformly heated tube were revisited here using direct numerical simulations. The single-phase and mixture models with constant and temperature-dependent properties were compared to the experimental data of Wen and Ding [227] and to the numerical simulations of Akbari *et al.* [3]. The mixture model with temperature-dependent properties was shown to perform best with a close agreement to the experimental data. The former simulations of Akbari *et al.* [3] using the same model were significantly improved with the use of an appropriate mesh grid.

The numerical model was then used confidently and extensively to investigate the influences of the Reynolds number ($600 \leq Re \leq 1600$), the concentration in nanoparticles ($\phi \leq 1.6\%$) and their diameter ($42 \leq d_{np} \leq 200$ nm) on the hydrodynamic and thermal fields. Al_2O_3/water based nanofluids have been considered first before evaluating the thermal performances of other nanoparticles such as: Cu, C, CuO, TiO_2, and SiO_2.
For Al_2O_3/water based nanofluids, the average heat transfer coefficient increased linearly with the nanoparticle concentration for all Reynolds numbers. At $Re = 1600$, the local heat transfer coefficient increased in average by 29%, 46% and 74% for $\varphi = 0.006$, 0.01 and 0.016, respectively. Increasing the nanoparticle concentration led to a more homogenous temperature field, impeding the hot temperature region observed at the top of the pipe wall for pure water flows. The flow field revealed two recirculation regions for all (r, θ) planes, only weakly influenced by φ. The maximum value of the axial velocity component observed at $(r/R \simeq -0.2, \theta = -90°)$ was also weakly affected by φ. The volume fraction in nanoparticles affected significantly the streamwise vorticity of the two recirculation cells. The flow and temperature fields exhibited a more homogeneous behavior. A particular attention was also paid to the sedimentation of the nanoparticles, which, as expected, increased for large size or high density nanoparticles. Finally, empirical correlations to predict both the Nusselt number and the average friction coefficient have been provided, summarizing all simulations presented here (in the range of $Pr \geq 1$ for Nu).
Further calculations are now required to extend the present simulations to the turbulent flow regime using large-eddy simulations. Further developments are also planned to improve the numerical model to take into account more complex phenomena like the thermophoresis effect and particle-particle interactions.

3.6.1 Acknowledgments

The authors would like to thank the NSERC chair on industrial energy efficiency funded by Hydro-Québec, CanmetEnergy and Rio Tinto Alcan established at Université de Sherbrooke for the period 2014-2019. The financial support of the CREEPIUS research center and the HPC resources of the Compute Canada network are also gratefully acknowledged.

3.6.2 Nomenclature

C_p	Specific heat, $J.K^{-1}.kg^{-1}$
D	Tube diameter, m
d_{np}	Nanoparticle diameter, m
f	Friction factor, $-$
h	Heat transfer coefficient, $W.m^{-1}.K^{-1}$
k	Thermal conductivity, $W.m^{-2}.K^{-1}$
L	Tube length, m
q	Heat flux, $W.m^{-2}$
R	Tube radius, m
r	Radial location, m
Re	Global Reynolds number, $-$
T	Temperature, K
w	Axial velocity component, $m.s^{-1}$
z	Axial position, m
φ	Volume fraction, $-$
μ	Dynamic viscosity, $Pa.s$
ρ	Density, $kg.m^{-3}$
τ	Wall shear stress, Pa
av	Average
bf	Base fluid
eff	Effective
in	Inlet
m, mix	Mixture
nf	Nanofluid
np	Nanoparticles
w	Wall

CHAPTER 4

Modeling of convective turbulent heat transfer of water-based Al_2O_3 nanofluids in an uniformly heated pipe

4.1 Avant-propos

Auteurs et affiliations:

1. Ghofrane Sekrani: étudiante au doctorat*
2. Sébastien Poncet: Professeur agrégé*
3. Pierre Proulx: Professeur titulaire†

*Université de Sherbrooke, Faculté de génie, Département de génie mécanique.
†Université de Sherbrooke, Faculté de génie, Département de génie chimique.

Date de soumission: 27 octobre 2017.

État de l'acceptation: version finale publiée le 28 octobre 2017.

Revue: Chemical Engineering Science.

Titre en français:

Modélisation du transfert de chaleur convectif en régime turbulent de nanofluide Al_2O_3-eau dans un tube uniformément chauffé.

Contribution au document:

Cet article contribue à la thèse en évaluant en détails les performances de huit modèles de turbulence sur les écoulements turbulents de nanofluides et les transferts thermiques par convection forcée dans une conduite uniformément chauffée.

Résumé en français: Les transferts thermiques convectifs d'un écoulement de nanofluide de type Al_2O_3-eau dans un tube circulaire uniformément chauffé sont étudiés numériquement en utilisant différents modèles de turbulence. Quatre concentrations volumiques de nanoparticules ($\varphi \leq 2\%$) sont considérées pour des nombres de Reynolds entre 3000 et 20000. Les effets de la concentration volumique en nanoparticules et du nombre de Reynolds sur le nombre de Nusselt et le coefficient de frottement sont quantifiés. Deux approches numériques différentes, comprenant un modèle monophasique et un modèle de mélange, avec des propriétés thermophysiques variables, sont favorablement comparées aux résultats expérimentaux obtenus dans la littérature pour de faibles concentrations en nanoparticules ($\varphi \leq 0.5\%$). Les résultats avec la concentration la plus élevée $\varphi = 2\%$ montrent la nécessité d'utiliser le modèle de mélange. Huit modèles de turbulence dans leur formulation à faible nombre de Reynolds sont ensuite comparés pour évaluer leur capacité à prédire l'effet de la turbulence sur les transferts de chaleur convectifs. Le modèle SST k-ω s'avère être le meilleur avec des erreurs en termes de nombre de Nusselt moyen et de coefficient de frottement de 0.44% et de 1.82% respectivement. Au contraire, le modèle de contraintes de Reynolds avec la corrélation linéaire pression-déformation n'a pas réussi à fournir les bonnes valeurs avec des écarts de 41.91% et 133.54%, respectivement. Enfin, les avantages de l'utilisation de ce nanofluide sont discutés en fonction de quatre critères de mérite.

Mots clés: Transfert de chaleur par convection, nanofluide, modèle monophasique, modèle de mélange, modélisation de la turbulence.

Abstract:

Turbulent convective heat transfers of Al_2O_3-water nanofluid flowing in a circular tube subjected to an uniform wall heat flux are numerically investigated using different turbulence models. Four nanoparticle volume concentrations φ up to 2% are considered for bulk Reynolds numbers within the range $3000 \leq Re \leq 20000$. The effects of the nanoparticle concentration and the Reynolds number on the Nusselt number and friction factor are reported. Two different numerical approaches including the single-phase and the mixture two-phase models with variable thermophysical properties are favorably compared to experimental results obtained from the literature for low nanoparticle concentrations ($\varphi \leq 0.5\%$). The results at a higher volume fraction $\varphi = 2\%$ show the necessity to use a mixture model. Eight turbulence models in their low-Reynolds number formulation are also compared to assess their ability to predict the effect of turbulence on the convective heat transfer. The SST k-ω model was found to perform the best with errors in terms of the average Nusselt number and friction coefficient of 0.44% and 1.82% respectively. On the contrary, the linear pressure-strain Reynolds Stress Model completely failed to provide the good values with discrepancies of 41.91% and 133.54%, respectively. Finally, the benefit of using this nanofluid is discussed regarding four merit criteria.

Keywords: Convective heat transfer, nanofluid, single-phase model, mixture model, turbulence modeling.

4.2 Introduction

Convective heat transfer plays an important role in various industrial sectors such as air-conditioning, transportation, chemical production, microelectronics and power generation. The conventional heat transfer fluids such as water, ethylene glycol or oil exhibit relatively limited heat transfer properties, which hinders the efficiency of the thermal systems. The recent advance in the field of nanotechnology gave rise to a new type of nanometeric metallic or non-metallic particles characterized by their substantially higher thermal conductivities. These particles, referred as nanoparticles, are dispersed into a conventional fluid, creating a new class of heat transfer fluids named nanofluids. Since the pioneering work of Choi and Eastman [47], the particularly increased thermal efficiency of nanofluids, compared to conventional fluids, has attracted the attention of researchers and engineers. Alive researches are still done to model appropriately natural convection in enclosures using ionic nanofluids [154] or including a porous medium [216]. The literature being too abundant, one will focus in the following on the turbulent convective heat transfer in pipes. One of the most common canonical experiments used to study the convective heat transfer performance of nanofluids, is the turbulent flow through a straight uniformly heated pipe as considered for example by Sundar and Sharma [206]. Both the average heat transfer coefficient and the friction factor of an Al_2O_3-water based nanofluid were measured in a straight pipe (with and without inserts) subjected to a constant heat flux at the wall for different axial Reynolds numbers $Re = W_0 D/\nu_{nf}$ (W_0 being inlet axial velocity, D the pipe diameter and ν_{nf} the kinematic viscosity of the nanofluid) and nanoparticle volume fractions φ. They observed that, for φ=0.5 %, the heat transfer coefficient increased by 15.62% and 54.54% for Reynolds numbers equal to 3000 and 18000, respectively, compared to pure water. Their results will serve, in the following, as the experimental database to validate the present simulations. Li and Xuan [133] measured the heat transfer coefficient and friction factor for Cu/water nanofluid flowing inside a tube in both laminar and turbulent flow regimes. They noted an enhancement up to 60% for $\varphi = 2\%$ compared to pure water at the same Reynolds number. Turbulent convective heat transfers and pressure drop of γ-Al_2O_3-water nanofluid inside a circular tube were investigated experimentally by Fotukian and Nasr Esfahany [75]. They affirmed that the addition of small quantity of alumina nanoparticles to pure water increased heat transfer remarkably. For example, for $Re = 10^4$ and $\varphi = 0.045\%$, the heat transfer coefficient was increased by 48%. Heyhat et al. [92] experimentally studied the turbulent heat transfer behavior of alumina/water nanofluid in a circular pipe under constant wall temperature condition. Their results showed that the heat transfer coefficient of Al_2O_3-water nanofluid was increased by 23%

for $\varphi = 2\%$ compared to pure water at Re around 12000. Noghrehabadi and Pourrajab [167] investigated experimentally the convective heat transfer of γ-Al_2O_3-water nanofluid in a circular tube with constant heat flux at the wall. Their results showed that the average heat transfer coefficient was increased by 16.8% for $\varphi = 0.9\%$ compared to distilled water at $Re = 2070$. They observed that the enhancement was particularly significant in the entrance region and decreased with the axial distance. The thermal enhancement by the use of nanofluids has been then widely demonstrated experimentally mainly by global temperature measurements as shown in the detailed review of Kakaç and Pramuanjaroenkij [106]. Numerical simulations appear then as a powerful tool to get a better insight into the flow dynamics and heat transfer processes associated with nanofluids and explain in detail the main mechanisms responsible for this enhancement.

Due to their excessive computational cost, only limited attention has been paid to use direct numerical simulations (DNS) [242],[105] or even large eddy simulations (LES) to investigate nanofluid turbulent flows in pipes or channels. Hu et al. [95] investigated by a LES-Lagraneg method the flow characteristics of nanofluids (water-based Cu or SiO_2) through a straight circular tube at $Re = 25000$ and $\varphi = 1\%$. Their mesh grid is composed of 1.3 millions of cells and their results sampled over 5 mean flow residence times but nothing is said about the computional resources required. Turbulence intensities are enhanced by the presence of nanoparticles, which may be responsible for the heat transfer enhancement. For any nanofluid, there was no evidence of coherent vortical structures within the flow requiring the use of advanced unsteady 3D calculations. Peng et al. [176] performed LES of turbulent nanofluid flows inside a cylindrical pipe and compared the predictions of Eulerian-Eulerian, Euler-Lagrangian, and Lagrangian multiphase models, in an attempt to better explain the flow field behavior and the mechanisms responsible for the heat transfer enhancement. The Lagrangian model was found to perform better than the two other models due to its capability to provide a more detailed information about the development and the interaction of the turbulent eddies with the nanoparticles.

The use of advanced DNS or LES models in the context of turbulent nanofluid flows in realistic geometries remains then marginal and most authors focused on Reynolds-Averaged Navier-Stokes (RANS) turbulence closures. Though being more simple and requiring less computational resources, they might be able to provide accurate data when coupled to the appropriate single or two-phase model and to the appropriate correlations for the nanofluid properties. The standard k-ε model has been successively used in the past to investigate turbulent nanofluid flows and heat transfers inside a cylindrical pipe [19, 21, 27, 55, 189]. For water-based Cu nanofluids, Behzadmehr et al. [21] reported discrepancies of around 7% in terms of averaged Nusselt number at $Re = 15000$ and $\varphi = 1\%$ when using the

standard k-ε model coupled to the mixture model. Akbari et al. [4] used also the Realizable k-ε model to evaluate the turbulent forced convection in a horizontal heated tube filled with water-based Al_2O_3 or Cu nanofluids. A relatively good agreement was found compared to the experimental data of Sundar and Sharma [207] using a single-phase approach. However the rate of increase of the Nusselt number with the Reynolds number was underestimated by the two k-ε models at low nanoparticle concentrations $\varphi < 1\%$. Roy et al. [186] considered turbulent convective flows of three water-based nanofluids flowing inside a radial cooling system using a single-phase model. They compared the predictions of four turbulence models using air as the working fluid and claimed that the shear stress transport SST k-ω model was the appropriate level of closure, compared to the RNG k-ε, k-ω and ϑ^2-f models, exhibiting a good agreement in terms of local Nusselt number and wall pressure distribution with published experimental data at $Re = 23000$. Saha and Paul [188] considered numerically the heat transport behavior of single-phase water-based alumina and titanium nanofluids in a circular pipe under turbulent flow condition. For pure water at $Re = 21800$, they compared the predictions of three k-ϵ models and concluded that the realizable k-ε model was the most appropriate turbulence closure. It has then been extensively used for Re up to 10^6 and $\varphi = 6\%$ with a close agreement in terms of the averaged Nusselt number compared to the Pak and Cho's correlation [172]. Recently, Boertz et al. [33] modeled the flows of SiO_2 ethylene-glycol or water-based nanofluids in a tube with constant heat flux at the wall. Their results obtained for $6000 \leq Re \leq 12000$ and $\varphi \leq 10\%$ using a single-phase model showed that the SST k-ω better predicted the Nusselt number compared to the standard k-ε or k-ω models with a mean deviation of 5% compared to published experimental data. It better predicted also the friction factor but with much larger deviations with the experiments. As a conclusion, there is not a clear consensus about the best turbulence model for investigating turbulent nanofluid flows in a cylindrical pipe and the confidence level depends also strongly on the choice of the single- or two-phase approach and of the modeling of the nanofluid thermophysical properties. An excellent review on different numerical approaches for the simulation of nanofluid flows can be found in the references [15] and [107]. One can notice that the standard k-ε coupled to a single-phase modeling is still widely considered today to model turbulent forced convective heat transfer of Cu [79] or TiO_2 [97] water-based nanofluids in a single pipe.
To the best of our knowledge, there is no detailed study evaluating in detail the performance of eight RANS turbulence models on the turbulent flow and forced convective heat transfer of nanofluids in a pipe. This work is then an attempt to fill this gap. A carefull attention should be paid also to the choice of the appropriate single- or two-phase approach. The solver will be validated first against the experimental data of Sundar and Sharma

[206] for low volume fractions $\varphi \leq 0.5\%$. Eight turbulence models in their low-Reynolds formulation will be then compared for $Re = 13380$ and $\varphi = 0.1\%$. A deep insight into the turbulence modeling enables to explain why the Reynolds Stress Model fails to predict such a flow compared to the SST $k-\omega$ model, which performs the best. The performances of water-based Al_2O_3 nanofluids in the forced convective turbulent regime will be finally discussed using four merit criteria. The rigourous built-in of the flow solver, the detailed comparisons of the turbulence models and the evaluation of the nanofluid performances certainly constitute the main novelties of the present paper compared to existing literature.

4.3 Numerical approach

4.3.1 Geometrical configuration

The present work investigates the turbulent flows and the corresponding convective heat transfers of water-based / Al_2O_3 nanofluids under steady-state conditions. The average diameter d_{np} of the alumina nanoparticles is fixed to 47 nm. The nanofluid flows inside a straight cylindrical pipe of length $L = 1.5$ m and diameter $D = 2R = 0.019$ m ($L/D \simeq 79$). The nanofluid enters with a constant temperature and uniform velocity. A constant heat flux Q is imposed at the tube wall (Figure 4.1). The numerical set-up is based on the experiments performed by Sundar and Sharma [206].

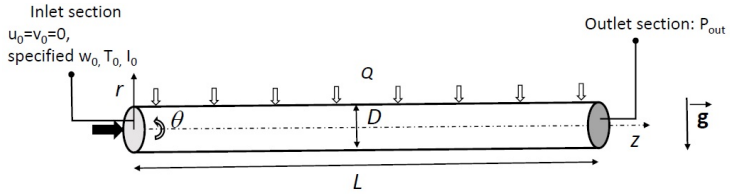

Figure 4.1 Schematic view of the geometrical model with relevant notations and boundary conditions.

4.3.2 Nanofluid properties

The thermophysical properties of water are considered to be temperature dependent while those of the alumina nanoparticles are constant. The following equations hold for the density and the specific heat [220], the thermal conductivity [57] and the dynamic viscosity [48] of pure water and they are used in all simulations.

$$\rho_{bf} = 2446 - 20.674T + 0.11576T^2 - 3.12895\times10^{-4}T^3 + 4.0505\times10^{-7}T^4 - 2.0546\times10^{-10}T^5 \tag{4.1}$$

$$Cp_{bf} = \exp\left(\frac{8.29041 - 0.012557T}{1 - 1.52373 \times 10^{-3}T}\right) \tag{4.2}$$

$$k_{bf} = -0.76761 + 7.535211 \times 10^{-3}T - 0.98249 \times 10^{-5}T^2 \tag{4.3}$$

$$\mu_{bf} = A \times 10^{\left(\frac{B}{T-C}\right)} \tag{4.4}$$

where $A = 2.414 \times 10^{-5}$, $B = 247.8$ and $C = 140$.
One of the main challenges for the modeling of single-phase nanofluid flows remains the accurate determination of the nanofluid properties using the appropriate correlations. The following expressions were used to evaluate the density [116] and the specific heat [116]:

$$\rho_{nf} = \rho_{np}\varphi + (1 - \varphi)\rho_{bf} \tag{4.5}$$

$$Cp_{nf} = \frac{\varphi(\rho Cp)_{np} + (1 - \varphi)(\rho Cp)_{bf}}{\rho_{nf}} \tag{4.6}$$

For the dynamic viscosity of the nanofluid, the correlations respectively proposed by Pak and Cho [172], Corcione [53] and Graham [83] have been considered:

$$\frac{\mu_{nf}}{\mu_{bf}} = 1 + 39.11\varphi + 533.9\varphi^2 = 1 + C_\mu\varphi \tag{4.7}$$

$$\frac{\mu_{nf}}{\mu_{bf}} = \frac{1}{1 - 24.3745 d_{np}^{-0.264}\varphi^{1.028}} \tag{4.8}$$

$$\frac{\mu_{nf}}{\mu_{bf}} = 1 + 2.5\varphi + 4.5\left[\frac{1}{\left(\frac{h}{d_{np}}\left(2 + \frac{h}{d_{np}}\right)\right)\left(1 + \frac{h}{d_{np}}\right)^2}\right] \tag{4.9}$$

where h is the inter-particle spacing.

For the thermal conductivity of the nanofluid, the correlations of Nan et al. [163] and Jang and Choi [102] have been considered:

$$\frac{k_{nf}}{k_{bf}} = \left[\frac{k_{np}(1+2\alpha)+2k_{bf}-2\varphi(k_{bf}-k_{np}(1-\alpha))}{k_{np}(1+2\alpha)+2k_{bf}+\varphi(k_{bf}-k_{np}(1-\alpha))}\right] = 1 + C_k\varphi \tag{4.10}$$

$$k_{nf} = k_{bf}(1-\varphi) + \gamma k_{np}\varphi + C_d\frac{d_{bf}}{d_{np}}k_{bf}{Re_{np}}^2 Pr\varphi \tag{4.11}$$

where $\alpha = 2R_b k_{np}/d_{np}$ is the particle Biot number and $R_b = 0.77 \times 10^{-8}\ m^2.K.W^{-1}$ is the interface thermal resistance. The indexes np and nf refer to the nanoparticles and to the nanofluid, respectively. In Equation 4.11, $\gamma = 0.01$ is a constant taking into account the Kapitza resistance per unit area, $C_d = 18 \times 10^{-6}$ and Re_{np} the particle Reynolds number defined as: $Re_{np} = \left(\frac{\bar{C}_{RM} d_{np}}{\nu_{bf}}\right)$. The random motion velocity $\bar{C}_{RM}$ is fixed to 0.1 m/s as recommended by [102].

The properties of the alumina nanoparticles are set to: $\rho_{np} = 3782\ kg.m^{-3}$, $Cp_{np} = 729\ J.kg^{-1}.K^{-1}$, and $k_{np} = 42\ W.m^{-1}.K^{-1}$ at 20°C. The reader can refer to [29, 223] for a complete view of the different correlations used to model the dynamic viscosity and thermal conductivity of nanofluids.

4.3.3 Numerical method

The governing equations for the conservation of mass, momentum and energy are solved using a finite volume solver in a Cartesian frame. A pressure-based solver has been used as the fluid is assumed to be incompressible. The pressure-velocity coupling is overcome using the SIMPLEC algorithm. It corresponds to a modified version of the SIMPLE algorithm, which converges about up to 30% faster due to the absence of under relaxation coefficients. All equations are discretized in space by a second-order upwind scheme achieving a higher-order accuracy at the cell faces through a Taylor series expansion of the cell centered solution about the cell centroid. All gradients are evaluated using the least squares cell based method without skewness correction. The calculations are performed in steady-state though it has been carefully checked that unsteady calculations led to similar results.

The single-phase and the mixture models were implemented to compare their ability to predict the flow dynamics. They are fully described in Sekrani and Poncet [192]. The Volume of Fluid (VOF) method has not been considered here since Davarnejad and Jamshidzadeh [55] demonstrated that it provides undistinguishable results compared to the mixture model for MgO-water turbulent flow in a straight tube for φ up to 1%. The mixture model takes here into account a relative velocity for the dispersed phase (nanoparticles), gravity and drag effects.

A comparison between eight different turbulence models was performed. These models include:

- The standard k-ε (S k-ε) model of Jones and Launder [104],
- The realizable k-ε (R k-ε) model [199], which includes a different formulation of the eddy viscosity compared to the previous model. The transport equation for the dissipation rate differs also and is derived from an exact equation for the transport of the mean-square vorticity fluctuation.
- The renormalization-group k-ε (RNG k-ε) model [236]. It results in a modified form of the ε equation which attempts to account for the different scales of motion through changes to the production term.
- The standard k-ω Wilcox model [229]. It is known to be more accurate and stable in the viscous sublayer for boundary layer flows with variable pressure gradients than the k-ε model. However it is more sensitive to the free stream conditions for shear flows.
- The Shear Stress Transport k-ω (SST k-ω) model developed by Menter [152]. It combines the robust and accurate formulation of the k-ω in the near wall region and the free stream independence of the k-ε out of the boundary layer. Blending functions are introduced in the transport equation of k and ω.
- The standard Shear Stress Transport (SST) model [152].
- The linear pressure-strain Reynolds-Stress Model of Gibson and Launder [80] using the enhanced wall treatment. It solves the equation of the dissipation rate of the turbulence kinetic energy ε as the seventh equation (RSM-ε).
- The low-Reynolds stress ω model (RSM-ω) based on the Launder-Reece-Rodi's model [126] and coupled to a transport equation for ω. Shear flow corrections are applied to this model.

The eight models are used in their low-Reynolds number formulation and include viscous dissipation terms in the energy equation. When available, a production limiter is applied to avoid any possible overproduction of the turbulence kinetic energy in low velocity regions. Moreover pressure gradient and thermal effects are included in the resolution of the effective velocity distribution close to the wall. The turbulent Prandtl number has been fixed to $Pr_t = 0.9$ in all models. These well-established models are fully described in the monograph of Wilcox [230].

4.3.4 Computational domain and boundary conditions

Several different grid arrangements were tested to ensure that the computed results were grid independent. The selected computational domain was a structured mesh which con-

sists of 6.048 millions of nodes in total (Figure 4.2). At any cross-section or (r,θ) plane, the grid is decomposed into two regions for a total of 4032 nodes. Around the pipe axis, the grid consists of a square of 16×16 mesh points. In the outer region, 68 nodes are used to discretize the tangential direction together with 2×60 nodes in the radial direction. Finally, the axial direction is discretized by 1500 regularly spaced nodes. A mesh refinement close to the pipe wall was deemed necessary to capture the development of viscous sublayer and ensure a wall coordinate always lower than $r^+ < 1$ for all models. The maximum value of r^+ remains around 0.57 for all turbulence closures expect for the RSM, for which it reaches 0.85. In the other directions, the maximum values of the wall coordinates remain in the ranges: $15 \leq z^+ \leq 40$ and $50 \leq (R\Delta\theta)^+ \leq 150$ for all models. For comparison, the mesh grid is 147 times thinner than the one used by Akbari et al. [4] to solve the same flow configuration with the same operating conditions. It is also 5 times thinner in the radial and axial directions than the thinnest one considered by Davarnejad and Jamshidzadeh [55] for a similar problem.

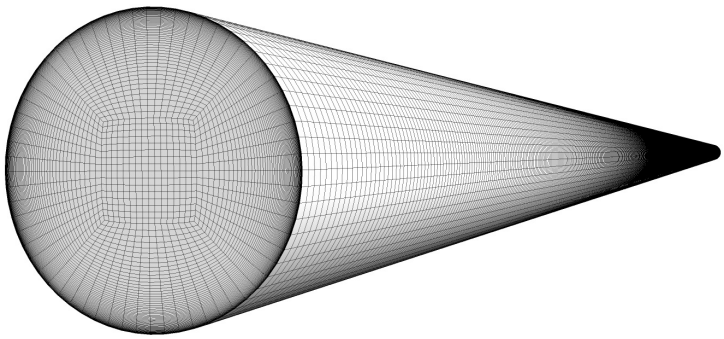

Figure 4.2 View of the mesh grid.

Following the experimental conditions considered by Sundar and Sharma [206], a uniform axial velocity W_0, which corresponds to an axial Reynolds number $Re = W_o D/\nu_{nf}$, (ν_{nf} is the nanofluid kinematic viscosity), and a constant temperature $T_0 = 303$ K, were imposed at the pipe inlet as shown in Figure 4.1. A turbulence intensity $I_0 = 5\%$ was also imposed at the inlet. Imposing higher turbulent intensities at the pipe inlet led to similar results. At the pipe outlet, the gauge pressure was set equal to zero and no re-entry of fluid at the outlet was observed. At the fluid-solid interface, a uniform heat flux of $Q = 1000$ W (corresponding to 11.169 kW/m^2) was imposed with a no-slip boundary condition for the velocity field ($U = V = W = 0$). The convergence criterion required that the maximum sum of the error for each of the conserved variables be smaller than 10^{-6}. The computations were performed in parallel using the cluster "Mammouth Serial" of Calcul Québec with 80 processors resulting into a CPU time per iteration of 10 ms.

4.4 Validation of the numerical solver

The solver is first validated against the experimental data of Sundar and Sharma [206] for low nanoparticle concentrations. The correlations for the dynamic viscosity and thermal conductivity as well as the use of the single-phase or mixture models are evaluated in terms of the averaged Nusselt number and friction factor. All results presented in this Section were obtained using the SST k-ω model.

4.4.1 Evaluation of the correlations used to predict the thermophysical properties of nanofluids

Table 4.1 displays the values of the averaged Nusselt number $Nu = hD/k_{nf}$ (h the heat transfer coefficient) and friction factor f for $Re = 13380$ and $\varphi = 0.1\%$. The results have been obtained using the single-phase mode and the SST k-ω closure. Four combinations of correlations for the dynamic viscosity and thermal conductivity have been compared to the experiments of [206] ($Nu = 108.78$ and $f = 0.0321$). The combination offering the best overall agreement is composed of Equation 4.7 [172] and Equation 4.10 [163] for the predictions of the dynamic viscosity and thermal conductivity, respectively. They will be used in the following sections when associated with the single-phase approach.

Table 4.1 Averaged Nusselt number and friction factor for $Re = 13380$ and $\varphi = 0.1\%$. Results obtained using the single-phase model, the SST k-ω and different correlations for the dynamic viscosity and thermal conductivity. The percentages indicate the deviations with the experimental data of Sundar and Sharma [206].

Dynamic viscosity			Thermal conductivity		Results	
Eq.4.7 [172]	Eq.4.8 [53]	Eq.4.9 [83]	Eq.4.10 [163]	Eq.4.11 [102]	Nu [−]	f [−]
X			X		108.15	0.0315
					(0.58%)	(1.87%)
X				X	108.12	0.0307
					(0.61%)	(4.27%)
	X		X		94.38	0.0336
					(13.24%)	(4.67%)
		X	X		109.98	0.0303
					(1.1%)	(5.61%)

4.4.2 Comparison between the single-phase and mixture models

Three nanoparticle concentrations, namely $\varphi = 0.02$, 0.1 and 0.5%, and Reynolds numbers between $Re = 3000$ and 20000 have been first considered. In order to validate the numerical models, the variations of the averaged Nusselt number Nu with the Reynolds number Re are reported in Figure 4.3. In this figure, the present results obtained using the single-phase and mixture models are compared to the experimental data of Sundar and Sharma [206]. The present predicted values are in quite good agreement with the experimental ones except at higher Reynolds numbers and nanoparticle concentrations. For all Reynolds numbers and different alumina volume fractions, the mixture and single-phase models provide the same profiles, in accordance with the findings of [19, 21] at low nanoparticle volume fractions. One can note that Nu increases with increasing values of Re and/or φ. For example, for $Re = 19500$, the Nusselt number increases by 7.6% when the dispersed quantity of alumina in pure water increased from 0.02% to 0.5%, with both single-phase and mixture models. However, it is noticeable that the numerical results vary weakly with the nanoparticle concentration when compared to the experiments.

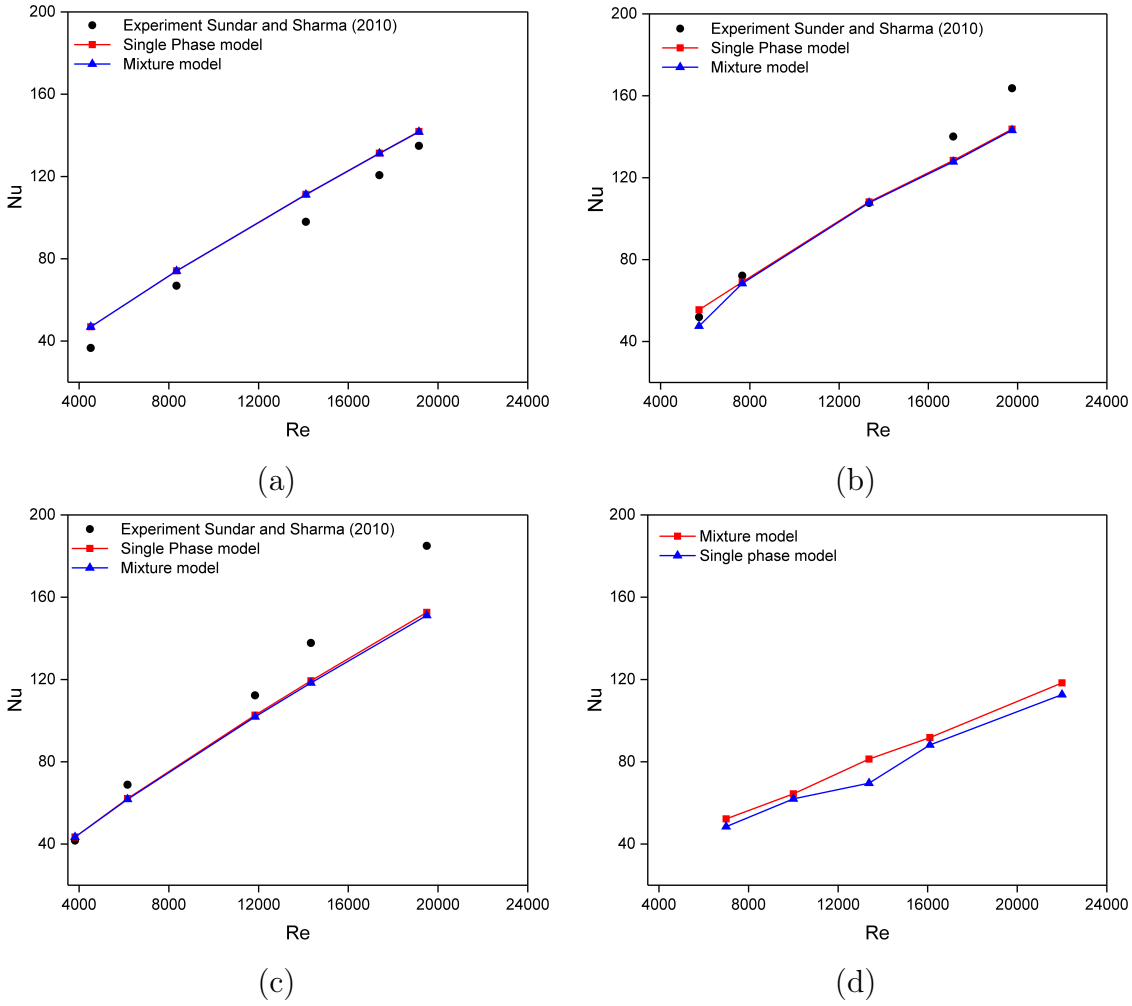

Figure 4.3 Variations of the average Nusselt number Nu as a function of the Reynolds number Re for: (a) $\varphi = 0.02\%$, (b) $\varphi = 0.1\%$, (c) $\varphi = 0.5\%$ and (d) $\varphi = 2\%$. Comparison between the present simulations using the SST k-ω model and the experimental data of Sundar and Sharma [206]

Figure 4.3d shows the Nusselt number distribution for $\varphi = 2\%$. For this nanoparticle concentration, some differences are reported between the single-phase and mixture models. The nanofluid can not be longer assumed to be a single-phase fluid with appropriate properties. Note that, at any given Reynolds number, the Nusselt number decreases when increasing φ from 0.5% to 2%. The heat transfer coefficient h increases when more slowly than the thermal conductivity k_{nf}.

For $\varphi \leq 0.5\%$, the single-phase and the mixture models exhibit the same behavior in terms of the Nusselt number distribution for all Reynolds numbers. This means that, the nanofluids can be treated as a pure single-phase fluid. Therefore, all the heat transfer and

friction factor correlations found in the literature for single-phase flows can be extended to nanofluids. The following expressions were used to evaluate the average Nusselt number:

- The correlation of Gnielinski [81] valid in the range $2300 \leq Re \leq 5 \times 10^6$ and $0.5 \leq Pr \leq 2000$:

$$Nu = \frac{(\frac{f}{2})(Re - 1000)Pr}{1 + 12.7(\frac{f}{2})^{0.5}(Pr^{2/3} - 1)} \tag{4.12}$$

$$f = \frac{1}{(1.58lnRe - 3.82)^2} \tag{4.13}$$

- The correlation of Dittus-Boelter [60] valid for $Re \geq 10^4$ and $0.6 \leq Pr \leq 20$:

$$Nu = 0.023Re^{0.8}Pr^{0.4} \tag{4.14}$$

- The correlation of Pak and Cho [172] valid for $0 \leq \varphi \leq 3\%$, $10^4 \leq Re \leq 10^5$ and $6.54 \leq Pr \leq 12.33$:

$$Nu = 0.021Re^{0.8}Pr^{0.5} \tag{4.15}$$

In Figure 4.4, the predicted values for the average Nusselt number are compared to those obtained from the correlations of Gnielinski [81], Dittus-Boelter [60] and Pak and Cho [172], as illustrated in Figure 3 for $\varphi = 0.1\%$. For example, *Gnielinski (SP)* refers to Equation in which the nanofluid properties are evaluated from the simulations based on the single-phase (SP) model. A good agreement is found between the results of the SP model and both the Gnielinski's and the Pak and Cho's correlations. On the contrary, a large discrepancy is observed with the Dittus-Boelter's equation, especially at high Reynolds numbers. Although the results of both SP and mixture models exhibit a similar behavior compared to the experimental data of Sundar and Sharma [206], a larger discrepancy is obtained between the mixture model and the empirical correlations (Equations 4.12, 4.14 and 4.15). It is noteworthy that a similar analysis was performed for nanoparticle volume fractions of 0.02 and 0.5% leading to similar conclusions. For brevity, the results of this analysis are not shown in this paper.

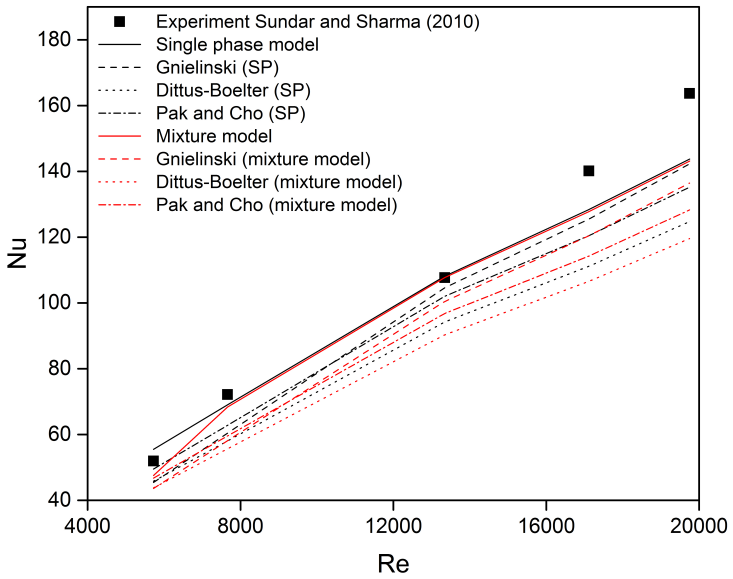

Figure 4.4 Comparison between the evolution of the predicted average Nusselt number using the single phase model and the mixture model together with the empirical correlations of Gnielinski [81], Dittus-Boelter [60] and Pak and Cho [172] as a function of the Reynolds number Re for $\varphi = 0.1\%$.

The variation of the average friction factor for the alumina-water nanofluid is assessed by comparing the predictions of both single phase and mixture models with the Blasius [32] equation. The average friction factor was calculated using:

$$f = \frac{8\tau_m}{\rho u_m^2} \tag{4.16}$$

where τ_m is the wall shear stress and u_m is the mean velocity. For comparison, the typical Blasius equation giving the friction coefficient for a single-phase fluid flow in a tube writes:

$$f = 0.316 Re^{-0.25} \tag{4.17}$$

The distributions of the averaged friction factor for both SP and mixture models, as a function of the Reynolds number are shown in Figure 4.5a-c for $\varphi = 0.02$, 0.1 and 0.5%, respectively. A reasonable agreement between the experimental and the numerical results computed either with the SP or the mixture models is clearly observed, particularly at high Reynolds numbers ($Re > 10000$). Similarly, the numerical results for the friction factor are found to be in conformity with the theoretical values evaluated using the Blasius equation. Nevertheless, a slight discrepancy is obtained at relatively lower Re for all volume fractions. The averaged friction coefficient decreases with increasing Re. However, the addition of

alumina nanoparticles to water has not noticeable effect on it for these low nanoparticle concentrations.

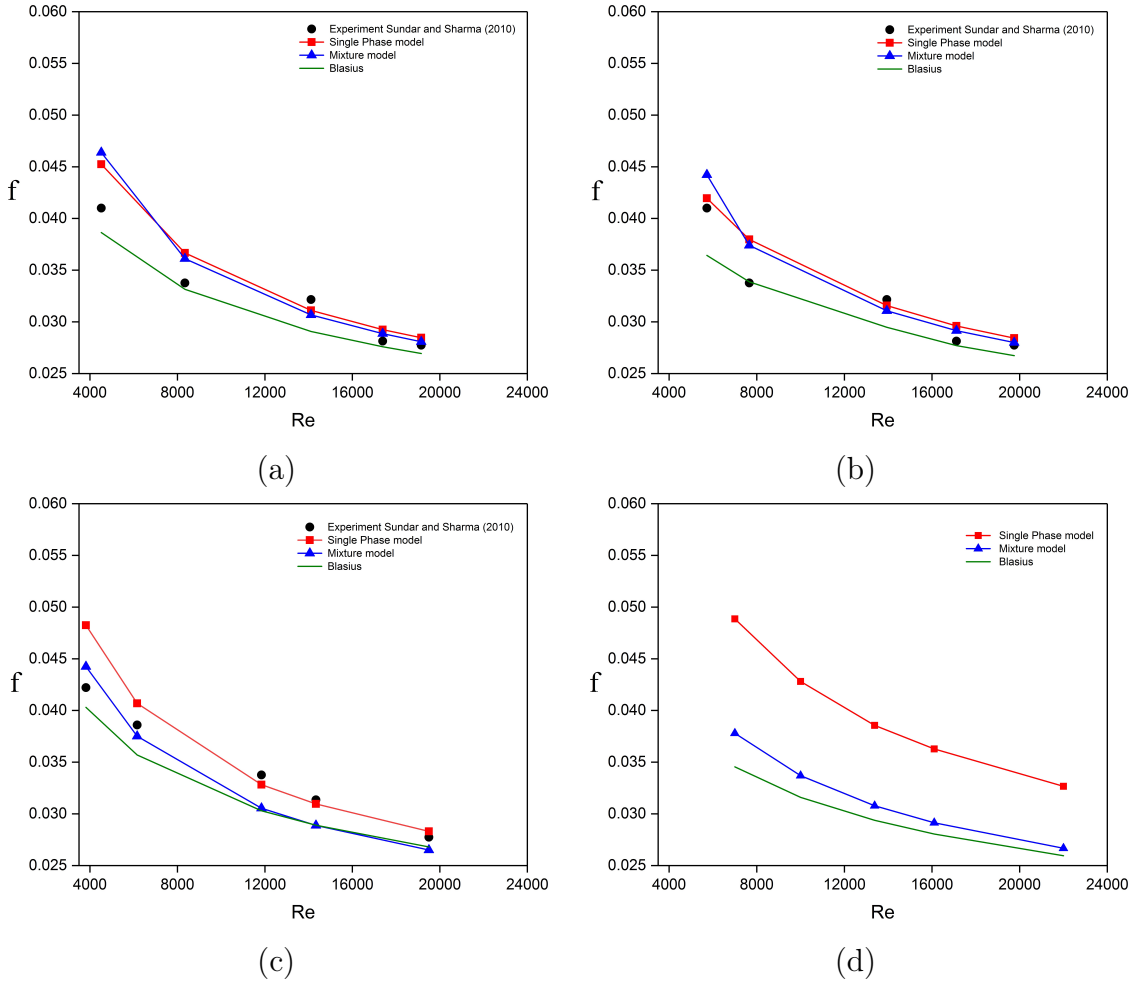

Figure 4.5 Comparison between the predicted averaged friction factor f using both single-phase and mixture models, the experimental results of Sundar and Sharma [206] and the theoretical equation of Blasius [32] for: (a) $\varphi = 0.02\%$, (b) $\varphi = 0.1\%$, (c) $\varphi = 0.5\%$ and (d) $\varphi = 2\%$. Variation of f as a function of the Reynolds number Re.

For the highest nanoparticle concentration $\varphi = 2\%$, all models predict a decrease of the friction factor with the Reynolds number with the good slope compared to the Blasius equation. However, the single-phase model predicts much higher values of the friction factor compared to the Blasius law and to the results of the mixture model as shown in Figure 4.5d. This large deviation compared to the mixture model indicates that the assumption of a single-phase fluid at $\varphi = 2\%$ is no more valid. For this particular value of φ, the mixture model will be used in the following section. These results confirm the distributions of the friction factor obtained by Hussein et al. [97] for TiO_2-water nanofluids ($1 \leq \varphi \leq 4\%$)

using a single-phase model coupled to the standard k-ε. These last authors showed however that the simulated friction factor gets much closer to the Blasius equation for high Reynolds numbers (around $Re = 80000$). Behzadmehr et al. [21] also demonstrated that the mixture model needs to be used for nanoparticle concentration higher than 1% in the case of turbulent Cu-water nanofluid flows in a heated straight pipe.
Akbari et al. [4] performed a detailed analysis of the different single-phase and two-phase approaches including the mixture, the VOF and the Eulerian methods. Surprisingly, while the single-phase model provided very satisfactory results compared to the experimental data of Xuan and Li [232], the two-phase models strongly overestimated the Nusselt number for Reynolds numbers up to $Re = 23000$. It points out the importance to use a very thin mesh grid and not to limit the grid independence study to very coarse meshes.

4.5 Numerical benchmark of the different RANS turbulence models

Since the single-phase and the mixture models provide similar results at low nanoparticle concentrations, the comparative study between the different RANS turbulence models, namely the S k-ε, R k-ε, RNG k-ε, k-ω, SST k-ω, SST and RSM (RSM based on ε or ω), is only based on the single-phase approach due to its simpler implementation as well as its less prohibitive computational cost. In the following section, the comparison between the different RANS models is performed for $Re = 13380$ and $\varphi = 0.1\%$.

4.5.1 Nusselt number and friction factor

The averaged Nusselt number Nu and friction factor f predicted by the different turbulence models are summarized in Table 4.2. The numerical results clearly showed that the SST k-ω model provides the closer predictions for both Nu and f compared to the experimental data of Sundar and Sharma [206], with averaged errors of about 0.43% and 1.8%, respectively. The superiority of the SST k-ω model over the k-ε or k-ω models was also observed by Boertz et al. [33]. The R k-ε, S k-ε, SST and k-ω models show also a reasonable agreement with the experimental values [206]. Interestingly, the RNG k-ε model fails to predict the good value for the Nusselt number (error of 21.97%), whereas it predicts quite well the friction factor. More surprisingly, the RSM model solving a transport equation for ε (7-equation model) strongly overestimates both quantities. The RSM based on ω better predicts the friction factor but underestimates the Nusselt number. Note that all models are used in their original version without any tuning of the modeling constants.

Table 4.2 Comparison in terms of the averaged Nusselt number and the friction factor between the different turbulence models. Results obtained using the single-phase model for $Re = 13380$ and $\varphi = 0.1\%$.

Relative errors are given in (%)	**Nu**	**f**
Experiment [206]	107.682 (-)	0.0321 (-)
S k-ε	108.779 (1.02)	0.0304 (5.22)
R k-ε	108.743 (0.99)	0.0305 (5.06)
RNG k-ε	131.344 (21.97)	0.0305 (4.9)
k-ω	103.145 (4.21)	0.0298 (7.27)
SST	106.223 (1.35)	0.0309 (3.83)
SST k-ω	**108.152 (0.44)**	**0.0315 (1.82)**
RSM-ε	152.808 (41.91)	0.0751 (133.54)
RSM-ω	73.024 (32.19)	0.028 (12.77)

Some comparisons between different turbulence closures are available in the literature for single-phase fluids without nanoparticles. The failure of the RSM-ε model to predict even the base flow has been highlighted for examples by Escue and Cui [70] for swirling pipe flows or Tunstall et al. [218] for curved pipe flows. After Escue and Cui [70], the RNG k-ε performs better than the RSM-ε to predict the distributions of the mean axial and tangential velocity components at loss Rossby numbers. Tunstall et al. [218] showed that the standard k-ε showed better overall performance compared the RSM-ε model and especially when predicting the mean vertical velocity profiles. Thakre and Joshi [212] compared twelve versions of the k-ε models with a RSM based on ε for turbulent flows in a heated pipe. They recommended the use of the k-ε model over the RSM for heat transfer application. For an impinging air jet in an interdisk cavity (without nanoparticle), Roy et al. [186] demonstrated that the SST k-ω model better predicts the radial distribution of the local Nussel number and the wall pressure compared to the standard k-ε, k-ω and ϑ^2-f models. In the following subsections, the eight present turbulence closures are compared into more details and their pros or cons are discussed.

4.5.2 Mean velocity and thermal fields

As a preliminary remark, turbulent pipe flows are considered as multi-scale shear flows with inhomogeneous turbulence characteristics, according to the classification found in [43]. This is also the case for turbulent flows in a plane channel or within a wall boundary

layer, such that some analogies and comparisons could be done, in the following section, with results obtained in these configurations.

In order to closely inspect the hydrodynamic behavior obtained by these turbulence models, the axial development of the centerline axial velocity is illustrated in Figure 4.6a. The centerline mean axial velocities exhibit a significant increase due to the axial development of the flow field and especially of the boundary layers. Then they reach peak values at locations ranging from $z/L = 0.15$ to 0.35 depending on the turbulence closures. Then, the centerline velocities slightly decrease towards an asymptotic value characteristic of the hydrodynamic fully-developed flow region. The rapid growth of the boundary layer in the entrance region tends to push the fluid towards the axis region resulting in an increased axial velocity to conserve mass.

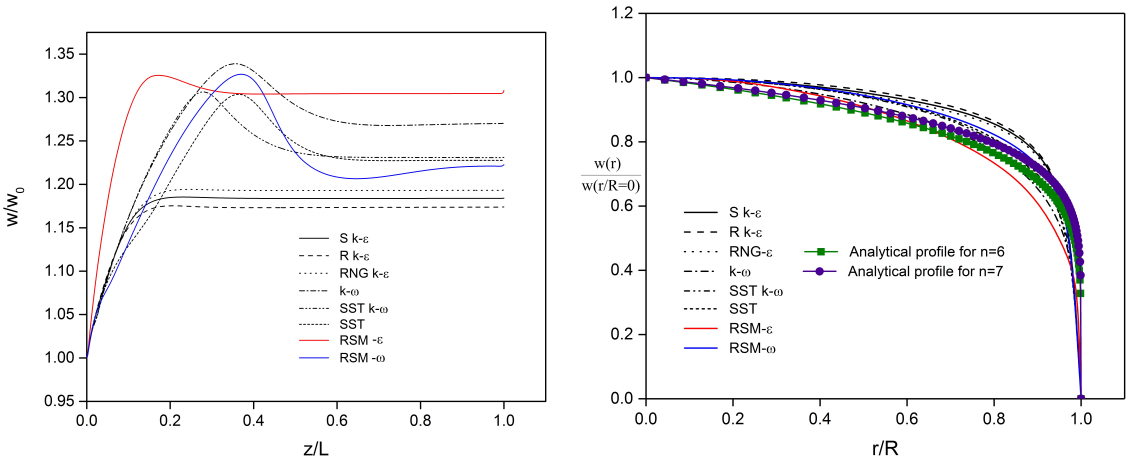

(a) (b)

Figure 4.6 (a) Axial evolution of the centerline mean axial velocity and (b) radial profiles of the mean axial velocity at $z/L = 0.733$. Results obtained for $Re = 13380$ and $\varphi = 0.1\%$.

Bhatti and Shah [25] provided a correlation to determine the length of the entrance region for a turbulent pipe flow: $L_{entry} = 1.359 \times D \times Re^{1/4}$, which corresponds in the present case to: $z = 0.278$ m or $z/L = 0.185$. Figure 4.6a clearly shows that the S k-ε, R k-ε and RNG k-ε models are the first to achieve the hydrodynamic fully developed state at a streamwise distance of about $z/L = 0.15$, close to value proposed by Bhatti and Shah [25]. It is noticeable also that their profiles do not exhibit any clear local maximum there. The k-ω, SST and SST k-ω models predict a fully developed flow further downstrean at $z/L \simeq 0.6$. Moreover the asymptotic values of W/W_0 predicted by these models are much higher than the ones predicted by the family of k-ε models. The profile obtained by the RSM-ω falls within the profiles obtained by SST and k-ω models. The RSM-ε model exhibits the

highest centerline mean axial velocity $W/W_0 = 1.3$ in the fully developed region, which is 6% higher than that of the SST k-ω model. This overprediction is characteristic of a weakly turbulent flow.

The previous results are corroborated by the radial distributions of the mean axial velocity at an axial position $z/L = 0.733$ located within the fully developed region shown in Figure 4.6b. The classical analytical profile for turbulent fully-developed pipe flows in a smooth tube is also plotted for comparison (see in [43]):

$$\frac{W}{W(r=0)} = \left(1 - \frac{r}{R}\right)^{1/n} \tag{4.18}$$

where n depends on the bulk Reynolds number. According to Nikuradse [166], $n = 6$ for $Re = 4 \times 10^3$ and $n = 7$ for $Re = 10^5$.

All k-ε models provide a similar boundary layer growth very close to the wall, which remains thinner than the ones predicted by the family of k-ω or SST models. The RSM-ε model exhibits the highest velocity gradient in the boundary layer region and highest mean axial velocity along the axis, which may be interpreted by a sign of flow relaminarization.

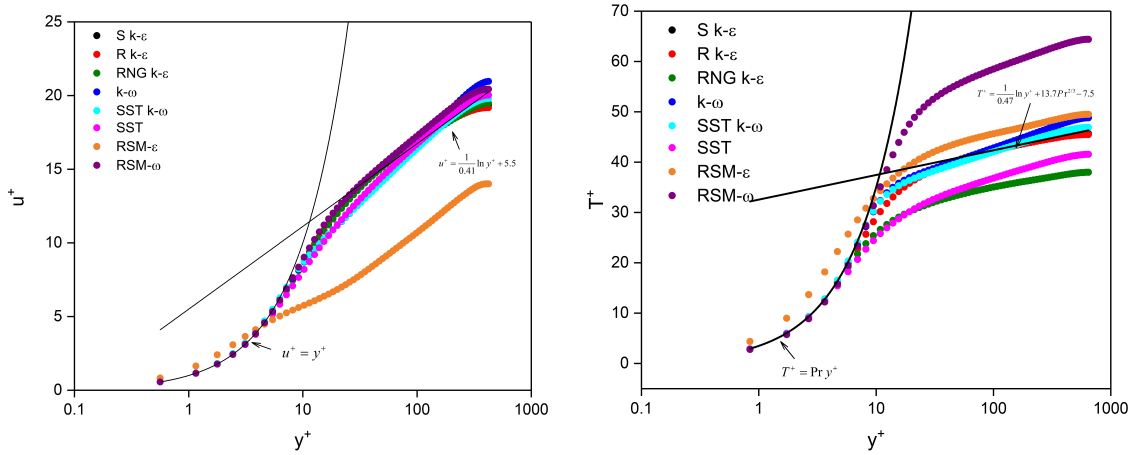

Figure 4.7 (a) Dynamic and (b) thermal boundary layers at $z/L = 0.733$ for $Re = 13380$ and $\varphi = 0.1\%$.

Figure 4.7a shows the radial variations of the normalized effective velocity $U^+ = |U|/U_\tau$ in wall coordinates $y^+(= r^+) = \Delta r U_\tau/\nu_{nf}$ obtained by the RANS models, where Δr is the distance to the wall, U_τ the friction velocity, $|U|$ the magnitude of the velocity vector. All the models except from the RSM-ε provide the same profiles. The linear region $U^+ = y^+$ of the velocity profile, called the viscous sublayer, expands to approximately $y^+ \simeq 7 - 8$.

A buffer region extends then between $y^+ \simeq 7-8$ and $y^+ \simeq 30-70$ (around 30 for the k-ε family and 70 for the SST or SST k-ω models). The logarithmic region (or inertial sublayer) is recovered for higher y^+ and the velocity profiles follow the logarithmic law of the wall : $U^+ = a \times ln(y^+) + b$. The constants $a = 1/\chi = 2.44$ ($\chi = 0.41$ the Von Kármán constant) and $b = 5.5$ are in perfect agreement with the expected values for for turbulent fully-developed boundary layer flows along a smooth wall (see in [43]) and close to the values $a = 2.5$ and $b = 5.5$ obtained by Eggels et al. [66] for fully turbulent pipe single-phase flows or Chung et al. [49] for turbulent flows in an annular pipe at $Re = 8900$. A deficit law starts from y^+ between 317 and 388 depending on the models. The RSM-ε fails to predict the right profile with an overestimation of the effective velocity within the sublayer and a loss profile in the buffer and logarithmic regions.
In the same way, Figure 4.7b displays the radial variations of the normalized effective temperature $T^+ = (T_w - T)/T_\tau$, where T_w is the wall temperature and $T_\tau = Q/(\rho_{nf} Cp_{nf} U_\tau)$ the friction temperature. Once again, all turbulence closures exhibit the same profiles except from the RSM-ε. The temperature profiles follow exactly the expected law $T^+ = Pry^+$ within the thermal sublayer up to $y^+ \simeq 7-8$. A buffer region extends then between $y^+ \simeq 7-8$ and $y^+ \simeq 30-70$ depending on the models. The thermal inertial sublayer is recovered after that and the temperature profiles follow the logarithmic law of the wall : $T^+ = a \times ln(y^+) + b$. The constants a and b differ from one model to another. The standard k-ε, realizable k-ε and SST k-ω follow relatively well the usual law with $a = 1/0.47 = 2.13$ and $b = 13.7Pr^{2/3} - 7.5$ encountered for turbulent fully-developed boundary layer flows along a smooth wall with a constant heat flux (see in [33]). The law of the wall with $a = 2.075$ and $b = 7.55Pr - 3.95$ validated by Juan-Cheng et al. [105] using DNS in the case of viscoelastic-fluid-based nanofluid turbulent channel flow with heat transfer leads to a similar profile and so is not shown here for sake of clarity. A deficit law is obtained for the RNG k-ε at $y^+ \simeq 590$. For comparison, Kasagi et al. [111] obtained $a = 2.78$ and $b = 2.09$ for turbulent channel flows at $Re = 4580$ with a constant heat flux at the walls. Both RSM models exhibit a peculiar behavior: the RSM-ε still overestimates the effective temperature in the viscous sublayer, which explains the overestimation of the Nusselt number previously observed. The RSM-ω behaves quite well very close to the wall but exhibits particularly high values of T^+ in the logarithmic region.

4.5.3 Turbulent field

The axial evolutions of the centerline turbulence kinetic energy k normalized by W_0^2 are displayed in Figure 4.8. The turbulence kinetic energy slightly decreases right after the pipe inlet and then strongly increases in the mixing region. In the latter, the significant

increase of the turbulent production is mainly attributed to the increased turbulent mixing caused by the interaction between the developing boundary layers. As soon as the fully fledged regime is attained, the flow starts to exhibit a rather more organized behavior and the velocity gradients caused by the shearing and stretching across the pipe are gradually smeared. Therefore, the turbulence kinetic energy starts to gradually slightly decrease as there is no production mechanism to maintain a constant turbulence kinetic energy along the pipe. It is especially true for the RSM-ω, SST and SST k-ω models. This decrease of k in the fully developed region has been reported by Akbari et al. [4], whereas Behzadmehr et al. [21] reported that the turbulence kinetic energy at the tube centerline exhibits an asymptotic behavior in the fully developed region.

The three k-ϵ models show similar profiles for k since these models share the same transport equation for the turbulence kinetic energy. The k-ω model predicts the lowest k values among the other turbulence models, which may be attributed to its strong sensitivity to the dissipation rate imposed at the pipe inlet. The highest values of k are obtained by the RSM-ε model. The streamwise development of the turbulence kinetic energy is roughly identical for the k-ω, SST k-ω and SST models with relatively higher values for the SST k-ω model. The SST k-ω model combines indeed the advantageous behavior of the k-ω and k-ε models, by using the free stream independence of the k-ϵ model in the outer part of the boundary layer and the accurate formulation of the k-ω model in the near wall region [152]. The RSM-ω model reproduces sensibly the profile obtained from the k-ω model with higher turbulence kinetic energy levels around mid-pipe $z/L \simeq 0.5$.

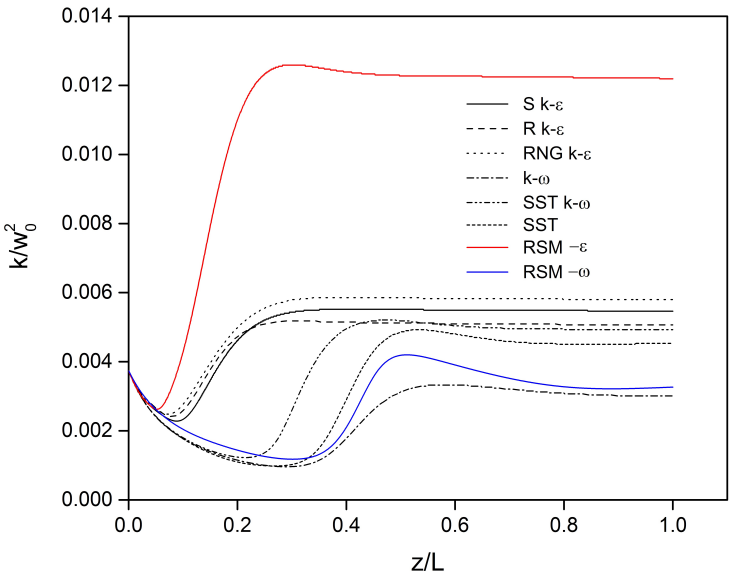

Figure 4.8 Axial evolutions of the centerline turbulence kinetic energy for $Re = 13380$ and $\varphi = 0.1\%$.

The radial profiles of the eddy viscosity μ_t are reported in Figure 4.9 at a streamwise distance $z/L = 0.733$. As expected, the eddy viscosity is low in low-Reynolds number regions and so especially in the viscous sublayer. For $0.68 \leq r/R \leq 1$, the three k-ε models provide the same profiles. When approaching the pipe axis, the turbulent viscosity calculated by the RNG k-ε model decreases until reaching a constant value around 0.04 Pa.s. The turbulent viscosity obtained by the S k-ε model is slightly higher close to the axis where μ_t reaches 0.05 $Pa.s$. The R k-ε model is much more dissipative in the inner region of the pipe as the turbulent viscosity μ_t increases suddenly having a peak value of 0.103 $Pa.s$ at the tube centerline. The same formulation is used by the S k-ε and RNG k-ε models to evaluate the turbulent viscosity [236]. The main difference lies in the constant $C_{2\varepsilon}$ introduced in the transport equation of the dissipation rate ε of the turbulence kinetic energy for the RNG k-ε model [236]. The values of ε predicted by the S k-ε are thus smaller than the ones predicted by the RNG k-ε model. Contrariwise to the former models, the R k-ε model possesses another transport equation for the dissipation rate derived from an exact equation for the transport of the mean square vorticity fluctuation. It includes also a different formulation for the turbulent viscosity, where the C_μ parameter takes into account the changes in both mean and fluctuating velocity fields [199]. This may explain the over-prediction of the turbulent viscosity by the R k-ε model. The SST and SST k-ω models share the same profiles with an eddy viscosity almost twice larger than those predicted by the k-ω and RSM-ω models at the pipe axis. This difference might be attributed to the strong sensitivity of the k-ω model to the freestream conditions. In average, the largest values of the turbulent viscosity are predicted by the RSM-ε model. However, the latter shows the highest gradient of μ_t in the viscous region among the other models. Both RSM models are not based on the hypothesis of an isotropic eddy-viscosity [126] and should have led to comparable results in terms of dissipation. However, it seems that the specific dissipation ω is a better candidate than the dissipation rate ε of the turbulence kinetic energy to evaluate the eddy viscosity for turbulent pipe flows.

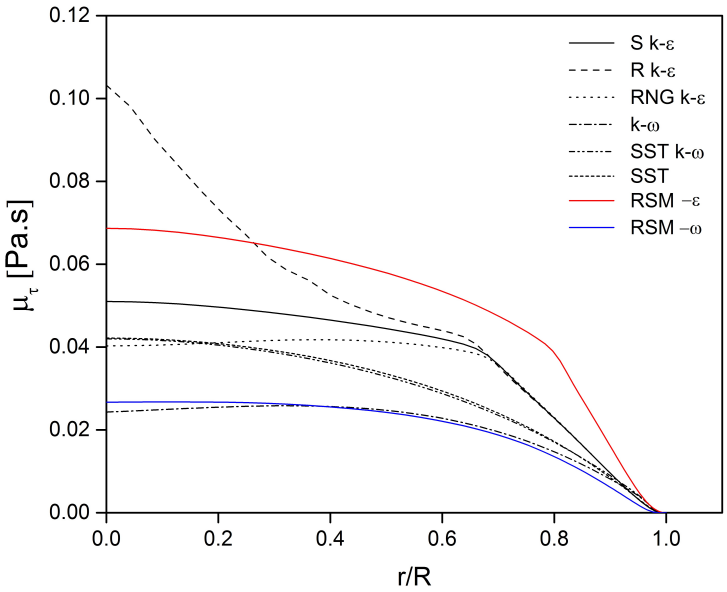

Figure 4.9 Radial profiles of the eddy viscosity at $z/L = 0.733$ for $Re = 13380$ and $\varphi = 0.1\%$.

Note that, at any axial location, the fields k and μ_t are axisymmetric within a cross-section.

4.5.4 Budgets for the turbulence kinetic energy equation

To better explain the discrepancies between the turbulence closures, budgets for the turbulence kinetic energy transport equation are here performed. In the steady-state regime, the general equation for the turbulence kinetic energy k may be written as:

$$A_k = P_k + D_k^{\nu} + D_k^{T} - \varepsilon_k \tag{4.19}$$

where $A_k = U_j \frac{\partial k}{\partial x_j}$ represents the advection term, P_k the production term, $D_k^{\nu} = \nu \frac{\partial^2 k}{\partial x_i \partial x_j}$ the viscous diffusion, $D_k^{T} = \frac{\partial}{\partial x_j}\left(\frac{\nu_T}{\sigma_k}\frac{\partial k}{\partial x_j}\right)$ the turbulent diffusion and $-\varepsilon_k$ the dissipation term. Note that the production term is solved by the RSM, while it is modeled for the two-equations closure using: $P_k = \nu_T \left(\frac{\partial U_i}{\partial x_j} + \frac{\partial U_j}{\partial x_i}\right)\frac{\partial U_i}{\partial x_j}$. ν_T is the turbulent kinematic viscosity and σ_k is a constant. Note that the pressure-strain correlation terms present in the RSM models do not contribute to that budget.

Budgets for the turbulence kinetic energy k are presented in Figure 4.10 at $z/L = 0.733$. $y^+ = 0$ corresponds to the top of the pipe. The mean advection term vanishes from $y^+ \simeq 20$ for all models and only presents large variations close to the wall. For all models except from the RSM-ε model, all terms exhibit profiles similar to those encountered in fully-developed wall flows (see in [43]). In the viscous sublayer, the main contributions come from the viscous dissipation and the dissipation, which compensate almost each other.

For $y^+ < 8$, the pressure and velocity contributions to the turbulent diffusion D_k^T act as sources in the budget. For $y^+ > 8$, both diffusion terms are sinks. The production term exhibits a maximum value around $y^+ = 12$ in agreement with the typical value observed for turbulent plane channel, annular pipe [49] or pure pipe flows [66, 69]. Around this location, only one part of the produced kinetic energy is dissipated locally. The rest is reinjected by the diffusion terms closer to the walls to feed the viscous sublayer. Further from the wall, in the logarithmic region, the production term compensates the dissipation. These two terms are also dominant over the other terms in the external region. The turbulent diffusion plays a significant role again, at the edge of the boundary layer. The shapes of these profiles agree particularly well with the DNS results of El Khouri et al. [69] for turbulent pipe flows at $3464 \leq Re \leq 23406$.

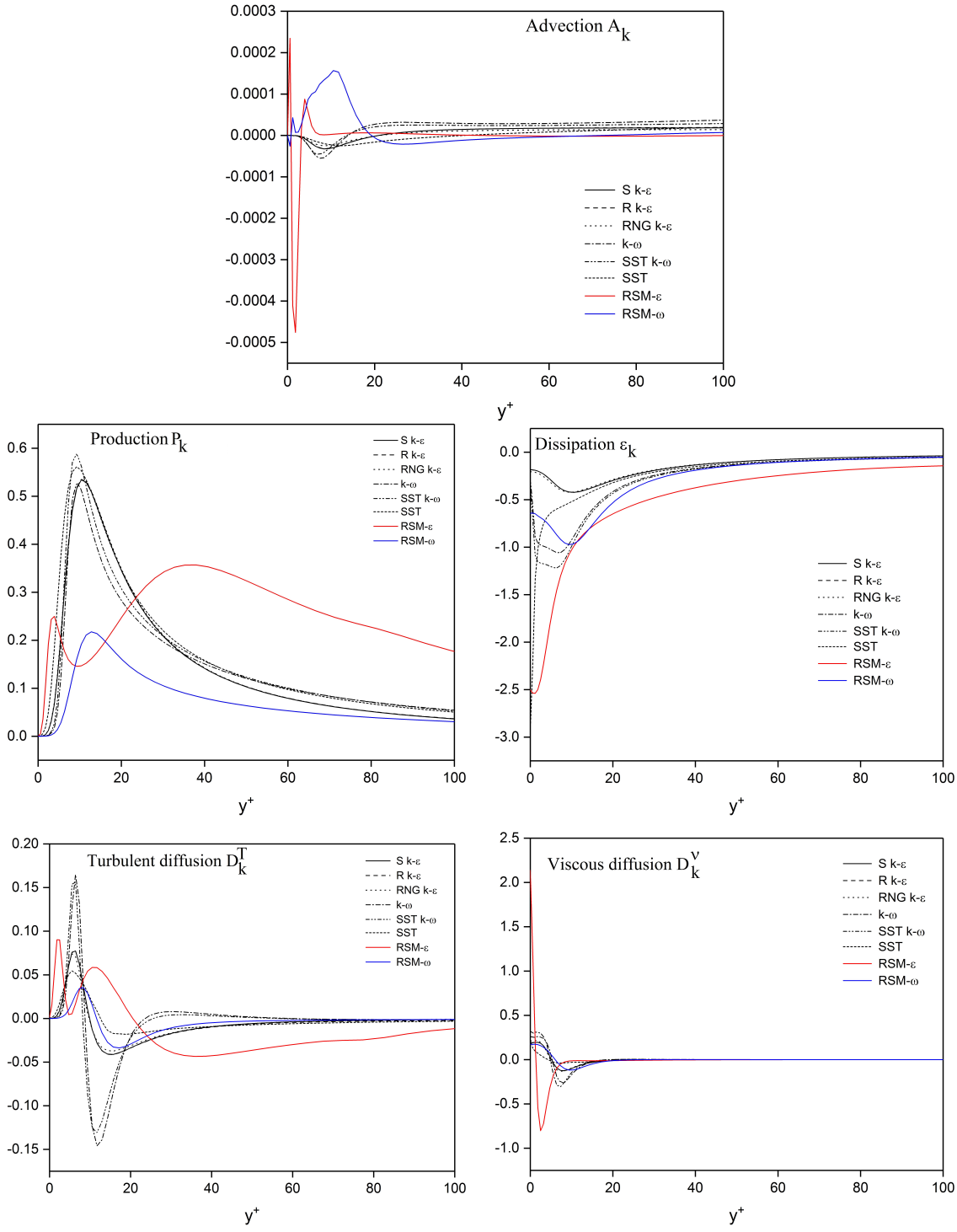

Figure 4.10 Turbulence kinetic energy budgets at $z/L = 0.733$ for $Re = 13380$ and $\varphi = 0.1\%$. Contributions of the advection, production, dissipation, turbulent diffusion and viscous diffusion respectively. Results obtained using the single-phase approach.

The RSM models exhibit peculiar and different behaviors. These second-order models solve seven equations accounting for the anisotropy of the turbulent flow field. The RSM-ω exhibit the same trends as the k-ε family with lower peak values for the production and dissipation terms but these peaks are located at the expected locations. The RSM-ε provides more intriguing results. The production term, which is solved and not modeled, reaches a local maximum at $y^+ \simeq 5$, which explains the overestimation of the effective velocity shown in Figure 4.7a. Its absolute maximum is located in the buffer region. The dissipation term acts more significantly than for the other models, which leads to lower turbulence intensities and confirms the previous results regarding the velocity profiles (Fig. 4.6 and 4.7a). Replacing the seventh transport equation of ε by the one for the specific dissipation ω leads to lower values of the dissipation term. Then, all the results regarding the Nusselt number, the friction velocity or the law of the wall obtained by the RSM-ω are quite comparable to those of the SST k-ω.

One explanation may come from the boundary conditions imposed for the Reynolds stress tensor components in the RSM-ε. Explicit wall boundary conditions for the Reynolds stresses are imposed by using the log-law and the assumption of equilibrium, disregarding advection and diffusion in the transport equations for the stresses. This is not the case for the RSM-ω. In his monograph, Chassaing [43] listed the improvements to be made to a RANS model depending on its failure regarding the budget of the turbulence kinetic energy equation. For the RSM-ε model, which predicts a maximum value of the production term at $y^+ \simeq 4$, it is recommended to modify the modeling of the diffusion terms. In the present case, the second drawback of this model lies in the maximum value reached by the production term itself, which is relatively too low compared to other models and published data in similar configurations. For that, the author recommended to modify the closure for the equation of the dissipation rate ε and more especially the closure of the source/sink terms. It falls out of the scope of the present paper since the main objective was to perform a benchmark of usual RANS models in their original formulation (without any tuning of the constants or modification of the different terms) using the same numerical parameters (mesh grid). All in all, the specific dissipation ω seems to be a better candidate than the dissipation rate of the turbulence kinetic energy ε to determine the turbulent properties of the flow and especially the scale of the turbulence for this particular application. Note that the same behavior for the RSM-ε model has been reported by Bordet et al. [35] for turbulent ice slurry flows in a straight pipe.

Further calculations are now required to investigate in detail the coherent structures, which may appear in the turbulent regime and affect the heat transfer distribution within the pipe. For this purpose, LES calculations using the WALE model associated with the

mixture model are still in progress. Population Balance Models are also an interesting way to improve the predictions of numerical models and account for a more realistic distribution of the nanoparticles within the base fluid.

4.6 Discussion on the performance of water-based Al_2O_3 nanofluids in the forced convective turbulent regime

The overall performance of water-based Al_2O_3 nanofluids in the forced convective turbulent regime is discussed in terms of four merit criteria. The two first ones are a priori criteria used to compare different heat transfer fluids, while the two others can be used to evaluate nanofluid overall energetic performance under operating conditions in a real system. They are:

- The ratio C_μ/C_k (Eqs.4.7 and 4.10) introduced by Prasher et al. [179];
- The Mouromtseff number Mo has been suggested for comparing two heat transfer fluids in fully developed turbulent flow regime through a given geometry. Based on the Dittus-Boelter equation, Timofeeva et al. [213] proposed the following definition:

$$Mo = \frac{\rho_{nf}^{0.8} k_{nf}^{0.67} Cp_{nf}^{0.33}}{\mu_{nf}^{0.47}} \tag{4.20}$$

- The heat transfer improvement and the pressure drop penalty can be gathered to form a kind of overall energetic efficiency η defined by:

$$\eta = \frac{Nu}{\Delta p} \frac{\Delta p_0}{Nu_0} \tag{4.21}$$

  where the index 0 represents quantities evaluated for the case $\varphi = 0\%$ (pure liquid water).
- The Performance Evaluation Criterion (or PEC) has been introduced by Ferrouillat et al. [73] and represents another way to plot the previous parameter. It is based on the ratio of heat transferred to the requiring pumping power. PEC is given by:

$$PEC = \frac{\dot{m} Cp_{nf} \Delta T}{\dot{V} \Delta p} \tag{4.22}$$

  where $\dot{m}$ and $\dot{V}$ are the mass and volumetric flow rates respectively. ΔT and Δp represent the temperature and pressure differences between the outlet and inlet pipe sections.

Figure 4.11 displays the four merit criteria as a function of the nanoparticle concentration φ for $Re = 13380$. The results are obtained using the SST k-ω model with the single-phase ($\varphi < 0.8$ %) or mixture model ($0.8 \leq \varphi \leq 2$ %). In the present case, the ratio C_μ/C_k and the Mouromtseff number Mo are evaluated as a function of the mean temperature deduced from the simulations and φ. As it can be clearly seen, the ratio C_μ/C_k increases with increasing nanoparticle concentrations and remains always larger than the limiting value $C_\mu/C_k = 4$ recommended by Prasher et al. [179] to keep the advantage of the nanofluid. These authors stated that $C_\mu/C_k > 4$ can be tolerated if $Nu > Nu_0$, which is not the case here. Regarding the Mouromtseff number Mo, the graph shows that it reaches a maximum value around $\varphi = 0.8\%$, which would the recommended concentration for this particular application.

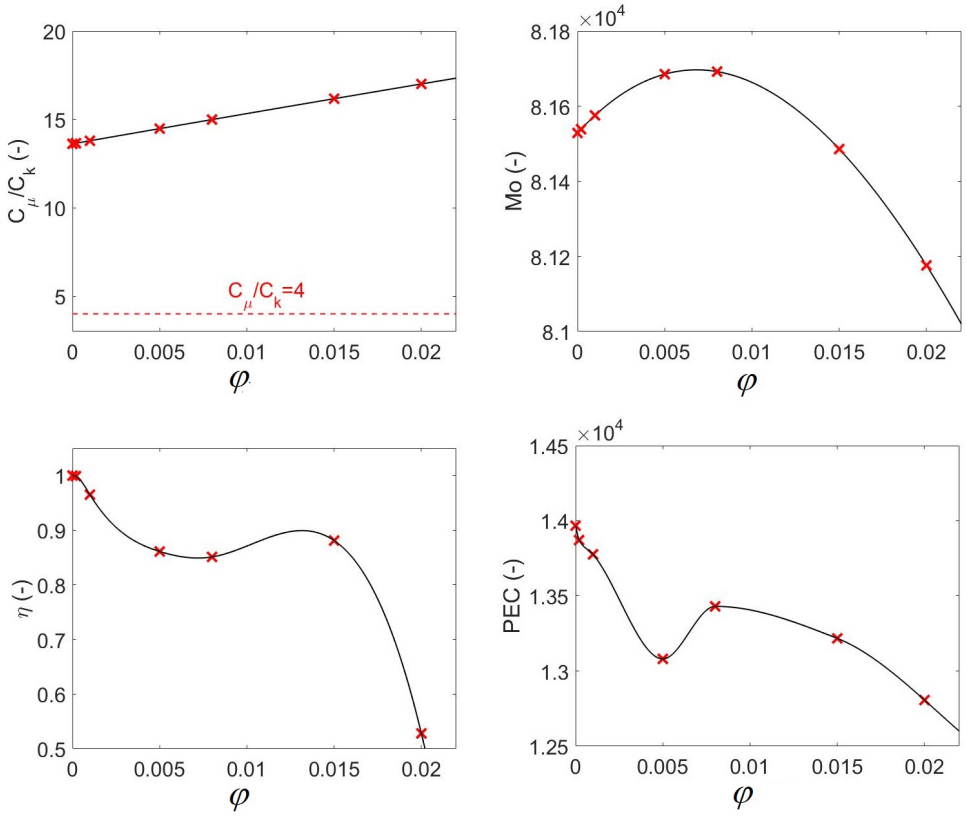

Figure 4.11 Four merit criteria, namely the ratio C_μ/C_k, the Mouromtseff number Mo, the overall efficiency η and the PEC number, as a function of the nanoparticle concentration φ for $Re = 13380$. Results obtained using the SST k-ω model.

The overall efficiency η and the PEC number are non monotonous function of the nanoparticle concentration φ. Though adding nanoparticles to the base fluid leads in general to a decrease of the heat transfer fluid performance, the PEC number exhibits a local maximum

at $\varphi = 0.8\%$, corresponding to the optimum of the Mouromtseff number. The optimum of the overall efficiency is more tricky to define but remains within the range $0.5 \leq \varphi \leq 1.5$ %. The Mouromtseff number seems then to be a good a priori estimate of the performance of nanofluids under realistic operating conditions. On the contrary, the ratio C_μ/C_k is not. Using Equations 4.8 or 4.9 to evaluate the nanofluid dynamic viscosity would indeed lead to similar results for η and PEC, while providing ratios C_μ/C_k lower than the critical value 4. The ratio C_μ/C_k, which does not take into account the density and heat capacity of the nanofluid, cannot then be used as the only a priori merit criterion to recommend or not a given nanofluid.

Ferrouillat et al. [73] measured the PEC number as a function of the Reynolds number for three concentrations of SiO_2 nanoparticles in water (5, 16 and 34%w) in the case of a straight pipe with imposed wall temperature. Roy et al. [186] investigated the influence of the type of nanofluid (water-based Al_2O3, CuO or TiO), nanoparticle concentration (2, 4 and 6%) and Reynolds number on the PEC for laminar and turbulent nanofluid flows in a radial interdisk cavity. Whatever the operating conditions and the type of nanofluid, pure water has a higher PEC, the PEC being a decreasing function of the Reynolds number (in a logarithmic way) and of the particle loading. These two series of authors considered only three very distinct and large values of φ, such that they could not capture the local maximum of the PEC at low φ. But more generally, the present results confirm the findings of [73] and [186] concerning the influence of φ on the PEC number.

All in all, the expected overall benefit of using nanofluids to enhance the thermal performance of real systems is not demonstrated here, confirming the former results of Pantzali et al. [174] (plate heat exchanger), Ferrouillat et al. [73] (straight pipe) or Roy et al. [186] (radial interdisk cavity) for other configurations and under different operating conditions.

4.7 Conclusions

In this paper, a numerical investigation of the hydrodynamic and thermal behaviors of alumina-water nanofluid flowing inside a uniformly heated tube was carried out. Both single-phase and mixture approaches were evaluated and showed a good agreement with the experimental data of Sundar and Sharma [206] for φ up to 0.5%. Both models performed well leading to the same distributions of the average Nusselt number and friction factor over a wide range of Reynolds numbers ($3000 \leq \mathrm{Re} \leq 20000$). This can be explained by both the use of the appropriate correlations for the nanofluid properties using the single-phase approach and by the relatively low nanoparticle concentrations considered here. Results obtained at higher nanoparticle concentrations $\varphi = 2\%$ demonstrated the

need for using the mixture model.

A comparative study between eight RANS models (six two-equation models and two Reynolds Stress Models) in their original formulation was also conducted using the single-phase approach for $Re = 13380$ and $\varphi = 0.1\%$. The SST k-ω was found to be the more appropriate turbulence model, in the present case, with average errors between the predicted values and the experimental data of Sundar and Sharma [206], of about 0.43% and 1.8%, for the averaged Nusselt number and friction factor, respectively. On the contrary, the RSM model based on ε showed its inadequacy to predict both the thermal and hydrodynamic fields, with a predicted friction coefficient twice higher than the experimental one and a discrepancy of 42% in terms of the average Nusselt number. An insight into the law of the wall revealed that this model overestimates the effective velocity in the viscous sublayer, while underpredicting it in the logarithmic region. Budgets of the turbulence kinetic energy have been then displayed to better understand this peculiar behavior. The RSM-ε fails to predict both the location of the maximum production and its value. More intriguing, a secondary local maximum of production appears in the logarithmic region. All in all, ω appears to be a better candidate than ε to determine the scale of the turbulence for this particular application.

To sum up, for future numerical simulations in the turbulent regime, it is recommanded to use the SST k-ω model in its low Reynolds number formulation to well account for the heat transfer in the near wall region. It could be coupled to a single-phase model with appropriate correlations for the thermophysical properties of the nanofluid at low nanoparticle concentrations (φ up to 0.8%) and to the mixture model for higher concentrations.

Finally, the benefit of using Al_2O_3 water-based nanofluids for heat transfer enhancement has been discussed for the first time in terms of four merit criteria. Pure water is shown to have better performances than these nanofluids at any concentration up to 2%. The overall efficiency and PEC are non monotonous functions of the nanoparticle concentration and exhibit both a local maximum, which agrees relatively well with the optimum Mouromtseff number at $\varphi \simeq 0.8\%$.

4.7.1 Acknowledgments

The authors would like to thank the NSERC chair on industrial energy efficiency established at Université de Sherbrooke in 2014 and supported by Hydro-Québec, Natural Resources Canada (CanmetEnergy in Varennes) and Rio Tinto Alcan. Calculations have been performed using the supercomputer Mammouth Parallèle 2 of Compute Canada's network.

4.7.2 Nomenclature

Symbols

C_p	heat capacity, $J.kg^{-1}.K^{-1}$
C_k, C_μ	constants, $-$
D	pipe diameter, m
d_{np}	nanoparticle diameter, m
f	friction coefficient, $-$
h	heat transfer coefficient, $W.m^{-2}.K^{-1}$
h	interparticle spacing, $-$
I	turbulence intensity, $-$
k	thermal conductivity, $W.m^{-1}.K^{-1}$
k	turbulence kinetic energy, $m^2.s^{-2}$
L	pipe length, m
Mo	Mouromtseff number, $-$
Nu	Nusselt number, $-$
p	pressure, Pa
Pr	Prandtl number, $-$
Q	heat flux, W
R	pipe radius, m
(r, θ, z)	radial, tangential and axial coordinates
r^+, $(R\Delta\theta)^+$, z^+	radial, tangential and axial wall coordinates, $-$
Re	Reynolds number, $-$
T	temperature, K
U, V, W	components of the mean velocity vector, $m.s^{-1}$
y^+	radial wall coordinate $(= r^+)$, $-$

Greek symbols

α	particle Biot number, $-$
Δ	difference
η	overall energetic efficiency, $-$
ε	dissipation rate of turbulence kinetic energy, $m^2.s^{-3}$
φ	particle volume fraction, $m^{-3}.m^{-3}$
μ	dynamic viscosity, $Pa.s$
μ_T	turbulent dynamic viscosity, $Pa.s$
ν	kinematic viscosity, $m^2.s^{-1}$
ν_T	turbulent kinematic viscosity, $m^2.s^{-1}$
ρ	density, $kg.m^{-3}$
τ	shear stress, Pa
ω	specific turbulence dissipation rate, s^{-1}

Abbreviations

DNS	Direct Numerical Simulation
LES	Large Eddy Simulation
PEC	Performance Evaluation Criterion, $-$
RANS	Reynolds-Averaged Navier-Stokes
RNG	ReNormalization Group
RSM	Reynolds Stress Model
SST	Shear Stress Transport
VOF	Volume Of Fluid

Indexes - exponents

0	quantity evaluated at the inlet
0	quantity for $\varphi = 0\%$ (section 5)
bf	refers to base fluid
m	mean quantity
nf	refers to nanofluid
nf	refers to nanoparticle
out	quantity evaluated at the outlet
w	quantity evaluated at the wall
τ	friction quantity
$+$	normalized wall quantity

CHAPTER 5

Conjugated heat transfer and entropy generation of Al_2O_3-water nanofluid flows over a heated wall-mounted obstacle

5.1 Avant-propos

Auteurs et affiliations:

1. Ghofrane Sekrani: étudiante au doctorat*
2. Sébastien Poncet: Professeur agrégé*
3. Pierre Proulx: Professeur titulaire†

*Université de Sherbrooke, Faculté de génie, Département de génie mécanique.
†Université de Sherbrooke, Faculté de génie, Département de génie chimique.

Date de soumission: 30 avril 2018.

État de l'acceptation: version finale publiée le 15 mai 2018.

Revue: Journal of Thermal Analysis and Calorimetry.

Titre en français:

Transfert de chaleur conjugué et génération d'entropie des écoulements de nanofluide Al_2O_3-eau autour d'un obstacle chauffé.

Contribution au document:

Cet article contribue à la thèse en quantifiant l'effet de la présence d'un obstacle chauffé dans un canal sur les distributions de transfert de chaleur, la génération d'entropie et les performances du nanofluide alumine-eau.

Résumé en français: Dans cette étude, on présente des simulations numériques d' écoulements laminaires de nanofluides alumine-eau dans un canal rectangulaire avec un obstacle chauffé. Les transferts de chaleur conjugués incluant la convection forcée dans le fluide et la conduction à l'intérieur de l'obstacle sont résolus numériquement en utilisant le modèle de mélange avec des propriétés dépendantes de la température. Le modèle a d'abord été soigneusement validé par rapport à des données disponibles dans la littérature. Ensuite, l'écoulement et les transferts de chaleur ont été étudiés pour six fractions volumiques de nanoparticules φ jusqu'à 1.8% et des nombres de Reynolds dans la gamme $100 \leq Re \leq 1600$. Les résultats montrent que seul le nombre de Reynolds a une influence sur le champ hydrodynamique, notamment sur la longueur de réattachement derrière l'obstacle. Le taux de transfert de chaleur augmente avec l'augmentation des concentrations de nanoparticules et/ou du nombre de Reynolds. Les irréversibilités dues aux transfert de chaleur et aux frottements visqueux sont ensuite étudiées. La génération d'entropie moyenne augmente linéairement avec le nombre de Reynolds. L'augmentation de la fraction volumique des nanoparticules réduit la génération d'entropie thermique tandis que celle par frottement augmente. Enfin, l'avantage de l'utilisation de ce nanofluide est discuté en ce qui concerne cinq critères de mérite.

Mots clés: Nanofluide, transfert de chaleur conjugué, écoulement en canal laminaire, obstacle chauffé, génération d'entropie, simulation numérique.

Abstract: The present study reports numerical simulations of water-based Al_2O_3 nanofluid flowing in a 2D channel with a heated wall mounted obstacle. The conjugated heat transfer problem including forced convection within the fluid and conduction inside the obstacle is numerically solved using the mixture model with temperature-dependent properties. The model has been first carefully validated against published data. Then the fluid flow and heat transfer have been investigated for six nanoparticle volume fractions φ up to 1.8% and bulk Reynolds numbers within the range $100 \leq Re \leq 1600$. The results show that only the Reynolds number has an influence on the hydrodynamic field, especially on the reattachment length behind the obstacle. The heat transfer rate increases with increasing nanoparticle concentrations and/or Reynolds number. The second law analysis is employed to study the heat transfer and fluid friction irreversibilities. The average entropy generation increases linearly with the Reynolds number. Increasing the nanoparticle volume fraction reduces the thermal entropy generation while the frictional one increases. Finally, the benefit of using this nanofluid is discussed regarding five merit criteria.

Keywords: Nanofluid, conjugated heat transfer, laminar channel flow, heated obstacle, entropy generation, numerical simulation.

5.2 Introduction

Industrial applications involving cooling/heating processes such as in heat exchangers, thermal storage systems, electronic equipments or solar collectors are widespread and inherently exhibit critical issues. The two main ones are the need to improve their energetic efficiency to face the energy demand and the development of effective cooling methods to prevent from hot spots. To achieve that objectives, different passive techniques have been considered in the literature such as employing rough walls [10], installing tabulators or swirl flow devices [10, 182] or inserting solid blocks or fins [219, 240].

Comprehensive investigations on the fluid flow and heat transfer in a two-dimensional channel, containing individual or array of heated obstacles mounted on the bottom wall, have been performed experimentally and numerically by Young and Vafai [238–240]. They conducted a parametric study for a wide range of operating parameters, namely the height and width of the obstacle, the inter-obstacle spacing, their number, the solid-fluid thermal conductivity ratio, the flow rate and the heating method. They showed that a proper placement of geometrically dissimilar obstacles, such as taller obstacles, might passively enhance the heat transfer in their vicinity, which would require a synchronization of the flow rate with the channel and obstacle geometries to control the reattachment region and its subsequent convective enhancement. Additionally, they found that the flow rates significantly increase the temperature of the obstacle due to reduced convective coefficient. They developed also empirical correlations for the obstacle mean Nusselt number as a function of these parameters. Wang and Vafai [225] carried out an experimental investigation on the convective heat transfer in a rectangular channel with protruding and flush-mounted discrete heat sources. They found that the latter distort the flow in the channel causing an increase in the heat transfer rate, accompanied with a pressure drop penalty. They also noted that the pressure loss coefficient increases with decreasing Reynolds number and/or increasing protruding height-width ratio. Korichi and Oufer [122] performed a numerical study on the laminar forced convective flow in a rectangular channel containing two obstacles alternatively attached to the upper and bottom walls of the channel and heated with a uniform heat flux. Their results suggest that, as the Reynolds number increases, the heat removed from the obstacles increases notably with a maximum heat removal around the obstacle corners. They also reported that the heat transfer along the obstacle surfaces may be enhanced by the vortex shedding generated by the obstacle attached to the upper channel wall. The effects of the flow conditions and the block geometry on the flow separation-reattachment regions and the heat transfer enhancement have been experimentally and numerically investigated by Umur et *al*. [219].

They demonstrated that the heat transfer is strongly dependent on the block thickness and the Reynolds number. Noticeably higher turbulence and heat transfer rates were obtained under the laminar regime compared to transitional or turbulent flows.

Though the above-mentioned techniques may improve the heat transfer performance, they possess a major limitation, which is the inherent low thermal conductivity of conventional heat transfer fluids, such as water, oil or ethylene glycol. The recent advances in nanotechnology led to the manufacturing of nanometer metallic and non-metallic particles referred as nanoparticles. These particles are characterized by their higher thermal conductivities compared to the base fluids. For example, the thermal conductivities of alumina or copper at room temperature are about 70 and 670 times greater than that of pure water, respectively [102]. The dispersion of nanoparticles into conventional host fluids gave rise to a new class of heat transfer fluids named nanofluids [47]. Since the pioneering study of Choi and Eastman [47], nanofluids have attracted the attention of many researchers because of their capability to improve the thermal conductivity of the working fluids, which can result in a higher energy efficiency and a better performance of the system. Alumina Al_2O_3 nanoparticles have been widely considered in the literature [135, 222] because they are cheap to produce and they do not oxidize compared to copper nanoparticles. As an example, Bouguerra et *al.* [36] reported recently that the thermal conductivity of water can be enhanced by 23% when adding a 2% volume fraction of Al_2O_3 nanoparticles.

The thermal performance of nanofluids, considered as the new generation of heat transfer fluid, has been the subject of many experimental, theoretical and numerical investigations on laminar and turbulent convective flows [2, 93, 140, 192, 194, 208]. They may be also combined to other passive techniques to enhance the performances of thermal systems. Heidary and Kermani [89] performed a parametric analysis to quantify the influence of φ and the addition of partial blocks along the bottom wall of a duct on the thermal performances of the system. As the Reynolds number increases, the size of the separated region behind the blocks grows leading to a pressure drop penalty. This may be due also to the large nanoparticle volume fractions considered in their work ($\varphi = 10\%$). As expected, such a high nanoparticle concentration improves significantly the heat transfer, by around 20%. Sidik et *al.* [201] numerically examined the effects of forced convective nanofluid flows across a channel with five mounted objects on the heat transfer performance using the lattice Boltzmann method. Their results showed that, as the alumina volume fraction increases, the heat transfer rate increases and this is accentuated at high Reynolds numbers. The heat transfer process was affected by the formation of vortices both at the fronts of the obstacles but also in their wakes. Esfe et *al.* [71] investigated a laminar mixed convection flow of Al_2O_3-water nanofluid in an adiabatic channel with

two heated obstacles. They found that the Nusselt number decreases by increasing the obstacle dimensions, and that using nanofluids improves the heat transfer rate. When φ increases from 0% to 5%, the Nusselt number averaged over the obstacles increases by 10%. Khoshvaght-Aliabadi and Hormozi [119] studied experimentally the combination of pin channel and copper-water nanofluids. The heat transfer coefficient increases by 30.4% and the pressure drop by 55.6% for the pin channel compared to the plain one. Adding copper nanoparticles to the base fluid inside the pin channel results in an improvement of the thermal-hydraulic performance of plate-fin heat exchangers. The laminar steady-state forced convective flow of copper-water nanofluids in a 2D rectangular channel containing curve and triangular blocks mounted on its bottom wall has been numerically carried out by Foroutani and Rahbari [74]. The heat transfer rate was found to strongly depend on the block shape. The curve obstacle exhibit higher local and average Nusselt numbers compared to the triangular one. They revealed that as the copper nanoparticle volume fraction increases, Nu increases for both block geometries. A laminar nanofluid flow over a heated backward-facing step with and without obstacle has been numerically investigated by Togun [215]. He considered four configurations of backward-facing step for Re between 75 and 225 and CuO nanoparticle volume fraction from 0 to 4%. The best overall thermal performance was found for $Re = 225$, $\varphi = 4\%$ and an obstacle of 4.5 mm height. The pressure drop increases with Re, φ and the height of the obstacle.

The major challenge when designing thermal systems is to find a compromise between the flow conditions and the appropriate configuration to ensure an effective heat transfer while avoiding energy losses. The optimal design and operating conditions can be determined by performing the entropy generation analysis first proposed by Bejan [22, 23] and successfully applied by different authors [7, 151]. The entropy generation may result from heat transfer irreversibility or fluid friction irreversibility. These irreversibilities destroy the useful energy within the system especially when dealing with mounted bluff bodies. Based on the second law of thermodynamics, irreversibilities cannot be avoided completely but they can be at least minimized. Excellent reviews about the entropy generation analysis can be found in [141, 171, 191]. Boghrati et *al.* [34] performed 2D simulations of laminar channel flows with a block. Their results showed that the total entropy generation is not modified by adding Al_2O_3 nanoparticles at different concentrations or a small fraction (0.08%) of carbon nanotubes in liquid water. Only few researchers investigated the entropy generation due to convective nanofluid flows in a channel with a mounted obstacle. Sheremet et *al.* [198] studied numerically the entropy generation and natural convection of Cu-water nanofluid flow inside a differentially heated cavity with a centered hot square block and corner cooler. They observed that the average Nusselt number, Bejan

number and total entropy generation are increasing functions of the nanoparticle volume fraction. They noticed that at high nanoparticle concentrations, the convective flow is reduced, which leads to a weaker cooling effect in the bottom part of the cavity. The heat transfer enhancement and entropy generation due to Al_2O_3-water nanofluid laminar flows in a microchannel with flow control devices have been numerically investigated by Li et *al*. [132]. Four control devices geometries were used: cylinder, rectangle, protrusion and v-groove. The nanofluids concentration varied from 0% to 3%, and the bulk Reynolds number ranged from 50 to 300. They found that the microchannels with cylinder and v-groove ribs exhibit the better heat transfer performance, especially at larger Reynolds numbers, while the microchannel with protrusion ribs was better from the perspective of entropy generation minimization. They noted that as the nanoparticles volume fraction increases, the finning friction factor increases. Rashidi et *al*. [182] evaluated the combined effects of nanofluid and transverse twisted-baffles on the thermo-hydrodynamics and entropy generation of a laminar flow inside a square duct. They found that the viscous entropy generation ratio increases by increasing the volume fraction of nanoparticles or employing the baffles inside the duct. At the same time, the thermal entropy generation decreases but remains the dominant contribution to irreversibilities. The reader can refer to the recent review of Rashidi et *al*. [183], which provides an exhaustive summary of the main contributions combining nanofluids and inserts to enhance the performance of heat transfer devices.

To the best of our knowledge, the present work is the first to investigate the thermal performances of Al_2O_3 water-based nanofluids flowing in a channel with a heated wall-mounted obstacle by considering the mixture phase approach. This model has already proven to provide very accurate results for the same nanofluids in laminar and turbulent pipe flows [192, 194] and so can be used here confidently to quantify the heat transfer distributions, the entropy generation and the performances of these nanofluids for a wide range of operating conditions ($0 \leq \varphi \leq 1.8\%$, $100 \leq Re \leq 1600$). This flow configuration is particularly relevant for the cooling of photovoltaic (PV) cells where nanofluids and inserts under different forms are combined to improve the amount of heat removed from the PV cells. While most authors tend to complexify the geometry (by inserting ribs with an unusual form) to improve the heat transfer, it is more relevant to consider a more canonical though relevant configuration to first fully validate the numerical model and second provide reference data before going any further. The flow around a wall-attached object is indeed an important classical benchmark for simulations and experiments of bluff bodies.

The paper is organized as follows: the numerical model is first described in Section 5.3

with all the details concerning the geometrical model, the thermophysical properties of the nanoparticles and base fluid, the mixture model and the numerical parameters. The results are then presented and discussed in Section 5.4 for different nanoparticle concentrations and Reynolds numbers. The hydrodynamic and thermal fields are first described before a deep analysis of the entropy generation and a discussion about the benefits from using nanofluids regarding five published merit criteria. The main conclusions and future views are summarized in Section 5.5.

5.3 Numerical approach

5.3.1 Geometrical modeling and operating conditions

One considers the forced convective laminar flows of Al_2O_3 water-based nanofluids in a 2D channel with a heated wall-mounted obstacle. The geometry under investigation is shown in Figure 5.1. An incompressible and Newtonian fluid enters the channel with an uniform temperature and a parabolic streamwise velocity distribution $u(y)$. The height of the channel is denoted H and the lengthes of the channel upstream and downstream the solid obstacle are denoted L_e and L_o, respectively. The height and width of the obstacle are denoted by h and w, respectively. The obstacle is heated from below by an uniform heat flux q (W/m^2), while the lower and upper channel walls are insulated. All the geometrical and operating parameters are summed up in Table 5.1. In cases I and II, which will serve for validation purpose, the operating conditions are similar to those considered by [238–240]. Note that the bulk Reynolds number is based on the channel height: $Re = U_m H/\nu_f$, where U_m is the average streamwise velocity imposed at the inlet and ν_f is the fluid kinematic viscosity (those of the nanofluid in case III).

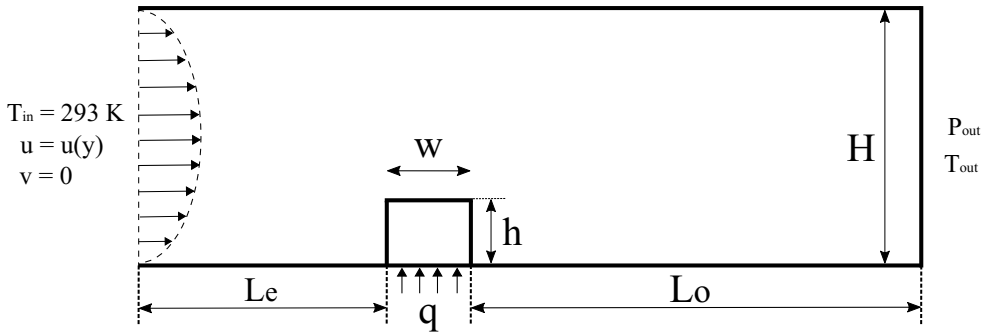

Figure 5.1 Schematic view of the computational domain with relevant notations.

Table 5.1 Operating conditions for the three test cases.

Case	L_e [m]	L_o [m]	H [m]	w [m]	h [m]
I [42, 118, 238]	2	8	2	0.25	0.25
II [240]	$0.25 - 1.7$	0.7714	0.088946	0.0286	0.025454
III	0.25	0.7714	0.088946	0.0286	0.025454
Case	fluid	q $[W/m^2]$	Re [-]	φ $[m^3.m^{-3}]$	k_s/k_f [-]
I [42, 118, 238]	air ($Pr = 0.72$)	1	500	0	10
II [240]	air ($Pr = 0.72$)	930	770	0	7051.3
III	Al_2O_3 water nanofluid (variable Pr)	930	$100 - 1600$	$0 - 1.8\%$	$k_s = 165\ W/(m.K)$ variable k_{nf}

5.3.2 Fluid properties and two-phase modeling

The choice of a suitable numerical approach, being either a single-phase (SP) or two-phase (volume of fluid (VOF), mixture, Eulerian, Discrete Phase Model (DPM)) model, remains the subject of an intense debate. For the sake of brevity, the reader can refer to the review papers proposed by [15] and [107]. The present mixture model with temperature-dependent properties exhibited better performances compared to the SP model for laminar [192] and turbulent [194] forced convective Al_2O_3 water-based nanofluid flows in a straight pipe subject to an uniform heat flux. It will be then considered in the following.

Thermophysical properties

For case III, the thermophysical properties of the alumina nanoparticles (np: nanoparticles) are considered as constant. Their density ρ_{np}, heat capacity Cp_{np} and thermal conductivity k_{np} are equal to: $\rho_{np} = 3880\ kg.m^{-3}$, $C_{p,np} = 729\ J.kg^{-1}.K^{-1}$ and $k_{np} = 42.3\ W.m^{-2}.K^{-1}$ (see in [192]). The nanoparticle diameter is fixed to $d_{np} = 47$ nm.
The nanoparticle dynamic viscosity μ_{np} is calculated based on the Syamlal et *al.*'s [209] correlation:

$$\mu_{np} = \frac{\varphi d_{np} \rho_{np} \sqrt{\pi T_{np}}}{6(3 - e_{ss})} \left[1 + \frac{2}{5}(1 + e_{ss})(3e_{ss} - 1)\varphi g_{0,ss} \right] \tag{5.1}$$

where $e_{ss} = 0.9$ is the coefficient of restitution for nanoparticle collisions, $g_{0,ss} = 0.63$ is the distribution function and T_{np} is the nanoparticle temperature.
The thermophysical properties of water (bf: base fluid) are considered to be temperature dependent. The following equations hold for the density ρ_{bf} and the specific heat Cp_{bf} [220], the thermal conductivity k_{bf} [57] and the dynamic viscosity μ_{bf} [48] of pure water:

$$\begin{aligned}\rho_{bf} = 2446 - 20.674T + 0.11576T^2 - 3.12895 \times 10^{-4}T^3 \\ +4.0505 \times 10^{-7}T^4 - 2.0546 \times 10^{-10}T^5\end{aligned} \tag{5.2}$$

$$Cp_{bf} = \exp\left(\frac{8.29041 - 0.012557T}{1 - 1.52373 \times 10^{-3}T}\right) \tag{5.3}$$

$$k_{bf} = -0.76761 + 7.535211 \times 10^{-3}T - 0.98249 \times 10^{-5}T^2 \tag{5.4}$$

$$\mu_{bf} = A \times 10^{\left(\frac{B}{T-C}\right)} \tag{5.5}$$

where $A = 2.414 \times 10^{-5}$, $B = 247.8$ and $C = 140$.

Mixture model

The mixture model treats the nanofluid as a single fluid (m: mixture) consisting of two strongly coupled phases. It defines the concept of phase volume fractions φ, which are continuous functions and their sum equals one. Each phase k has its own velocity. The governing equations of the two-phase model are:

– Conservation of mass:

$$\nabla \cdot (\rho_m \vec{V}_m) = 0 \tag{5.6}$$

– Conservation of momentum:

$$\rho_m \vec{V}_m \cdot \nabla \vec{V}_m = -\nabla P_m + \nabla \cdot (\mu_m \nabla \vec{V}_m) + \nabla \cdot (\sum_{k=1}^{n} \varphi_k \rho_k \vec{V}_{dr,k} \vec{V}_{dr,k}) \tag{5.7}$$

where P is pressure. The mixture velocity, density and dynamic viscosity are respectively:

$$\vec{V}_m = \frac{\sum_{k=1}^{n} \varphi_k \rho_k \vec{V}_k}{\rho_m} \tag{5.8}$$

$$\rho_m = \sum_{k=1}^{n} \varphi_k \rho_k \tag{5.9}$$

$$\mu_m = \sum_{k=1}^{n} \varphi_k \mu_k \tag{5.10}$$

The drift velocity of the k^{th} phase writes:

$$\vec{V}_{dr,k} = \vec{V}_k - \vec{V}_m \tag{5.11}$$

– Conservation of energy:

$$\nabla \cdot (\sum_{k=1}^{n} \varphi_k \rho_k \vec{V}_k H_k) = -\nabla \cdot q_m - \tau_m : \nabla \vec{V}_m \tag{5.12}$$

Note that the thermal conductivity of the mixture k_m contained in the term $q_m = -k_m \nabla T$ is evaluated through a mixing-type law: $k_m = \sum_{j=1}^{n} \varphi_j k_j$.

– Conservation of the volume fraction in nanoparticles:

$$\nabla \cdot (\varphi_{np} \rho_{np} \vec{V}_m) = -\nabla \cdot (\varphi_{np} \rho_{np} \vec{V}_{dr,np}) \tag{5.13}$$

The slip velocity is defined as the velocity of a second phase (np: nanoparticles) relative to the primary phase (bf: base fluid):

$$\vec{V}_{pf} = \vec{V}_{np} - \vec{V}_{bf} \tag{5.14}$$

The drift velocity is related to the relative velocity by:

$$\vec{V}_{dr,np} = \vec{V}_{pf} - \sum_{k=1}^{n} \frac{\varphi_k \rho_k}{\rho_m} \vec{V}_{fk} \tag{5.15}$$

The relative velocity is evaluated through the following equation proposed by Manninen *et al.* [145]:

$$\vec{V}_{pf} = \frac{\tau_{np}}{f_{drag}} \frac{(\rho_{np} - \rho_m)}{\rho_{np}} \vec{a} \tag{5.16}$$

where τ_{np} is the particle relaxation time defined as: $\tau_{np} = \rho_{np} d_{np}^2 / (18 \mu_{bf})$ and f_{drag} is the drag function proposed by Schiller and Naumann [190]:

$$f_{drag} = \begin{cases} 1 + 0.15 Re_{np}^{0.687} & Re_{np} \leq 1000 \\ 0.0183 Re_{np} & Re_{np} > 1000 \end{cases} \tag{5.17}$$

with Re_{np} the nanoparticle Reynolds number defined as $Re_{np} = V_m d_{np} / \nu_m$ and $\vec{a} = -(\vec{v}_m \cdot \nabla)\vec{v}_m$. Re_{np} increases with the bulk Reynolds number Re (or V_m) and slightly varies with the nanoparticle concentration φ. It ranges between 3.5×10^{-5} and 6×10^{-4} in the present simulations.

Note that the present model accounts for the drag force while the thermophoretic force and Brownian motion are ignored. The thermophoretic force can be indeed neglected since the temperature gradient along the computational domain remains small (maximum 3 K) in all cases. Regarding the Brownian motion, Wang and Xu [224] showed that for a 10% alumina volume fraction, the nanofluid thermal conductivity increased only by roughly 0.5% when accounting for the Brownian motion. In the same way, the added mass force can be also neglected here since the nanoparticle (alumina) density is about 4 times larger than the base fluid (water) density.

5.3.3 Numerical method and parameters

The governing equations for the conservation of mass, momentum and energy are solved using ANSYS Fluent 16.0 based on the finite volume method in a Cartesian frame. These equations are discretized in space by a second-order upwind scheme achieving a higher-order accuracy at the cell faces through a Taylor series expansion of the cell centered solution about the cell centroid. The pressure-velocity coupling is achieved using the SIMPLE algorithm. All gradients are evaluated using the least squares cell based method without skewness correction. The calculations are performed in steady-state though it has been carefully checked that unsteady calculations led to similar results.
Following to the numerical and experimental conditions considered by Young and Vafai [238, 240], for all studied cases, the fluid enters the channel at the ambient temperature with a fully developed parabolic velocity profile (Fig.5.1):

$$u(y) = 4 v_{max} \left[\frac{y(H-y)}{H^2} \right], \quad v = 0 \quad and \quad T_{in} = 293K \tag{5.18}$$

Both the upper and lower channel walls are insulated ($q = 0$). An uniform heat flux q is imposed at the obstacle lower wall. On all solid surfaces, no-slip boundary conditions are employed for the velocity field ($u = v = 0$). On the fluid-obstacle interfaces, a C^1 continuity condition is imposed:

$$u = v = 0, \quad T_f = T_s, \quad k_f \frac{\partial T_f}{\partial n} = k_s \frac{\partial T_s}{\partial n} \tag{5.19}$$

where f and s refer to the fluid and solid respectively and n is the normal direction to the surface.

Finally, at the channel outlet, the gauge pressure is set to zero and all the normal diffusion flux and the mass balance correction are applied.

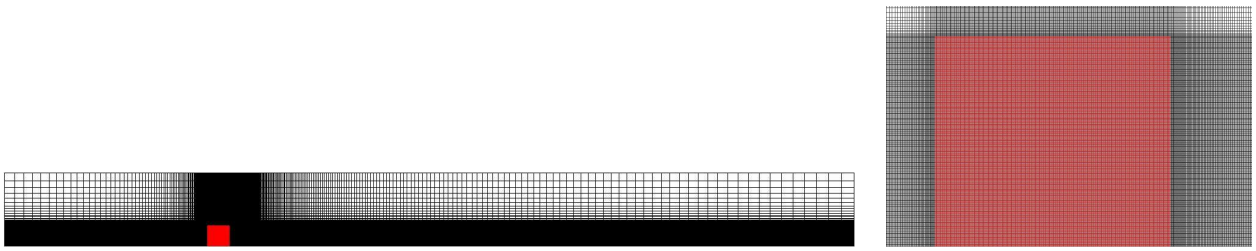

(a) (b)

Figure 5.2 Schematic view of the mesh grid in the (a) whole computational domain and (b) near the obstacle. The obstacle is in red.

A Cartesian structured mesh grid was used throughout the fluid and solid domains with a mesh refinement close to the obstacle (Figure 5.2). The refinement rate is fixed to 1.1. Cases II and III sharing the same geometrical parameters, the grid sensitivity has been performed in case II for which reference data have been obtained experimentally by Young and Vafai [240]. The geometrical dimensions and operating conditions are given in Table 5.1. The entrance length L_e is fixed to 1.7 m. Four mesh arrangements have been considered and the results compared in terms of the Nusselt number Nu_{av} averaged along the obstacle walls. The results of the grid sensitivity analysis are summarized in Table 5.2 where the relative error of the present calculations (for a given mesh) is compared to the experimental value $Nu_{av} = 34$ of Young and Vafai [240]. An acceptable relative error is obtained for mesh 2 and the results get grid independent for a total number of nodes equal to 260865 (relative error of 0.79%).

Table 5.2 Grid independence study for test case II.

Total number of grid nodes	Nu_{av}	relative error %
95702	21.509	36.74
192335	33.503	1.46
260865	34.268	0.79
330615	34.267	0.79

5.3.4 Validation of the flow solver

The present model has been already validated for forced convective Al_2O_3 water-based nanofluid flows inside a heated straight pipe subject to an uniform heat flux. In the laminar regime [192], the present mixture model has been favorably compared to the experimental data of Wen and Ding [227] in terms of the local and average heat transfer coefficients for φ up to 1.6%, $Re = 1600$ and $d_{np} = 42$ nm. It besides improved the predictions of the single-phase model. It has been later extended to the turbulent regime [194] for the same geometry and nanofluid for $d_{np} = 47$ nm, φ up to 2% and Re up to 20000. Once again it showed its superiority compared to the single-phase model when compared to the experimental data of Sundar and Sharma [206]. To further validate the model and especially the conjugated heat transfer problem, two other cases, namely test cases I and II (Table 5.1) are considered here.

Case I corresponds to the configuration investigated numerically by Young and Vafai [238] and Kheirandish et *al*. [118]. The total number of mesh nodes is equal to 78262, whose 12000 nodes in the solid domain. The streamwise distribution of the local Nusselt number is displayed in Figure 5.3 and the results compared also to the analytical solution provided by Cess and Shaffer [42]. The location $x = 0$ corresponds to the left bottom corner of the obstacle. The present results are found to be in excellent agreement with the analytical and numerical results of [42] and [238], respectively. Only small discrepancies remain at the top of the obstacle. The present results clearly improve the former numerical results of Kheirandish et *al*. [118].

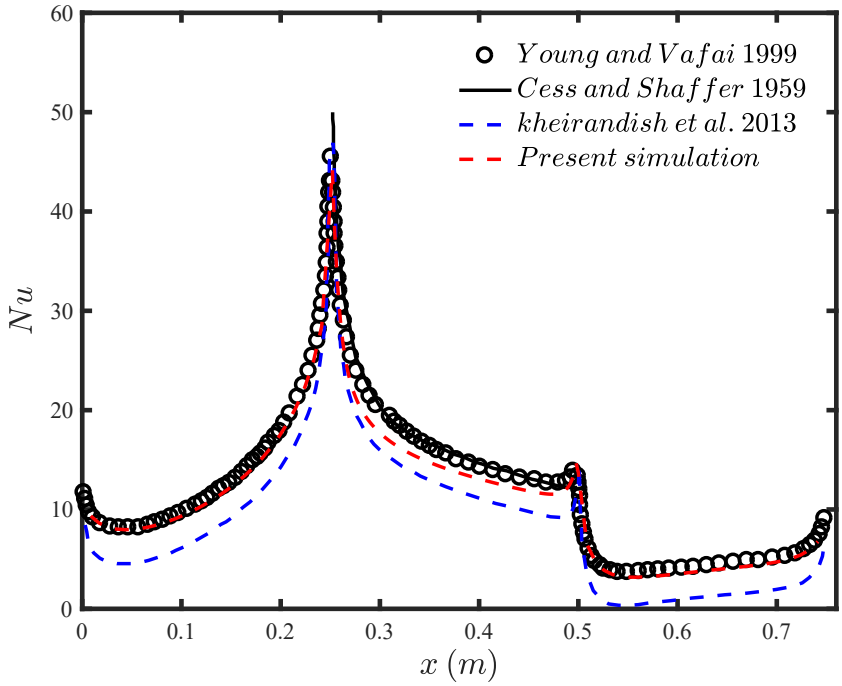

Figure 5.3 Comparison of the local Nusselt number distribution along the obstacle walls with the results of [42, 118, 238] for test case I (Table 5.1).

As already mentioned, test case II corresponds to the experiments of Young and Vafai [240] (see Table 5.1) and a mesh with 260865 nodes provides an average Nusselt number along the heated obstable with a discrepancy of 0.79%. The entrance length is equal to $L_e = 1.7$ m in the experiments of [240], which seems to be very long compared to the total channel length, $L = 2.5$ m. Therefore, to reduce the computational cost without affecting the accuracy of the simulations, four different entrance lengthes within the range $[0.25 - 1.7]$ have been considered. In all cases, the reattachment length L_r in the wake of the obstacle is found to be equal to $L_r/h = 1.05406$. Note that L_r is defined as the position at which the friction coefficient is equal to 0 along the bottom channel wall. No distinguishable differences are found also for the whole thermal and hydrodynamic fields. Then, in the rest of this work, the value $L_e = 0.25$ m will be used since it led to the same results as for $L_e = 1.7$ m but with a mesh being about 1.46 times smaller. It comprises 637 nodes in the streamwise direction and 280 nodes in the vertical direction, with a total number of cells equal to 71214 in the solid domain. The 2D nature of the flow has been also carefully checked. Thus 3D simulations have also been performed for case II using a mesh grid 20 times higher compared to the 2D case. The channel width in the z direction is equal to 0.305 m as in the experiments of [240]. Figure 5.4 displays 3D views of the temperature and streamwise velocity fields. Apart very close to the side walls, there is no

evidence of 3D effects for these operating conditions. The average Nusselt number along the obstacle walls is besides not improved with a discrepancy of 0.82% compared to the experimental value $Nu_{av} = 34$ in the 3D case. The 2D simulation provides the correct Nu_{av} value with a difference of 0.72%. In the following, all calculations for case III will be then performed in 2D.

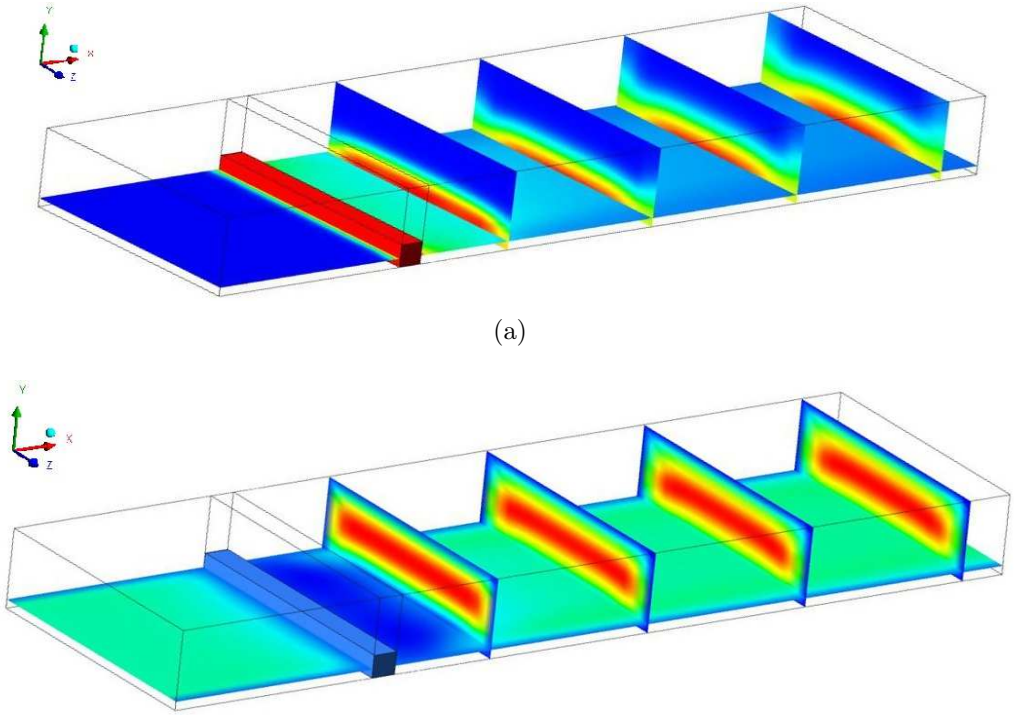

(a)

(b)

Figure 5.4 3D views of the (a) temperature and (b) streamwise velocity fields. Results displayed in a (x, z) plane located at $y/H = 0.11$ and in different (y, z) planes located at $x/h = 11.8$, 23.6, 31.4 and 39.3. The origin of the x axis is located at the channel inlet.

5.4 Results and discussion

In this section, the laminar forced convective Al_2O_3 water-based nanofluid flows over a heated obstacle are investigated in 2D for an entrance length of $L_e = 0.25$ m. The influences of the Al_2O_3 volume fraction φ and bulk Reynolds number Re on the hydrodynamic and thermal fields then on the entropy generation are discussed in detail. All the geometrical and operating parameters correspond to case III and are displayed in Table 5.1. The section ends with the potential benefit of using such nanofluids regarding five merit criteria.

5.4.1 Hydrodynamic field

Figure 5.5 shows the streamlines for the nanofluid flows over the mounted obstacle as a function of the Reynolds number for $\varphi = 1\%$. The streamlines are deflected toward the upper wall of the duct as the flow approaches the obstacle and two clockwise vortexes are generated before and after the heated obstacle, named respectively, the stagnant zone and the recirculation zone. The length and the relative strength of the downstream recirculation zone in the wake of the obstacle increases as Re increases. The forming of the bypass region at the top of the obstacle leads to an increase of the axial fluid momentum there, which inhibits the expansion of the recirculation zone into the full channel downstream of the obstacle [238]. The weak vortex ahead the obstacle also increases in size and strength with increasing Re. The height reached by the first recirculation bubble observed before the obstacle increases from $0.275h$ for $Re = 100$ to $0.432h$ for $Re = 1600$. Similarly, its length increases too from $0.29h$ for $Re = 100$ to $1.1h$ for $Re = 1600$. These results are in close agreement with the findings of Young and Vafai [238, 239]. Contrariwise, the weak vortexes in the stagnant region were not found in [18, 89, 122], which can be attributed to mesh coarseness in their case. This recirculation has besides been reported by Diaz-Daniel et *al*. [59] using sixth-order 3D numerical simulations at $Re = 500$.

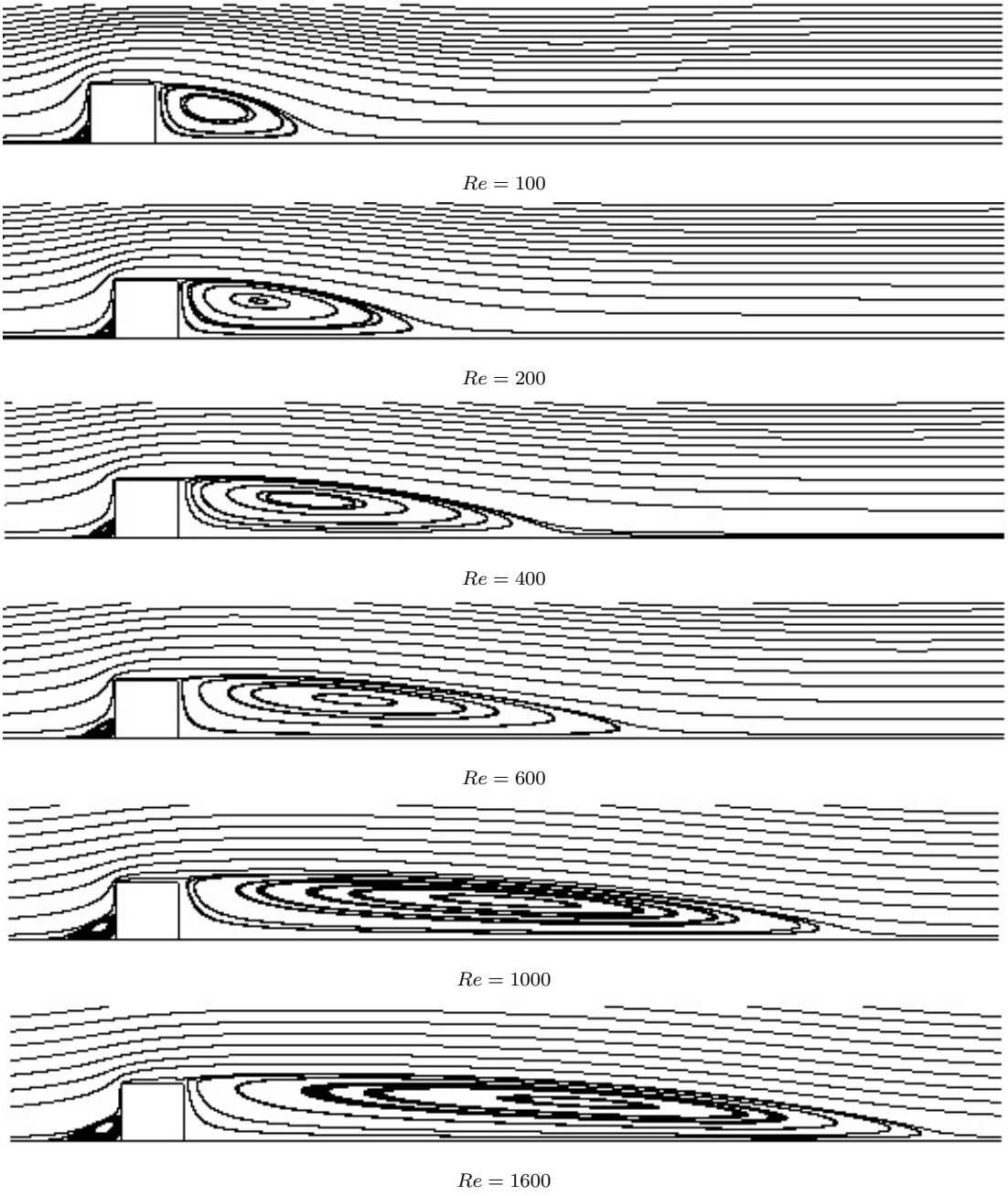

Figure 5.5 Streamline contours as a function of the Reynolds number Re for $\varphi = 1\%$.

The size and the intensity of the two clockwise vortexes are mainly dominated by the Reynolds number. On the contrary, the nanoparticle concentration has no noticeable effect, which explains why the streamline contours for different nanofluid volume fractions are not shown here. However Table 5.3 summarizes the value of the the reattachment

length L_r as a function of both the Reynolds number and nanoparticle volume fraction. It confirms the former observations regarding the streamline patterns: L_r increases with increasing Re values and is not strongly affected by φ. L_r slightly increases with φ for all Reynolds numbers. Without nanoparticles, the present results agree well with the numerical results of Eslami et *al.* [72] for a two wall-mounted cube configuration. These last authors reported indeed that the reattachment length L_r/h varies between 2 and 4 for Re between 100 and 500.

An interesting quantity for engineering applications is the variations of the average skin friction factor $C_{f_{av}} = \frac{\tau_w}{\frac{1}{2}\rho_{nf}U_m^2}$ as a function of the bulk Reynolds number Re, where τ_w is the wall shear stress. The variations of $C_{f_{av}}$ as a function of Re are displayed along the left, top and right sides of the obstacle, the top and bottom channel walls on Figure 5.6 for six nanoparticle volume fractions. For all considered locations, $C_{f_{av}}$ decreases with increasing Re because of the thinning of the boundary layer, which consequently reduces the frictional effect. The addition of alumina nanoparticles to pure water has not noticeable effect on the friction factor, even at high Re, which confirms the former results on the streamline patterns and reattachment length. This outcome is in good agreement with the former results of Sekrani et *al.* [192, 194] for laminar then turbulent nanofluid pipe flows and of Benhampour et *al.* [18] for nanofluid flows in microchannels with ribs. Aghaei et *al.* [2] reported that the skin friction factor is sensitive to both Re and φ for turbulent nanofluid pipe flows, which can be partly inferred to the use of the single-phase model in their study. Figure 5.6 illustrates that at the lowest Reynolds number, $Re = 100$, the highest $C_{f_{av}}$ is observed along the top wall of the obstacle, while its right side wall exhibits the smallest value of the friction coefficient. At a constant inlet mean velocity U_m, it can be simply explained by the fact that the local streamwise velocity at the top of the obstacle increases to conserve mass, which increases significantly the wall shear stress compared to the other walls. For Re within the range $[600; 1600]$, $C_{f_{av}}$ on the obstacle left side wall becomes

Table 5.3 Dimensionless reattachment length, L_r/h, for different Reynolds numbers and nanoparticle volume fractions.

φ \ Re	100	400	600	1000	1600
0	1.96582	4.78223	6.03174	9.16245	10.37888
0.002	1.96582	4.88457	6.03174	9.35503	10.59648
0.006	2.01021	4.88457	6.1813	9.35503	10.59648
0.01	2.01021	4.88457	6.15985	9.35503	10.81853
0.014	2.05555	4.98907	6.15985	9.55154	10.81853
0.018	2.05555	4.98907	6.29056	9.55154	10.81853

higher than along the other walls. The recirculation bubble in the stagnation zone gets indeed larger with higher intensities when Re increases. Finally, both the obstacle right side wall and the channel bottom wall provide the lowest and similar values of $C_{f_{av}}$. Due to the presence of the mounted obstacle, the distributions of $C_{f_{av}}$ cannot be easily compared to the classical Blasius or Shah correlations.

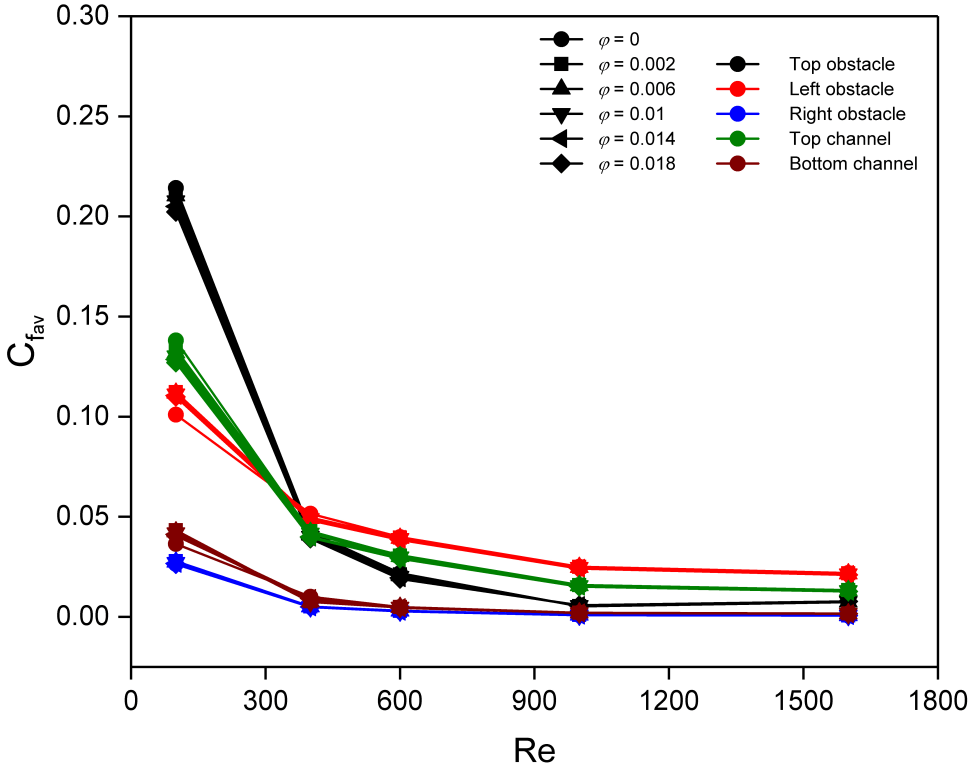

Figure 5.6 Friction factor as a function of the bulk Reynolds number for different alumina volume fractions along the top, left and right sides of the obstacle and along the top and bottom channel walls.

5.4.2 Thermal field

The effects of Reynolds number and nanoparticle volume fraction on the temperature distributions along the computational domain are presented in Figure 5.7. The contours of temperature are plotted at $Re = 1000$ for different nanofluid volume fractions ranging from 0 to 1.8% (Figure 5.7a). The temperature levels within the obstacle indicate that the metallic block absorbed heat transfer from its bottom surface by direct conduction. As the nanoparticle volume fraction increases, the obstacle temperature decreases and becomes more homogeneous, which results in a decrease of the temperature gradient ΔT between the solid and the fluid. For example, at $\varphi = 1.8\%$, ΔT decreases from 2 K to 0.8 K compared to the base fluid case. This improvement may be attributed to the

increase of the thermal conductivity, as mentioned previously, and it can associated also to the decrease of the thermal boundary layer thickness [90, 93]. Moreover, at higher nanoparticle volume fractions, more nanoparticles take part in the heat transfer medium, such that the exchange surface area between the particles and the base fluid is larger, which enhances the heat transfer process. Figure 5.7b shows the temperature contours as a function of the Reynolds number for $\varphi = 1\%$. For low Reynolds numbers, the temperature of the solid is higher and a relatively hot fluid region remains in the wake of the obstacle. When the Reynolds number increases, the isotherms shrink wrap around the obstacle with a notable decrease in the temperature distributions within the channel, precisely in the neighborhood of the solid block. Only weak temperature gradients are observed in the shear layer formed at the top of the obstacle. Buoyancy effects are found to be negligible in the present case such that the forced convective heat transfers are dominant.

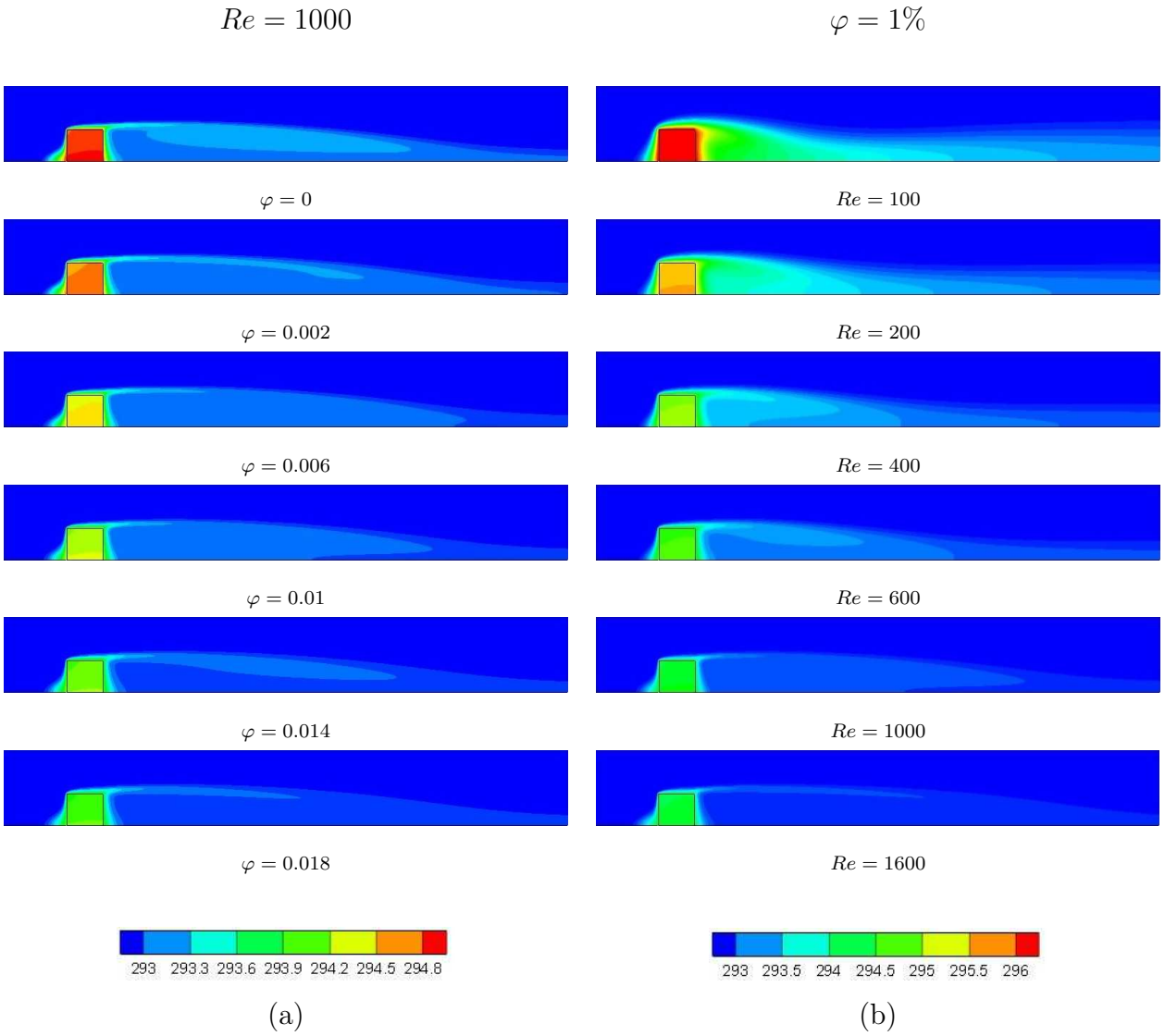

Figure 5.7 Temperature contours (in K) for (a) different Al_2O_3 volume fractions at $Re = 1000$ and for (b) different Reynolds numbers at $\varphi = 1\%$.

The distributions of the local Nusselt number Nu_x along the obstacle walls are displayed in Figure 5.8a for different nanoparticle volume fractions at $Re = 1000$. The variations of Nu_x are very similar to case I (Fig.5.3) for air and do not depend so much on the nanoparticle concentration φ. Along the left wall of the obstacle, the Nusselt number is minimum at $x = 0$ before rising up. The incoming flow impinges on the front surface of the obstacle and creates a vortex on the left lower corner causing a decrease in the heat transfer rate. Above the stagnation zone, the increasing streamwise velocity causes a rapidly increase in the heat transfer towards the left upper corner reaching a maximum local Nusselt number. Along the top surface, there is a decreasing trend for the convection

coefficient which is due to the growth of the thermal boundary layer. Near the upper right corner, the heat transfer increases slightly before an abrupt drop takes place at the rear of the obstacle due to the separated domain and the recirculation zone which acts as an insulation layer. Similar profiles for the local Nusselt number have been obtained for all other Reynolds numbers but for brevity, the profiles are not shown here. For more clarity, the distributions of Nu_x along the left, top and right obstacle sides are displayed in Figures 5.8b to 5.8d. As the Al_2O_3 volume fraction increases, the local Nusselt number decreases. However, the global heat transfer is enhanced, which means that conductive heat transfer is more important than the convective one. For instance, at $Re = 1000$, the heat transfer coefficient and the thermal conduction increase by about 1.8 and 2.25 times when φ increases from 0 to 1.8%. It confirms the former results of Sekrani et *al*. [192, 194] for laminar and turbulent Al_2O_3 water-based nanofluid flows in pipes. However, Mehrez et *al*. [151] reported that Nu_x increases when φ increases, which may be explained by the single-phase model they used, in which the nanofluid properties are not temperature-dependent.

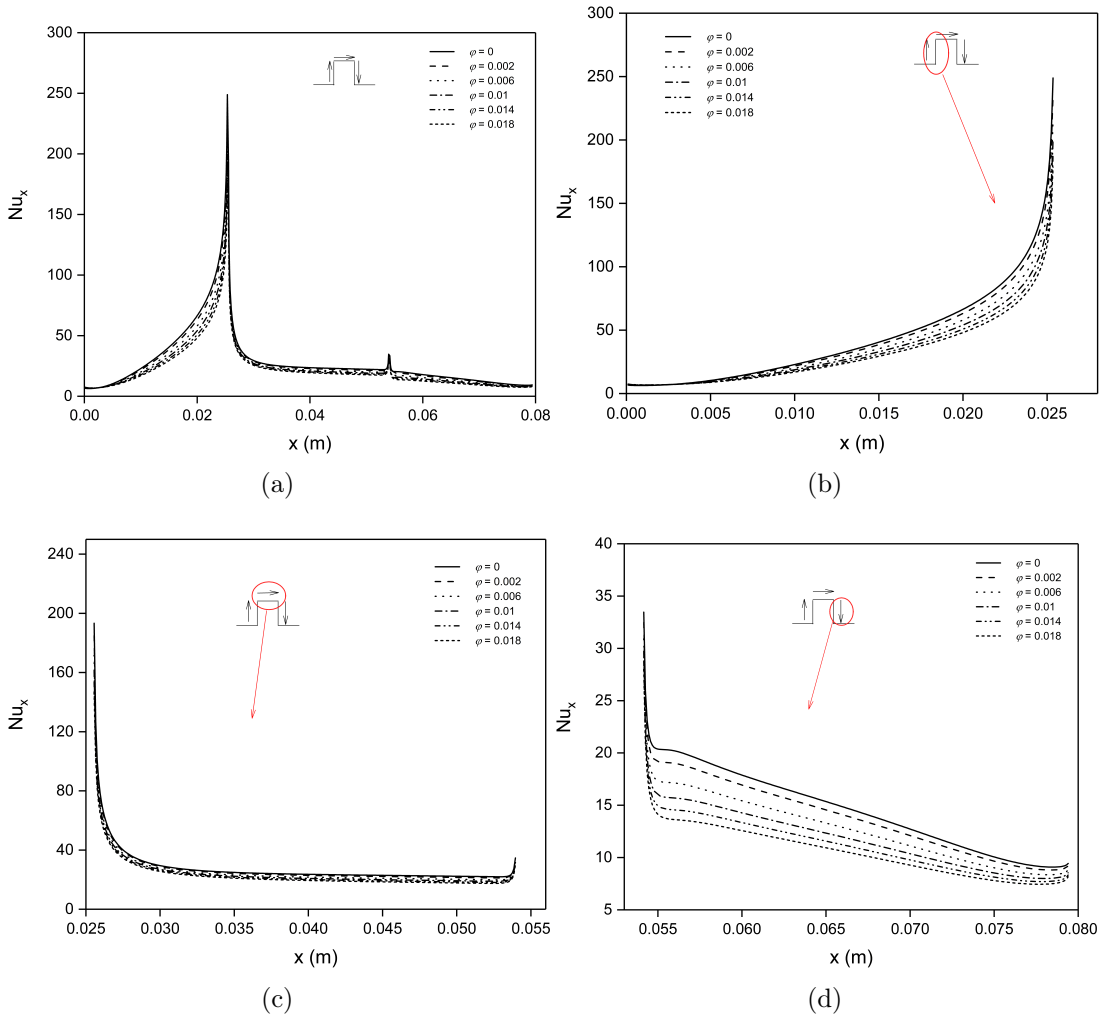

Figure 5.8 Variations of the Nusselt number along the (a) obstacle walls, with a zoom on the (b) left, (c) top and (d) right sides for different Al_2O_3 volume fractions at $Re = 1000$.

Figure 5.9 displays the variations of the average Nusselt number Nu_{av} and average heat transfer coefficient h_{av} as a function of alumina volume fraction for five Reynolds numbers. One recalls that the average is performed along the obstacle walls. The dashed lines with circular symbols represent the variations of h_{av} and the same color refers to the same Reynolds number. This figure illustrates that both Nu_{av} and h_{av} increase sharply when increasing Re whatever the nanoparticle volume fractions tested here. For example, at $\varphi = 1.8\%$, increasing Re from 100 to 1600 leads to an increase of both Nu_{av} and h_{av} by about 140.36% and 135.41%, respectively. The reason for that is a better mixing of the cooling fluid at higher Reynolds numbers [18, 192, 194]. For all studied Reynolds numbers, the average heat transfer coefficient rises with increasing nanoparticle volume

fraction, whereas the average Nusselt number shows an opposite trend. For instance, at $Re = 1000$, adding 1.8% of alumina nanoparticles increases h_{av} by 71.2%. At the same time, Nu_{av} decreases by 23.63% compared to pure water, which is due to the abrupt enhancement of the thermal conductivity, which increases by 124%. Note that similar trends are obtained by considering the mass flowrate instead of the bulk Reynolds number and are then not shown here for sake of clarity. The present results indicate that adding nanoparticles remarkably improves also the rate of heat transfer by conduction [2, 201]. It is worthy to note that the heat transfer enhancement is not only attributed to the increase of thermal conductivity but also to many other phenomena such as the mixing in the near wall regions and the reduction of the boundary layer thickness. Other authors attributed it partly to the Brownian motion [102, 135], which is not accounted for in the present model.

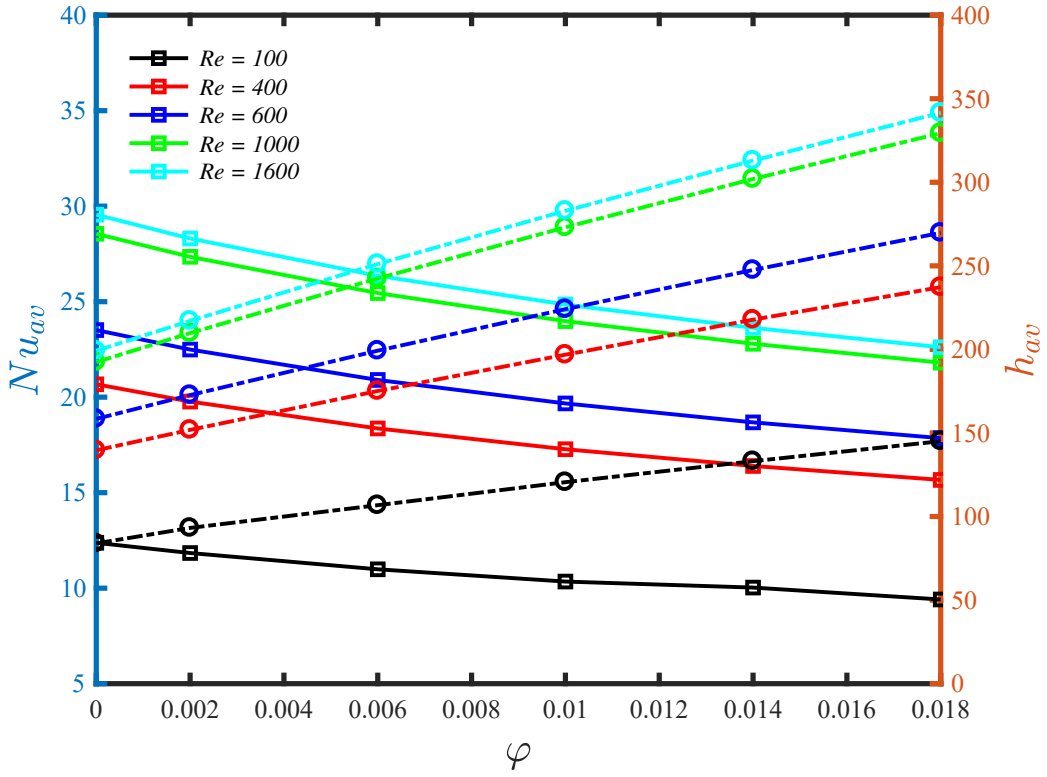

Figure 5.9 Variations of the average Nusselt number (solid lines) and the average heat transfer coefficient (dashed lines) as a function of the alumina volume fraction for different Reynolds numbers.

5.4.3 Exergy analysis and entropy generation

The exergy analysis allows to compare the energy performance of any system in terms of the energy quality rather than the energy amount. Through the open channel, there is no heat or work transfers to the surroundings. The exergy analysis enables to understand the occurring losses. Exergy represents the maximum amount of work theoretically available between any specific state and a reference dead state, typically environmental conditions. The total exergy variation ΔE between the inlet (index *in*) and the outlet (index *out*) of the channel writes [13, 123] :

$$\dot{m}\Delta E = \dot{m}\left[h_{out} - h_{in} - T_0\left(s_{out} - s_{in}\right)\right] \tag{5.20}$$

where $\dot{m}$ is the mass flow rate (kg/s), h is the specific enthalpy (kJ/kg) and s is the specific entropy $(kJ/(kg.K))$. The subscript 0 refers to dead state conditions ($T_0 = 288.25$ K, $P = 101325$ Pa).

Figure 5.10 displays the distribution of the exergy variation ΔE as a function of the alumina volume fraction φ for five Reynolds numbers. The heat flux imposed at the bottom of the mounted cube represents a source of exergy for the nanofluid flow. On the contrary, the main source of exergy losses is the friction along the channel and cube walls. Positive values of ΔE mean thus that the exergy gain due to the heat flux is higher than the exergy losses due to friction. Whatever the Reynolds number, ΔE is positive for pure liquid water. Then it decreases for increasing values of φ. For all Re values, $\Delta E \simeq 0$ for $\varphi \simeq 0.6\%$. At higher nanoparticle concentration, exergy losses due to friction get higher than the exergy gain due to the imposed heat flux. At $\varphi \simeq 1.8\%$, for example, the exergy losses due to friction are higher at low Reynolds numbers as already shown through the friction coefficient distribution in Figure 5.6.

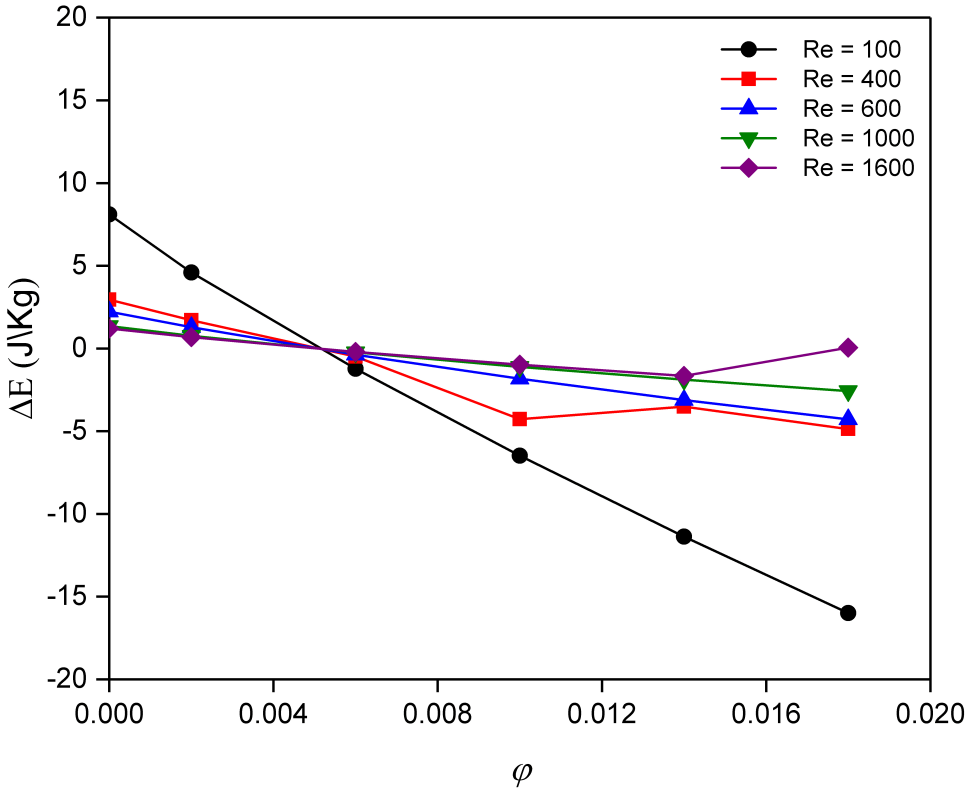

Figure 5.10 Influence of the alumina volume fraction φ on the exergy variation ΔE at five Reynolds numbers.

The entropy generation analysis is an important tool to identify the causes of inefficiency of thermal systems and so lead to the design of optimized systems. It gets very popular since it can be applied to any type of energy conversion system (see the review of [191]). According to the local thermodynamic equilibrium with linear transport theory, the rate of local entropy generation in a two-dimensional flow field can be quantified as follows [22, 23]:

$$\begin{aligned}\dot{S}_{gen} &= \dot{S}_{gen,h} + \dot{S}_{gen,f} \\ &= \frac{k_{nf}}{T^2}\left[\left(\frac{\partial T}{\partial x}\right)^2 + \left(\frac{\partial T}{\partial y}\right)^2\right] + \frac{\mu_{nf}}{T}\left\{2\left[\left(\frac{\partial u}{\partial x}\right)^2 + \left(\frac{\partial v}{\partial y}\right)^2\right] + \left(\frac{\partial v}{\partial x} + \frac{\partial u}{\partial y}\right)^2\right\}\end{aligned} \tag{5.21}$$

Note that the first term $\dot{S}_{gen,h}$ on the right-hand side of the above equation represents the local entropy generation rate due to heat transfer irreversibility, while the second term $\dot{S}_{gen,f}$ represents the local entropy generation rate due to fluid friction irreversibility. To

assess the contribution rates of each irreversibility type on the total entropy generation rate $\dot{S}_{gen}$, one generally considers the Bejan number $Be = \dot{S}_{gen,h}/\dot{S}_{gen}$. The values of Be usually range from 0 to 1.

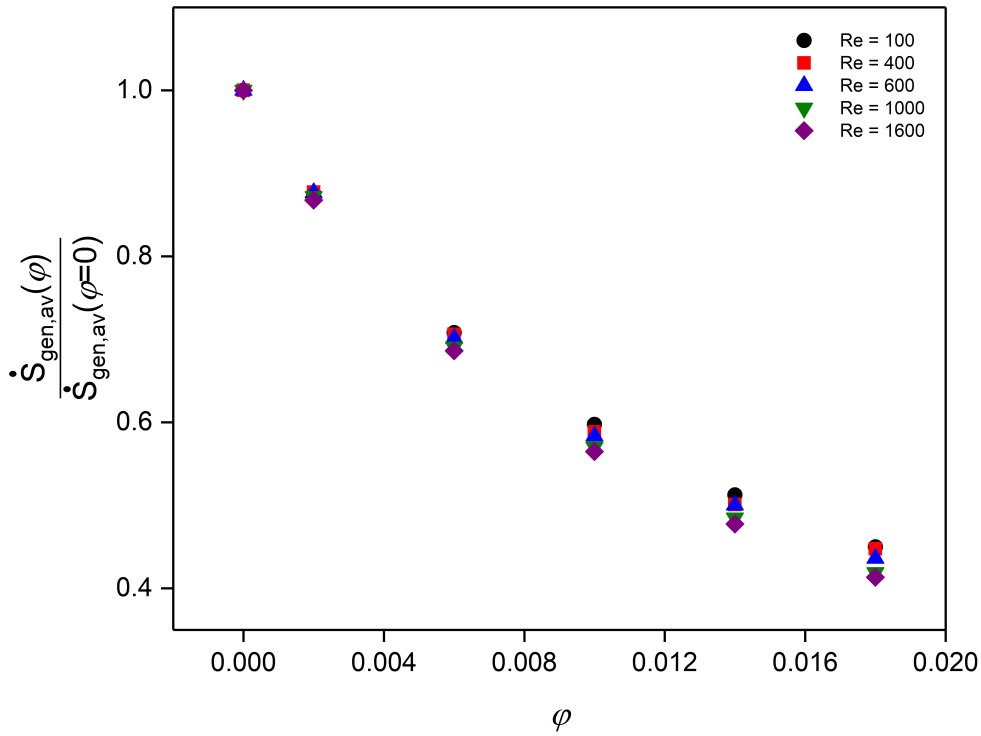

Figure 5.11 Normalized average entropy generation rate versus the alumina volume fraction for different Reynolds numbers.

Figure 5.11 displays the influence of Re and φ on the average entropy generation rate $\dot{S}_{gen,av}$ (averaged along the obstacle walls). For each Reynolds number, $\dot{S}_{gen,av}$ is normalized by the value obtained for the base fluid ($\varphi = 0$). The ratio $\dot{S}_{gen,av}/\dot{S}_{gen,av}(\varphi = 0)$ slightly decreases with Re. This second behavior is due to the normalization used here. The term $\dot{S}_{gen,av}$ increases indeed systematically with increased Re, particularly at low alumina concentrations. This may be attributed to the fact that as the Reynolds number increases, the frictional entropy generation rate increases more rapidly than the thermal one. For instance, at $\varphi = 1.8\%$, when Re increases from 1000 to 1600, the average thermal and frictional entropy generation rates increase by about 6.7% and 76.54%, respectively. Figure 5.11 reveals that $\dot{S}_{gen,av}$ decreases as the nanoparticle volume fraction increases. The reported behavior can be explained in the following way: both thermal conductivity and dynamic viscosity increase when increasing φ but the increase of μ is less important, therefore, the frictional entropy generation rate contributes less to the total entropy generation rate within the channel the system. Moreover lower temperature gradients obtained

close to the obstacle walls (Figure 5.7) reduce the thermal entropy generation rate. For example, at $Re = 1600$, suspending 1.8% of alumina nanoparticles into pure water decreases the thermal entropy generation by about 58% but increases the fluid friction irreversibility by 3%. The present results are in agreement with the works of Bianco et *al.* [28] and Rashidi et *al.* [182] but not with the study of Selimafendigil et *al.* [195], in which they affirmed that both thermal and frictional entropy generation rates are linear increasing functions of the nanoparticle concentration. This difference can be also attirbuted to the use of a single-phase model with different thermophysical correlations and especially to the application of an external electromagnetic field.

It is noteworthy that regardless of Re and φ, the Bejan number Be is very close to 1 and so is not shown here for sake of clarity. It suggests that heat transfer irreversibilities dominate over the fluid friction irreversibilities [23]. The present results confirm the former simulations of Mehrez et *al.* [149] for four nanofluids in an open cavity. They obtained Bejan numbers ranging between 0.9 and 0.99 for mixed convective flows and showed that when the Richardson number decreases, Be increases. Similarly, Bianco et *al.* [28] obtained $0.98 \leq Be < 1$ for turbulent forced convective nanofluid flows in a circular tube.

5.4.4 Thermo-hydraulic performances of water-based Al_2O_3 nanofluids

The potential benefit from using water-based Al_2O_3 nanofluids in laminar channel flows with a heated wall-mounted obstacle is evaluated in terms of five merit criteria for six nanoparticle volume fractions and five Reynolds numbers. Amongst these merit criteria, four have been reported in the literature and previously considered by Sekrani et *al.* [194] for the same nanofluids in turbulent pipe flows are as follows:

- The ratio C_μ/C_k introduced by Prasher et al. [179], where C_k and C_μ are defined as:

$$\frac{k_{nf}}{k_{bf}} = 1 + C_k\varphi \tag{5.22}$$

$$\frac{\mu_{nf}}{\mu_{bf}} = 1 + C_\mu\varphi \tag{5.23}$$

- The Mouromtseff number Mo has been suggested for comparing two heat transfer fluids in fully developed laminar flows through a given geometry. Simons [202] proposed the following definitions for fully developed laminar flows:

$$Mo = \frac{\rho_{nf}^{0.3} k_{nf}^{0.736} Cp_{nf}^{0.264}}{\mu_{nf}^{0.036}} \tag{5.24}$$

which is valid for $0.0005 \leq L/(H.Re.Pr) < 0.013$, where L is the total length of the channel.

– The heat transfer improvement and the pressure drop penalty can be gathered to form a kind of overall energetic efficiency η defined by:

$$\eta = \frac{Nu_{nf}}{\Delta P_{nf}} \frac{\Delta P_{bf}}{Nu_{bf}} \tag{5.25}$$

– The Performance Evaluation Criterion (or PEC) has been introduced by Ferrouillat et *al*. [73]. It is based on the ratio of heat transferred to the requiring pumping power. PEC is given by:

$$PEC = \frac{\dot{m} Cp_{nf} \Delta T}{\dot{V} \Delta P} \tag{5.26}$$

where $\dot{m}$ and $\dot{V}$ are the mass and volumetric flow rates respectively. ΔT and ΔP represent the temperature and pressure differences between the outlet and inlet channel sections.

Figure 5.12 displays the four merit criteria as a function of the nanoparticle volume fraction φ for three different Reynolds number Re. The ratio C_μ/C_k decreases with increasing both Re and φ. At a given nanofluid concentration, as the Reynolds number increases, the viscosity decreases while the thermal conductivity increases. Adding nanoparticles to pure water increases both dynamic viscosity and thermal conductivity, but the increase of the latter is more important, as shown previously. For all cases, the ratio C_μ/C_k remains always lower than the limiting value $C_\mu/C_k = 4$ recommended by Prasher et *al*. [179]. One recalls first that the ratio C_μ/C_k is deduced from the a priori correlations used for the simulations. Second, it does not highlight any optimum set of parameters (φ, Re). Thus no definitive conclusion can be drawn from this merit criterion.

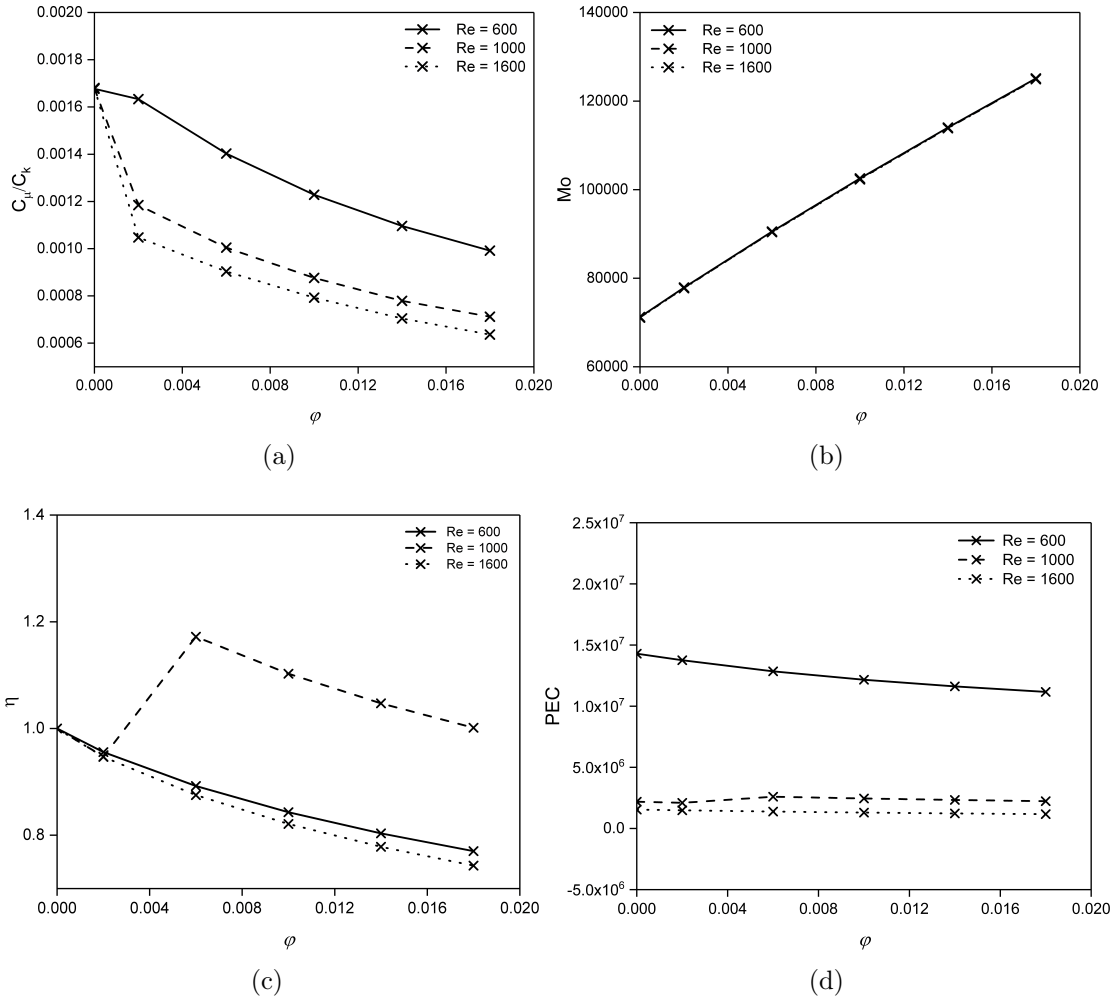

Figure 5.12 Four merit criteria, namely (a) the ratio C_μ/C_k, (b) the Mouromtseff number Mo, (c) the overall efficiency η and (d) the PEC number as a function of the nanoparticle concentration φ for three Reynolds numbers Re.

The influence of Re and φ on the Mouromtseff number Mo is shown in Figure 5.12b. Mo increases when increasing the nanoparticle concentration but seems to be no sensitive to the Reynolds number. From the Mouromtseff number distribution, the highest volume fraction $\varphi = 1.8\%$ could be then recommended whatever the Reynolds number.

The overall efficiency η decreases with increasing the alumina volume fraction for $Re = 600$ and 1600 as shown in Figure 5.12c. However η exhibits a local maximum for $Re = 1000$ and $\varphi = 0.6\%$, which would be the recommended operating conditions for this particular flow configuration. For the two other Reynolds numbers, the results agree with the former ones of Derakhshan et *al.* [58] for multi-wall carbon nanotubes–oil nanofluid flows in a vertical plain tubes, for which η remains always lower than 1 in the forced convection regime.

At any given nanoparticle concentration φ, the PEC number decreases considerably as Re increases from $Re = 600$ to 1000 (Figure 5.12d). On the contrary, φ has only a weak influence on the PEC number, which slightly decreases when φ increases. For example at $Re = 1600$, the PEC number decreases by about 21% when φ increases from 0.2% to 1.8%. For the ranges of φ and Re considered here, suspending nanoparticles into the base fluid does not lead to large pressure drop penalties, while the temperature gradients and specific heat decrease at the same time. At $Re = 1000$ and $\varphi = 1.8\%$, Cp_{nf} and ΔT decrease by 5.36% and 23%, respectively, compared to the base fluid. The distribution of the PEC number as a function of Re and φ confirms the former results of Ferrouillat et *al.* [73] and Roy et *al.* [186] in different flow configurations. Contrary to the turbulent pipe flows of Al_2O_3 water-based nanofluids [194], no local minimum of the PEC number is observed here.

The efficiency of nanofluids based on the first and the second laws of thermodynamics can be tackled by considering the performance parameter PE proposed by Siavashi and Jamali [200]:

$$PE = \frac{Nu_{nf}}{N_{s,nf}} \frac{N_{s,bf}}{Nu_{bf}} \tag{5.27}$$

where $N_s = ST_b/q$ is the dimensionless entropy generation with S, T_b and q are the total entropy generation of the whole domain, the bulk temperature and the heat flux imposed on the obstacle, respectively.

As shown in Figure 5.13, the performance parameter PE increases almost linearly with the particle volume fraction. On the contrary, the bulk Reynolds number has only a weak influence on PE, especially at low nanoparticle concentrations. It confirms the former numerical results of Siavashi and Jamali [200] for turbulent nanofluid flows in annuli.

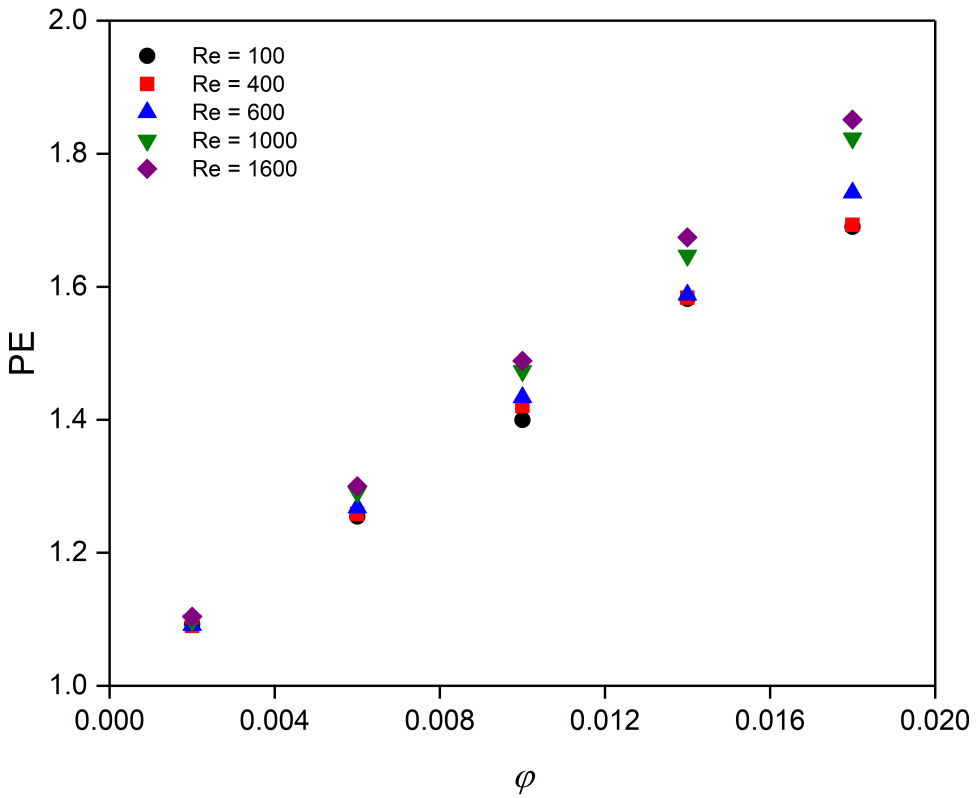

Figure 5.13 Performance evaluation criterion PE of the Al_2O_3-water nanofluid as a function of the nanoparticle volume fraction at different Reynolds numbers.

All in all, the overall efficiency η exhibits a local maximum for $Re = 1000$ and $\varphi = 0.6\%$, which could be the recommended set of operating conditions for the this flow configuration. The present results demonstrate also that there is a clear need to define an unified and more reliable merit criterion to evaluate the performance of nanofluids.

5.5 Conclusions

The present paper investigated the heat transfer performance and entropy generation of water-based Al_2O_3 nanofluids flowing within a 2D channel with a heated wall mounted obstacle. The conjugated heat transfer problem has been solved in the laminar regime for Reynolds numbers up to 1600 and nanoparticle volume fractions up to $\varphi = 1.8\%$.

The model was formerly validated for both laminar [192] and turbulent [194] water-based Al_2O_3 nanofluid flows in a straight pipe. It has been also favorably compared here to the numerical results of Young and Vafai [238] and the analytical law of Cess and Shaffer [42] for a forced convective air flow over a mounted obstacle in a 2D channel then to the experimental data of Young and Vafai [240] for a similar configuration.

Three-dimensional simulations revealed that the flow may be considered as 2D. For all

studied cases, two clockwise recirculation zones form before and after the heated obstacle. Only the Reynolds number has a noticeable influence on the hydrodynamic field. The reattachment length of the recirculation in the wake of the obstacle increases by increasing the Reynolds number.

The heat transfer rate increases linearly with the nanoparticle concentration and/or Reynolds number. For $Re = 1000$, the average heat transfer coefficient increased by 71.2% for $\varphi = 1.8\%$, compared to pure water. Loading alumina nanoparticles into the base fluid and/or increasing the Reynolds number leads to a more homogeneous temperature field with a reduce of the temperature gradients around the heated obstacle. It is worth to note that the heat transfer by conduction is enhanced more than the convective one, when increasing the nanofuid concentration. For instance, at $\varphi = 1.8\%$ and $Re = 1000$, the average heat transfer coefficient and the thermal conductivity are multiplied by 1.8 and 2.25 compared to pure water, respectively.

The influences of the Reynolds number and nanoparticle concentration on the exergy variation and the average entropy generation have been also evaluated. Exergy losses due to friction are predominant compared to exergy gains by the imposed heat flux at higher nanoparticle concentrations and low Reynolds numbers. Increasing Re leads to an increase of both the thermal and frictional entropy generations but with a higher increase on the latter especially at higher Re. For example, at $\varphi = 1.8\%$, the average thermal and frictional entropy generations are increased by 16% and 76.55%, respectively, when Re increases from 1000 to 1600. When the nanoparticle volume fraction increases, the viscous (resp. thermal) entropy generation increases (resp. decreases). The Bejan number remains close to unity whatever the values of the operating parameters considered here.

Finally, the benefit of using water-based Al_2O_3 nanofluid for heat transfer enhancement has been discussed for the first time in this configuration regarding five merit criteria. An optimum in terms of the overall efficiency is obtained for $Re = 600$ and $\varphi = 0.6\%$.

5.6 Acknowledgements

The authors would like to thank the NSERC chair on industrial energy efficiency established at Université de Sherbrooke in 2014 and supported by Hydro-Québec, Natural Resources Canada (CanmetEnergy in Varennes) and Rio Tinto Alcan. Calculations have been performed using the supercomputer Mammouth Parallèle 2 of Compute Canada's network, which is also here gratefully acknowledged.

CHAPTER 6
CONCLUSION GÉNÉRALE

Malgré les études approfondies sur l'amélioration des transferts de chaleur par l'utilisation de nanofluides au cours des dernières décennies, les chercheurs ont encore du mal à formuler un modèle définitif qui peut raisonnablement prédire les propriétés des nanofluides et les paramètres agissant sur leur performance thermique. Par conséquent, le présent projet de recherche a pour principal objectif de développer une approche numérique à la fois performante et ayant un coût de calcul abordable. Elle doit intégrer des corrélations appropriées pour les propriétés des nanofluides et prendre en compte les mécanismes physiques pertinents pour la prédiction du comportement des nanofluides.

6.1 Principaux résultats

Comme première étape de cette thèse, une comparaison entre la capacité des modèles monophasiques et multiphasiques sur la prédiction du comportement des nanofluides a été étudiée pour des écoulements laminaires à travers un tube uniformément chauffé. L'influence du nombre de Reynolds, du type et de la taille des nanoparticules sur les champs hydrodynamiques et thermiques a été considérée en mettant l'accent sur le processus de sédimentation. Les contributions originales de ces études ont été publiées dans un article de revue [192] et sont résumées ci-dessous:

- Le modèle de mélange avec des propriétés dépendantes de la température a montré une meilleure performance que l'approche monophasique avec un accord proche des données expérimentales [227].
- L'ajout de nanoparticules au fluide de base améliore le taux de transfert de chaleur. Par exemple, à $Re = 1600$, l'ajout de 1.6% de nanoparticules d'alumine à l'eau pure a augmenté le coefficient de transfert thermique d'environ 74%.
- On a aussi trouvé que le type et la taille des nanoparticules affectent fortement le phénomène de sédimentation. Quatre diamètres de nanoparticules ont été considérés, 10, 42, 100 et 200 nm à la fois pour les nanofluides cuivre-eau et alumine-eau. Pour le plus grand dimètre, $d_{np} = 200$ nm, les nanoparticules de Cu étaient plus sédimentées d'environ 80%, tandis que les nanoparticules d'Al_2O_3 étaient seulement sédimentées de 2.5%.

- L'effet de six nanofluides différents à base d'eau sur le coefficient de transfert thermique a été étudié. Les résultats ont montré que le nanofluide Cu-eau atteignait le coefficient de transfert de chaleur le plus élevé, suivi par C, Al_2O_3, CuO, TiO_2 et SiO_2, respectivement.
- Des corrélations empiriques pour le coefficient de frottement et le nombre de Nusselt moyen ont également été fournies.

Dans un second temps, les performances des différents modèles multiphasiques et de turbulence ont été soigneusement comparées dans le cadre d'un benchmark numérique. Les principaux résultats concernant les performances des modèles sont publiés dans une revue à comité de lecture [194]. L'approche monophasique et le modèle de mélange ont été évalués et un bon accord avec les données expérimentales de Sundar et Sharma [206] a été trouvé pour les concentrations en nanoparticules d'alumine jusqu'à 0.5%. Cependant, pour des concentrations plus élevées en nanoparticules, $\varphi = 2\%$, les résultats ont montré la nécessité d'utiliser le modèle de mélange. Une étude comparative entre huit modèles RANS (six modèles à deux équations et deux modéles aux contraintes de Reynolds) a montré que le SST k-ω était le modèle de turbulence le plus approprié avec des erreurs moyennes entre les valeurs prédites et les données expérimentales [206], d'environ 0.43% et 1.8%, pour le nombre de Nusselt moyen et le coefficient de frottement, respectivement. Au contraire, le modèle RSM basé sur ε a montré son incapacité à prédire les champs thermiques et hydrodynamiques, avec un coefficient de frottement prédit deux fois plus élevé que le coefficient expérimental et un écart de 42% par rapport au nombre de Nusselt moyen issu des expériences.

La présente étude a également été étendue pour étudier les transferts de chaleur et la génération d'entropie du nanofluide Al_2O_3-eau circulant dans un canal rectangulaire avec un obstacle chauffé. Bien que l'écoulement soit laminaire, le problème est plus complexe puisque les transferts thermiques se font à la fois par convection forcée dans le canal et par conduction au sein de l'obstacle. Les résultats originaux et pertinents de ces analyses ont été récemment publiés dans un article de revue [193] et sont présentés dans ce qui suit:

- Le taux de transfert de chaleur augmente linéairement avec la concentration en nanoparticules et/ou le nombre de Reynolds. Pour $Re = 1000$, le coefficient moyen de transfert de chaleur a augmenté de 71.2% pour $\varphi = 1.8\%$ par rapport à l'eau pure.
- On a montré que le transfert de chaleur par conduction était plus favorisé que celui par convection forcée, en augmentant la concentration de nanofluides. Par exemple, à

$\varphi = 1.8\%$ et $Re = 1000$, le coefficient de transfert thermique moyen et la conductivité thermique ont été multipliés respectivement par 1.8 et 2.25 par rapport à l'eau pure.
- Les pertes d'exergie dues aux frottements visqueux ont été jugées prédominantes par rapport aux gains d'exergie par le flux de chaleur imposé pour la concentration la plus élevée en alumine et le plus faible nombre de Reynolds.
- L'augmentation de Re a conduit à une augmentation des générations d'entropie thermique et de frottement, mais avec une augmentation plus importante sur cette dernière, en particulier à Re plus élevé. Par exemple, à $\varphi = 1.8\%$, lorsque Re augmente de 1000 à 1600, les générations d'entropie thermique et de frottement moyennes augmentent respectivement de 16% et 76.55%.
- Pour la première fois dans cette configuration, l'avantage d'utiliser le nanofluide alumine-eau pour améliorer le transfert de chaleur a été discuté selon cinq critères de mérite et un optimum en termes d'efficacité globale est obtenu pour $Re = 600$ et $\varphi = 0.6\%$.

Cette thèse a montré la faisabilité de l'utilisation de nanofluides dans l'amélioration des transferts de chaleur dans différentes géométries typiques de la plupart des applications industrielles. Il a également prouvé que la CFD est un outil numérique important pour étudier les caractéristiques hydrodynamiques et les comportements thermiques des nanofluides.

6.2 Perspectives

6.2.1 Modèle de bilan de population (PBM)

Outre l'amélioration des propriétés thermiques du fluide de base, l'ajout de nanoparticules induit d'autres phénomènes tels que la sédimentation ou l'agrégation des nanoparticules. Plusieurs chercheurs ont évalué expérimentalement l'effet de la distribution de la taille des nanoparticules sur le comportement des nanofluides [36, 100, 237], mais très peu l'ont évalué numériquement [40, 124]. Pour modéliser ce concept, une équation d'équilibre est nécessaire pour décrire la distribution des nanoparticules en plus des équations de conservation de la masse, de quantité de mouvement et d'énergie. Cette méthode est capable de fournir des informations détaillées importantes sur le processus d'agglomération des nanoparticules, ou sur les interactions particule-particule. Pour cette raison, la stabilité des nanofluides et les distributions de taille des nanoparticules, PSD, seront étudiées en utilisant le modèle de bilan de population. De plus, les paramètres affectant l'agglomération et les effets de l'agglomération sur les caractéristiques rhéologiques et de transfert de chaleur

des nanofluides seront étudiés en détail.
Des résultats préliminaires de la distribution de la taille de nanoparticules sont présentés dans l'annexe B.

6.2.2 Simulation des grandes échelles (LES) d'écoulements de nanofluides

Indépendamment du fait que les modèles RANS et spécialement le SST k-ω ont montré leur capacité à prédire l'effet de la turbulence sur les nanofluides et le transfert de chaleur par convection forcée, ils restent toujours incapables de fournir des informations détaillées sur les caractéristiques de l'écoulement à des échelles plus petites où des structures cohérentes peuvent apparaître et influencer grandement les transferts de chaleur. Par conséquent, la simulation des grandes échelles est jugée nécessaire car elle est capable de révéler plus de détails sur l'écoulement et le représenter d'une façon plus réaliste.
Les modèles LES sont basés sur le comportement différentiel des petites et grandes structures, où on suppose que les plus petites structures sont généralement isotropes et ne sont pas influencées par la géométrie de l'écoulement, alors que les grandes structures qui interagissent avec l'écoulement moyen et en extraient de l'énergie doivent être simulées et dépendent de la géométrie. La LES résout les grandes structures dépendantes du temps et de la géométrie et modélise les petites structures. Les équations gouvernantes employées pour la LES sont obtenues en filtrant les équations de Navier-Stokes en espace à l'échelle de la maille de calcul.
A cette fin, les paramètres du solveur seront d'abord validés en comparant les résultats numériques d'un écoulement dans un tube isotherme avec les résultats issus d'une simulation numérique directe (DNS) d'El Khoury et al. [69]. Des simulations LES d'un écoulement de nanofluides dans un tube uniformément chauffé seront ensuite réalisées sur la base des travaux expérimentaux de Sundar et Sharma [206]. Enfin, une étude comparative des différents modèles RANS et LES sera accomplie pour évaluer leur capacité à prédire le champ turbulent et les transferts de chaleur par convection d'un écoulement de nanofluides.
La LES d'un écoulement dans une conduite isotherme est actuellement en cours. Le modèle de viscosité turbulente locale adaptative (WALE) a été adopté et la méthode de vortex (VM) a été utilisée à l'entrée pour générer de la turbulence. La distribution des structures turbulentes instantanées, identifiées par le critère Q et colorées par la vitesse totale, est illustrée sur la Figure 7.1. Le modèle WALE s'avère plus performant que le modèle de Smagorinsky car il est moins dissipatif et moins cher en coût de calcul que le modèle de Smagorinsky dynamique, car il ne nécessite aucune procédure de moyennage de la

pseudo-constante. La Figure 7.1 montre des “streaks”, structures cohérentes alignées avec la direction principale de l’écoulement et caractéristiques des écoulements turbulents en conduite. Ces structures peuvent avoir une influence non négligeable sur les transferts de chaleur en proche paroi.

CHAPTER 7

GENERAL CONCLUSION

Despite the extensive studies about the effects of nanofluids on the heat transfer enhancement during the last decades, investigators are still struggling to formulate a definitive model that can reasonably predict the nanofluid properties and the parameters acting on their thermal performance. Therefore, in the present research project, an attempt to highlight the importance of using a suitable numerical approach, appropriate nanofluid properties and take into account the pertinent physical mechanisms on the prediction of nanofluid behaviours has been carried out under different conditions and configurations.

7.1 Summary of the main results

As a first step in this thesis, a comparison between the capacity of the single phase and the mixture models on the prediction of the nanofluid behavior has been investigated for laminar forced convective flows through an uniformly heated pipe. The influence of the Reynolds number, nanoparticle type and size on the hydrodynamic and thermal fields with an emphasis on the sedimentation process was considered. The original contributions of this study have been published in a peer-reviewed article [192] and can be summarized as follows:

- The mixture model with temperature dependent properties performs better than the single phase approach with a close agreement with the experimental data [227].
- Adding nanoparticles to a base fluid enhances significantly the heat transfer rate. For example, at $Re = 1600$, adding 1.6% alumina nanoparticle to pure water increases the heat transfer coefficient by about 74%.
- It was also found that the nanoparticle type and size affect strongly the sedimentation phenomenon. Four nanoparticle diameters have been considered: 10, 42, 100 and 200 nm for both copper-water and alumina-water nanofluids. For the largest diameter, $d_{np} = 200$ nm, the Cu nanoparticles were more sedimented by around 80%, while the Al_2O_3 nanoparticles were only sedimented by 2.5%.
- The effect of six different water-based nanofluids on the heat transfer coefficient was investigated. The results showed that the Cu-water nanofluid achieved the highest heat transfer coefficient, followed by C, Al_2O_3 , CuO, TiO_2 and SiO_2, respectively.

– Empirical correlations for the friction coefficient and the average Nusselt number were also provided.

In the second step, the performance of the different multiphase and turbulence models have been carefully compared in the framework of a numerical benchmark. The key results regarding the model performances have been published in a peer reviewed journal [194]. Both single phase and mixture approaches were evaluated and a good agreement with the experimental data of Sundar and Sharma [206] was found for alumina nanoparticle concentrations up to 0.5%. However, at high nanoparticle concentrations, $\varphi = 2\%$, the results showed the need for using the mixture model. A comparative study between eight RANS models (six two-equation models and two Reynolds Stress Models) has been then performed. The SST k-ω was the most appropriate turbulence model with average errors between the predicted values and the experimental data [206], of about 0.43% and 1.8%, for the average Nusselt number and friction factor, respectively. On the contrary, the RSM model based on ε showed its inadequacy to predict both the thermal and hydrodynamic fields, with a predicted friction coefficient twice higher than the experimental one and a discrepancy of 42% in terms of the average Nusselt number.

The present study was also extended to investigate the heat transfer performance and the entropy generation of water-based Al_2O_3 nanofluid flowing within a rectangular channel with a heated wall mounted obstacle. Conjugated heat transfer is considered with forced convection within the channel and conduction through the obstacle. The original and relevant results have been recently published in a peer-reviewed article [193] and they are outlined in the following:

– The heat transfer rate increases linearly with the nanoparticle concentration and/or Reynolds number. For $Re = 1000$, the average heat transfer coefficient increases by 71.2% for $\varphi = 1.8\%$, compared to pure water.
– It was shown that the heat transfer by conduction was enhanced more than the convective one, when increasing the nanofluid concentration. For instance, at $\varphi = 1.8\%$ and $Re = 1000$, the average heat transfer coefficient and the thermal conductivity are multiplied by 1.8 and 2.25 compared to pure water, respectively.
– Exergy losses due to friction were found to be predominant compared to exergy gains by the imposed heat flux at higher nanoparticle concentrations and low Reynolds numbers.
– Increasing Re led to an increase of both the thermal and frictional entropy generations but with a higher increase on the latter especially at higher Re. For example, at

$\varphi = 1.8\%$, when Re increases from 1000 to 1600, the average thermal and frictional entropy generations increase by 16% and 76.55%, respectively.

– For the first time in this configuration, the benefit of using water-based Al_2O_3 nanofluid for heat transfer enhancement has been discussed regarding five merit criteria and an optimum in terms of the overall efficiency is obtained for $Re = 600$ and $\varphi = 0.6\%$.

This thesis showed the feasibility of using nanofluids to enhance the heat transfer process in different industrial applications. It also proved that the CFD is an important numerical tool to study the flow characteristics and thermal behaviour of nanofluids, giving more information which is usually not accessible by experimental methods.

7.2 Future perspectives

7.2.1 Population Balance Model (PBM)

Beside the improvement in thermal properties of the base fluid, adding nanoparticles into the former induces other phenomena such as sedimentation, breakage and aggregation. Several investigators have evaluated the effect of nanoparticle size and nanoparticle distribution on the nanofluid behavior experimentally [36, 100, 237], but only few ones assessed it numerically [40, 124]. To model this concept, a balance equation is required to describe the nanoparticle population in addition to mass, momentum and energy balances. This method is capable of providing important detailed information about the nanoparticle aggregation process, collision mechanism and particle-particle interactions. For this reason, the nanofluid stability and nanoparticle size distributions, PSD, will be investigated based on the population balance model. In addition, the parameters affecting agglomeration and the effects of the agglomeration on the fluid flow and heat transfer characteristics of nanofluids will be studied in detail.
Preliminary results on the distribution of the nanoparticle size are shown in Appendix B.

7.2.2 Large Eddy Simulation (LES) of nanofluid flows

Regardless that the RANS models and specially the SST k-ω showed their ability to predict the effect of turbulence on the convective heat transfer and nanofluid flow, they are still unable to exhibit detailed flow informations, such as the vortical structures and Reynolds stresses, which are key parameters of the turbulent flow characteristics. Therefore, Large Eddy Simulations are deemed necessary since they provide greater details at smaller scales. The LES models are based on the different behaviors of small and large eddies, where the

former are generally assumed isotropic and are not influenced by the geometry of the flow, whereas the large eddies which interact with the mean flow and extract or provide energy to it are very problem and geometry dependent. Consequently, LES resolves the time and geometry-dependent large eddies and uses models only for the nearly-isotropic small eddies. The governing equations employed for LES are obtained by filtering the time-dependent Navier-Stokes equations in space, usually at the mesh cell scale. Further simulations will be then conducted using LES for the uniformly heated pipe case. To this end, the solver settings will be first validated by comparing the numerical results of an isothermal fully developed pipe flow with the results of the direct numerical simulation (DNS) study of El Khoury et al. [69]. LES of a nanofluid flow in a uniformly heated pipe will be then carried out based on the experimental work of Sundar and Sharma [206]. Finally, a comparative study of the different RANS models and the LES formulation will be performed to assess their ability to predict the turbulent flow field and the convective heat transfer of a nanofluid flow.

Numerical simulations of an isothermal pipe flow using LES formulation are currently in progress. The wall-adaptive local-eddy viscosity model (WALE) was adopted and the vortex method (VM) was used at the inlet to generate turbulence. The WALE subgrid scale model has proven to perform better than the Smagorinsky model, which is too dissipative, while saving computational efforts compared to the dynamic Smagorinsky model, since it does not require any averaging procedure of the pseudo-constant. The distribution of the instantaneous turbulent structures, identified by the Q criterion and colored by the velocity magnitude, is illustrated in Figure 7.1. Streaks aligned in the streamwise direction are clearly visible and are characteristic of turbulent pipe flows. They may have a large impact on the wall heat transfer.

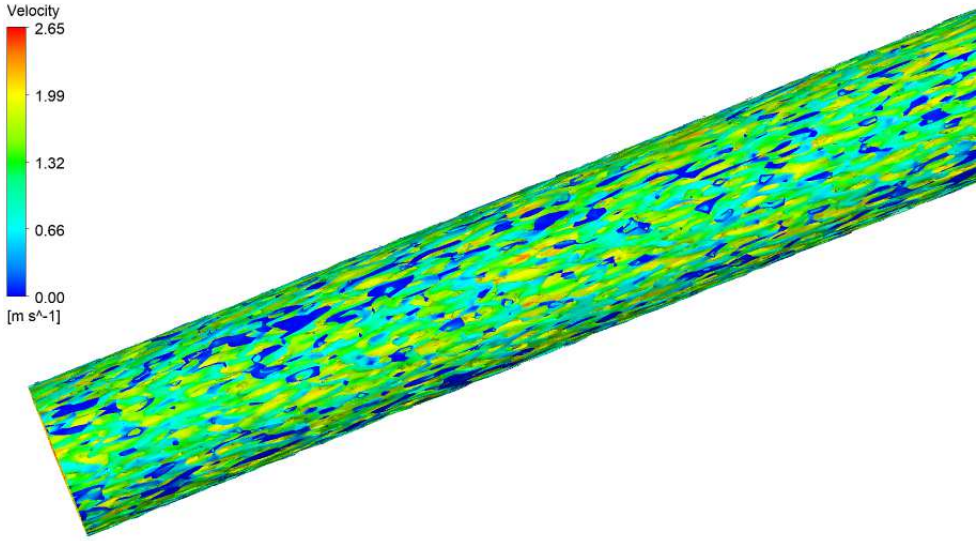

Figure 7.1 Iso-value $Q = 1$ of the Q criterion, colored by the magnitude of the velocity vector.
Iso-valeur $Q = 1$ du critère Q coloré par la norme du vecteur vitesse.

The results shown in this thesis have been published in international conferences, journals and projects namely:

Journals

- Sekrani, G., Poncet, S. and Proulx, P. (2018). Conjugated heat transfer and entropy generation of Al_2O_3–water nanofluid flows over a heated wall-mounted obstacle. Journal of Thermal Analysis and Calorimetry, 1-17.
- Sekrani, G., Poncet, S. and Proulx, P. (2018). Modeling of convective turbulent heat transfer of water-based Al2O3 nanofluids in an uniformly heated pipe. Chemical Engineering Science, 176, 205-219.
- Sekrani, G. and Poncet, S. (2016). Further investigation on laminar forced convection of nanofluid flows in a uniformly heated pipe using direct numerical simulations. Applied Sciences, 6(11), 332.

Conferences

- Sekrani, G. and Poncet, S. Numerical investigation on the turbulent convective heat transfer of nanofluid flows in a uniformly heated pipe. 2nd Thermal and Fluids Engineering Conference and 4th International Workshop on Heat Transfer, 2-5 April 2017, Las Vegas, Nevada, USA.
- Sekrani, G. and Poncet, S. Simulations aux grandes échelles du transfert de chaleur convectif pour des écoulements turbulents de nanofluides dans un tube uniformément chauffé. 85^{me} Congrès de l'ACFAS Colloque, Enjeux de la recherche 11 : Le calcul informatique de pointe pour l'avancement des connaissances et l'innovation, 8-12 May 2017, Montréal, Canada.
- Sekrani, G. and Poncet, S. Simulations numériques d'écoulement de nanofluides en conduite chauffée. 84^{me} Congrès de l'ACFAS Colloque 202: Efficacité Énergétique Industrielle, 9-13 May 2016 ,Montréal, Canada.
- Sekrani, G. and Poncet, S. and Bouterra, M. Numerical simulations of Al_2O_3 nanofluid flows in the laminar and turbulent regimes in a uniformly heated pipe. 3^{rd} International Conference on Fluid Flow, Heat and Mass Transfer (FFHMT'16), 2–3 May, 2016, Ottawa, Canada.

Project An article under preparation for an European round robin test for nanofluid simulations, more details can be found in Appendix B.

APPENDIX A
Reynolds Averaged Navier-Stokes modelling

The use of advanced direct numerical simulation (DNS) or large eddy simulation (LES) models in the context of turbulent nanofluid flows in realistic geometries remains marginal and most authors focus on Reynolds Averaged Navier Stokes turbulence closures (RANS). The latter do not distinguish between the various sizes of eddies, contrary to DNS and LES techniques. With this method all turbulence scales are modeled. RANS models are based on the statistical averaging of the the Navier-Stockes (NS) equations. In Reynolds averaging, the solution variables in the instantaneous NS equations are decomposed into mean (ensemble- or time-averaged) and fluctuating components. All scalars can be written as:

$$\phi = \bar{\phi} + \phi' \tag{A.1}$$

where ϕ denotes a scalar such as pressure, energy, or species concentration, $\bar{\phi}$ and ϕ' are the mean and fluctuating scalar components.

For example, the velocity components: $u_i = \bar{u}_i + u'_i$, where $\bar{u}_i$ and u'_i are the mean and fluctuating velocity components (i = 1, 2, 3).

Substituting expressions of this form for the flow variables into the governing equations, a new additional term appears in the momentum equation to represent the effects of turbulence:

$$\rho(\frac{\partial \bar{u}_i}{\partial t} + \bar{u}_k \frac{\partial \bar{u}_i}{\partial x_k}) = -\frac{\partial \bar{p}}{\partial x_i} + \frac{\partial}{\partial x_j}(\mu \frac{\partial \bar{u}_i}{\partial x_j}) + \frac{\partial \boxed{R_{ij}}}{\partial x_j} \tag{A.2}$$

where R_{ij} is the Reynolds stress tensor.

The number of new unknown quantities arose during the statistical averaging process are more than the number pf equations and closure assumptions are needed to close the system equations. The RANS models can be close the governing equations using one of the following two ways:

* Eddy viscosity models

These methods employ the Boussinesq hypothesis to relate the Reynolds stresses to the mean velocity gradients using an eddy (or turbulent) viscosity, μ_T,:

$$R_{ij} = -\rho\overline{u'_i u'_j} = \mu_T(\frac{\partial \bar{u}_i}{\partial x_j} + \frac{\partial \bar{u}_j}{\partial x_i}) - \frac{2}{3}\mu_T \frac{\partial \bar{u}_k}{\partial x_k}\delta_{ij} - \frac{2}{3}\rho k \delta_{ij} \tag{A.3}$$

* Reynolds-Stress model (RSM)

The RSM closes the Reynolds-averaged Navier-Stokes equations by solving directly transport equations for the Reynolds stresses, avoiding the isotropic eddy-viscosity hypothesis.

There are several mainstream turbulence models and usually there are classified by the number of additional differential equations needed to close the original set of conservation equations. Some of turbulence models used to close the RANS are presented in Table A.1:

Table A.1 The most common eddy-viscosity models

One-Equation Model	Spalart-Allmaras [205]	
Two-Equation Model	$*$ k-ε variants	Standard k-ε (S k-ε)[128]
		Realizable k-ε (R k-ε) [199]
		Re-Normalisation Group k-ε (RNG k-ε) [170]
	$*$ k-ω variants	Standard k-ω (k-ω) [230]
		SST k-ω [152]
Four-Equation Model	Shear Stress Transport (SST) [152]	
Seven-Equation Model	Reynolds-Stress Model [80, 126, 127]	

where k is the turbulence kinetic energy $k = \frac{1}{2}\overline{u_i' u_j'}$
ε is the turbulence dissipation rate $\varepsilon = \upsilon \overline{\frac{\partial u_i'}{\partial x_j}(\frac{\partial u_i'}{\partial x_j} + \frac{u_j'}{\partial x_i})}$
ω is the specific dissipation rate $\omega = \frac{\varepsilon}{k}$

Though the RSM needs more CPU time and memory than two-equation models, it still offers huge computational savings when compared to DNS and LES. Therefore, RANS models are the most computationally practical method when dealing with turbulent flows and they are able to provide accurate data for nanofluids if the appropriate single or two-phase model and the appropriate correlations for the nanofluid properties are used.

APPENDIX B
Nanoround European Benchmark

The nanoround project proposes an European round robin test case comparing and evaluating different numerical models for the simulation of the flow and heat transfer with nanofluids. An experimentally investigated and well documented test case is chosen for which the initial and boundary conditions are described [50]. Research groups are invited to simulate the chosen test case using their nanofluid models and numerical tools.
At the end of this project, a joint scientific paper will be prepared which will review and compare all results.

B.1 Numerical method

At Université de Sherbrooke, the choice has been done to model the nanofluid flow using the mixture model together with a population balance model to account for the polydispersed nature of the nanoparticles within the base fluid. The thermophysical properties of the base fluid are assumed to be temperature-dependent only and those of the nanofluid are directly computed from the mixture model, such that no correlations are required.

B.1.1 Test case set-up

We performed numerical simulations for four flow rate/heating combinations for three fluids: pure water, 1 % TiO_2-water suspension and 2.5 % TiO_2-water suspension based on the experimental study of Colla et al. [50]. Studied cases with their names are outlined in Table B.1:

Table B.1 Nanoround numerical cases.

	100 W, 6 g/s	100 W, 8 g/s	200 W, 5 g/s	100 W, 6 g/s
Water	W-100-6	W-100-8	W-200-5	W-200-6
1% TiO_2-water	1-100-6	1-100-8	1-200-5	1-200-6
2.5% TiO_2-water	2.5-100-6	2.5-100-8	2.5-200-5	2.5-200-6

The measurement section is a horizontal straight pipe with 8 mm inner diameter and 2 m length. The pipe is divided into 8 subsections, where every 250 mm, 4 thermocouples are placed circumferentially, as shown in Figure B.1.

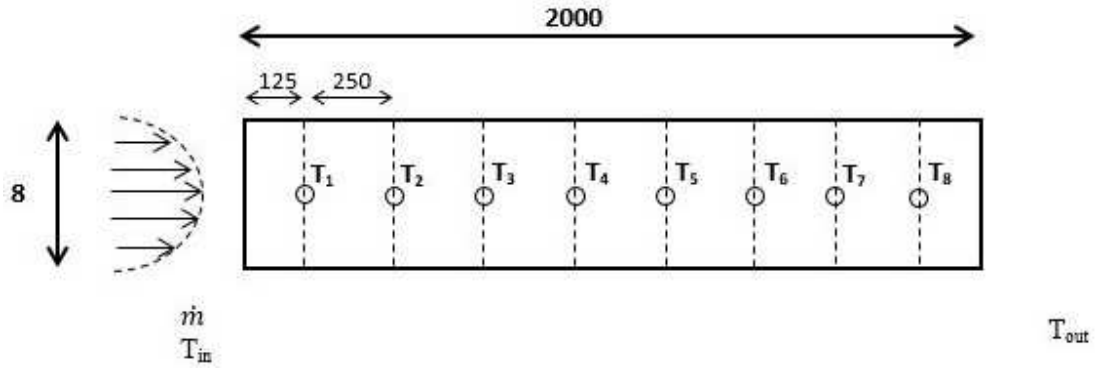

Figure B.1 Schematic sketch of the Nanoround test rig [50].

B.1.2 Boundary conditions

Laminar water flow inside a pipe is numerically investigated in the present work. The flow is considered to be incompressible and under steady-state conditions. A constant heat flux is imposed along the pipe wall. A fully developed flow with constant temperature enters the test section. The effect of the consideration the shell conduction at the tube wall on the prediction of experimental data has been tested and discussed. One fluid domain is considered in the numerical simulation. Results of the simulation are the bulk and wall temperatures at 8 locations along the wall, which have also been measured experimentally. The measured wall temperature is given by the average of 4 sensors placed around the circumference of the pipe (one on the top, one the left, one the right and one at the bottom). The bulk temperature is determined by the area weighted average temperature at each section.

– **Momentum conservation in the fluid domain:**

At the inlet: a developed velocity profile; prior simulation profile was used.

At the wall: no-slip boundary condition (flow velocity is zero).

At the outlet: constant static pressure is known, a relative pressure equal to zero is chosen.

– **Energy conservation in the fluid domain:**

At the inlet: constant temperature is known.

At the wall: heat flux in the solid domain is conserved.

At the outlet: pressure outlet boundary condition is used.

– **Energy conservation in the solid domain:**

At the inlet: zero heat flux.

At the wall: heat flux into the solid domain is known from experimental data.

At the outlet: zero heat flux.

B.1.3 Water properties

The physical properties of water are considered to be temperature-dependent while those of the solid nanoparticles are kept constant and given in Table B.2.

Table B.2 Thermophysical properties of water and TiO_2 nanoparticles

	$\rho\ (m^2/kg)$	$C_p\ (J/kg.K)$	$k\ (W/m.K)$	$\mu\ (N.s/m^2)$
Pure water	998.295	4184.36	0.597685	0.001012429
TiO_2	3972	692	8.4	$---$

The following equations are used to evaluate the properties of pure liquid water as a function of temperature T:

– Density [220]:

$$\begin{aligned}\rho_{bf} = 2446 - 20.674T + 0.11576T^2 - 3.12895 \times 10^{-4}T^3 \\ + 4.0505 \times 10^{-7}T^4 - 2.0546 \times 10^{-10}T^5\end{aligned} \tag{B.1}$$

– Viscosity [48]:

$$\mu_{bf} = A10^{\left(\frac{B}{T-c}\right)} \tag{B.2}$$

where, $A = 2.414 \times 10^{-5}$, $B = 247.8$ and $C = 140$.

– Specific heat [156]:

$$\begin{aligned}Cp_{bf} = 4217.1148898243 - 2.99500832260219T \\ + 0.0902711920148249T^2 - 1.37712095636289 \times 10^{-3}T^3 \\ + 1.17146192195605 \times 10^{-5}T^4 - 4.088550653591 \times 10^{-8}T^5\end{aligned} \tag{B.3}$$

– Conductivity [57]:

$$k_{bf} = -0.76761 + 7.535211 \times 10^{-3}T - 0.98249 \times 10^{-5}T^2 \tag{B.4}$$

B.2 First set of analysis on water simulations

To validate the numerical results, two sets of simulation were considered; with and without the shell conduction at the pipe wall. The grid independency analysis and the code validation, are based on the W-200-6 case. Five grids were tested: 4, 6, 8, 17 and 53 million nodes. The prediction of the wall and bulk temperatures by consideration of the shell conduction are compared in Tables B.3 and B.4.

Table B.3 Grid independence test considering the wall temperature.

y/D	Experiment [50]	4 million nodes	6 million nodes	8 million nodes	17 million nodes	53 million nodes
15.625	26.6	30.92	30.88	30.86	30.826	30.535
46.875	28.972	33.9	33.925	33.915	33.902	33.872
78.125	29.66	35.343	35.354	35.35	35.347	35.318
109.375	30.386	36.747	36.755	36.752	36.753	36.764
140.625	31.194	38.311	38.314	38.312	38.313	38.331
171.875	31.881	40.058	40.056	40.054	40.054	40.09
203.125	32.89	41.895	41.89	41.887	41.8875	41.937
234.375	33.857	43.76	43.75	43.74	43.747	43.951

Table B.4 Grid independence test considering the bulk temperature.

y/D	Experiment [50]	4 million nodes	6 million nodes	8 million nodes	17 million nodes	53 million nodes
15.625	20.861	22.313	22.298	22.28	22.273	22.147
46.875	21.87	24.833	24.828	24.832	24.822	24.788
78.125	22.958	26.685	26.68	26.667	26.671	26.647
109.375	24	28.517	28.494	28.493	28.5	28.486
140.625	25.014	30.517	30.364	30.352	30.374	30.373
171.875	25.982	32.318	32.313	32.3075	32.295	32.324
203.125	26.99	34.295	34.285	34.287	34.253	34.296
234.375	28	36.264	36.242	36.207	36.252	36.281

From the tables, a small difference of about 1 % between the smallest and the biggest grids is noted. However, one can see that the numerical values are not in a good agreement with the experimental data with discrepancies between 6 % and 30 % in terms of both wall and bulk temperatures, respectively. Therefore, a second set of simulations was performed without considering the shell conduction. The grid independency test was also done with the same meshes and it was decided that all next simulations will be performed with 6 million nodes. Figure B.2 illustrates the comparison between the numerical results with and without shell conduction for the wall and bulk temperatures and the experimental data.

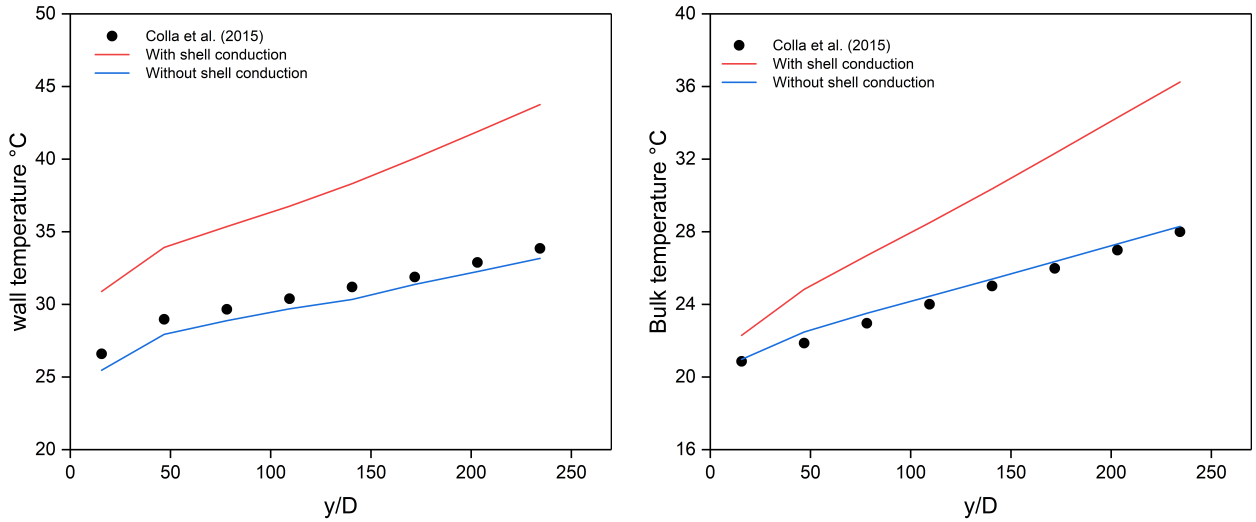

(a) (b)

Figure B.2 Axial development of the (a) wall and (b) bulk temperatures for the W-200-6 case.

It can be clearly seen in the previous figures, the case without the shell conduction is found to perform better with maximum errors of both wall and bulk temperatures of 4.2 % and 2.7 %, respectively. Therefore, all the next numerical simulations will be done without the shell conduction boundary condition.

B.3 Second set of analysis on TiO_2–water nanofluid simulations

The mixture model was used to analyse the nanofluid flows for two nanoparticle concentrations: 1 wt.% and 2.5 wt.%. The axial development of the wall and bulk nanofluid temperatures for all boundary conditions are presented in Figure B.3.

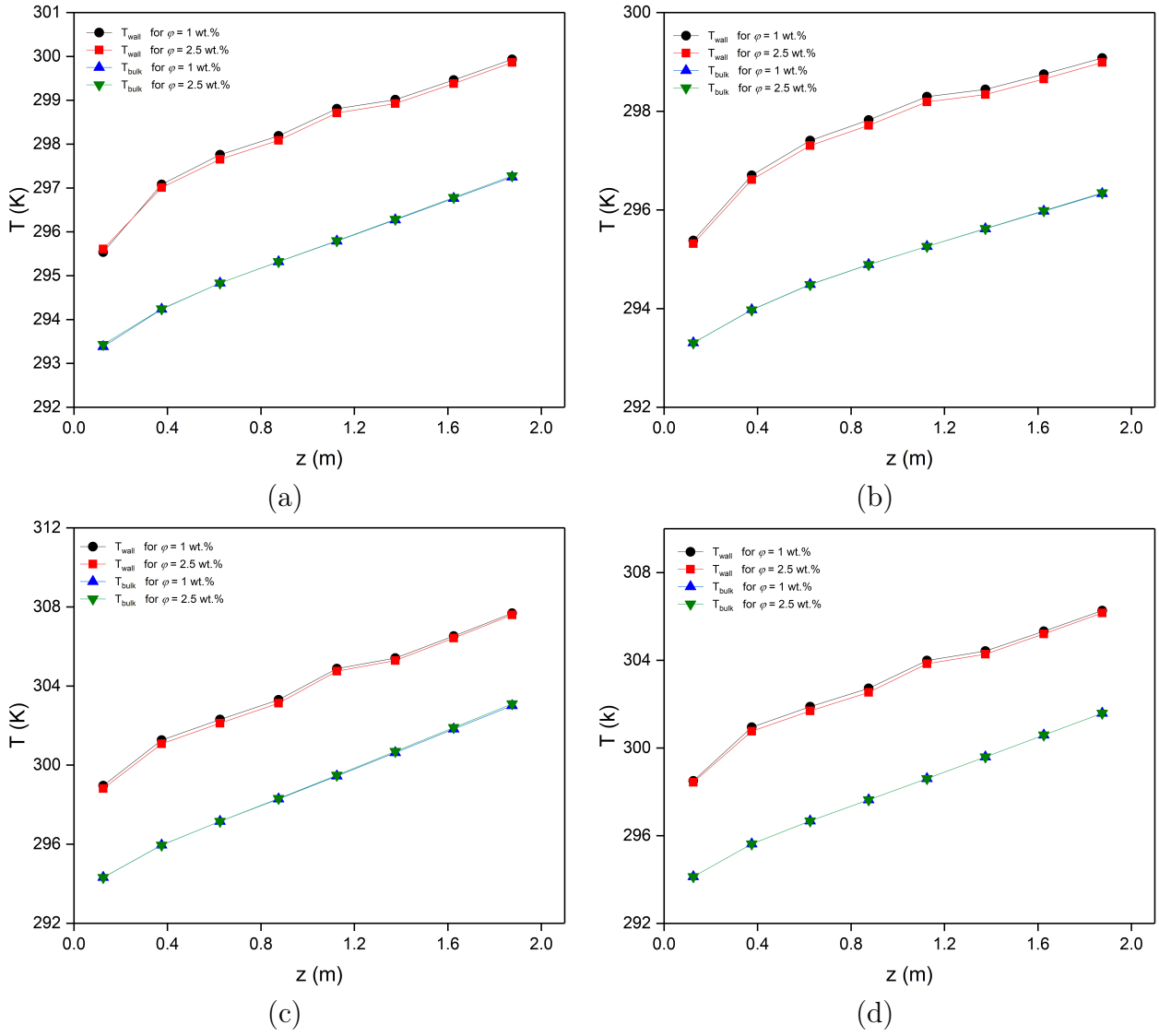

Figure B.3 Axial development of the wall and bulk nanofluid temperatures for the (a) 100-6, (b) 100-8, (c) 200-5 and (d) 200-6 test cases.

All the results were also discussed in terms of streamwise and spanwise profiles.

B.4 Population balance modelling for nanoparticles agglomeration

Adding nanoparticles to a base fluid not only enhances the transport properties of the mixture, but may also arise other phenomena such as agglomeration, coagulation and sedimentation. Therefore, the stability of nanofluids is a major problem hindering their shelf life and their industrial applications. In the last decades, a significant amount of experimental studies has been conducted to evaluate the nanoparticles agglomeration, dispersion and stability behaviour [36, 100, 237]. However, a very limited numerical ones were done

[40, 134, 203].
In the present study, the agglomeration phenomenon of nanoparticles is numerically analysed by evaluating the nanoparticle size and the volume fraction distribution. To this end, a number density function is introduced to account for the nanoparticle distribution. The governing equation which describes the evolution of the particle size distribution, in general, is called the population balance equation and it is given as follows [144]:

$$\frac{\partial n(t,x)}{\partial t} + \frac{\partial [G(t,x)n(t,x)]}{\partial x} = A_{agg}(t,x) + N_{nuc}(t,x) + B_{break}(t,x) \tag{B.5}$$

where n(t,x), G(t,x), A_{agg}, N_{nuc} and B_{break} are the number density, the growth term, the aggregation reaction term , the nucleation term and the breakage term, respectively.
This concept is referred in general to as the population balance model, PBM, and it is based on the assumption that the particles of size x born (formed) when particles of sizes x_i and x_j aggregate, as well as the particles x_i and x_j die (vanish) via a volume balance x which is a function of x_i and x_j. It can also be noted that the PBM is a tool for keeping track of the number of nanoparticles and their properties.
In our case, only the nanoparticle agglomeration phenomenon is evaluated, then equation (B.5) is reduced to the following expression:

$$\frac{\partial n(x)}{\partial t} = B'_{agg}(n,x) - D'_{agg}(n,x) \tag{B.6}$$

where B_{agg} and D_{agg} are the birth and death rates due to the pure aggregation, respectively, and they are defined as fellows:

$$B_{agg}(t,x) = \frac{1}{2}\int_0^{\nu} \beta(\nu-\nu',\nu')n(\nu-\nu',t)n(\nu',t)d\nu' \tag{B.7}$$

$$D_{agg}(t,x) = n(\nu,t)\int_0^{\infty} \beta(\nu,\nu')n(\nu',t)d\nu' \tag{B.8}$$

Note that ν is the volume of single particle.

To model the TiO_2 agglomeration, the discrete model is used. The latter is based on representing directly the continuous particle size distribution (PSD) in terms of a set of discrete size classes or bins. The nanoparticle aggregate is a result of different acting forces such as particle-particle interaction, diffusion force, thermophoresis and Brownian force. The random collision due to Brownian motion, in general, should not be avoided especially for nanoparticles. Therefore, the free molecular aggregation Kernel model is used, where the frequency of nanoparticle collision is size dependent and it is expressed as follows:

$$\beta(x_i, x_j) = \frac{2K_B T}{3\mu} \frac{(x_i + x_j)^2}{x_i x_j} \tag{B.9}$$

where K_B, T and μ are the Boltzmann constant, the absolute temperature and the host fluid viscosity, respectively. This frequency collision is also known as the Brownian kernel or the perikinetic kernel.

Two nanoparticle concentrations were tested: 2.5 wt.% and 4 wt.% under the same boundary conditions where the mass flow rate ($\dot{m}$) is 6 g/s and the imposed heat flux (Q) along the wall pipe is equal to 200 W (6-200). For both nanoparticle concentrations, the initial sizes are distributed on six bins from 2.1 nm to 2.1 μm.
Figure B.4 shows the nanoparticle diameter distribution at different locations along the tube. It is clear that the two concentrations possess the same trend of the size radial distribution with higher values for 4 wt.% TiO_2. As the flow evolves downstream, the nanoparticle diameter increases especially in the fluid core. The highest sizes are found to be in the regions near the pipe top and bottom, which can be attributed to the no slip velocity boundary condition.

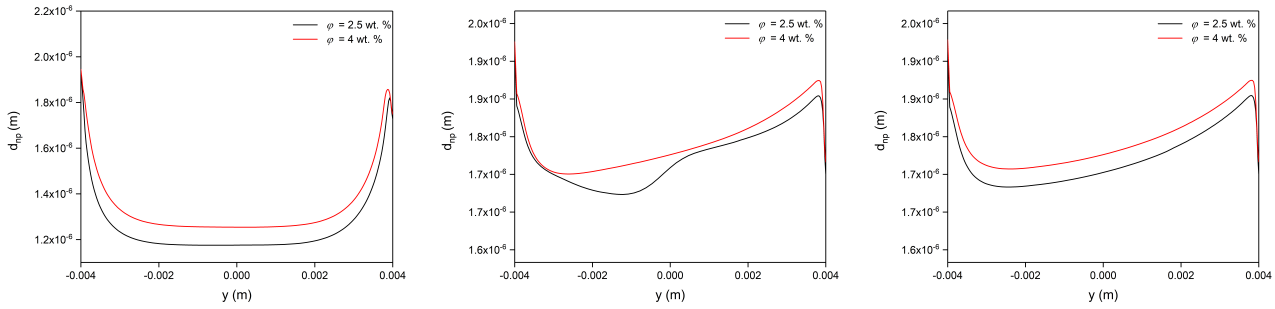

(a) (b) (c)

Figure B.4 Radial variation of the nanoparticle diameter at (a) $z = 0.125$ m, (b) $z = 1.125$ m and (c) $z = 1.875$ m for two different nanoparticle concentrations.

The volume averaged number density distribution at φ_{TiO_2} equal to 2.5 wt.% and 4 wt.% is displayed in Figure B.5. The later illustrates the change in the nanoparticle size distribution in the fluid domain, which confirms the important contribution of the Brownian motion on the agglomeration phenomenon. To provide more detail, Figure B.6 displays the radial distribution of the density number of all the existed bins in the fluid at z = 1.125 m. It is worthy to note that bin-1 corresponds to the highest-class size and bin-6 to the smallest one. The two considered concentrations exhibit the same behaviour for each nanoparticle size class. One can see, from Figure B.6, that the agglomeration rate is more accentuated for higher nanoparticle concentration. For instance, at $\varphi_{TiO_2} = 4$ wt.%, the number density distributions for both bin-5 and bin-6 are negligible compared to those of φ_{TiO_2} =2.5 wt.%.

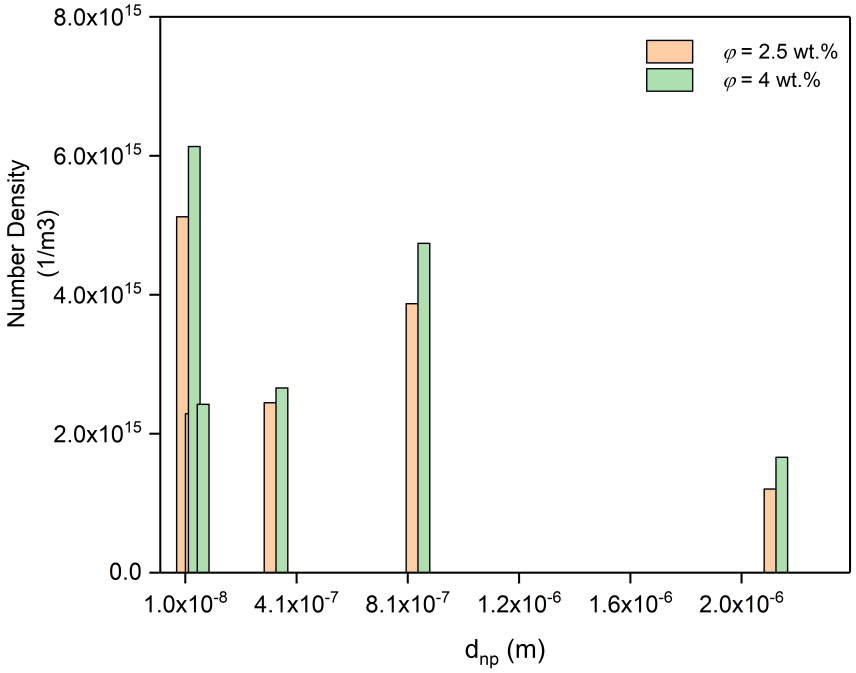

Figure B.5 Volume averaged number density distribution histogram for φ_{TiO_2} = 2.5 wt.% and φ_{TiO_2} = 4 wt.%.

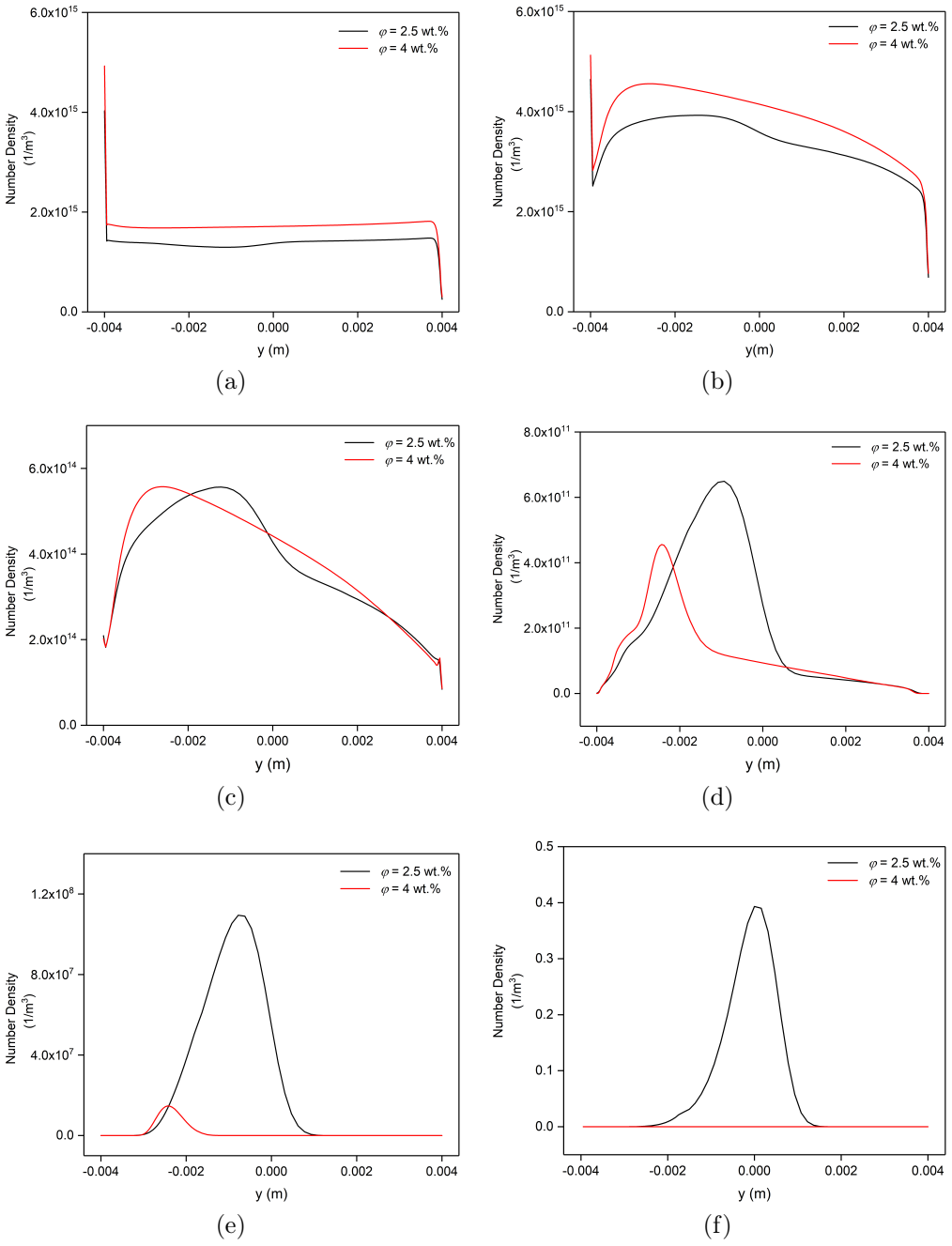

Figure B.6 Radial distribution of the number density of (a) Bin-1, (b) Bin-2, (c) Bin-3, (d) Bin-4, (e) Bin-5 and (f) Bin-6 at $z = 1.125$ m for two different nanoparticle concentrations: 2.5 wt.% and 4 wt.%.

In order to quantify the effect of nanoparticle aggregation on the heat transfer rate, the average Nusselt number is calculated for Q = 200 w and m = 6 g/s. Two nanofluid concentrations are tested for both cases: with and without the population balance model (PBM), as illustrated in Table B.5. The latter clearly shows that, with these particular operating

conditions, the agglomeration process has no effect on the thermal field throughout the domain.

Table B.5 Averaged Nusselt number for two nanoparticle concentrations: 2.5 wt.% and 4 wt.% with and without PBM.

	Without PBM	With PBM
2.5 wt.%	7.87	7.9
4 wt.%	8.1	8.12

Nanoparticles agglomeration is an important phenomenon that is generally studied experimentally by measuring the size distribution using a zeta-sizer devise based on the dynamic light scattering method [124, 187]. However, this technique was shown to be only suitable for very low nanoparticle concentrations. Additionally, zeta-sizer measurements are usually taken in static conditions which are essentially different from real industrial applications. Because of the lack of adequate experimental techniques capable of evaluating the aggregation process, collision mechanism and their interactions, the use of suitable numerical models is therefore deemed necessary.
The so-called population balance model has been widely used by researchers to evaluate the aggregation size distribution in various processes such as; bubble columns [16, 113, 114, 196], particle synthesis [31, 45, 136] and fluidized bed reactors [6, 12]. However, a few number of studies used this model used to evaluate nanoparticles size distribution in a base fluid and to assess nanofluids stability. Amongst these studies, Song et al. [203] investigated the coagulation and fragmentation phenomena of magnetic nanoparticles in nanofluids using a modified population balance model based on a discrete method. The authors reported that the Brownian motion dominated the coagulation process of nanoscale particles, while the shear deformation was more important for suspension containing micro-scale particles. The population balance equation solved with the discrete method was also used by Zerradi et al. [241] to predict the effect of agglomeration on the thermal conductivity of nanofluids. The effect of nucleation, growth, breakage and aggregation of nanoparticles inside the base fluid were taken into account in their numerical model. They reported that the aggregation and growth mechanisms largely affected the nanofluid thermal conductivity compared to the other processes.
It is noteworthy that the main advantage of the use of the discrete model is its capability to directly compute the particle size distribution. However, a large number of bins ($\gg 6$ bins) is usually required for a better estimate of the particle size distribution which entails high CPU time. Therefore, we suggest as a future work to compare the capability of the different population balance approaches, such as the standard method of moments and the quadrature method of moments, in predicting the nanoparticle size distribution and the agglomeration process. In addition, we intend to extend our study to the turbulent regime to explore additional phenomena associated with the presence of nanoparticle in a host fluid such as coagulation and breakage, which cannot be modeled for a laminar flow.

LIST OF REFERENCES

[1] Abu-Nada, E. (2010). Effects of variable viscosity and thermal conductivity of CuO-water nanofluid on heat transfer enhancement in natural convection: mathematical model and simulation. *Journal of Heat Transfer*, volume 132, number 5, pp. 052401–052410.

[2] Aghaei, A., Sheikhzadeh, G. A., Dastmalchi, M. and Forozande, H. (2015). Numerical investigation of turbulent forced-convective heat transfer of Al_2O_3–water nanofluid with variable properties in tube. *Ain Shams Engineering Journal*, volume 6, number 2, pp. 577–585.

[3] Akbari, M., Galanis, N. and Behzadmehr, A. (2011). Comparative analysis of single and two-phase models for CFD studies of nanofluid heat transfer. *International Journal of Thermal Sciences*, volume 50, number 8, pp. 1343–1354.

[4] Akbari, M., Galanis, N. and Behzadmehr, A. (2012). Comparative assessment of single and two-phase models for numerical studies of nanofluid turbulent forced convection. *International Journal of Heat and Fluid Flow*, volume 37, pp. 136–146.

[5] Akilu, S., Baheta, A. T., Minea, A. A. and Sharma, K. (2017). Rheology and thermal conductivity of non-porous silica (SiO_2) in viscous glycerol and ethylene glycol based nanofluids. *International Communications in Heat and Mass Transfer*, volume 88, pp. 245–253.

[6] Alavi, S., Mirmomen, L. and Saleh, K. (2007). Experimental study and particle population modeling of coating in a jet-fluidized bed. *Advanced Powder Technology*, volume 18, number 3, pp. 311–328.

[7] Alfaryjat, A., Stanciu, D., Dobrovicescu, A., Badescu, V. and Aldhaidhawi, M. (2016). Numerical investigation of entropy generation in microchannels heat sink with different shapes. In *IOP Conference Series: Materials Science and Engineering*, IOP Publishing. Volume 147. pp. 012134–012143.

[8] Aminfar, H. and Motallebzadeh, R. (2011). Numerical investigation of the effects of nanoparticle diameter on velocity field and nanoparticle distribution of nanofluid using Lagrangian-Eulerian approach. *Journal of Dispersion Science and Technology*, volume 32, number 9, pp. 1311–1317.

[9] Aminfar, H. and Motallebzadeh, R. (2012). Investigation of the velocity field and nanoparticle concentration distribution of nanofluid using Lagrangian-Eulerian approach. *Journal of Dispersion Science and Technology*, volume 33, number 1, pp. 155–163.

[10] Amirahmadi, S., Rashidi, S. and Esfahani, J. A. (2016). Minimization of exergy losses in a trapezoidal duct with turbulator, roughness and beveled corners. *Applied Thermal Engineering*, volume 107, pp. 533–543.

[11] Anoop, K., Sundararajan, T. and Das, S. (2009). Effect of particle size on the convective heat transfer in nanofluid in the developing region. *International Journal of Heat and Mass Transfer*, volume 52, pp. 2189–2195.

[12] Ashrafi, O., Mostoufi, N. and Sotudeh-Gharebagh, R. (2008). Particle size distribution in gas-phase polyethylene reactors. *Advanced Powder Technology*, volume 19, pp. 321–327.

[13] Aspelund, A., Berstad, D. and Gundersen, T. (2007). An extended pinch analysis and design procedure utilizing pressure based exergy for subambient cooling. *Applied Thermal Engineering*, volume 27, number 16, pp. 2633–2649.

[14] Azari, A., Kalbasi, M. and Rahimi, M. (2014). CFD and experimental investigation on the heat transfer characteristics of alumina nanofluids under the laminar flow regime. *Brazilian Journal of Chemical Engineering*, volume 31, number 2, pp. 469–481.

[15] Bahiraei, M. (2014). A comprehensive review on different numerical approaches for simulation in nanofluids: traditional and novel techniques. *Journal of Dispersion Science and Technology*, volume 35, number 7, pp. 984–996.

[16] Bannari, R., Kerdouss, F., Selma, B., Bannari, A. and Proulx, P. (2008). Three-dimensional mathematical modeling of dispersed two-phase flow using class method of population balance in bubble columns. *Computers & Chemical Engineering*, volume 32, number 12, pp. 3224–3237.

[17] Batchelor, G. (1977). The effect of Brownian motion on the bulk stress in a suspension of spherical particles. *Journal of Fluid Mechanics*, volume 83, number 01, pp. 97–117.

[18] Behnampour, A., Akbari, O. A., Safaei, M. R., Ghavami, M., Marzban, A., Shabani, G. A. S., Mashayekhi, R. *et al.* (2017). Analysis of heat transfer and nanofluid fluid flow in microchannels with trapezoidal, rectangular and triangular shaped ribs. *Physica E: Low-dimensional Systems and Nanostructures*, volume 91, pp. 15–31.

[19] Behroyan, I., Ganesan, P., He, S. and Sivasankaran, S. (2015). Turbulent forced convection of Cu–water nanofluid: CFD model comparison. *International Communications in Heat and Mass Transfer*, volume 67, pp. 163–172.

[20] Behroyan, I., Vanaki, S. M., Ganesan, P. and Saidur, R. (2016). A comprehensive comparison of various CFD models for convective heat transfer of Al_2O_3 nanofluid inside a heated tube. *International Communications in Heat and Mass Transfer*, volume 70, pp. 27–37.

[21] Behzadmehr, A., Saffar-Avval, M. and Galanis, N. (2007). Prediction of turbulent forced convection of a nanofluid in a tube with uniform heat flux using a two phase approach. *International Journal of Heat and Fluid Flow*, volume 28, number 2, pp. 211–219.

[22] Bejan, A. (1980). Second law analysis in heat transfer. *Energy*, volume 5, number 8-9, pp. 720–732.

[23] Bejan, A. (1982). *Entropy generation through heat and fluid flow*. Wiley, New York.

[24] Bhattacharya, P., Saha, S., Yadav, A., Phelan, P. and Prasher, R. (2004). Brownian dynamics simulation to determine the effective thermal conductivity of nanofluids. *Journal of Applied Physics*, volume 95, number 11, pp. 6492–6494.

[25] Bhatti, M. (1987). *Turbulent and Transition Flow Convective Heat Transfer in Ducts*. John Wiley, New-York.

[26] Bianco, V., Chiacchio, F., Manca, O. and Nardini, S. (2009). Numerical investigation of nanofluids forced convection in circular tubes. *Applied Thermal Engineering*, volume 29, number 17, pp. 3632–3642.

[27] Bianco, V., Manca, O. and Nardini, S. (2011). Numerical investigation on nanofluids turbulent convection heat transfer inside a circular tube. *International Journal of Thermal Sciences*, volume 50, number 3, pp. 341–349.

[28] Bianco, V., Manca, O. and Nardini, S. (2013). Second law analysis of Al_2O_3-water nanofluid turbulent forced convection in a circular cross section tube with constant wall temperature. *Advances in Mechanical Engineering*, volume 5, pp. 920278–920290.

[29] Bianco, V., Manca, O., Nardini, S. and Vafai, K. (2015). *Heat Transfer Enhancement with Nanofluids*. CRC Press, Boca Raton (USA).

[30] Biercuk, M., Llaguno, M. C., Radosavljevic, M., Hyun, J., Johnson, A. T. and Fischer, J. E. (2002). Carbon nanotube composites for thermal management. *Applied Physics Letters*, volume 80, number 15, pp. 2767–2769.

[31] Bilodeau, J.-F. and Proulx, P. (1996). A mathematical model for ultrafine iron powder growth in a thermal plasma. *Aerosol Science and Technology*, volume 24, number 3, pp. 175–189.

[32] Blasius, H. (1907). *Grenzschichten in Flüssigkeiten mit kleiner Reibung*. Druck von BG Teubner, Leipzig.

[33] Boertz, H., Baars, A., Cieśliński, J. T. and Smoleń, S. (2016). Turbulence model evaluation for numerical modelling of turbulent flow and heat transfer of nanofluids. In *Applied Mechanics and Materials*, volume 831. pp. 165–180.

[34] Boghrati, M., Bajestan, E. E. and Etminan, V. (2010). Entropy generation minimization of confined nanofluids laminar flow around a block. In *ASME 2010 10th Biennial Conference on Engineering Systems Design and Analysis*. pp. 729–736.

[35] Bordet, A., Poncet, S., Poirier, M. and Galanis, N. (2018). Advanced numerical modeling of turbulent ice slurry flows in a straight pipe. *International Journal of Thermal Sciences*, volume 127, pp. 294–311.

[36] Bouguerra, N., Poncet, S. and Elkoun, S. (2018). Dispersion regimes in alumina/water-based nanofluids: simultaneous measurements of thermal conductivity and dynamic viscosity. *International Communications in Heat and Mass Transfer*, volume 92, pp. 51–55.

[37] Brinkman, H. (1952). The viscosity of concentrated suspensions and solutions. *The Journal of Chemical Physics*, volume 20, number 4, pp. 571–571.

[38] Brites, C. D., Xie, X., Debasu, M. L., Qin, X., Chen, R., Huang, W., Rocha, J., Liu, X. and Carlos, L. D. (2016). Instantaneous ballistic velocity of suspended brownian nanocrystals measured by upconversion nanothermometry. *Nature Nanotechnology*, volume 11, number 10, pp. 851–856.

[39] Bruggeman, V. D. (1935). Berechnung verschiedener physikalischer Konstanten von heterogenen Substanzen. i. Dielektrizitätskonstanten und Leitfähigkeiten der Mischkörper aus isotropen Substanzen. *Annalen der Physik*, volume 416, number 7, pp. 636–664.

[40] Bück, A., Peglow, M., Naumann, M. and Tsotsas, E. (2012). Population balance model for drying of droplets containing aggregating nanoparticles. *AIChE Journal*, volume 58, number 11, pp. 3318–3328.

[41] Buongiorno, J. (2006). Convective transport in nanofluids. *Journal of Heat Transfer*, volume 128, number 3, pp. 240–250.

[42] Cess, R. D. and Shaffer, E. C. (1959). Summary of laminar heat transfer between parallel plates with unsymmetrical wall temperatures. *Journal of the Aerospace Sciences*, volume 26, number 8, pp. 538–538.

[43] Chassaing, P. (2000). *Turbulence en mécanique des fluides*. Cépaduès Éditions, Toulouse.

[44] Chen, H., Ding, Y., He, Y. and Tan, C. (2007). Rheological behaviour of ethylene glycol based titania nanofluids. *Chemical Physics Letters*, volume 444, number 4, pp. 333–337.

[45] Chen, M., Lin, T., Ma, C. Y. and Wang, X. Z. (2012). Population balance modelling and experimental study for synthesis of TiO_2nanoparticles using continuous hydrothermal process. In *Advanced Control of Chemical Processes*, volume 8. pp. 609–613.

[46] Choi, M. and Cho, K. (2001). Effect of the aspect ratio of rectangular channels on the heat transfer and hydrodynamics of paraffin slurry flow. *International Journal of Heat and Mass Transfer*, volume 44, pp. 55–61.

[47] Choi, S. U. S. and Eastman, J. A. (1995). Enhancing thermal conductivity of fluids with nanoparticles. In *ASME International Mechanical Engineering Congress and Exposition*, volume 231. pp. 99–106.

[48] Chon, C. H., Kihm, K. D., Lee, S. P. and Choi, S. U. S. (2005). Empirical correlation finding the role of temperature and particle size for nanofluid (Al_2O_3) thermal conductivity enhancement. *Applied Physics Letters*, volume 87, p. 153107.

[49] Chung, S., Rhee, G. and Sung, H. (2002). Direct numerical simulation of turbulent concentric annular pipe flow. *International Journal of Heat and Fluid Flow*, volume 23, pp. 426–440.

[50] Colla, L., Fedele, L. and Buschmann, M. (2015). Laminar mixed convection of TiO_2–water nanofluid in horizontal uniformly heated pipe flow. *International Journal of Thermal Sciences*, volume 97, pp. 26–40.

[51] Colla, L., Fedele, L. and Buschmann, M. H. (2015). Nanofluids suppress secondary flow in laminar pipe flow. In *Proceedings of the World Congress on Mechanical, Chemical, and Material Engineering*. pp. 279–1–279–4.

[52] Corcione, M. (2011). Rayleigh-Bénard convection heat transfer in nanoparticle suspensions. *International Journal of Heat and Fluid Flow*, volume 32, number 1, pp. 65–77.

[53] Corcione, M. (2012). A semi-empirical model for predicting the effective dynamic viscosity of nanoparticle suspensions. *Heat Transfer Engineering*, volume 33, number 7, pp. 575–583.

[54] Das, S. K., Choi, S. U. S., Yu, W. and Pradeep, T. (2008). *Nanofluids Science and Technology*. John Wiley & Sons, Inc., New Jersey.

[55] Davarnejad, R. and Jamshidzadeh, M. (2015). CFD modeling of heat transfer performance of MgO-water nanofluid under turbulent flow. *Engineering Science and Technology*, volume 18, number 4, pp. 536–542.

[56] Davis, R. (1986). The effective thermal conductivity of a composite material with spherical inclusions. *International Journal of Thermophysics*, volume 7, number 3, pp. 609–620.

[57] de Castro, C. N., Li, S., Nagashima, A., Trengove, R. and Wakeham, W. (1986). Standard reference data for the thermal conductivity of liquids. *Journal of Physical and Chemical Reference Data*, volume 15, number 3, pp. 1073–1086.

[58] Derakhshan, M. M., Akhavan-Behabadi, M. A. and Mohseni, S. G. (2015). Experiments on mixed convection heat transfer and performance evaluation of MWCNT–oil nanofluid flow in horizontal and vertical microfin tubes. *Experimental Thermal and Fluid Science*, volume 61, pp. 241–248.

[59] Diaz-Daniel, C., Laizet, S. and Vassilicos, J. C. (2017). Direct numerical simulations of a wall-attached cube immersed in laminar and turbulent boundary layers. *International Journal of Heat and Fluid Flow*, volume 68, pp. 269–280.

[60] Dittus, F. and Boelter, L. (1985). Heat transfer in automobile radiators of the tubular type. *International Communications in Heat and Mass Transfer*, volume 12, number 1, pp. 3–22.

[61] Drew, D. and Lahey, R. (1993). In particulate two-phase flow. *Butterworth Heinemann, Boston*, volume 509, number 0, p. 566.

[62] Drew, D. A. and Passman, S. L. (1999). *Theory of multicomponent fluids, volume 135 of Applied Mathematical Sciences*. Springer-Verlag, New-York.

[63] Duan, F. (2012). Thermal property measurement of $Al_2\ O_3$-water nanofluids. *Smart Nanoparticles Technology*, volume 23, pp. 336–356.

[64] Duangthongsuk, W. and Wongwises, S. (2009). Measurement of temperature-dependent thermal conductivity and viscosity of TiO_2-water nanofluids. *Experimental Thermal and Fluid Science*, volume 33, number 4, pp. 706–714.

[65] Ebrahimnia-Bajestan, E. and Niazmand, H. (2011). Convective heat transfer of nanofluids flows through an isothermally heated curved pipe. *Iranian Journal of Chemical Engineering*, volume 8, number 2, pp. 81–97.

[66] Eggels, J., Unger, F., Weiss, M., Westerweel, J., Adrian, R., Friedrich, R. and Nieuwstadt, F. (1994). Fully developed turbulent pipe flow: a comparison between direct numerical simulation and experiment. *Journal of Fluid Mechanics*, volume 268, pp. 175–209.

[67] Einstein, A. (1906). Eine neue Bestimmung der Moleküldimensionen. *Annalen der Physik*, volume 324, number 2, pp. 289–306.

[68] Einstein, A. (1956). *Investigations on the Theory of the Brownian Movement*, volume 58. Courier Corporation, New-York.

[69] El Khoury, G., Schlatter, P., Noorani, A., Fischer, P., Brethouwer, G. and Johansson, A. (2013). Direct numerical simulation of turbulent pipe flow at moderately high Reynolds numbers. *Flow, Turbulence and Combustion*, volume 91, pp. 475–495.

[70] Escue, A. and Cui, J. (2010). Comparison of turbulence models in simulating swirling pipe flows. *Applied Mathematical Modelling*, volume 34, pp. 2840–2849.

[71] Esfe, M. H., Arani, A. A. A., Niroumand, A. H., Yan, W.-M. and Karimipour, A. (2015). Mixed convection heat transfer from surface-mounted block heat sources in a horizontal channel with nanofluids. *International Journal of Heat and Mass Transfer*, volume 89, pp. 783–791.

[72] Eslami, M., Tavakol, M. M. and Goshtasbirad, E. (2010). Laminar fluid flow around two wall-mounted cubes of arbitrary configuration. *Proc. IMechE - Part C: J. Mechanical Engineering Science*, volume 224, pp. 2396–2407.

[73] Ferrouillat, S., Bontemps, A., Ribeiro, J., Gruss, J. and Soriano, O. (2011). Hydraulic and heat transfer study of SiO_2/water nanofluids in horizontal tubes with imposed wall temperature boundary conditions. *International Journal of Heat and Fluid Flow*, volume 32, number 2, pp. 424–439.

[74] Foroutani, S. and Rahbari, A. (2017). Numerical investigation of laminar forced convection heat transfer in rectangular channels with different block geometries using nanofluids. *Thermal Science*, volume 21, number 5, pp. 2129–2138.

[75] Fotukian, S. and Esfahany, M. N. (2010). Experimental investigation of turbulent convective heat transfer of dilute γ-Al_2O_3/water nanofluid inside a circular tube. *International Journal of Heat and Fluid Flow*, volume 31, number 4, pp. 606–612.

[76] Frankel, N. and Acrivos, A. (1967). On the viscosity of a concentrated suspension of solid spheres. *Chemical Engineering Science*, volume 22, number 6, pp. 847–853.

[77] Fujita, M. and Yamaguchi, Y. (2007). Multiscale simulation method for self-organization of nanoparticles in dense suspension. *Journal of Computational Physics*, volume 223, number 1, pp. 108–120.

[78] Galanis, N. and Ouzzane, M. (1999). Developing mixed convection in an inclined tube with circumferentially nonuniform heating at its outer surface. *Numerical Heat Transfer: Part A: Applications*, volume 35, number 6, pp. 609–628.

[79] Ganesan, P., Behroyan, I., He, S., Sivasankaran, S. and Sandaran, S. (2016). Turbulent forced convection of Cu–water nanofluid in a heated tube: Improvement of the two-phase model. *Numerical Heat Transfer, Part A: Applications*, volume 69, number 4, pp. 401–420.

[80] Gibson, M. and Launder, B. E. (1978). Ground effects on pressure fluctuations in the atmospheric boundary layer. *Journal of Fluid Mechanics*, volume 86, number 03, pp. 491–511.

[81] Gnielinski, V. (1976). New equations for heat and mass-transfer in turbulent pipe and channel flow. *International Chemical Engineering*, volume 16, number 2, pp. 359–368.

[82] Godson, L., Raja, B., Lal, D. M. and Wongwises, S. (2010). Experimental investigation on the thermal conductivity and viscosity of silver-deionized water nanofluid. *Experimental Heat Transfer*, volume 23, number 4, pp. 317–332.

[83] Graham, A. L. (1981). On the viscosity of suspensions of solid spheres. *Applied Scientific Research*, volume 37, number 3-4, pp. 275–286.

[84] Hachey, M., Nguyen, C., Galanis, N. and Popa, C. (2014). Experimental investigation of Al_2O_3 nanofluids thermal properties and rheology e effects of transient and steady-state heat exposure. *International Journal of Thermal Sciences*, volume 76, pp. 155–167.

[85] Halelfadl, S., Estellé, P. and Maré, T. (2014). Heat transfer properties of aqueous carbon nanotubes nanofluids in coaxial heat exchanger under laminar regime. *Experimental Thermal and Fluid Science*, volume 55, pp. 174–180.

[86] Hamilton, R. and Crosser, O. (1962). Thermal conductivity of heterogeneous two-component systems. *Industrial & Engineering Chemistry Fundamentals*, volume 1, number 3, pp. 187–191.

[87] He, Y., Men, Y., Zhao, Y., Lu, H. and Ding, Y. (2009). Numerical investigation into the convective heat transfer of TiO_2 nanofluids flowing through a straight tube under the laminar flow conditions. *Applied Thermal Engineering*, volume 29, number 10, pp. 1965–1972.

[88] Hedayati, F., Malvandi, A., Kaffash, M. and Ganji, D. (2015). Fully developed forced convection of alumina/water nanofluid inside microchannels with asymmetric heating. *Powder Technology*, volume 269, pp. 520–531.

[89] Heidary, H. and Kermani, M. (2012). Heat transfer enhancement in a channel with block(s) effect and utilizing nano-fluid. *International Journal of Thermal Sciences*, volume 57, pp. 163–171.

[90] Heris, S. Z., Esfahany, M. N. and Etemad, S. G. (2007). Experimental investigation of convective heat transfer of Al_2O_3/water nanofluid in circular tube. *International Journal of Heat and Fluid Flow*, volume 28, number 2, pp. 203–210.

[91] Heris, S. Z., Kazemi-Beydokhti, A., Noie, S. and Rezvan, S. (2012). Numerical study on convective heat transfer of Al_2O_3-water, CuO-water and Cu-water nanofluids through square cross-section duct in laminar flow. *Engineering Applications of Computational Fluid Mechanics*, volume 6, number 1, pp. 1–14.

[92] Heyhat, M., Kowsary, F., Rashidi, A., Esfehani, S. A. V. and Amrollahi, A. (2012). Experimental investigation of turbulent flow and convective heat transfer characteristics of alumina water nanofluids in fully developed flow regime. *International Communications in Heat and Mass Transfer*, volume 39, number 8, pp. 1272–1278.

[93] Heyhat, M. M., Kowsary, F., Rashidi, A. M., Momenpour, M. H. and Amrollahi, A. (2013). Experimental investigation of laminar convective heat transfer and pressure drop of water-based Al_2O_3 nanofluids in fully developed flow regime. *Experimental Thermal and Fluid Science*, volume 44, pp. 483–489.

[94] Ho, C., Liu, W., Chang, Y. and Lin, C. (2010). Natural convection heat transfer of alumina-water nanofluid in vertical square enclosures: an experimental study. *International Journal of Thermal Sciences*, volume 49, number 8, pp. 1345–1353.

[95] Hu, C., Wang, P., Bai, M., Lv, J., Wang, Y. and Li, X. (2013). Numerical study of nanofluids flow characteristics using LES-Lagrange method and molecular dynamics simulation. In *ASME 4th Int. Conf. on Micro/Nanoscale Heat and Mass Transfer*, volume V001T02A001.

[96] Huminic, G. and Huminic, A. (2012). Application of nanofluids in heat exchangers: a review. *Renewable and Sustainable Energy Reviews*, volume 16, number 8, pp. 5625–5638.

[97] Hussein, A., Dawood, H., Bakara, R. and Kadirgamaa, K. (2017). Numerical study on turbulent forced convective heat transfer using nanofluids TiO_2 in an automotive cooling system. *Case Studies in Thermal Engineering*, volume 9, pp. 72–78.

[98] Hussein, A. M., Bakar, R., Kadirgama, K. and Sharma, K. (2014). Heat transfer enhancement using nanofluids in an automotive cooling system. *International Communications in Heat and Mass Transfer*, volume 53, pp. 195–202.

[99] Hwang, K. S., Jang, S. P. and Choi, S. U. S. (2009). Flow and convective heat transfer characteristics of water-based Al_2O_3 nanofluids in fully developed laminar flow regime. *International Journal of Heat and Mass Transfer*, volume 52, pp. 193–199.

[100] Ilyas, S. U., Pendyala, R. and Marneni, N. (2014). Preparation, sedimentation, and agglomeration of nanofluids. *Chemical Engineering and Technology*, volume 37, pp. 2011–2021.

[101] Jang, S. P. and Choi, S. U. S. (2004). Role of Brownian motion in the enhanced thermal conductivity of nanofluids. *Applied Physics Letters*, volume 84, number 21, pp. 4316–4318.

[102] Jang, S. P. and Choi, S. U. S. (2007). Effects of various parameters on nanofluid thermal conductivity. *Journal of Heat Transfer*, volume 129, number 5, pp. 617–623.

[103] Jeffrey, D. J. (1973). Conduction through a random suspension of spheres. *Proceedings of the Royal Society of London A*, volume 335, number 1602, pp. 355–367.

[104] Jones, W. and Launder, B. (1972). The prediction of laminarization with a two-equation model of turbulence. *International Journal of Heat and Mass Transfer*, volume 15, number 2, pp. 301–314.

[105] Juan-Cheng, Y., Feng-Chen, L., Wei-Hua, C., Hong-Na, Z. and Bo, Y. (2015). Direct numerical simulation of viscoelastic-fluid-based nanofluid turbulent channel flow with heat transfer. *Chinese Physics B*, volume 24, number 8, pp. 084401–1–084401–17.

[106] Kakaç, S. and Pramuanjaroenkij, A. (2009). Review of convective heat transfer enhancement with nanofluids. *International Journal of Heat and Mass Transfer*, volume 52, number 13, pp. 3187–3196.

[107] Kakac, S. and Pramuanjaroenkij, A. (2016). Single-phase and two-phase treatments of convective heat transfer enhancement with nanofluids - A state-of-the-art review. *International Journal of Thermal Sciences*, volume 100, pp. 75–97.

[108] Kalteh, M., Abbassi, A., Saffar-Avval, M., Frijns, A., Darhuber, A. and Harting, J. (2012). Experimental and numerical investigation of nanofluid forced convection inside a wide microchannel heat sink. *Applied Thermal Engineering*, volume 36, pp. 260–268.

[109] Kalteh, M., Abbassi, A., Saffar-Avval, M. and Harting, J. (2011). Eulerian–Eulerian two-phase numerical simulation of nanofluid laminar forced convection in a microchannel. *International Journal of Heat and Fluid Flow*, volume 32, number 1, pp. 107–116.

[110] Karthikeyan, N., Philip, J. and Raj, B. (2008). Effect of clustering on the thermal conductivity of nanofluids. *Materials Chemistry and Physics*, volume 109, number 1, pp. 50–55.

[111] Kasagi, N., Tomita, Y. and Kuroda, A. (1992). Direct numerical simulation of passive scalar field in a turbulent channel flow. *Transactions of the ASME, Journal of Heat Transfer*, volume 114, pp. 598–606.

[112] Keblinski, P., Phillpot, S. R., Choi, S. U. S. and Eastman, J. A. (2002). Mechanisms of heat flow in suspensions of nano-sized particles (nanofluids). *International Journal of Heat and Mass Transfer*, volume 45, number 4, pp. 855–863.

[113] Kerdouss, F., Bannari, A. and Proulx, P. (2006). Cfd modeling of gas dispersion and bubble size in a double turbine stirred tank. *Chemical Engineering Science*, volume 61, number 10, pp. 3313–3322.

[114] Kerdouss, F., Bannari, A., Proulx, P., Bannari, R., Skrga, M. and Labrecque, Y. (2008). Two-phase mass transfer coefficient prediction in stirred vessel with a CFD model. *Computers & Chemical Engineering*, volume 32, number 8, pp. 1943–1955.

[115] Khanafer, K. and Vafai, K. (2011). A critical synthesis of thermophysical characteristics of nanofluids. *International Journal of Heat and Mass Transfer*, volume 54, pp. 4410–4428.

[116] Khanafer, K., Vafai, K. and Lightstone, M. (2003). Buoyancy-driven heat transfer enhancement in a two-dimensional enclosure utilizing nanofluids. *International Journal of Heat and Mass Transfer*, volume 46, number 19, pp. 3639–3653.

[117] Khdher, A. M., Mamat, R. and Sidik, N. A. C. (2011). The effects of turbulent nanofluids and secondary flow on the heat transfer through a straight channel. Volume 1368. pp. 118–124.

[118] Kheirandish, Z., Gandjalikhan Nassab, S. and Vakilian, M. (2013). Study of conjugate convection flow and entropy generation in a channel containing a heated obstacle. *Caspian Journal of Applied Sciences Research*, volume 2, number 3, pp. 104–116.

[119] Khoshvaght-Aliabadi, M. and Hormozi, F. (2015). Heat transfer enhancement by using copper-water nanofluid flow inside a pin channel. *Experimental Heat Transfer*, volume 28, number 5, pp. 446–463.

[120] Koo, J. and Kleinstreuer, C. (2004). A new thermal conductivity model for nanofluids. *Journal of Nanoparticle Research*, volume 6, number 6, pp. 577–588.

[121] Koo, J. and Kleinstreuer, C. (2005). Impact analysis of nanoparticle motion mechanisms on the thermal conductivity of nanofluids. *International Communications in Heat and Mass Transfer*, volume 32, number 9, pp. 1111–1118.

[122] Korichi, A. and Oufer, L. (2005). Numerical heat transfer in a rectangular channel with mounted obstacles on upper and lower walls. *International Journal of Thermal Sciences*, volume 44, number 7, pp. 644–655.

[123] Kotas, T. (1995). *The Exergy Analysis Method of Thermal Plant Analysis*. Malabar, Florida: Krieger Publishing Company.

[124] Krishna, K. H., Neti, S., Oztekin, A. and Mohapatra, S. (2015). Modeling of particle agglomeration in nanofluids. *Journal of Applied Physics*, volume 117, number 9, pp. 094304–094313.

[125] Labonté, J., Nguyen, C. T. and Roy, G. (2006). Heat transfer enhancement in laminar flow using Al_2O_3-water nanofluid considering temperature-dependent properties. In *Proceedings of the 4th WSEAS International Conference on Heat Transfer, Thermal Engineering and Environment*. pp. 21–23.

[126] Launder, B., Reece, G. J. and Rodi, W. (1975). Progress in the development of a Reynolds-stress turbulence closure. *Journal of Fluid Mechanics*, volume 68, number 3, pp. 537–566.

[127] Launder, B. E. (1989). Second-moment closure: present and future? *International Journal of Heat and Fluid Flow*, volume 10, number 4, pp. 282–300.

[128] Launder, B. E. and Spalding, D. B. (1972). *Lectures in mathematical models of turbulence*. Academic Press, London.

[129] Lee, J. and Mudawar, I. (2007). Assessment of the effectiveness of nanofluids for single-phase and two-phase heat transfer in micro-channels. *International Journal of Heat and Mass Transfer*, volume 50, number 3, pp. 452–463.

[130] Lee, S.-H. and Jang, S. P. (2015). Mechanisms and models of thermal conductivity in nanofluids. In *Heat Transfer Enhancement with Nanofluids*. CRC Press, pp. 73–102.

[131] Li, C. H. and Peterson, G. (2006). Experimental investigation of temperature and volume fraction variations on the effective thermal conductivity of nanoparticle suspensions (nanofluids). *Journal of Applied Physics*, volume 99, number 8, pp. 084314–084323.

[132] Li, P., Xie, Y., Zhang, D. and Xie, G. (2016). Heat transfer enhancement and entropy generation of nanofluids laminar convection in microchannels with flow control devices. *Entropy*, volume 18, number 4, p. 134.

[133] Li, Q. and Xuan, Y. (2002). Convective heat transfer and flow characteristics of Cu-water nanofluid. *Science in China Series E: Technolgical Science*, volume 45, number 4, pp. 408–416.

[134] Lin, J.-Z., Xia, Y. and Ku, X.-K. (2014). Pressure drop and heat transfer of nanofluid in turbulent pipe flow considering particle coagulation and breakage. *Journal of Heat Transfer*, volume 136, number 11, pp. 111701–111710.

[135] Liu, M., Ding, C. and Wang, J. (2016). Modeling of thermal conductivity of nanofluids considering aggregation and interfacial thermal resistance. *RSC Advances*, volume 6, pp. 3571–3577.

[136] Lopes, S., Proulx, P., Gouriet, J. and Rambaud, P. (2014). Applcation of an integrated cfd modle to aluminum nanoparticle production. In *Proc. of the 15th International Heat Transfer Conference, IHTC-15*.

[137] Lotfi, R., Saboohi, Y. and Rashidi, A. M. (2010). Numerical study of forced convective heat transfer of nanofluids: comparison of different approaches. *International Communications in Heat and Mass Transfer*, volume 37, number 1, pp. 74–78.

[138] Lu, S.-Y. and Lin, H.-C. (1996). Effective conductivity of composites containing aligned spheroidal inclusions of finite conductivity. *Journal of Applied Physics*, volume 79, number 9, pp. 6761–6769.

[139] Lundgren, T. S. (1972). Slow flow through stationary random beds and suspensions of spheres. *Journal of Fluid Mechanics*, volume 51, number 02, pp. 273–299.

[140] Mahdavi, M., Sharifpur, M. and Meyer, J. P. (2015). CFD modelling of heat transfer and pressure drops for nanofluids through vertical tubes in laminar flow by Lagrangian and Eulerian approaches. *International Journal of Heat and Mass Transfer*, volume 88, pp. 803–813.

[141] Mahian, O., Kianifar, A., Kleinstreuer, C., Mohd A, A., Pop, I., Sahin, A. and Wongwises, S. (2013). A review of entropy generation in nanofluid flow. *International Journal of Heat and Mass Transfer*, volume 65, pp. 514–532.

[142] Maiga, S. E. B., Nguyen, C. T., Galanis, N. and Roy, G. (2004). Heat transfer behaviours of nanofluids in a uniformly heated tube. *Superlattices and Microstructures*, volume 35, number 3, pp. 543–557.

[143] Maiga, S. E. B., Palm, S. J., Nguyen, C. T., Roy, G. and Galanis, N. (2005). Heat transfer enhancement by using nanofluids in forced convection flows. *International Journal of Heat and Fluid Flow*, volume 26, number 4, pp. 530–546.

[144] Majumder, A., Kariwala, V., Ansumali, S. and Rajendran, A. (2012). Lattice Boltzmann method for population balance equations with simultaneous growth, nucleation, aggregation and breakage. *Chemical Engineering Science*, volume 69, number 1, pp. 316–328.

[145] Manninen, M., Taivassalo, V. and Kallio, S. (1996). On the mixture model for multiphase flow. *VTT Publications*, volume 88, pp. 1–67.

[146] Mansour, R. B., Galanis, N. and Nguyen, C. T. (2007). Effect of uncertainties in physical properties on forced convection heat transfer with nanofluids. *Applied Thermal Engineering*, volume 27, number 1, pp. 240–249.

[147] Maré, T., Halelfadl, S., Sow, O., Estellé, P., Duret, S. and Bazantay, F. (2011). Comparison of the thermal performances of two nanofluids at low temperature in a plate heat exchanger. *Experimental Thermal and Fluid Science*, volume 35, pp. 1535–1543.

[148] Maxwell, J. C. (1881). *A Treatise on electricity and magnetism, Second Edition*. Clarendon, Oxford.

[149] Mehrez, Z., Bouterra, M., El Cafsi, A. and Belghith, A. (2013). Heat transfer and entropy generation analysis of nanofluids flow in an open cavity. *Computers & Fluids*, volume 88, pp. 363–373.

[150] Mehrez, Z., El Cafsi, A., Belghith, A. and Le Quéré, P. (2015). The entropy generation analysis in the mixed convective assisting flow of Cu-water nanofluid in an inclined open cavity. *Advanced Powder Technology*, volume 26, pp. 1442–1451.

[151] Mehrez, Z., El Cafsi, A., Belghith, A. and Le Quéré, P. (2015). MHD effects on heat transfer and entropy generation of nanofluid flow in an open cavity. *Journal of Magnetism and Magnetic Materials*, volume 374, pp. 214–224.

[152] Menter, F. R. (1994). Two-equation eddy-viscosity turbulence models for engineering applications. *AIAA journal*, volume 32, number 8, pp. 1598–1605.

[153] Michaelides, E. E. (2013). Heat transfer with nanofluids–a critical review. *Journal of Non-Equilibrium Thermodynamics*, volume 38, number 1, pp. 1–79.

[154] Minea, A. and El-Maghlany, W. (2017). Natural convection heat transfer utilizing ionic nanofluids with temperature-dependent thermophysical properties. *Chemical Engineering Science*, volume 174, pp. 13–24.

[155] Minea, A. A. (2014). Uncertainties in modeling thermal conductivity of laminar forced convection heat transfer with water alumina nanofluids. *International Journal of Heat and Mass Transfer*, volume 68, pp. 78–84.

[156] Minea, A. A. (2017). *Advances in New Heat Transfer Fluids: From Numerical to Experimental Techniques*. CRC Press, Boca Raton, Florida.

[157] Moldoveanu, G. M., Ibanescu, C., Danu, M. and Minea, A. A. (2018). Viscosity estimation of Al_2O_3, SiO_2 nanofluids and their hybrid: an experimental study. *Journal of Molecular Liquids*, volume 253, pp. 188–196.

[158] Moldoveanu, G. M. and Minea, A. A. (2015). A study on uncertainties in estimations of thermal conductivity of alumina nanofluids. *Applied Mechanics and Materials*, volume 809-810, pp. 525–530.

[159] Moldoveanu, G. M., Minea, A. A., Iacob, M., Ibanescu, C. and Danu, M. (2018). Experimental study on viscosity of stabilized Al_2O_3, TiO_2 nanofluids and their hybrid. *Thermochimica Acta*, volume 659, pp. 203–212.

[160] Moraveji, M. K. and Ardehali, R. M. (2013). CFD modeling (comparing single and two-phase approaches) on thermal performance of Al_2O_3/water nanofluid in mini-channel heat sink. *International Communications in Heat and Mass Transfer*, volume 44, pp. 157–164.

[161] Murshed, S., Leong, K. and Yang, C. (2008). Investigations of thermal conductivity and viscosity of nanofluids. *International Journal of Thermal Sciences*, volume 47, number 5, pp. 560–568.

[162] Namburu, P. K., Das, D. K., Tanguturi, K. M. and Vajjha, R. S. (2009). Numerical study of turbulent flow and heat transfer characteristics of nanofluids considering variable properties. *International Journal of Thermal Sciences*, volume 48, number 2, pp. 290–302.

[163] Nan, C. W., Birringer, R., Clarke, D. R. and Gleiter, H. (1997). Effective thermal conductivity of particulate composites with interfacial thermal resistance. *Journal of Applied Physics*, volume 81, number 10, pp. 6692–6699.

[164] Nguyen, C., Desgranges, F., Galanis, N., Roy, G., Maré, T., Boucher, S. and Mintsa, H. A. (2008). Viscosity data for Al_2O_3-water nanofluid hysteresis: is heat transfer enhancement using nanofluids reliable? *International Journal of Thermal Sciences*, volume 47, number 2, pp. 103–111.

[165] Nguyen, C., Desgranges, F., Roy, G., Galanis, N., Maré, T., Boucher, S. and Mintsa, H. A. (2007). Temperature and particle-size dependent viscosity data for water-based nanofluids–hysteresis phenomenon. *International Journal of Heat and Fluid Flow*, volume 28, number 6, pp. 1492–1506.

[166] Nikuradse, J. (1933). Stromungsgesetze in rauhen Rohren. volume 361, pp. 1–22.

[167] Noghrehabadi, A. and Pourrajab, R. (2016). Experimental investigation of forced convective heat transfer enhancement of γ-Al_2O_3/water nanofluid in a tube. *Journal of Mechanical Science and Technology*, volume 30, number 2, pp. 943–952.

[168] O'Hanley, H., Buongiorno, J., McKrell, T. and Hu, L.-W. (2012). Measurement and model validation of nanofluid specific heat capacity with differential scanning calorimetry. *Advances in Mechanical Engineering*, volume 4, pp. 181079–181085.

[169] Orfi, J. and Galanis, N. (2002). Developing laminar mixed convection with heat and mass transfer in horizontal and vertical tubes. *International Journal of Thermal Sciences*, volume 41, number 4, pp. 319–331.

[170] Orszag, S. A., Yakhot, V., Flannery, W. S., Boysan, F., Choudhury, D., Maruzewski, J. and Patel, B. (1993). Renormalization group modeling and turbulence simulations. In *International conference on Near-wall turbulent flows*. pp. 1031–1046.

[171] Oztop, H. F. and Al-Salem, K. (2012). A review on entropy generation in natural and mixed convection heat transfer for energy systems. *Renewable and Sustainable Energy Reviews*, volume 16, number 1, pp. 911–920.

[172] Pak, B. C. and Cho, Y. I. (1998). Hydrodynamic and heat transfer study of dispersed fluids with submicron metallic oxide particles. *Experimental Heat Transfer an International Journal*, volume 11, number 2, pp. 151–170.

[173] Palm, S. J., Roy, G. and Nguyen, C. T. (2006). Heat transfer enhancement with the use of nanofluids in radial flow cooling systems considering temperature-dependent properties. *Applied Thermal Engineering*, volume 26, number 17, pp. 2209–2218.

[174] Pantzali, M., Mouza, A. and Paras, S. (2009). Investigating the efficiency of nanofluids as coolants in plate heat exchangers (PHE). *Chemical Engineering Science*, volume 64, number 14, pp. 3290–3300.

[175] Patel, H. E., Sundararajan, T. and Das, S. K. (2010). An experimental investigation into the thermal conductivity enhancement in oxide and metallic nanofluids. *Journal of Nanoparticle Research*, volume 12, number 3, pp. 1015–1031.

[176] Peng, W., Minli, B., Jizu, L., Chengzhi, H. and Yuyan, W. (2014). Numerical study on the microflow mechanism of heat transfer enhancement in nanofluids. *Nanoscale and Microscale Thermophysical Engineering*, volume 18, number 2, pp. 113–136.

[177] Philip, J., Shima, P. and Raj, B. (2008). Evidence for enhanced thermal conduction through percolating structures in nanofluids. *Nanotechnology*, volume 19, number 30, p. 305706.

[178] Prasher, R., Bhattacharya, P. and Phelan, P. E. (2006). Brownian-motion-based convective-conductive model for the effective thermal conductivity of nanofluids. *Journal of Heat Transfer*, volume 128, number 6, pp. 588–595.

[179] Prasher, R., Song, D. and Phelan, J. (2006). Measurements of nanofluid viscosity and its implications for thermal applications. *Applied Physics Letters*, volume 89, number 133108–133112.

[180] Putra, N., Thiesen, P., Roetzel, W. *et al.* (2003). Temperature dependence of thermal conductivity enhancement for nanofluids. *Journal of Heat Transfer*, volume 125, pp. 567–574.

[181] Ranz, W. and Marshall, W. (1952). Evaporation from drops - Part I. *Chemical Engineering Progress*, volume 48, pp. 141–146.

[182] Rashidi, S., Akbarzadeh, M., Karimi, N. and Masoodi, R. (2018). Combined effects of nanofluid and transverse twisted-baffles on the flow structures, heat transfer and irreversibilities inside a square duct-a numerical study. *Applied Thermal Engineering*, volume 130, pp. 135–148.

[183] Rashidi, S., Eskandarian, M., Mahian, O. and Poncet, S. (2018). Combination of nanofluid and inserts for heat transfer enhancement - Gaps and challenges. *Journal of Thermal Analysis and Calorimetry*, volume corrected proofs.

[184] Rea, U., McKrell, T., Hu, L. and Buongiorno, J. (2009). Laminar convective heat transfer and viscous pressure loss of alumina-water and zirconia-water nanofluids. *International Journal of Heat and Mass Transfer*, volume 52, pp. 2042–2048.

[185] Riazi, H., Murphy, T., Webber, G. B., Atkin, R., Mostafavi Tehrani, S. S. and Taylor, R. A. (2016). Specific heat control of nanofluids: A critical review. *International Journal of Thermal Sciences*, volume 107, pp. 25–38.

[186] Roy, G., Gherasim, I., Nadeau, F., Poitras, G. and Nguyen, C. T. (2012). Heat transfer performance and hydrodynamic behavior of turbulent nanofluid radial flows. *International Journal of Thermal Sciences*, volume 58, pp. 120–129.

[187] Sadeghy, R., Haghshenasfard, M., Etemad, S. G. and Keshavarzi, E. (2016). Investigation of alumina nanofluid stability using experimental and modified population balance methods. *Advanced Powder Technology*, volume 27, number 5, pp. 2186–2195.

[188] Saha, G. and Paul, M. C. (2014). Numerical analysis of the heat transfer behaviour of water based Al_2O_3 and TiO_2 nanofluids in a circular pipe under the turbulent flow condition. *International Communications in Heat and Mass Transfer*, volume 56, pp. 96–108.

[189] Salman, B., Mohammed, H. and Kherbeet, A. (2016). Numerical study of three different approaches to simulate nanofluids flow and heat transfer in a microtube. *Heat Transfer–Asian Research*, volume 45, number 1, pp. 46–58.

[190] Schiller, L. and Naumann, Z. (1935). A drag coefficient correlation. *Zeitschrift des Vereins Deutscher Ingenieure*, volume 77, pp. 318–320.

[191] Sciacovelli, A., Verda, V. and Sciubba, E. (2015). Entropy generation analysis as a design tool - a review. *Renewable and Sustainable Energy Reviews*, volume 43, pp. 1167–1181.

[192] Sekrani, G. and Poncet, S. (2016). Further investigation on laminar forced convection of nanofluid flows in a uniformly heated pipe using direct numerical simulations. *Applied Sciences*, volume 6, number 332, pp. 1–24.

[193] Sekrani, G., Poncet, S. and Proulx, P. (2018). Conjugated heat transfer and entropy generation of Al_2O_3–water nanofluid flows over a heated wall-mounted obstacle. *Journal of Thermal Analysis and Calorimetry*, pp. 1–17.

[194] Sekrani, G., Poncet, S. and Proulx, P. (2018). Modeling of convective turbulent heat transfer of water-based Al_2O_3 nanofluids in an uniformly heated pipe. *Chemical Engineering Science*, volume 176, pp. 205–219.

[195] Selimefendigil, F. and Öztop, H. F. (2016). Numerical study of forced convection of nanofluid flow over a backward facing step with a corrugated bottom wall in the presence of different shaped obstacles. *Heat Transfer Engineering*, volume 37, number 15, pp. 1280–1292.

[196] Selma, B., Bannari, R. and Proulx, P. (2010). Simulation of bubbly flows: Comparison between direct quadrature method of moments (DQMOM) and method of classes (CM). *Chemical Engineering Science*, volume 65, number 6, pp. 1925–1941.

[197] Shah, R. K. (1975). Thermal entry length solutions for the circular tube and parallel plates. In *Third National Heat and Mass Transfer Conference*, volume 1. pp. 11–75.

[198] Sheremet, M. A., Oztop, H. F., Pop, I. and Abu-Hamdeh, N. (2015). Analysis of entropy generation in natural convection of nanofluid inside a square cavity having hot solid block: Tiwari and Das' model. *Entropy*, volume 18, number 1, pp. 1–15.

[199] Shih, T.-H., Liou, W. W., Shabbir, A., Yang, Z. and Zhu, J. (1995). A new k-ε eddy viscosity model for high Reynolds number turbulent flows. *Computers & Fluids*, volume 24, number 3, pp. 227–238.

[200] Siavashi, M. and Jamali, M. (2016). Heat transfer and entropy generation analysis of turbulent flow of TiO_2-water nanofluid inside annuli with different radius ratios using two-phase mixture model. *Applied Thermal Engineering*, volume 100, pp. 1149–1160.

[201] Sidik, N. A. C., Khakbaz, M., Jahanshaloo, L., Samion, S. and Darus, A. N. (2013). Simulation of forced convection in a channel with nanofluid by the lattice Boltzmann method. *Nanoscale Research Letters*, volume 8, number 1, pp. 178–186.

[202] Simons, R. (2006). Comparing heat transfer rates of liquid coolants using the Mouromtseff number. *Calculation Corner*, volume 12, number 2.

[203] Song, D., Jing, D., Geng, J. and Ren, Y. (2015). A modified aggregation based model for the accurate prediction of particle distribution and viscosity in magnetic nanofluids. *Powder Technology*, volume 283, pp. 561–569.

[204] Song, S., Peng, C., Gonzalez-Olivares, M., Lopez-Valdivieso, A. and Fort, T. (2005). Study on hydration layers near nanoscale silica dispersed in aqueous solutions through viscosity measurement. *Journal of Colloid and Interface Science*, volume 287, number 1, pp. 114–120.

[205] Spalart, P. R. and Allmaras, S. R. (1994). A one-equation turbulence model for aerodynamic flows. *La Recherche Aérospatiale*, volume 1, pp. 5–21.

[206] Sundar, L. and Sharma, K. (2010). Heat transfer enhancements of low volume concentration Al_2O_3 nanofluid and with longitudinal strip inserts in a circular tube. *International Journal of Heat and Mass Transfer*, volume 53, number 19, pp. 4280–4286.

[207] Sundar, L. and Sharma, K. (2010). Turbulent heat transfer and friction factor of Al_2O_3 nanofluid in circular tube with twisted tape inserts. *International Journal of Heat and Mass Transfer*, volume 53, number 7, pp. 1409–1416.

[208] Suresh, S., Chandrasekar, M. and Sekhar, S. C. (2011). Experimental studies on heat transfer and friction factor characteristics of CuO/water nanofluid under turbulent flow in a helically dimpled tube. *Experimental Thermal and Fluid Science*, volume 35, number 3, pp. 542–549.

[209] Syamlal, M., Rogers, W. and OBrien, T. (1993). *MFIX documentation theory guide* (Technical report). USDOE Morgantown Energy Technology Center, USA.

[210] Tarybakhsh, M. R., Lotfi Neyestanak, A. A. and Tarybakhsh, H. (2013). CFD study on wall/nanoparticle interaction in nanofluids convective heat transfer. *Advances in Materials Science and Engineering*, volume 2013, pp. 1–7.

[211] Teng, T.-P., Hung, Y.-H., Teng, T.-C., Mo, H.-E. and Hsu, H.-G. (2010). The effect of alumina/water nanofluid particle size on thermal conductivity. *Applied Thermal Engineering*, volume 30, number 14, pp. 2213–2218.

[212] Thakre, S. and Joshi, J. (2000). CFD modeling of heat transfer in turbulent pipe flows. *AICHE Journal*, volume 46, number 9, pp. 1798–1812.

[213] Timofeeva, E., Yu, W., France, D., Singh, D. and Routbort, J. (2011). Nanofluids for heat transfer: an engineering approach. *Nanoscale Research Letters*, volume 6, number 182.

[214] Timofeeva, E. V., Gavrilov, A. N., McCloskey, J. M., Tolmachev, Y. V., Sprunt, S., Lopatina, L. M. and Selinger, J. V. (2007). Thermal conductivity and particle agglomeration in alumina nanofluids: experiment and theory. *Physical Review E*, volume 76, number 6, pp. 061203–1–061203–16.

[215] Togun, H. (2016). Laminar CuO–water nano-fluid flow and heat transfer in a backward-facing step with and without obstacle. *Applied Nanoscience*, volume 6, number 3, pp. 371–378.

[216] Toosi, M. and Siavashi, M. (2017). Two-phase mixture numerical simulation of natural convection of nanofluid flow in a cavity partially filled with porous media to enhance heat transfer. *Journal of Molecular Liquids*, volume 238, pp. 553–569.

[217] Tseng, W. J. and Lin, K.-C. (2003). Rheology and colloidal structure of aqueous TiO_2 nanoparticle suspensions. *Materials Science and Engineering A*, volume 355, number 1, pp. 186–192.

[218] Tunstall, R., Laurence, D., Prosser, R. and Skillen, A. (2016). Benchmarking LES with wall-functions and RANS for fatigue problems in thermal-hydraulics systems. *Nuclear Engineering and Design*, volume 308, pp. 170–181.

[219] Umur, H., Yemenici, O., Umur, Y. and Sakin, A. (2017). Flow and heat transfer characteristics over rectangular blocked surfaces. *Experimental Heat Transfer*, volume 30, number 3, pp. 192–204.

[220] Vargaftik, N. B. (1975). *Tables on the thermophysical properties of liquids and gases: in normal and dissociated states*. Hemisphere Publishing Corporation, Washington, DC.

[221] Wang, L. and Fan, J. (2010). Nanofluids research: key issues. *Nanoscale Research Letters*, volume 5, number 8, pp. 1241–1252.

[222] Wang, X. and Li, X. (2009). Influence of pH on nanofluids' viscosity and thermal conductivity. *Chinese Physics Letters*, volume 26, number 5, pp. 056601–1–056601–6.

[223] Wang, X. and Mujumdar, A. (2008). A review on nanofluids - Part I: theoretical and numerical investigations. *Brazilian Journal of Chemical Engineering*, volume 25, number 4, pp. 613–630.

[224] Wang, X., Xu, X. and Choi, S. U. S. (1999). Thermal conductivity of nanoparticle-fluid mixture. *Journal of Thermophysics and Heat Transfer*, volume 13, number 4, pp. 474–480.

[225] Wang, Y. (1999). Heat transfer and pressure loss characterization in a channel with discrete flush-mounted and protruding heat sources. *Experimental Heat Transfer*, volume 12, number 1, pp. 1–16.

[226] Wasp, E. J., Kenny, J. P. and Gandhi, R. L. (1977). Solid-liquid flow: slurry pipeline transportation. *Bulk Materials Handling, United States*, volume 1, number 4.

[227] Wen, D. and Ding, Y. (2004). Experimental investigation into convective heat transfer of nanofluids at the entrance region under laminar flow conditions. *International Journal of Heat and Mass Transfer*, volume 47, number 24, pp. 5181–5188.

[228] Wen, D., Zhang, L. and He, Y. (2009). Flow and migration of nanoparticle in a single channel. *Heat and Mass Transfer*, volume 45, number 8, pp. 1061–1067.

[229] Wilcox, D. (1988). Reassessment of the scale-determining equation for advanced turbulence models. *AIAA Journal*, volume 26, number 11, pp. 1299–1310.

[230] Wilcox, D. (2006). *Turbulence Modeling for CFD, 3rd Edition*. DCW Industries, Lake Arrowhead (USA).

[231] Wong, K. V. and De Leon, O. (2010). Applications of nanofluids: Current and future. *Advances in Mechanical Engineering*, volume 2010, pp. 519659–1–519659–11.

[232] Xuan, Y. and Li, Q. (2003). Investigation on convective heat transfer and flow features of nanofluids. *Journal of Heat Transfer*, volume 125, number 1, pp. 151–155.

[233] Xuan, Y., Li, Q. and Hu, W. (2003). Aggregation structure and thermal conductivity of nanofluids. *AIChE Journal*, volume 49, number 4, pp. 1038–1043.

[234] Xuan, Y. and Roetzel, W. (2000). Conceptions for heat transfer correlation of nanofluids. *International Journal of Heat and Mass Transfer*, volume 43, number 19, pp. 3701–3707.

[235] Xue, Q. (2005). Model for thermal conductivity of carbon nanotube-based composites. *Physica B: Condensed Matter*, volume 368, number 1, pp. 302–307.

[236] Yakhot, V. and Orszag, S. A. (1986). Renormalization group analysis of turbulence. I. Basic theory. *Journal of Scientific Computing*, volume 1, number 1, pp. 3–51.

[237] Yang, Y., Oztekin, A., Neti, S. and Mohapatra, S. (2012). Particle agglomeration and properties of nanofluids. *Journal of Nanoparticle Research*, volume 14, number 5, pp. 1–10.

[238] Young, T. J. and Vafai, K. (1998). Convective cooling of a heated obstacle in a channel. *International Journal of Heat and Mass Transfer*, volume 41, number 20, pp. 3131–3148.

[239] Young, T. J. and Vafai, K. (1998). Convective flow and heat transfer in a channel containing multiple heated obstacles. *International Journal of Heat and Mass Transfer*, volume 41, number 21, pp. 3279–3298.

[240] Young, T. J. and Vafai, K. (1999). Experimental and numerical investigation of forced convective characteristics of arrays of channel mounted obstacles. *Trans. ASME, Journal of Heat Transfer*, volume 121, pp. 34–42.

[241] Zerradi, H., Mizani, S., Loulijat, H., Dezairi, A. and Ouaskit, S. (2016). Population balance equation model to predict the effects of aggregation kinetics on the thermal conductivity of nanofluids. *Journal of Molecular Liquids*, volume 218, pp. 373–383.

[242] Zonta, F., Marchioli, C. and Soldati, A. (2008). Direct numerical simulation of turbulent heat transfer modulation in micro-dispersed channel flow. *Acta Mechanica*, volume 195, number 1-4, pp. 305–326.